Development of open source microscopy including optical autofocus for automated imaging and single molecule localisation microscopy

Jonathan Peter Edwards Lightley

Photonics Group

Department of Physics

Imperial College London

Supervised by Prof. Paul M. W. French & Prof. Christopher Dunsby

2023

Thesis submitted in partial fulfilment of the requirements for the degree of Doctor of Philosophy (PhD)

Abstract

This PhD thesis presents the development of a cost-effective and open (hardware and software) microscopy platform able to perform automated single molecule localisation microscopy (SMLM) for super-resolved high-content analysis (HCA). The work is motivated by the desire to increase access to advanced microscopy techniques like SMLM and HCA, including in lower resourced communities. For SMLM I have utilised and refined *easySTORM*, a low-cost and robust implementation of *dSTORM*. For automated microscopy I have developed a novel optical autofocus module that can maintain focus lock during extended *easySTORM* acquisitions and maintain focus as the microscope images multiple fields of view (FOV) across a multiwell plate. Initially I worked with commercial microscope frames and then extended automated microscopy and *easySTORM* to a cost-effective, modular, open microscopy platform, "*openFrame*" that can be adapted to a wide range of microscopy modalities. For this, I combined the *openFrame* with a low-cost multimode diode laser bank and novel low-cost, cooled CMOS sensor cameras.

I developed two different hardware-based autofocus systems focussing near infrared laser beams from fibre-coupled diode laser sources onto the microscope coverslip with the back reflection being imaged at a secondary autofocus camera. The first autofocus technique presented uses two cylindrical lenses to create a collimated elliptical beam profile with differing confocal parameters (and therefore different range/precision) in orthogonal directions. The second autofocus technique presented utilises a slit to form the elliptical beam profile and then uses a convolutional neural network (CNN) to determine the microscope defocus from the autofocus camera images. The CNN autofocus was then able to operate robustly for months over a range of ±100µm and achieve an accuracy of greater than 200nm. I integrated this autofocus system with an automated multiwell plate *easySTORM* microscope applied to image focal adhesion structures within melanoma cells and bacteria undergoing phagocytosis in THP1 cells.

Declaration

I confirm that the work submitted in this thesis is my own, except where specifically referenced or acknowledged. I reuse content from my own published work in the Wiley's Journal of Microscopy and Wiley's Journal of Pathology Clinical Research. I have adapted figures from third-party works with permissions for Figure 2.4, Figure 2.5, and Figure 2.6.

The development of the neural network, presented in Chapter 6, was undertaken in collaboration with Dr Arinbjorn Kolbeinsson and Professor Seth Flaxman from the Department of Mathematics at Imperial College London. Throughout this thesis, I make use of *easySTORM* (presented in Chapter 3) repeatably, which was developed by members of the Photonics group at Imperial College London.

The *openFrame* concept, presented in Chapter 4, was conceived by Professor Paul French with contributions from others within the Photonics group at Imperial College London. The initial design and development of the *openFrame* was undertaken by Simon Johnson and Martin Kehoe at the Optomechanical Instrumentation workshop within the Optics section at Imperial College London. The *openFrame* CAD design was further developed by Dr Frederik Görlitz of the Photonics Group in collaboration with Cairn Research Ltd. Further development has been undertaken in collaboration with Cairn Research Ltd, developing additional modules which are compatible with the *openFrame*.

The nuclear pore complex U-2OS-CRISPR-NUP96-SNAP cells, that were imaged in Chapters 3, 4 and 5, were prepared by Dr Edwin Garcia and Ms. Mi Qi Lim within the Photonics Group at Imperial College London. The HeLa cells, presented in Chapter 4, the HEK293 cells, presented in Chapter 5, the FRTL5 Rat Follicular thyroid cells, presented in Chapters 4 and 5, and the NIH3T3 cells, presented in Chapter 7, were all prepared for imaging by Dr Edwin Garcia. The novel synthesised iFluor647 SNAP-tag-substrate which labels the nucleoporin NUP96 of the nuclear pore complexes was developed by Johannes Broichhagen from Leibniz-Forschungsinstitut für Molekulare Pharmakologie, Berlin.

The kidney histological biopsy samples, presented in Chapters 3 and 4, were provided by Dr Candice Roufosse from the Department of Immunology and Inflammation at Imperial College London and prepared for imaging by Dr Edwin Garcia.

The WM2664 melanoma cells, imaged in Chapter 7, were provided by Dr Vicky Bousgouni and Professor Chris Bakal at the Institute for Cancer Research, and were prepared for imaging by Dr Edwin Garcia. The THP-1 cells, presented in Chapter 7 were provided, and prepared for imaging, by Dr Riccardo Wysoczanski at the National Heart and Lung Institute.

Copyright Declaration

Publications and Conference Presentations

Journal Articles

- J. Lightley et al. Robust deep learning optical autofocus system applied to automated multiwell plate single molecule localization microscopy, J Microscopy 2021; https://doi.org/10.1111/jmi.13020
- E. Garcia et al. Application of direct stochastic optical reconstruction microscopy (dSTORM) to the histological analysis of human glomerular disease, Journal of Pathology Clinical Research 2021, Vol: 7, Pages: 438-445; http://doi.org/10.1002/cjp2.217
- R. Kalita et al. Single-shot phase contrast microscopy using polarisation-resolved differential phase contrast, Journal of Biophotonics 2021, Vol: 14, ISSN: 1864-063X; https://doi.org/10.1002/jbio.202100144
- J. Lightley et al. *openFrame*: A modular, sustainable, open microscopy platform with single-shot, dual-axis optical autofocus module providing high precision and long range of operation, J Microscopy 2023; https://doi.org/10.1111/jmi.13219

Conference Presentations

- F. Görlitz, J. Lightley, et al., Automated multiwell plate STORM: towards open source super-resolved high content analysis European Conference on Biomedical Optics 2019, Proc. SPIE 11076, Advances in Microscopic Imaging II, 1107605, https://doi.org/10.1117/12.2526940
- F. Görlitz, et al., Towards easier, faster super-resolved microscopy, BiOS: Conference on Single Molecule Spectroscopy and Superresolution Imaging XIII 2020, Proc. SPIE 11246, Single Molecule Spectroscopy and Superresolution Imaging XIII, 112460R (3 March 2020); https://doi.org/10.1117/12.2550682
- J. Lightley et al., Robust optical autofocus system utilizing neural networks applied to automated multiwell plate storm microscopy, Focus on Microscopy 2021 (oral presentation)
- J. Lightley et al. Robust Optical Autofocus System Utilizing Neural Networks Applied to Automated Multiwell Plate Storm Microscopy, Biophotonics Congress 2021: Optics in the

Life Sciences; https://doi.org/10.1364/BODA.2021.DTh2A.7 , (oral presentation, student paper prize finalist)

- J. Lightley et al. Robust optical autofocus system utilizing neural networks applied to automated multiwell plate STORM microscopy, European Conference on Biomedical Optics 2021 (invited talk)
- R. Kalita et al. Single-shot quantitative phase contrast using polarisation-resolved differential phase microscopy, European Conference on Biomedical Optics 2021
- J. Lightley, et al., Modular, sustainable, low-cost, open microscopy and high content analysis, Microscience Microscopy Congress 2021 (Poster presentation first prize in Frontiers in Bioimaging)
- S. Kumar, J. Lightley, et al., Low-cost, sustainable, modular open microscopy and high content analysis, European Light Microscopy Initiative 2021 (poster presentation)
- E. Garcia, J. Lightley, et al., Application of low-cost stochastic optical reconstruction microscopy to the histological analysis of human glomerular disease, European Light Microscopy Initiative 2021 (poster presentation)
- E. Garcia, J. Lightley, et al., Application of low-cost stochastic optical reconstruction microscopy (dSTORM) to the histological analysis of human glomerular disease, 33rd European Congress of Pathology 2021 (poster won the Mihatsch-Ferluga-Award of the ESP Nephropathology Working Group)
- J. Lightley, et al., Open-Source High Content Analysis Platform Including Automated Multiwell Plate Super-Resolved Microscopy, Focus on Microscopy conference 2022 (oral presentation)
- W. Flanagan, Huihui Liu, et al., Single-shot semi-quantitative phase contrast microscopy using polarisation-resolved differential phase contrast, Focus on Microscopy conference 2022

To my family

Acknowledgments

Firstly, I would like to thank my PhD supervisors Paul French and Chris Dunsby for giving me the opportunity to undertake this project and for all the guidance, support, ideas, and advice they have provided throughout my PhD.

A lot of the work presented in this thesis would not have been possible without the support of many people. Particularly, I would like to thank Sunil Kumar for all your wisdom and your constant willingness to help in the lab, and Edwin for your enthusiasm and for staying late for the countless late night imaging sessions! I would also like to give special thanks to Frederik Görlitz for your friendship and guidance during the beginning of my project.

I would like to thank all the members of the Photonics Group: Connor, Liuba, Anita, Daniel, Sam, Jack, Joel, Riccardo, Meizhu, Meizhen, Ara, Leo, HuiHui, Andrew, Yuchen, Cheryl, Mark, James, Mike, Ranjan, Hugh, Nathan, Nils, Yuriy, Hai, Anupam, Terry, Wenjun, MiQi, Zhonghe, Bill, Dan, Matt, Wenzhi, Karishma, Wim, Will, Abdul, Ronan, Goronwy, Niall, Steven, Sara and many others. Thank you all for the trips to the pub, afternoon teas, summer trips, Christmas parties (and infusions!), Photonics film nights, badminton, squash, 5-a-side football, table tennis, board game nights and pub quizzes. A special thank you to the members of the “Core Crew” and “MUBI gang” for the many trips to Curzon Mayfair and the BFI Southbank to watch films together!

I would like to thank Martin, Simon and John in the Optics workshop for all the hardware components they have designed and built, after a rather poor description from myself, and for all the chats about James Bond, football, 80’s films and running. Thank you to Judith and Marcia for all your help with navigating the complexities of college’s administration.

Thank you to Hortense for your patience, support and understanding whilst I was writing up.

I would like to acknowledge the Engineering & Physical Sciences Research Council for funding my PhD.

Finally, I would like to thank all my family and friends for all the love and support you have provided throughout my PhD and beyond. Thank you especially to my parents for their constant assistance, patience, and encouragement.

Contents

Abstract 2
Declaration 4
Copyright Declaration 5
Publications and Conference Presentations 6
Acknowledgments 9
List of Figures 13
List of Tables 23
1. Thesis Overview 24
2. Optical Microscopy 27
2.1 Brief History of Optical Microscopy 27
2.2 High Content Analysis 29
2.3 Diffraction limited resolution 30
2.4 Fluorescence 32
2.5 Optical Microscopy Imaging Modalities 38
2.5.1 Brightfield Microscopy 38
2.5.2 Widefield fluorescence microscopy 38
2.5.3 Confocal Microscopy 40
2.5.4 Multiphoton Microscopy 43
2.5.5 TIRF Microscopy 45
2.5.7 Light sheet Microscopy 48
2.5.8 Optical projection Tomography 49
2.6 Super resolution modalities 50
2.6.1 Structured illumination microscopy 51
2.6.2 Stimulated emission depletion microscopy 53
2.6.3 Single molecule Localisation microscopy 54
2.7 Conclusion 63
3. EasySTORM 65
3.1 Implementation of *easySTORM* on commercial microscope frames 65
3.1.1. *openExcite* module 68
3.1.2 TIRF and HILO microscopy 69
3.2 easySTORM images of Nuclear Pore Complexes 71
3.3 histoSTORM 75
3.4 Conclusion 80
4. Low-cost, modular, sustainable open-source microscopy 82

4.1 Exemplar open microscope systems 83
4.2 Design and implementation of *openFrame* microscopes 86
4.2.1. *openExcite* 90
4.3. Cost-effective multiline laserbank 92
4.3.1 Low-cost laser drivers 92
4.3.2 Low-cost multiline laserbank 96
4.3.3 Uniformity of excitation using multimode diode lasers and optical fibres 98
4.4 Low-cost cameras for fluorescence microscopy and SMLM 100
4.5 Implementation of *easySTORM* on *openFrame* microscope 108
4.6 Conclusion 115
5. Development of an optical autofocus module 116
5.1 Motivation for high-throughput microscopy 116
5.2 Introduction to autofocus techniques 117
5.2.1 Software-based autofocus techniques 118
5.2.2 Hardware-based autofocus techniques 121
5.3 Knife-edge centroid autofocus 124
5.3.1 HCA STORM using knife-edge autofocus 127
5.4 Slit-based autofocus 128
5.4.1 Implementation of slit-based optical autofocus on an *openFrame* microscope 131
5.4.2 Comparison of slit-based and knife-edge-based autofocus systems: temperature variations 131
5.4.3 Comparison of slit-based and knife-edge-based autofocus systems: simulated system drift 133
5.5 Cylindrical lens autofocus 136
5.5.1 Single shot autofocus 138
5.5.2 Closed-loop autofocus 142
5.5.3 Incoherent light sources 145
5.6 Autofocus control software 147
5.7 Conclusion 148
6. Neural network-enabled optical autofocus module 149
6.1 Introduction to neural networks 149
6.2 Previous autofocus neural networks 151
6.3 MobileNetV2 Autofocus 154
6.3.1 Network architecture 154
6.3.2 Optical setup 160
6.2.3 Implementation 162

6.3.4 Data Acquisition and Preparation 164
6.4 Autofocus performance using a single-day training dataset 166
6.5 Autofocus performance using a multiple-day training dataset 170
6.6 Performance of Autofocus 171
6.7 Conclusion 176
7. Automated easySTORM High Content Analysis 178
7.1 Implementation of automated multiwell plate *easySTORM* for super-resolved HCA 179
7.1.1 Automated easySTORM implemented on an Olympus IX81 microscope 179
7.1.2 Automated easySTORM implemented on an *openFrame* microscope 181
7.1.3 Development of HCA-STORM *µManager* plugin 182
7.1.4 Simultaneously acquired two-channel *easySTORM* 185
7.2 exemplar easySTORM HCA applications to cell biology 186
7.2.1 Melanoma WM2664 multiwell plate STORM 187
7.2.2 THP1 cells 189
7.3 Conclusion 190
8. Conclusions and Outlook 192
8.1 Concluding remarks 196
References 197
Appendix 212
A1. Permission to reproduce third party work 212
A2. Open source EasySTORM component parts lists 234
A3. Components list for an easySTORM microscope implemented on an openFrame 238
A4. Github links 242

List of Figures

Figure 2.1. A Jablonski diagram showing the processes of fluorescence and phosphorescence. The ground state is $S0$, $S1$ and $S2$ are the first and second excited singlet states. $T1$ is the first excited triplet state. Non radiative processes are indicated by dashed lines. 34
Figure 2.2. Diagrams showing different illumination techniques for microscopy imaging; (a) widefield epi-fluorescent illumination, (b) light-sheet illumination, (c) illumination for optical projection tomography (OPT), (d) confocal microscopy illumination, (e) multi-photon excitation 37
Figure 2.3. Diagram showing TIRF illumination (orange), HILO illumination (green) and widefield epi-illumination (blue) for a high numerical aperture oil immersion objective (NA≈1.45). An evanescent field extends for a few hundred nanometres above the interface between the coverslip (n≈1.518) and the sample media (n≈1.33-1.38) for TIRF illumination. The HILO illumination excitation beam is introduced at a smaller radial distance from the centre of the back focal plane compared to TIRF. HILO can illuminate to greater depths than TIRF 48
Figure 2.4. The concept of Gustafsson's method for SIM. (a) Region of support for the microscope. Low spatial frequencies are at the origin and higher spatial frequencies are further from the origin. The edge of the region of support is given by Abbe's limit and represents the maximum spatial frequency that can be resolved by the microscope. (b) Fourier transform of a coherently illuminated sinusoidal grating with the ±1st orders positioned at the edge of the back aperture of the objective (c) the extended observable region with two offset regions demonstrating frequencies that have been shifted by Moiré fringes (d) The extended OTF formed from three rotations of (c) formed by using different orientation and phase of the illuminated pattern, it is possible to recover spatial frequencies up to twice that defined by Abbe's diffraction limit. (Images recreated from those presented by (Gustafsson, 2000)) 52
Figure 2.5. Image of a PSF distribution from a single fluorescent emitter recorded by a pixelated sensor. A small shift in the emitter's lateral position results in a noticeable asymmetry in the measured pixel digital number values. A Gaussian can be fitted to these distributions to give a prediction of the localisation to sub-pixel precision. Image from Small et al. (Small & Stahlheber, 2014) 55
Figure 2.6. Schematic of first implementation of STORM. Cy5-Cy3 dye switch pairs are used to label a sample. The Cy5 dye is all initially switched to a stable dark state using a high power 633nm pulse. A random subset of fluorophores are switched to the on-state after illumination by a 532nm source. The sample is then re-excited by a continuous 633nm source exciting fluorescence before the cy5 dye returns to the dark state. The fluorophores that have emitted are localised. Then another subset of fluorophores is switched to the "on" fluorescent state by the 532nm source. This cycle repeats until all the fluorophores have been localised. Figure adapted from Rust el al. (Rust, Bates & Zhuang, 2006) 57
Figure 2.7. Jablonski diagram showing the energy levels involved in dSTORM. A fluorophore is excited to the first singlet state $S1$ from the ground state $S0$, under excitation from a single laser source. Then it can either fluoresce or undergo intersystem crossing into a triplet state $T1$. In the presence of a reducing agent, e.g., a thiol, the triplet state can be reduced to a radical anion $F \cdot -$. This is the very long lived dark "off" state of the dye used in dSTORM. The fluorophore can then return to the ground state through either irradiance by UV light or interaction with oxygen. Some dyes can be fully reduced from the radical anion state to the leuco-form of the fluorophore (FH). From here they can react with oxygen to return to the ground state $S0$ 62

Figure 3.1. Diagram of optical configuration of *easySTORM* implemented on a standard inverted fluorescence microscope frame using an *openExcite* laser excitation module. By adjusting the tip and or tilt of the mirror (M1) in the *openExcite* module, the position where the beam focusses in the back aperture of the objective lens can be adjusted (see inset top right) to switch between epi-illumination (dashed line), HILO (shaded), or TIRF (solid) if supported by the objective lens. To realise TIRF, it is necessary to focus the excitation laser within the indicated annular region, δ. See Figure 4.6 for diagram of multimode laser diode laserbank. 67
Figure 3.2. *openExcite* CAD rendition (Thorlabs and Edmund Optics component part numbers indicated) 68
Figure 3.3. (a) image of U-2OS nuclei showing Nup96 proteins in nuclear pore complexes endogenously labelled with a SNAP-tag AF647; (b) magnified region of interest from (a) containing a nucleus; (c) magnified region of interest of nuclear pore complexes within the nucleus shown in (b). A line profile across the diameter of one of the nuclear pore complexes is shown. A double Gaussian fit has been plotted to the line profile (d), where the amplitudes, stand deviations and central positions of the two Gaussians are used as fit parameters together with a global offset to account for the background intensity level..... 72
Figure 3.4. (Top) Rendered *easySTORM* images of U-2OS nuclei acquired on the Zeiss Axiovert 200 microscope frame under TIRF, HILO and epi-illumination. Each FOV was acquired using the Photometrics Prime 95B sCMOS camera with 20,000 frames of 80 ms exposure. (Bottom) Corresponding magnified ROIs showing individual nuclear pore complexes for the respective illumination modalities. 75
Figure 3.5. (a-b) Widefield immunofluorescence images of frozen membranous glomerulonephritis biopsy samples with (a) the laminin labelled with Alexa Fluor 555 (green) and (b) IgG deposits labelled with iFluor 647 (red). (c) shows a two colour merged image of the ROI indicated in (a, b). (d, e) show the widefield IF image and corresponding *histoSTORM* image of the ROI indicated in (c). (e) has been rendered at 25 nm resolution. (f) shows an EM image acquired at 5500x magnification of a similar structure as (e) from the same biopsy. (g, h) show magnified widefield and *easySTORM* images of the 3.2 µm x 2.4 µm ROI indicated in (d, e). (i) shows the magnified EM ROI indicated in (f), in which the yellow dashed line indicates the location of the GBM (light grey), and the purple arrows point to the dark grey regions indicating the immune complexes that contain IgG on the subepithelial side. Reproduced from (Garcia et al., 2021) 77
Figure 3.6. Widefield (a, c) and easySTORM (b, d) images of minimal change disease in FFPE section from a biopsy. (c) and (d) show enlarged ROIs indicated by the yellow boxes in (a) and (b). Laminin present in the GBM is labelled with iFluor 647. (e) shows an EM image of the GBM from a different section within the same biopsy imaged with a magnification of 15,500x. The GBM thickness was measured using EM to be 281 nm. The FWHM of the line profile of the yellow lines in (c) and (d) measure the thickness of the GBM from the widefield and STORM reconstruction. The widefield gives a measured thickness of 657 nm and the STORM gives a measured thickness of 212 nm. Reproduced from (Garcia et al., 2021) 78
Figure 3.7. Widefield (a, d, e, f) and dSTORM (b, g, h, i) images of Lupus nephritis type IV in frozen sections. The basement membrane is labelled by staining of the laminin using Alexa Fluor 555 (green) and the IgG deposits are stained with ifluor 647 (red). The yellow box indicates the expanded regions in (d) and (g) showing Lupus Nephritis presenting mesangial deposits. The blue boxes indicate the expanded regions in (e) and (h), and present regions with subendothelial deposits. The purple boxes indicate the expanded regions as shown in (f) and (i) presenting regions with subepithelial deposits. (c) shows an EM of a similar structure from within the same sample imaged at 8000x magnification. The dark grey regions represent electron dense deposits that contain IgG. The purple arrows indicate deposits on the subepithelial side of the GBM. The blue arrows show deposits

on the subendothelial side of the GBM, and the yellow star indicates mesangial deposits. Reproduced from (Garcia et al., 2021) 79
Figure 4.1. (a) shows a schematic of a simple arrangement of an openFrame for automated easySTORM (Kwakwa et al., 2016). The top layer contains a short pass dichroic and has the objective mounted on a L-shaped bracket attached to an encoded linear Z-stage. There is an automated XY stage with a sample above. The excitation source is introduced from the layer below the autofocus layer. The excitation beams are reflected by a multiline dichroic and fluorescence is transmitted by the dichroic. The fluorescence is then focused by the tube lens mounted horizontally inside the openFrame and forms an image on the camera after the signal is reflected by a mounted mirror. (b) shows a CAD of the openFrame showing the different layers, stage adaptor plate, and base plate with mounting slots and countersunk holes. (c) shows the openFrame arranged for HCA STORM imaging. There is a vertical transilluminator, the openExcite module which provides the multiline excitation via a multimode fibre source. There is an automated XY stage and an automated piezo Z-stage. 86
Figure 4.2. (a) shows a photo of the original prototype *openFrame*. This version was built in Imperial Photonics group's Optomechanical Instrumentation Workshop. The layers were machined using a lathe and CNC milling machine. The setup above shows the frame arranged with an Olympus manual XY stage mounted on a stage adaptor top layer plate. Beneath the stage layer is the excitation layer with a Thorlabs dichroic cube mounted and a 30mm input for the excitation laser source. Below the excitation layer is a layer housing the tube lens. Below the tube lens is the camera layer with a 60mm smooth bore output to the camera and 60mm spaced Thorlabs cage system. And finally, at the bottom of the frame is a base layer which can be fixed to an optical bench using L-shaped brackets and M6 screws. (b) shows a view looking down the centre of the frame along the optical axis defined by the objective and the centred tube lens. The dichroic cube containing the dichroic, excitation filter and emission filter can be seen mounted and positioned in the centre of the optical axis. Beside the dichroic is the mounting bracket that a piezo linear Z-stage could be mounted to, and the objective is attached to the stage using an L-shaped bracket 87
Figure 4.3. *openExcite* CAD rendition (Thorlabs and Edmund Optics component part numbers indicated) 91
Figure 4.4. A schematic showing the wiring for the TLV5618AIP DAC to convert the digital output signal to an analogue modulation signal for the Lasertack iLD series laser diode drivers. 93
Figure 4.5. (a) Schematic of homebuilt laser driver and TEC controller built with a Lasertack iLD Series Laser diode driver, TLV5618AIP DAC and Arduino Uno (b) Photos of laser driver controller 95
Figure 4.6. Home-bult multiline laserbank for *easySTORM* excitation using high power multimode diode lasers. 98
Figure 4.7. Improvement in field homogeneity through the vibration of a multimode fibre. Figures (a, b) show images acquired by an Andor Zyla 5.5 when imaging a thin film of fluorescent highlighter pen fluid illuminated by a 635nm Lasertack multimode diode via a multimode fibre. Left (a, c): shows the FOV when the fibre is vibrated using a CAIRN despeckler unit. Right (b, d): The fibre is not vibrated and there is a speckle pattern in the illumination. The yellow lines in (a) and (b) indicate where the line profiles shown in (c) and (d) are taken from. 99
Figure 4.8. Top images: Widefield and *easySTORM* reconstructions of tubulin in a FRTL5 Rat Follicular thyroid cell line decorated with AF488 for the CellCam Centro, CellCam Kikker and Andor Zyla 5.5 camera. All images acquired on the same day and reconstructed from 10000 frames with 30ms exposure. 104
Figure 4.9. NanoJ-SQUIRREL SMLM reconstruction analysis of cameras and FOVs as shown in Figure 4.8. Images on the left show an error map from comparing the super-resolved reconstructions with the widefield images. Regions with a low error are shown in purple, regions with higher error are

shown in yellow. The middle column images show Fourier ring correlation (FRC) maps of the same FOVs. The localisations were split into odd and even frames and used to create two reconstructions. The images were segmented into 100 regions and FRC analysis was then performed on each region. The minimum FRC value in each image is given and the resolution scaled Pearson-correlation (RSP) is provided for each error map. Images on the right show an overlap image of the STORM reconstruction and the FRC map to highlight the FRC regions containing localisations. 105
Figure 4.10. *easySTORM* reconstructions of tubulin in a FRTL5 Rat Follicular thyroid cell line decorated with AF647 acquired using the CellCam Centro, CellCam Kikker and Photometrics Prime 95B cameras. All images reconstructed from 10000 frames with 30 ms exposure. 108
Figure 4.11. NanoJ-SQUIRREL SMLM reconstruction analysis of cameras and FOVs as shown in Figure 4.10. Images on the left show an error map from comparing the super-resolved reconstructions with the widefield images. Regions with a low error are shown in purple, regions with higher error are shown in yellow. The middle column images show Fourier ring correlation (FRC) maps of the same FOVs. The minimum FRC value in each image is given and the resolution scaled Pearson-correlation (RSP) is provided for each error map. Images on the right show an overlap image of the STORM reconstruction and the FRC map to highlight the FRC regions containing localisations. 110
Figure 4.12. *easySTORM* implementation on the openFrame using the *openExcite* module 111
Figure 4.13. Widefield (left) and *easySTORM* (right) images of HeLa cells with tubulin immunolabelled with iFluor 647 and acquired on the openFrame using a Photometrics Iris 9 camera. Top row shows whole FOV imaged, and centre and bottom rows show zoomed in views of the top and bottom regions respectively indicated by the yellow squares in the top left panel. 112
Figure 4.14. Whole FOV (a) epifluorescence widefield and (b) *easySTORM* images of a FFPE section presenting with Lupus nephritis imaged on the *openFrame* using a CellCam Kikker, with a 0.35X Motic adaptor. (c) shows a zoomed Roi indicated in (b) by the yellow box. (d) shows a line profile section through the GBM, with an indicated FWHM thickness of 89nm. 113
Figure 4.15. HILO illuminated whole FOV (a) widefield and (b) *easySTORM* reconstruction of fixed U-2OS-CRISPR-NUP96-SNAP-iFluor647 cells from 80000 frames at 60ms exposure. (c-f) show zoomed ROIs indicated in (b). The expanded ROIs show the sub-units are resolved within the nuclear pore complexes. Images were acquired on an *openFrame* microscope and imaged using a CellCam Kikker, using a 0.35X Motic adaptor. Axial drift was continuously corrected using the closed loop autofocus presented in Chapter 5. 114
Figure 5.1. showing the optical setup for a knife-edge-based centroid autofocus using an infrared, 830 nm, fibre coupled source implemented on an Olympus IX81. The path of the autofocus beam is represented by the red line. The output from the fibre is collimated by an 18.4 mm focal length aspheric lens, (Thorlabs C280TMD-B), and bisected by a knife-edge mask. The beam then passes an excitation filter, CU1 (Edmund 65-119), and is steered by a pair of mirrors. The beam is reflected by a 50:50 beamsplitter, BS1 (Edmund 47-026), a short pass dichroic, BS2 (Edmund 69-220) and a custom multiline dichroic, BS3 (Chroma ZT405_465_625_825rpc-UF2). An image of the knife-edge is formed on the back focal plane of the objective (Olympus UplanFL 100x, NA 1.3, oil) using a 100 mm focal length lens L3 (Thorlabs AC254-100-B-ML) and a 200 mm focal length Lens L4 (Edmund 49-364). The bisected beam is reflected at the interface between the coverslip and the sample before propagating back through the system. Here it is transmitted by the 50:50 beam splitter, BS1, and a clean-up bandpass filter, CU2 (Edmund 65-180), before being imaged onto a secondary autofocus USB camera (FLIR CM3-U3-31S4M-CS). 120
Figure 5.2. showing the image formed on the full FLIR CM3-U3-31S4M-CS camera sensor (2048x1536 pixels) of the bisected autofocus beam as the sample is passed axially through focus. The images were acquired every 5 microns. The defocus in the images increase in axial height scanning from left

to right along each row from -110µm (top left) to +90µm (bottom right) through focus. A 6.4mm focal length lens was used to collimate the beam out of the fibre. 123
Figure 5.3. Centre of mass (CoM) position of the distribution of light on the camera as a function of sample defocus for the knife-edge-based autofocus system shown in Figure 5.2. This calibration data was used as a look-up table for the image data shown in Figure 5.4. The linear range is approx. 13 µm. The raw image data was acquired in 200 nm step intervals. 125
Figure 5.4 A figure showing automatically acquired HCA acquisition of HEK293 cells arrayed in two wells of an 8 well chamber slide. 4 FOV's were acquired in each well. The cells in A1 were labelled with a mouse primary antibody (Sigma Aldrich T8203 clone AA13, Lot:013M4788V, 1:1000) and the secondary antibody was a donkey anti-mouse conjugated with Alexa Fluor 647 (ThermoFisher Scientific catalogue A31571, Lot:1692912). The cells in A2 were labelled with a rabbit primary polyclonal antibody (Abcam ab18251, Lot:GR275948-1, 1:1000) and a goat anti-rabbit secondary antibody (ThermoFisher Scientific A-21244) conjugated with Alexa Fluor 647. (a) shows the automatically acquired widefield images of the same super-resolved reconstructed FOV's shown in figure (b). The focus was maintained using the knife-edge centroid autofocus technique. 126
Figure 5.5. The optical system for the slit-based autofocus implemented on an Olympus IX81 frame. An 830 nm laser diode (Ushio HL8337MG), was coupled into a single mode fibre with a 0.1 NA and the output of the fibre was used as the source for the autofocus. The beam was collimated using an 18.4 mm aspheric lens (Thorlabs C280TMD-B). The collimated beam was masked using a rectangular slit with a slit size of 1.2 mm. This resulted in a collimated rectangular beam (3.6 mm and 1.2 mm respective diameters), propagating through the optical system. The beam diameter was magnified by a factor of 2 using a 100 mm focal length lens, lens L3 (Thorlabs AC254-100-B-ML), and a 200 mm focal length lens, L4 (Edmund 49-364). In between these lenses, the beam was reflected first by a 50:50 beamsplitter, BS1 (Edmund 47-026), and then by an 800 nm shortpass filter, BS2 (Edmund 69-220). The beam was then reflected by a purpose designed multiline dichroic for use with multi-channel STORM excitation, BS3 (Chroma ZT405_465_625_825rpc-UF2). The rectangular beam was then focused onto the sample by a 100x objective (Olympus UplanFL 100x, NA 1.3, oil) and reflected at the refractive index change between the coverslip and the sample's media. The reflected signal then propagated back through the system and was transmitted by the 50:50 beamsplitter, BS1, before being imaged by an auxiliary autofocus camera, Flir Chameleon3 (FLIR CM3-U3-31S4M-CS). CU1 (Edmund 65-110) and CU2 (Edmund 65-180) are clean up bandpass filters 129
Figure 5.6 Implementation of the slit autofocus on the openFrame. An 830 nm laser diode (Ushio HL8337MG) was coupled into a single mode fibre with a 0.1 NA and the output of the fibre was used as the source for the autofocus. The beam was collimated using an 18.4 mm aspheric lens (Thorlabs C280TMD-B). The collimated beam was masked using a rectangular slit with a slit size of 1.2 mm. This resulted in a collimated rectangular beam (3.6 mm and 1.2 mm respective diameters), propagating through the optical system. The beam was transmitted first by a 50:50 beamsplitter, BS1 (Edmund 47-026), and then reflected by an 800 nm shortpass filter, BS2 (Edmund 69-220). The rectangular beam was then focused onto the sample by a 100x objective (Olympus UplanSApo 100x, NA 1.40, oil), and reflected at the refractive index change between the coverslip and the sample's media. The reflected signal then propagated back through the system and was reflected by the 50:50 beamsplitter, BS1, before being imaged by an auxiliary autofocus camera, Flir Chameleon3 (FLIR CM3-U3-31S4M-CS) using lens L3 (Thorlabs AC254-200-B-ML). CU1 (Edmund 65-110) and CU2 (Edmund 65-180) are clean up bandpass filters 130
Figure 5.7. 96-well plate image acquisitions of one 100 nm tetraspeck bead in each well acquired using (a) centroid metric utilising a knife edge and (b) standard deviation of the mean projection intensity along the axes. Each sub-image shows the bead image acquired in a different well. The wells were acquired starting in the top left well (A1), moving straight down column 1, one well at a

time until after imaging H1. After imaging H1, the image in H2 was acquired. Then the acquisition proceeded vertically up column 2. The wells were then accordingly acquired in this snake pattern down and up the columns. After 1hr20min into the experiment, the system was imaging well A4. After 2hr40min since experiment start, the system was imaging well A8. 132
Figure 5.8. Simulated drift of translated cropped images from the autofocus camera. Images were shifted in half integer values of the focal spot size. The results for the knife-edge centroid based autofocus are shown on the left (a, c) and the slit-based standard deviation autofocus results on the right (b, d). As the drift was induced in the images, the current defocus was predicted from the original calibration stack. The induced drift caused the centroid values, associated with the knife-edge, to be shifted to larger values. This created an error when predicting the defocus with a constant offset. Whereas the standard deviation approach was able to correctly predict the defocus as the drift was introduced and the values did not shift from the calibration plot. 134
Figure 5.9 Induced drift of images acquired from the autofocus camera using a micrometre stage to shift the image position on the sensor. Images were shifted in half integer values of the focal spot size. The results for the knife-edge centroid based autofocus are shown on the left (a, b) and the slit-based standard deviation autofocus results on the right (b, d). As the drift was induced in the images, the current defocus was predicted from the original calibration stack. The induced drift caused the centroid values, associated with the knife-edge, to be shifted to larger values. This created an error when predicting the defocus in the form of a constant offset. In contrast, the standard deviation approach was able to perform better at predicting the defocus as the drift was introduced. The maximum error predicted from the knife-edge approach was 700 nm, compared with 125 nm for the standard deviation technique when considering an image drift up to three times the focal spot size. 136
Figure 5.10. Implementation of the cylindrical lens autofocus on the openFrame. An 830 nm laser diode (Ushio HL8337MG), or an 840nm SLD (Superlum SLD-840F50P05S-TOSA9), is coupled into a single mode fibre with a 0.1 NA and the output of the fibre was used as the source for the autofocus. The beam is collimated in by a 6.4 mm focal length cylindrical lens, CL1 (Thorlabs LJ1227L1-B), and by a 20 mm focal length cylindrical lens, CL2 (Thorlabs LJ1960L1-B), which are orientated at 90^{O} to each other to produce an elliptical beam profile. CU1 (Edmund 65-180) is a clean-up long pass filter. The beam is steered using a mirror and a 50:50 beamsplitter, BS1 (Edmund 47-026), which it reflects off, and then is reflected by an 800 nm shortpass filter, BS2 (Edmund 69-220). The elliptical beam is then focused onto the sample by a 100x objective (Olympus UplanSApo 100x 1.40 oil) and reflected at the refractive index change between the coverslip and the sample's media. The reflected signal was then propagated back through the system and was transmitted by the 50:50 beamsplitter, BS1, before being imaged by an auxiliary autofocus camera (FLIR Chameleon3 CM3-U3-31S4M-CS) by a 200mm focal length lens L5 (Thorlabs AC254-200-B-ML). Reproduced from (Lightley et al., 2023) . 137
Figure 5.11. FWHM of the Fourier transform power spectrum of the two projections of average intensity along the horizontal and vertical axes of the sensor of the FLIR Chameleon3 CMOS camera. The red and blue peaks represent the autofocus metrics for the short confocal parameter and long confocal parameter respectively. The Green plot shows the average intensity in the image after a background subtraction. As the 20 mm focal length lens has been positioned slightly further away than its focal length from the fibre, it focuses onto the sample 2 microns axially above the blue peak. This enables closed loop single-shot autofocus..... 139
Figure 5.12. (a) shows a 96 well plate arrayed with 100 nm Tetraspeck beads that was scanned using autofocus with a z-stack acquired in each well. PSFJ was used to determine the in-focus axial plane for each bead and the mean offset from the centre image provided the error in the defocus for each well - shown with associated heatmap of defocus in microns. (b) shows a histogram of errors in defocus for the 96-wellplate. The grey region shows the depth of field. Figures (c, d), system was

refocussed 10 times from range of known defocus offsets for the longer (c) and shorter (d) range autofocus prediction. Errors in predicted defocus are plotted (boxplots with mean error, interquartile range and outliers). Red highlighted region shows depth of field of microscope objective lens. The depth of field for this fluorescence microscope with 100x, 1.4 NA objective lens was ~0.65 µm for an emission wavelength of 680 nm. Reproduced from (Lightley et al., 2023)..... 141
Figure 5.13. STORM reconstruction of thyroid cells with the tubulin labelled with ifluor647 acquired on the openframe using a CellCam kicker camera. (a) Continuous closed-loop autofocus correction was used (b) Continuous closed loop autofocus correction was not used 143
Figure 5.14. *easySTORM* reconstructions of fixed U-2OS-CRISPR-NUP96-SNAP-iFluor647 cells from 80000 frames at 30 ms exposure with HILO illumination acquired on the *openFrame* using the CellCam Kikker camera. Top row: frames were acquired with continuous autofocus correction. Bottom row: 80000 frames were acquired without autofocus correction. (A, B) show zoomed regions indicated in easySTORM reconstruction with continuous autofocus correction. (C, D) show zoomed regions indicated in easySTORM reconstruction without autofocus correction. The sub-units within the NPC are resolved when using the autofocus correction but are not without using the autofocus. Reconstructions performed using Picasso (Schnitzbauer et al., 2017)..... 144
Figure 5.15. (a) and (b) show montages of images of an axial fly-through of focus of the cylindrical lens autofocus when using a laser diode and SLD source respectively. The montages show images every 5 µm over a range of ±60 µm. The top left image in each montage is acquired at -60 µm. The axial defocus increases from left to right along the columns and from top to bottom. The bottom right image in each montage is at +60 µm. Figures (c) and (d) show the same axial z-stacks but with a background subtraction for the laser diode and SLD sources. As can be seen in figures (a) and (c), the background subtraction couldn't remove all structured features from the background as the source is coherent. This meant the interference pattern changed with focus. This interference structures prevented the autofocus from working when using the Fourier transform metric. Whereas in figures (b) and (d), it can be seen that the background can be subtracted as it is a constant background from an incoherent source. This meant that there is a better signal, for the autofocus metric. 146
Figure 5.16. User interface of *µManager* 2.0 autofocus plug-in. 147
Figure 6.1. Figure showing the function of a standard convolutional layer: (a) shows an input feature map with shape $F = DF \times DF \times M$ into a convolutional layer to produce an output feature map with shape $G = DG \times DG \times N$; (b) shows the N standard convolutional kernel filters with shape $DK \times DK \times M$ 155
Figure 6.2. A figure demonstrating how a standard convolutional layer can be replaced by a depthwise convolutional filters followed by pointwise convolutional figures. (a) shows a set of standard convolutional filters (b) shows a set of depthwise convolutional layers and (c) shows a set of pointwise convolutional layers 156
Figure 6.3. Diagram showing the function of the 2 step depthwise convolutional layer on an example 9x9x3 input feature map. The 3x3x1 depthwise kernel filters are used to produce an intermediate feature map of shape 7x7x3. The pointwise convolutions, with shape 1x1x3, are then used on the intermediate feature maps to produce the final output feature map. 5 pointwise filters are used to achieve 5 output channels. The output is the same as would be achieved with a standard convolutional layer with 5 kernel filters, each with a shape of 3x3x3, using a stride of 1 and zero padding 157
Figure 6.4. (a) table of the MobileNetV2 architecture used. Every row represents a sequence of layers, and these are repeated by the number indicated in the repeats column. For each sequence, the first layer uses the stride length indicated in the final column and a stride length of 1 is used for the remaining layers. This maintains the number of output channels for each repeat within each sequence of repeated bottleneck layers. When a stride of 2 is used, the dimensionality for the input

of the next row of the table is halved. (b) shows the different architectures of the stride = 1 and stride = 2 bottleneck blocks in the model. Figure reproduced from (Lightley et al., 2022) 159
Figure 6.5. Schematic of the optical autofocus implemented on an Olympus IX81 microscope frame used for HCA easySTORM (Kwakwa et al., 2016). The objective lens was an oil immersion 1.3 NA 100x lens (Olympus, UplanFl 100x, NA 1.3, oil) with a depth of field of ~600 nm. The focal lengths of the other lenses were L1: 50mm (Thorlabs, AC254-050-A-ML), L2: 18.4mm (Thorlabs C280TMD-B), L3: 100mm (Thorlabs, AC254-100-B-ML), L4: 200mm (Edmund Optics 49-364), L5: 180mm (Olympus tube lens). Figure reproduced from (Lightley et al., 2022) 161
Figure 6.6. Map of variation of axial focus position of bottom of glass 96-well plate in µm relative to the focus at the centre of well A1 (Brooks life Science Systems, MGB096-1-2-LG-L). Figure reproduced from (Lightley et al., 2022). 163
Figure 6.7. Images of exemplar image z-stacks acquired on the autofocus camera as the sample coverslip is translated through the focus of the microscope objective lens: (a) shows a z-stack used to train the “short-range” model over a range of -10 µm to +10 µm acquired in 50 nm step intervals. An image is shown every 1 µm in the stack. (b) shows a z-stack stack used to train the “long-range” model over a range of -100 µm to +100 µm acquired in 1 µm step intervals. An image is shown every 10 µm in the stack. The grey feature visible on the left-hand side of the FOV is a back-reflection from the excitation lens, L4 in Figure 6.5. 164
Figure 6.8. Exemplar through-focus plots, used for determining and labelling the in-focus plane of the training stacks, of the standard deviation of the power spectrum of the autofocus camera intensity distribution averaged (a) across the pixel rows for the short-range autofocus training data and (b) across the pixel columns for the long-range autofocus data. The graphs are plotted as a function of defocus for the images in a z-stack. A Savitzky-Golay filter was passed along these distributions of (averaged) intensities to produce a smoothly varying function. Figure reproduced from (Lightley et al., 2022) 166
Figure 6.9. Schematic of workflow process to train and apply CNN for optical autofocus. Figure reproduced from (Lightley et al., 2022) 167
Figure 6.10. Plots of predicted vs actual defocus for 10 through-focus axial z-stacks. Each stack is plotted in a different colour in (a, d) for both the short range and long-range models respectively. The corresponding mean of the residual errors are shown in (b, e) resulting when using the short-range and long-range CNN training sets acquired and validated on data acquired on the same day. Figures (c, f) show plots of the changing training and validation loss with increasing epochs during training for the short range and long-range CNN training sets respectively. Figure reproduced from (Lightley et al., 2022) 167
Figure 6.11. Diagram of data process workflow and use for two-step CNN autofocus. Figure reproduced from (Lightley et al., 2022) 168
Figure 6.12. Plot of predicted vs actual defocus (a, c) and the corresponding mean of the residual errors (b, d) when using the short-range and long-range CNN training sets acquired (separately and sequentially) on a single day and applied to data stacks acquired on different subsequent days. Figures (a) and (c) show data acquired from multiple days with 10 repeated stacks plotted for each day, with all data from a single day plotted in the same colour. Figure reproduced from (Lightley et al., 2022) 170
Figure 6.13. Plot of predicted vs actual defocus for 10 through focus axial z-stacks, with each z stack plotted in a different colour (a, c), and the corresponding mean of the residual errors (b, d) when using the aggregate CNN training sets, acquired over a period of 10 days and applied to measurements undertaken on a subsequent day for the short-range and long-range models respectively. Figure reproduced from (Lightley et al., 2022) 171

Figure 6.14. Plots of the prediction error vs known initial defocus for 10 measurements at each defocus position. The right-hand column shows same data as left-hand column on expanded vertical scale. (a) shows data for applying only the short-range model, (b) shows data for only applying the long-range model and (c) shows the data for sequentially applying the long-range and then the short-range CNN training models trained with data acquired over 10 previous days. The red band corresponds to the ~600 nm depth of field of the fluorescence microscope. Box plot shows the interquartile range of the prediction errors, the orange line shows the mean prediction error, and the whiskers show any outlier predictions for each of the 10 repeats at the known defocus offsets. Figure reproduced from (Lightley et al., 2022) 173
Figure 6.15. Results obtained when automatically imaging 100 nm diameter fluorescent beads (TetraSpeck, T7279) arrayed in a 96-well plate (Brooks life Science Systems, MGB096-1-2-LG-L), for which a through-focus image axial z-stack was automatically recorded in each well. The plate was traversed following a horizontal (row-by-row) snake pattern. (a-c) show heat maps of the mean defocus of the beads imaged in each well calculated using *PSFj*. In the top row, the heatmaps summarize the results for when (a) only the short-range autofocus, (b) only the long-range autofocus and (c) the combined 2-step autofocus were employed. The amount of defocus error in each well is encoded in a colour scale in μm, with red indicating that the autofocus failed to locate within +/- 2 μm. Where *PSFj* was unable to determine the defocus of the bead images, or where the mean defocus was outside the +/-2 μm range, the heat map presents a red coloured well with either "Fail" or the mean (out-of-range) defocus value. In the bottom row (e-g), histograms of the mean defocus for each well, with bin widths of 100 nm, are displayed for the bead image z-stacks for which *PSFj* could determine the defocus. Figure reproduced from(Lightley et al., 2022) 174
Figure 6.16. Results obtained when automatically imaging 100 nm diameter fluorescent beads (TetraSpeck, T7279) arrayed in a 96-well plate (Brooks life Science Systems, MGB096-1-2-LG-L), for which a through-focus image axial z-stack was automatically recorded in each well. The plate was traversed following a vertical (column-by-column) snake pattern. (a-c) show heat maps of the mean defocus of the beads imaged in each well calculated using *PSFj*. In the top row, the heatmaps summarize the results for when (a) only the short-range autofocus, (b) only the long-range autofocus and (c) the combined 2-step autofocus were employed. The amount of defocus error in each well is encoded in a colour scale in μm, with red indicating that the autofocus failed to locate within +/- 2 μm. Where *PSFj* was unable to determine the defocus of the bead images, or where the mean defocus was outside the +/-2 μm range, the heat map presents a red coloured well with either "Fail" or the mean (out-of-range) defocus value. In the bottom row (e-g), histograms of the mean defocus for each well, with bin widths of 100 nm, are displayed for the bead image z-stacks for which *PSFj* could determine the defocus. Figure reproduced from (Lightley et al., 2022) 176
Figure 7.1. Schematic of easySTORM microscope utilizing optical autofocus. The objective lens was an oil immersion 1.3 NA 100x lens with a depth of focus of 600 nm. The focal lengths of the other lenses were L1: 50mm, L2: 18.4mm, L3: 100mm, L4: 200mm, L5: 180mm. 179
Figure 7.2. Super-resolved HCA microscope with *easySTORM* (Kwakwa et al., 2016) implemented on the *openFrame* configured with two spectrally-resolved fluorescence imaging channels. 180
Figure 7.3. STORMhelper GUI showing the input variables in the table to control the laser and camera settings during the automated acquisition 183
Figure 7.4. (a) *easySTORM* image of NIH3T3 cells with the tubulin labelled with AF488 and mitochondria labelled with MitoTracker™ deep red. The two channels were acquired simultaneously on the *openFrame* using a fan-cooled CMOS camera (CellCam, model Centro 200MR) with 1.4 NA objective lens. (b) shows enlarged ROIs identified by the yellow boxes in (a). 186
Figure 7.5. Automatically acquired widefield and easySTORM images of fixed WM266-6 Melanoma cells that were arrayed in 6x4 wells of a 96 well plate. An anti-Paxillin antibody conjugated to AF488

was used to label the focal adhesions and the F-actin was labelled using phalloidin-Atto 647. The cells were either mock treated as a control (row F), or they were incubated with siRNA to knock down the ARHGEF9 (rows C and D) and Anillin proteins (row E). The top set of images show a montage of the FOVs acquired in each well. These had a FOV of 125.8 µm x 125.8 µm. The bottom set of images show the expanded ROIs (12.8 µm x 12.8 µm) indicated by the yellow boxes in the top set of images. 187
Figure 7.6. Automatically acquired easySTORM images of THP-1 cells arrayed in a 96-well plate. The THP-1 cells were incubated with Streptococcus pneumoniae bacteria and fixed for imaging. The incubation time was increased down the plate in 15-minute intervals. The alpha-tubulin was labelled with AF647 (red) and the Streptococcus pneumoniae was labelled with AF488. Exemplar expanded widefield and easySTORM images of the ROIs from some of the wells are shown in the right-hand side image. As the incubation time increased the uptake of bacteria also increased 190

List of Tables

Table 3.1. Components list and part numbers used to build openExcite module 69
Table 4.1. Camera Specifications for sCMOS and CMOS sensors used for *easySTORM* at Imperial .. 101

1. Thesis Overview

This thesis reports my work towards a low-cost microscopy platform capable of performing single molecule localisation microscopy (SMLM) and automated high throughput imaging. SMLM represents a family of super resolved (SR) fluorescence microscopy techniques that can provide image resolution beyond the diffraction limit. A key requirement of such microscopes is to maintain focus during extended SMLM data acquisitions and/or when moving between fields of view (FOV) during automated microscopy. To this end I developed two different active hardware autofocus modules able to correct for axial focal drift during long image data acquisitions and to correct for varying focal positions when moving laterally across multiwell plates. To reduce the cost of fluorescence microscopy and SMLM, I implemented a low-cost implementation of SMLM ("*easySTORM")* that utilises multimode laser diodes in an open-source instrument built around a novel low-cost and modular microscope stand ("*openFrame*"). For this system, I designed and assembled a computer-controlled multiline fibre coupled excitation laserbank and demonstrated its efficacy for SMLM, including with recently-commercially-available low-cost cooled CMOS cameras. These advances enable a research-grade SMLM instrument to be assemble for a component cost of less than 10% of the cost of a commercial system.

Chapter 2 provides a brief overview of the history of optical microscopy, outlining the photophysics of fluorescence and the classical diffraction limit for optical microscopy resolution. I then describe the commonly used (diffraction limited) microscopy techniques, including widefield fluorescence, laser scanning confocal and multiphoton microscopy, light-sheet microscopy and optical projection tomography. I then describe the most widely used techniques to achieve image resolution beyond the diffraction limit, i.e., structural illumination microscopy (SIM), stimulated emission depletion (STED) microscopy and SMLM, - focussing on stochastic optical reconstruction microscopy (STORM), which is the technique I employed in this thesis.

In **Chapter 3**, I describe *easySTORM*, a low-cost implementation of direct STORM (*dSTORM*), which is introduced in Chapter 2. I explain how easySTORM achieves SMLM through the use of low-cost but high-power multimode diode lasers delivered via multimode optical fibres to provide uniform excitation over large (>120 x120 µm) FOV. By vibrating the multimode optical fibres, the excitation laser speckle pattern can be time-averaged to produce a uniform power density across a large FOV that can take advantage of large camera (CMOS and sCMOS) sensors. I demonstrate that *easySTORM* can be implemented with a high numerical aperture objective lens to image nuclear pores with <50 nm resolution using total internal reflection fluorescence (TIRF) illumination, highly

inclined and laminar optical sheet (HILO) illumination or even epi-illumination. I also demonstrate the potential of *easySTORM* to image ultrastructure in renal pathology as an alternative to electron microscopy, which is the current state of the art for clinical diagnosis. A protocol to immunolabel frozen or formalin-fixed and paraffin-embedded (FFPE) kidney tissue sections for SMLM using clinical antibodies and subsequent easySTORM imaging is described as "*histoSTORM"*.

In **chapter 4**, I report my work implementing a low-cost open-source SMLM instrument utilising a robust and modular microscope stand called the *openFrame*, which was designed to be machined using standard mechanical workshop equipment (CNC milling machine and lathe) and is composed of stackable cylindrical layers centred on the optical axis of the microscope. These layers can provide different functionalities including an excitation layer with dichroic beam splitter and couplings for various light sources and detection layers coupled to cameras. I developed and built a low-cost, computer-controlled multiline, multimode optical fibre coupled laserbank utilising high power multimode diode lasers to provide the excitation for *easySTORM*. This SMLM instrument is controlled using the open-source *µManager* software. An Arduino uno is used to facilitate communication with the low-cost diode laser controllers that modulate the drive current to the lasers, provide temperature control and include an inbuilt safety interlock. This chapter also describes how next generation, low-cost and cooled CMOS sensors can be used to replace more expensive sCMOS sensors for *dSTORM*. I demonstrate that cooled CMOS cameras originally developed for astronomy, can be used for *easySTORM* and present imaging of nuclear pore complexes (NPCs) and a FRTL5 Rat Follicular thyroid cell line. The performance of these new cooled CMOS cameras is characterised and compared with that of commercial sCMOS cameras that are typically used for STORM.

Chapter 5 presents my development of a hardware based autofocus module that can be implemented on both the *openFrame* and standard commercial microscope frames to facilitate automated imaging and maintain focus during long image data acquisitions. The chapter initially reviews previously reported autofocus techniques and then describes our initial experiments exploring a previously published approach that made use of a knife edge to bisect a collimated autofocus laser beam transmitted through the microscope objective lens and back reflected off the microscope coverslip to form an "autofocus beam image" on a dedicated camera. In principle, the degree of defocus can be determined from this autofocus camera image. I replaced this knife-edge with a slit mask to produce a rectangular beam profile that provided different precision/range in the two orthogonal axes of the slit but found both approaches to be sensitive to drift and misalignment of the autofocus laser beam with respect to the knife-edge/slit mask. I then explored the use of orthogonally orientated cylindrical lenses to collimate a fibre coupled super luminescent diode (SLD)

laser source to produce an elliptical beam profile with different confocal parameters along the two respective orthogonal axes. As with the slit mask, the differing confocal parameters of the autofocus laser beam provided a faster and slower expanding beam diameter along the respective axes, yielding both a long-range less precise defocus metric and a more accurate metric for the defocus when near the focus condition. I demonstrated that this new autofocus technique could be implemented to run in closed loop, and I characterised its performance compared to the earlier approaches with respect to repeatability, robustness, and response to temperature fluctuations.

Chapter 6 describes an alternative approach to a robust optical autofocus where I developed a convolutional neural network (CNN) based readout of the autofocus camera image to determine defocus. Noting that most optical autofocus techniques can be impacted by (thermal or mechanical) drift of the autofocus laser beam, I found that the CNN based autofocus approach could be trained over a time period that captured the fluctuations in the autofocus camera image due to thermal/mechanical drift such that it did not need regular recalibration and provided robust operation for months. This CNN-based optical autofocus utilises the MobileNetV2 model architecture and was implemented using tensorflow within a Python conda environment. It communicates via a socket connection with the java-based *µManager* 2.0 software. The optical design of this autofocus set-up was based on the slit mask to produce a rectangular autofocus beam, which provided robust operation since any drift was taken into account by the CNN. I incorporated this autofocus system into a commercial motorised epi-fluorescence microscope that I then applied to explore automated SMLM for super-resolved high content analysis (HCA).

Chapter 7 presents the application of (autofocus-enabled) automated *easySTORM* to high content microscopy, utilising the CNN-based autofocus system described in the previous chapter, which was coupled to a commercial Olympus IX81 microscope stand. I developed a *µManager* plug-in for STORM to control the hardware components, including the communication of the python controlled autofocus module using a socket connection. In two separate demonstration experiments, I applied automated high throughput SMLM to melanoma WM2664 cells and THP1 cells arrayed in multiwell plate formats. I also implemented the cylindrical lens-based optical autofocus approach on an *openFrame*-based *easySTORM* microscope and started work to demonstrate low-cost HCA with two spectral detection channels.

Chapter 8 provides a summary of my work reported in this thesis, presenting my conclusions and describing the potential opportunities for future development of the instrumentation presented.

2. Optical Microscopy

In this chapter, a brief description of the history of optical microscopy will be presented, with a discussion of fluorescence and the classical diffraction limited resolution limit of conventional optical microscopes. Next, the most widespread illumination techniques and imaging modalities will be discussed. Finally, there is a more detailed description of super resolution (SR) imaging modalities with a particular focus on single molecule localisation microscopy (SMLM).

2.1 Brief History of Optical Microscopy

The history of optical microscopy presented in this section is based on the articles "From Animaculum to single molecules: 300 years of the light microscope" by Wollman et al (Wollman et al., 2022), and "Notes on the Early History of Microscopy" by Singer (Singer, 1914). Magnifying "lenses" have been used as far back as the 1st century. Here glass spheres which were filled with water were used as lenses to magnify handwritten letters as described by Seneca in A.D. 63.

The term "microscope" was first provided by Giovanni Faber in 1625 to describe a compound microscope that was developed by Galileo Galilei in 1609 (Wollman et al., 2022). However, this wasn't the first microscope ever built. A father and son, Hans and Zacharias Janssen, are believed to have built the first compound microscope in 1590, which was composed from lenses positioned within a tube. However, the first people to apply microscopy to investigate biology were Robert Hooke and Antonie van Leeuwenhoek.

Robert Hooke used a compound microscope, which was composed of three lenses. Hooke used a candle as a light source and a condenser lens to illuminate a sample and imaged the sample using a compound microscope formed from 2 lenses. He published his observations, which included his illustrations of seeds, plants and his famous illustrations of the structure of cork, in Micrographia in 1665 (Hooke, 1665). It was Hooke who first used the term "cell" to describe the pores inside the cork.

Antonie van Leeuwenhoek made use of single lenses rather than a compound microscope from at least 1675. Since there were significant optical aberrations in lenses manufactured at this time, van Leeuwenhoek arguably produced superior results compared to others using compound microscope designs (Wollman et al., 2022). Antonie van Leeuwenhoek is credited as the first microbiologist and

it can be argued that he made the discovery of bacteria, cell vacuoles and spermatozoa (Wollman et al., 2022).

There was significant further development in microscopy at the end of the 19th century when improvements were made in lens design. This was largely introduced by the work performed by Carl Zeiss, Otto Schott and Ernst Abbe. Carl Zeiss founded a microscope design company and Otto Schott was the glass technologist responsible for improving lens design. Ernst Abbe was hired by Carl Zeiss, and he worked developing the theoretical work describing the diffraction limit for resolution and for reducing optical aberrations in lens design (Abbe, 1873).

Subsequent important advances in microscopy included phase contrast microscopy (Zernike, 1942a, 1942b) to reveal structures in otherwise transparent cell samples and innovation in labelling techniques for cell biology, including the development of dyes for colour absorption contrast and fluorescence contrast. In combination with fluorescence microscopes, the latter yielded molecular specificity, which was further enhanced through the development of immunolabelling (Coons, Creech & Jones, 1941; Coons et al., 1942), i.e., using antibodies to label specific proteins. Optical resolution and contrast were enhanced through the development of confocal microscopy (Minsky, 1957), which provided optical sectioning and enhanced contrast and, when implemented in laser scanning microscopes (White & Amos, 1987), led to electronic image acquisition and computer-based image processing. In parallel, the development of electronic cameras combined with computational image processing further stimulated the development of new optical microscopy techniques, e.g., facilitating ratiometric imaging (e.g., for spectral or polarisation resolved imaging) and quantitative phase imaging. The advent of time-resolved detection electronics led to fluorescence lifetime imaging (FLIM), initially implemented on a laser scanning microscope (Bugiel, König & Wabnitz, 1989).

More recently, Betzig, Moerner and Hell won the 2014 Nobel Prize in Chemistry for the development of super-resolved microscopy (“nanoscopy”) techniques. Betzig was recognised for inventing a technique described as photo-activated localisation microscopy (PALM) (Betzig et al., 2006), which was the first implementation of single molecule localisation microscopy (SMLM), which built on the single molecule imaging work of Moerner, e.g., (Moerner & Kador, 1989). Hell was recognised for the invention of stimulated emission depletion (STED) microscopy (Hell & Wichmann, 1994). SMLM and STED circumvent the diffraction limit in optical microscopes, leading to far-field spatial resolution below 10 nm. These techniques are discussed below.

Today the combination of advanced light sources and detectors with computational image processing has led to a wealth of advanced microscopy techniques and sophisticated microscopes at

the cutting edge frequently cost $100,000 - $1M. The pace of innovation is such that these expensive complex instruments are superseded after only a few years and their complex design makes them difficult to upgrade. However, the underlying principles are often relatively simple to implement if the required software for image data acquisition and analysis is available and this is driving a growing trend towards open-source microscopy. Open-source software for image processing, such as ImageJ, is well established but the open sharing of microscope hardware is a more recent phenomenon.

2.2 High Content Analysis

The use of optical microscopy to study cell biology became a key tool for drug discovery and the drive to rapidly explore perturbations to cell biology, e.g., in a screen of drug candidates or gene knock downs, led to the development of automated microscopy platforms applied to arrays of samples in multiwell plates. The ability to replicate microscopy experiments over thousands of fields of view in an unsupervised acquisition of image data from samples prepared under essentially identical conditions but with (replicates of) specific perturbations offers many advantages over manual microscopy.

In order to achieve high-throughput microscopy, the number of cells that can be imaged, saved, processed and analysed within a particular time period must be maximised (Oheim, 2011). However, fluorescence microscopy imaging modalities are often slow and labour intensive. In order to increase the throughput of imaging, automation needs to be introduced to the sample preparation, sample handling, the image acquisition and the data management and analysis pipelines. These steps are part of a linear workflow, which follow on from each other. Therefore, all of them need to be accelerated otherwise a bottleneck will be introduced, which will limit the amount of data that can be produced within a certain time period. The total throughput can be increased by either increasing the speed at which the system can automatically cycle through the workflow or by parallelising the acquisitions across multiple systems. In order to image multiple conditions faster, samples can also be prepared in multi-well plates and can allow for more repeats of a phenotype condition faster. The use of multiwell plates parallelises the sample preparation process. High-throughput microscopy is important in drug-discovery, where many different conditions or drugs need to be imaged in as short a period as possible, and as many repeats need to be taken as possible to identify any rare events or side effects that could occur. By automating the system, the possibility of bias introduced by the user can be reduced also.

High-content analysis (HCA) has been made possible due to two major technological advances over recent decades. The first being the significant hardware improvements including the development of autofocuses and cell positioning XY stages that have led to robust automated microscopes (Zanella, Lorens & Link, 2010). The second advance has been the developments in image analysis software. HCA has been used widely for automated widefield, spinning Nipkow disc (Petráň et al., 1968; Guo et al., 2019; Talbot et al., 2008), line scanning confocal and multiphoton techniques (Barber et al., 2013; Kumar et al., 2007). These techniques have been sometimes used to acquire spectrally resolved information involved in fluorescence lifetime (FLIM) and Förster resonance energy transfer (FRET) high content assays (Görlitz et al., 2017). However, now there is a growing need to adapt other advanced microscopy imaging modalities for HCA.

In this thesis, the work developing a low-cost, robust and open-source platform implemented to enable automated, modular high throughput microscopy is presented, referred to as openHCA. The system can be adapted for a range of different imaging modalities, either separately or in combination, but there has been a focus on developing an automated platform for single molecule localisation microscopy (SMLM) in this thesis. The work describing the development of the platform is described in detail in chapter 4. One of the key components to automate a multi-well plate or slide scanning imaging system is to build an autofocus module which is able to maintain focus axially whilst the slide or plate is being scanned laterally. The development of two hardware autofocus methods is described in chapters 5 and 6.

2.3 Diffraction limited resolution

The achievable resolution by light microscopes is limited by diffraction. It was Abbe who first described, when using incoherent illumination, how that in the object space, features are only distinguishable if the objective lens can collect at least one diffracted order of the illuminating light which is scattered by those features (Köhler, 1981). Abbe provided a definition for the numerical aperture and used this to provide a definition for the diffraction limit of resolution. Abbe explained that features within a periodic structure, like a diffraction grating, can be resolved provided the angle of the first diffraction order is within the acceptance angle of the optical imaging system. This means that the minimum period of a grating that can be resolved is d_{Abbe}.

$$d_{Abbe} = \frac{\lambda}{2 \cdot n \sin(\alpha)} = \frac{\lambda}{2 \cdot NA} \qquad \text{Equation 2.1}$$

Where *NA* is the numerical aperture, *n* is the refractive index of the immersion media, λ is the wavelength and α is the acceptance angle of the microscope objective.

An alternative way to define Abbe's resolution limit is by describing the maximum intensity spatial frequency that can be transmitted by an optical imaging system, k_{Abbe}.

$$k_{Abbe} = \frac{2 \cdot NA}{\lambda} \qquad \text{Equation 2.2}$$

There are alternative definitions provided for the achievable resolution of a microscope. One of the definitions is the Rayleigh definition for resolution (Rayleigh, 1879). Diffracted light collection is limited by the circular apertures within a typical objective lens. This corresponds to a spatial frequency cut-off, which results in point sources in a sample that scatter the illuminating light, to appear as spots in the image with a bright central peak surrounded by concentric rings. These "spots", corresponding to the images of infinitely small point like objects with spatial frequencies being limited by a circular aperture function, can be described using a mathematical function called an Airy function - the theoretical explanation of which was first presented by George Airy in 1835 (Airy, 1835). The Airy disk is composed of a bright central intensity peak with surrounding dimmer disks. The term given for the image of a point source formed by an optical instrument is described as the point spread function (PSF) and gives the spatial resolution of the instrument – which is diffraction limited for an ideal microscope.

Rayleigh provided a criterion, known as the "Rayleigh Criterion", to describe the resolution limit in telescopes. The criterion stated that two separate point objects could be considered to be distinguished if the separation between the two maxima of their two respective Airy functions was not smaller than the distance between the Airy function peak and its first minimum (Rayleigh, 1879). This provided the following equation describing the Rayleigh resolution.

$$d_{Rayleigh} = \frac{0.61 \cdot \lambda}{NA} \qquad \text{Equation 2.3}$$

Commonly, the diffraction limited resolution of a microscope can also be described in terms of the full width half maximum (FWHM) of the PSF. A Gaussian distribution is commonly used as an approximation for the central peak of the Airy function and to describe the PSF. By fitting a Gaussian function to the image of a sub diffraction limited size object, it is possible to measure the FWHM and

therefore quantify the resolution. The lateral resolution, as defined using the FWHM, is given using the following equation

$$d_{FWHM\_xy} = \frac{0.51 \cdot \lambda}{NA} \qquad \text{Equation 2.4}$$

The relationship, for a Gaussian function, between the FWHM and the standard deviation, σ, is given by the following expression.

$$FWHM = 2\sqrt{2 \cdot \ln(2)}\,\sigma \qquad \text{Equation 2.5}$$

In order to not lose information in an image - the PSF needs to be adequately sampled by the detector according to the Nyquist criterion (Nyquist, 1928; Vesely, 2007). In order to achieve Nyquist sampling of a peaked function, the pixel size in image space needs to be less than half the size of the FWHM of the PSF (ideally 2.3 times smaller than the PSF FWHM (Pawley, 2006)). There is no benefit to oversampling beyond this requirement and, if the pixel size is made smaller, the size of the FOV being imaged may be reduced.

2.4 Fluorescence

The emission of light from a substance is referred to as luminescence, which can be categorised as either fluorescence or phosphorescence (Lakowicz, 2011). In fluorescence, electrons excited to a singlet excited state in an atom or molecule relax to the ground state by emitting a photon. Since the electron in the excited singlet states have opposite spin to the electron present in the ground state, the transition is allowed by the Pauli-exclusion principle (Pauli, 1925) and so this emission of a fluorescence photon will happen quickly, with a typical fluorescent lifetime on the order of 10 ns (Lakowicz, 2011). The fluorescence lifetime is the average time taken for a fluorophore to return to its ground state after being excited. Molecules that can fluoresce are referred to as fluorochromes and the component of the molecule which can fluoresce is described as a fluorophore (Murphy & Davidson, 2012). The fluorophore may be conjugated with a larger macro-molecule, serving as a fluorescent label for that macro-molecule. Fluorophores can absorb (excitation) photons over a finite range of wavelengths, called the excitation spectrum and will emit (fluorescence) photons over a finite wavelength range, referred to as the emission spectrum. Excitation and emission spectra can

have a single or multiple peaks that correspond to transitions between possible excited electronic energy levels and the ground state of the fluorophores.

Phosphorescence also involves the relaxation of an electron from an excited state back to the ground state. However, in phosphorescence, the electron relaxes from an excited triplet state. This means that the transition to the ground state is spin-forbidden because the electron in the excited state has the same spin orientation as the electron in the ground state. Hence, the lifetimes for phosphorescence decays are longer than for fluorescence and are on the order of microseconds to seconds (Lakowicz, 2011; Murphy & Davidson, 2012). Both the processes of fluorescence and phosphorescence are shown in the Jablonski diagram in Figure 2.1.

The Jablonski diagram shows the available electronic energy states that fluorophores can occupy and hence indicates the available transitions. Energy increases along the vertical axis to higher energy levels. S_0, S_1 and S_2 represent the ground, first and second singlet states respectively. Within each electronic state, the fluorophore can occupy a number of different vibrational energy levels. There may also be rotational energy levels associated with the electronic energy levels, which will be more closely spaced than the vibrational energy levels. These vibrational energy levels are represented on Figure 2.1 by the lines marked 0,1,2. In equilibrium, the rotational and vibrational energy levels will be populated according to the Boltzmann distribution. The energy difference between the electronic states S_0 and S_1 is large enough such that the fluorophores cannot populate S_1 through thermal excitation whilst at room temperature, hence, to induce fluorescence, absorption of a photon is needed to excite the fluorophore from the ground state to a higher energy level. The energy of the absorbed photon is given by, $E = h\nu_{Abs}$, and is equal to the energy gap between the ground state and a higher energy electronic state.

After a photon is absorbed, fluorophores are excited (within 10^{-15}s) to higher rotational/vibrational levels of the first or higher electronic energy levels. The fluorophores then usually relax to the lowest rotational/vibrational level of the first excited singlet state via non-radiative processes of internal conversion and vibrational relaxation on a time scale of 10^{-12} s (Lakowicz, 2011), which is much shorter than typical fluorescence lifetimes (~10^{-8} s). Hence, fluorescence emission will occur from the lowest rotational/vibrational states of S_1 to one of the rotational/vibrational levels of the ground

state S_0 through the emission of a photon with energy $E = h\nu_{fl}$. Fluorophores will then rapidly (<~10^{-12} s) thermalise to the lowest rotational/vibrational levels.

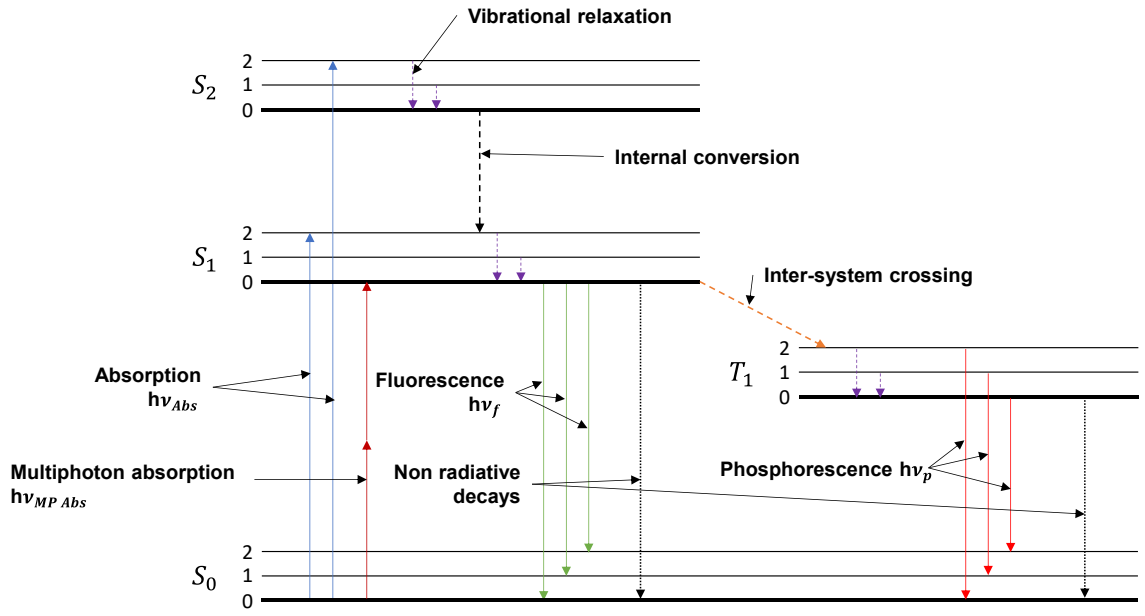

Figure 2.1. A Jablonski diagram showing the processes of fluorescence and phosphorescence. The ground state is S_0, S_1 and S_2 are the first and second excited singlet states. T_1 is the first excited triplet state. Non radiative processes are indicated by dashed lines.

Since the initial internal conversion and/or vibrational relaxation occurs rapidly compared to the fluorescence lifetime, emission generally occurs from the lowest vibrational/rotational state of *S1*. The loss of energy during the initial (fast) relaxation means that the fluorescence photons will generally have lower energies than the absorbed photons – and therefore longer wavelengths. This phenomenon is referred to as the Stokes Shift (Stokes, 1852), which can be characterised by the difference between the maxima of the excitation and emission spectra of a fluorophore (Murphy & Davidson, 2012). The shift can be over 200 nm, as is the case for porphyrins, or be on the order of 10 nm, as is the case for fluorescein, which has a shift of approximately 25 nm (Murphy & Davidson, 2012). A second general observation of fluorescence is referred to as Kasha's rule (Kasha, 1950), which states that the same fluorescence emission spectrum is observed regardless of the excitation wavelength. This is because, regardless of the state to which the fluorophore is initially excited, the emission usually occurs from the same lowest rotational/vibrational states of the first excited energy level. Another observation of fluorescence is that the emission spectrum is usually a mirror image to the absorption spectra of the S_0 to S_1 transition (Lakowicz, 2011). The similarities between the spectra occurs because the nuclear geometry is not changed significantly when the fluorophore is in

an electronic excited state, so the rotational/vibrational energy levels in the first electronic excited state have similar spacings to those seen in the ground state.

As can be seen in Figure 2.1, the fluorophores in S_1can also undergo a process called "intersystem crossing". Here, the fluorophore undergoes a spin conversion, such that the fluorophore is now in the first triplet state T_1. However, the transition from the triplet T_1 state to the ground state S_0 is spin forbidden, so the emission time from the triplet state is orders or magnitude longer than fluorescence. The emission from the triplet state to the ground state is described as phosphorescence. Typically, phosphorescence photons have lower energy than fluorescence photons and therefore longer wavelengths.

A fluorophore can also de-excite from the singlet excited state or the triplet excited state through non-radiative decays which are indicated by a dashed line in Figure 2.1.

Quantum yield, or quantum efficiency, is used to characterise fluorophores and is defined as the ratio of the number of emitted photons compared to the number of absorbed photons (Lakowicz, 2011). A higher the quantum yield of a fluorophore means that it will have a brighter emission for a given number of absorbed photons. The quantum yield can be defined in terms of the radiative decay rate of the fluorophore, k_r, and the non-radiative decay rate, k_{nr}:

$$Q = \frac{k_r}{k_r + k_{nr}} \qquad \text{Equation 2.6}$$

The emission of a photon through fluorescence is a stochastic process with a sub-Poissonian probability distribution over excitation/de-excitation cycles (Osad'ko, 2005). The lifetime, τ, of the excited fluorophore is the average time the fluorophore is in the excited state before de-exciting via any of the multiple possible decay paths back to the ground state and can also be given in terms of the radiative and non-radiative decay rates:

$$\tau = \frac{1}{k_r + k_{nr}} \qquad \text{Equation 2.7}$$

For a population of excited fluorophores, e^{-1} (37%) of the population will still be in the excited state after one fluorescence lifetime. For most fluorophores used in microscopy, this upper state lifetime (fluorescence lifetime) is on the order of 1 - 10 ns.

Fluorophores can be classified as either intrinsic or extrinsic. Intrinsic fluorophores occur naturally within the sample, whereas extrinsic fluorophores are introduced to the sample, e.g., to specifically

target and label a structure of interest. Most biological samples do not inherently provide sufficient convenient fluorescence contrast, so extrinsic fluorophores may be required to distinguish specific cellular or tissue components.

One of the most common techniques for extrinsic labelling is via the use of antibodies, which can achieve highly specific labelling of individual target protein structures of interest (antigens). These antibodies can be chemically conjugated with a large variety of convenient fluorophores, such as visibly fluorescing organic dyes including rhodamine, Alexa fluor and cyanine dyes (Samanta et al., 2019). These dyes can either be conjugated to primary or secondary antibodies. However, the cell membrane is not permeable for antibodies. Hence samples need to be fixated and permeabilised, which means that antibody-conjugated dyes cannot be used inside living cells.

Another fluorescence labelling technique makes use of genetically expressed fluorescent proteins (FPs). FPs are created by genetic modification techniques such that target proteins tagged with FP are made within the cell (Kremers et al., 2011). This allows for live cell imaging as the FP labels are intrinsic. The first FP discovered was the green fluorescent protein (GFP) in 1962 during the study of the bioluminescent properties of the *Aequorea Victoria* jellyfish (Shimomura, Johnson & Saiga, 1962). Then the gene was cloned in 1992 (Prasher et al., 1992), and used to track gene expression in bacteria (Chalfie et al., 1994). GFP was then modified to produce different coloured FPs including cyan (CFP), and yellow (YFP). Since then, further proteins have been discovered to provide more colours of FP at longer wavelengths including Orange (OFP) and Red (RFP) (Davidson & Campbell, 2009). The downside of using FPs, is that they are generally larger than synthetic dyes (Kremers et al., 2011) and may alter the function of the proteins to which they are attached. For example, the fluorescent dye Alexa Fluor 488 has a molecular weight of 643 Da (Paës, 2014), whereas a fluorescent protein like GFP has a molecular wight of ~27000 Da and has a cylindrical shape of 4.2nm in length and 2.4nm in diameter (Hink et al., 2000).

Fluorescence quenching and photobleaching are processes that reduce the amount of fluorescence produced by a fluorophore. In quenching, the fluorescence is decreased due to a reduction of the quantum efficiency – usually through an increase in the rate of non-radiative decay processes – and so fewer photons are emitted for each photon absorbed (Murphy & Davidson, 2012). Quenching can be caused by interactions of the fluorophore with other molecules, for example quenching can occur with proximity to a different molecule, as is the case in Förster resonance energy transfer (FRET) (Lakowicz, 2011). FRET occurs when the emission spectrum of a donor fluorophore overlaps with the absorption spectra of another acceptor fluorophore in close (<~10 nm) proximity and a dipole-dipole

interaction couples the donor and acceptor fluorophore excitation. The FRET efficiency has a strong molecule separation, *r*, dependency, scaling by a r^{-6} factor (Lakowicz, 2011).

Photobleaching is a photochemical process that breaks covalent bonding, which can result in the permanent loss of the fluorescent ability of a fluorophore (Murphy & Davidson, 2012), and is more likely when a fluorophore is in an excited state. Photobleaching typically involves the conversion of an excited singlet state electron to a triplet excited state. Since the lifetime of a triplet state is longer, due to its spin-forbidden decay pathway, it is then more likely that a chemical reaction with its surroundings can occur. The average time it takes for a fluorescent species to bleach varies greatly. Photodynamic photobleaching is a subclass of photobleaching, in which the fluorescent species interacts with both light and oxygen molecules (Murphy & Davidson, 2012). These reactions with oxygen will permanently prevent fluorescence and can produce a highly reactive free-radical oxygen species. These free radicals are cytotoxic, and such "phototoxicity" can compromise live cell imaging experiments. They can also permanently bleach other fluorophores in the sample. Therefore, the concentration of oxygen in the sample will impact the rate of photobleaching. Photobleaching can be minimised by limiting the light dosage delivered to the sample through reducing the exposure time or using a lower excitation power.

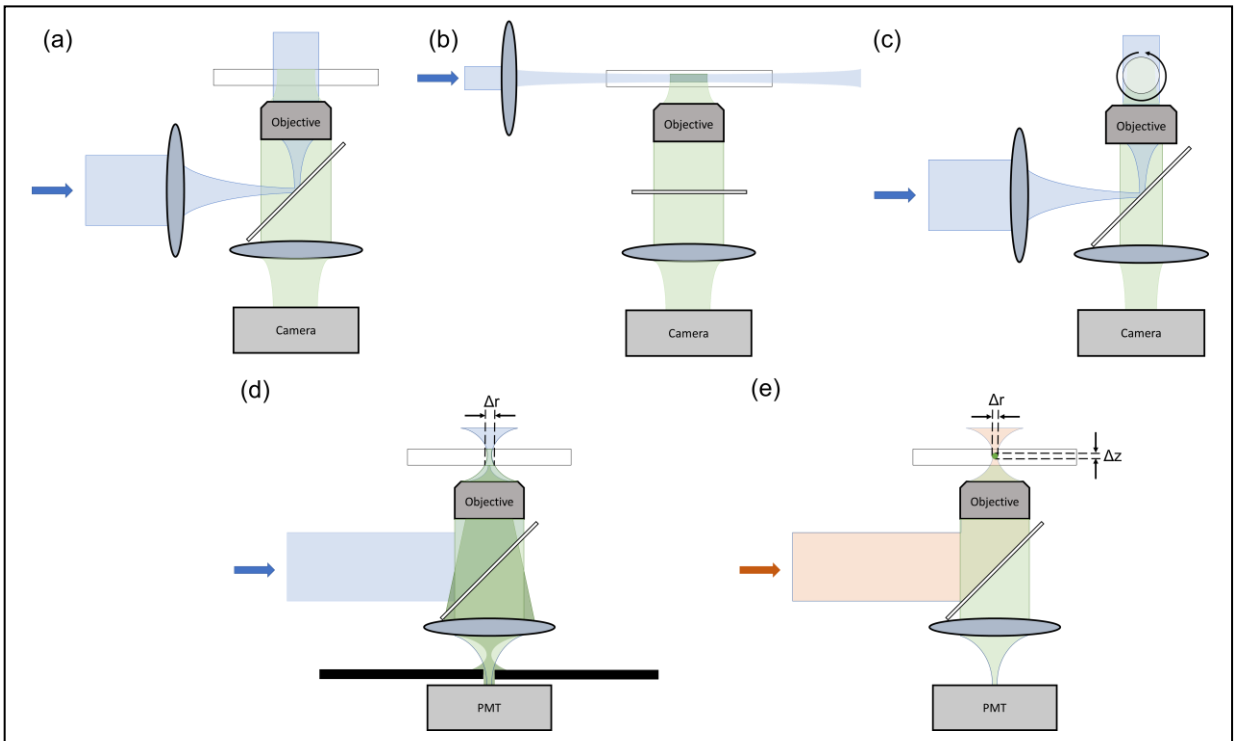

Figure 2.2. Diagrams showing different illumination techniques for microscopy imaging; (a) widefield epi-fluorescent illumination, (b) light-sheet illumination, (c) illumination for optical projection tomography (OPT), (d) confocal microscopy illumination, (e) multi-photon excitation

2.5 Optical Microscopy Imaging Modalities

This section will provide an overview of the most widely used optical microscopy modalities, for which the most commonly used sample illumination techniques are depicted in Figure 2.2.

2.5.1 Brightfield Microscopy

The simplest form of optical microscopy is brightfield microscopy where a thin sample is trans-illuminated with white light that is scattered or absorbed by the sample. The transmitted light signal will vary across the sample depending on its thickness, structure and refractive index. The transmitted light within the collection NA of the objective lens is relayed to a camera sensor using a tube lens to form an image with a magnification determined by the ratio of the effective focal lengths of the objective and the tube lenses. The regions in the sample with increased scattering and/or absorption will appear darker in the image. Brightfield microscopy does not provide high contrast in unlabelled biological samples (which are mostly transparent in thin sections) and is frequently used with absorbing dyes (such as haematoxylin and eosin) to stain specific tissue components. Alternatively, phase contrast techniques may be used to highlight structural components of transparent biological samples (Zernike, 1942a, 1942b; Park, Depeursinge & Popescu, 2018; Mehta & Sheppard, 2009; Tian & Waller, 2015; Kalita et al., 2021). In general, brightfield and/or phase contrast microscopy cannot provide the specificity or sensitivity of fluorescent microscopy.

2.5.2 Widefield fluorescence microscopy

Brightfield and phase contrast microscopy techniques form images based on heterogeneity in the absorption, refractive index and birefringence within a sample. In general, fluorescence microscopy modalities can achieve higher (e.g., single molecule) sensitivity and molecular specificity, thanks to targeted labelling, enabling sub-cellular structures and specific molecular distributions to be imaged within a sample. Critically, the Stokes shifted emission of the fluorophores enables fluorescence emission to be detected at a different wavelength from the excitation radiation, which can be blocked so that weak fluorescence signals are imaged background-free.

The simplest form of fluorescence microscopy is widefield epifluorescence microscopy as represented in Figure 2.2(a). One of the most important advances that led to practically useful fluorescence microscopes was the development of interference filters and dichroic mirrors. These were used in 1967 to create a vertical epi-illuminator that could use interchangeable dichroic mirrors, depending on the dye being used, for fluorescence microscopy (Ploem, 1967). The excitation filter in a fluorescent microscope ensures that only a well-defined spectral range of illumination for inducing fluorescence reaches the sample, and the dichroic mirror and emission filter block the excitation light from reaching the detector whilst transmitting the longer wavelength (Stokes-shifted) fluorescence. With modern low nose detectors, this background-free imaging of fluorescence provides single molecule sensitivity.

In an epi-fluorescent microscope, the sample is illuminated and imaged through the same lens. Often, a laser will be used as an excitation source for fluorescence microscopy because its narrow spectral range can efficiently excite a specific fluorophore. The wavelength of the excitation source should be as close to the absorption peak of the targeted fluorophore as possible, without overlapping with the desired detection spectral window. A broader spectral source, such as a lamp or light emitting diode (LED) can be used if an appropriate excitation filter is chosen to limit the excitation spectrum to a narrower band.

In the set up shown in Figure 2.2(a), the excitation source is imaged to the back focal plane (BFP) of the objective lens. This means that for the sample in the focal plane above the objective lens, the image of the excitation source is at infinity, leading to a uniform illumination across the FOV. This illumination technique is called Köhler illumination (Köhler, 1893, 1894). The objective lens is used to both illuminate the sample and collect the fluorescent emission within its numerical aperture (NA). Until the 1980s, microscopes were mostly designed to operate with an eyepiece separated by a mechanical tube from the objective lens (Murphy & Davidson, 2012), the length of which was standardised to 160 mm. This microscope design was not intended for (real) image detection using a camera and the fixed tube length between eyepiece and objective lenses made it difficult to introduce additional optical components between the eyepiece and the objective lens, since this would change the optical path and could introduce spherical aberration into the microscope (Murphy & Davidson, 2012). This could be addressed using additional lenses and optical components, but this would likely change the magnification and potentially introduce aberrations.

Today, most microscopes are configured as an “infinity-corrected microscope”, as developed by a German microscope manufacturer called Reichert (Murphy & Davidson, 2012). Here, the objective lenses are designed such that fluorescence emitted from each point in the sample is collimated and

a tube lens is then used to form a real image of the sample in its BFP. This can serve as an intermediate image to be imaged by the eyepiece or it can be the image recorded on a detector. The region between the tube lens and the objective lens is called the “infinity space” and in this region additional optical components can be inserted without introducing optical aberrations.

The dichroic mirror is positioned in the infinity space and used to reflect the excitation source to the sample while transmitting the fluorescence emission to the detector. The tube lens forms a magnified image of the sample on the detector.

One drawback of widefield illumination is that the entire 3D sample is illuminated and, for a thick specimen, out of focus light will also be collected by the objective lens. This means there can be a large out-of-focus background fluorescence signal in the acquired images. For this reason, wide-field microscopy is usually applied to thin samples and thick samples must be cut into thin “sections” before imaging.

2.5.3 Confocal Microscopy

Out of focus fluorescence can increase the background signal and reduce the contrast when imaging extended samples using widefield microscopy. This can be addressed using “optical sectioning” that only forms an image from light from the focal plane of the microscope. For a thick fluorescent sample, light emitted from above and below the focal plane needs to be rejected. This can be realised using a confocal microscope as depicted in Figure 2.2(d). Epi-illumination is once again used, meaning the light source and detection optics are both on the same side of the sample. An illuminating laser beam fills the NA of the BFP of the objective lens and a diffraction limited spot is formed on the sample. This diffraction limited spot can be raster scanned in the plane perpendicular to the optical axis to acquire 2D image data and if in addition the sample or objective is scanned along the optical axis then 3D image data can be acquired.

Fluorescence excited by the point illumination is collected by the objective lens and transmitted through the dichroic beamsplitter to be focussed by the tube lens onto the detector. A pinhole aperture is placed in front of the detector at a conjugate plane to the focused raster scanned spot at the sample. This aperture performs spatial filtering to block most of the out of focus fluorescence from reaching the detector, as is shown in Figure 2.2(d) where the out of focus fluorescence is depicted in dark green. For any finite sized pinhole, some out of focus fluorescence will pass through the pinhole and reach the detector, which can create a small background fluorescent signal. If there

are multiple scattering events in the sample, these can result in more out-of-focus emission passing the pinhole and reducing the amount of in-focus light passing the pinhole.

The pinhole is positioned just before a photomultiplier tube (PMT) that produces an analogue or digital voltage signal that is proportional to the fluorescent intensity recorded (Murphy & Davidson, 2012). The voltage signal is binned at regular time intervals to record an array of image pixel data on a computer. The image is formed by acquiring each pixel sequentially and displaying the data on a monitor. In order to raster scan the sample quickly, a pair of galvanometric (galvo) mirrors may be used to sweep the excitation beam in orthogonal directions across the FOV. The speed of the galvo mirrors is negligible compared to the speed of light, so the excitation light and emitted fluorescent light will follow the same optical path. Hence, the fluorescence light passes back though the scanning mirrors to the stationary pinhole before the detector. This is called de-scanned detection.

Since the excitation light is focused onto the sample, the maximum intensity at the sample is usually larger than for widefield illumination. This means that confocal microscopy can lead to increased photobleaching of the sample and greater phototoxicity for live cell imaging. The technique is also usually slower than widefield imaging as the detection spot needs to be point scanned to sequentially acquire the image pixel data. This makes the technique less appropriate for live imaging, since the sample could move during a single image acquisition, or for high content microscopy where the aim is to image as many cells as possible within the shortest time.

In confocal microscopy the resolution is dependent on both the emission and excitation wavelength as well as the NA of the objective lens. It also depends on the size of the pinhole used and the raster scan speed, since these parameters determine whether the PSF is adequately sampled. As the pinhole size is reduced, the transverse and axial spatial resolution approach the confocal diffraction limit, which is approximately 1.4 times better than widefield microscopy for an ideal (infinitely small) pinhole (Murphy & Davidson, 2012). The equations for confocal lateral and the axial full width at half maximum resolutions for widefield and confocal microscopy are given below (Wilson, 2011b)

$$d_{Confocal\_xy} = \frac{0.37 \cdot \lambda}{NA} \qquad \text{Equation 2.8}$$

$$d_{Confocal\_z} = 0.64 \frac{\lambda}{n - \sqrt{n^2 - NA^2}} \qquad \text{Equation 2.9}$$

$$d_{widefield\_z} = 0.89 \frac{\lambda}{n - \sqrt{n^2 - NA^2}} \qquad \text{Equation 2.10}$$

where n is the refractive index and λ is wavelength. However, an infinitely small confocal pinhole would pass negligible signal to the detector. In practice, the confocal pinhole is often set to a width corresponding to the FWHM of the Airy function of the microscope, which results in similar lateral resolution to widefield microscopy and an axial sectioning strength close to the PSF FWHM for wide-field diffraction-limited imaging (Wilson, 2011b). Although, confocal and widefield have similar resolutions, conventional widefield illumination is non-sectioning. The sectioning ability of confocal microscopy is its ability to image only the regions, within a 3D sample volume, that are within a thin section around the focal plane (Wilson, 2011a). In conventional widefield microscopy, out of focus light contributes to a constant background and reduces the contrast of the image. The optical sectioning can be defined in terms of the attenuation of spatial frequencies with defocus. For conventional widefield fluorescence microscopes, the non-zero spatial frequencies attenuate with defocus, but the zero spatial frequency component does not attenuate. Meaning that the spatially uniform background signal does not change. However, in confocal microscopy, all the spatial frequencies attenuate as defocus is introduced, including the background fluorescence. This means that the confocal microscope can only image fluorescence from within the optical in-focus plane and this is what leads to the improved optical sectioning ability of confocal microscopes (Wilson, 2011b)

To increase the imaging speed, the sample can be scanned by multiple beams in parallel using a spinning Nipkow disk scanner (Petráň et al., 1968) rather than raster scanning a single point. A modern Nipkow disk has thousands of pinholes that are arranged in an outward spiral pattern. The commercial Yokogawa spinning disc microscopes incorporate a two-disk design comprising a top disk with a microlens array that rotates together with a lower disk of pinholes. The top disk of microlenses focuses incident collimated light through the pinholes on the lower disk, which greatly increasese the efficiency with which excitation light reaches the sample. The pinholes of the second disk are in conjugate planes with the sample and a camera sensor. There is a dichroic mirror positioned between the two disks that transmits the focused excitation light from the microlens array but reflects the fluorescent emission which has passed the pinhole disk. The performance of the Yokogawa CSU-10 spinning disk confocal relative to a standard scanning confocal was reviewed by Wang et al. (WANG, BABBEY & DUNN, 2005). The advantage of the spinning disk approach is that, since multiple excitation spots are formed and imaged simultaneously, the acquisition time to image a sample is decreased and the whole FOV can be imaged at comparable rates to widefield fluorescence if the disk scanning is synchronised to the camera's frame rate. However, one disadvantage is that there can be crosstalk between the pinholes; this limits the suppression of out-

of-focus light when imaging extended samples and the suppression of scattered light when imaging scattering samples.

2.5.4 Multiphoton Microscopy

The depth to which a microscope can image with high resolution into thick tissue is limited by the scattering of light. For confocal microscopy, excitation light is scattered reducing the power in the focussed spot. Scattering of fluorescence photons produces interpixel crosstalk at wide-field detectors and increases the number of out-of-focus photons reaching a confocal detector. The predominant form of scattering in biological samples is Mie scattering (Mie, 1908) because the cells and sub-cellular structures are larger than the wavelength of the light. The amount of scattering decreases with wavelength, and the number of un-scattered photons in an optical signal decreases exponentially with sample thickness. The mean free path (MFP) is defined as the average distance a photon can travel in tissue between two scattering events occurring, i.e., the distance an average photon will travel without being scattered in tissue (Ntziachristos, 2010). For tissue, the MFP is approximately 100 μm. Therefore, in order to ensure the majority of photons are not scattered the imaging depth and sample thickness needs to be less than this for widefield microscopy. In widefield microscopy, tissue with a thickness of 10-20 μm is commonly used to ensure that only a small proportion of the photons are scattered and hence a high-resolution image can be formed (Ntziachristos, 2010). Confocal and multiphoton microscopy techniques are able to image more deeply into tissue up to tens or hundreds of microns deep into the sample (Ntziachristos, 2010). Both confocal and multiphoton microscopy have their penetration depths limited by the transport mean free path (TMFP). The TMFP considers not just the MFP average distance between scattering events but also the average angle of scattering in each scattering event. The TMFP describes the average distance a photon travels before it loses its relationship with its initial propagation direction. The TMFP can be tens of times greater than the MFP (Ntziachristos, 2010). Confocal microscopy can achieve penetration depths of on the order of 2-3 MFP and multiphoton microscopy can achieve penetration depths of 3-4 MFP. Multiphoton microscopy is able to image to greater depths in biological tissue because it uses excitation radiation at longer wavelengths, usually in the infrared region: in two-photon microscopy, instead of absorbing a single photon, two longer wavelength (lower energy) photons are absorbed simultaneously by a fluorophore to excite an electron and induce fluorescence, as is depicted in Figure 2.1. Two-photon absorption was described theoretically by Maria Göppert-Mayer in 1931 (Göppert-Mayer, 1931). For most dyes used for fluorescence

microscopy in the visible spectral range, the photons absorbed in two-photon excitation are in the near infrared (NIR) region of the spectrum. Biological tissues are less scattering for longer wavelength NIR light - with approximately half as many excited photons being scattered for every 100 µm of tissue (Murphy & Davidson, 2012). A further consideration is that tissue absorption in the visible is usually significantly higher than in the NIR, so excitation at longer wavelengths is less attenuated. Tissue autofluorescence is also more efficiently excited at shorter wavelengths, so using NIR excitation can reduce the unwanted background signal associated with autofluorescence. Multiphoton microscopy is able to penetrate to about twice the physical distance than confocal microscopy (Ntziachristos, 2010).

Multiphoton excitation is a non-linear process as more than one photon is absorbed, but only a single photon is re-emitted. The probability of multiple photons being absorbed simultaneously depends on the light intensity at the fluorophore. Two-photon and three-photon excitation probabilities are proportional to the square and the cube of the excitation intensity respectively. To reach the high intensities needed to generate practically detectable signals, the excitation sources used for two-photon microscopy are usually femtosecond pulsed lasers, which provide high peak intensity from a low average power laser beam. Mode locked Ti:Sapphire lasers are most commonly used for two-photon excitation and two-photon excitation was first demonstrated in 1990 by Denk et al. (Denk, Strickler & Webb, 1990) .

The square relationship of the light intensity and two-photon excitation probability means that to increase the rate of two-photon excitation by a factor of 4, the excitation intensity needs to be increased by a factor of 2 (Murphy & Davidson, 2012). The highest excitation light intensity will be at the focus of a beam where there is the greatest photon density, and so the two-photon fluorescence signal will fall off quadratically away from the focal plane. This provides improved optical sectioning compared to confocal microscopy in biological tissue, as well as increased imaging depth. The laser scanning microscope design for multi-photon excitation is shown in Figure 2.2(e). It is similar to a laser scanning confocal microscope, but the pinhole is no longer needed as all of the fluorescence can be considered to originate from within the focus of the excitation source at the sample. Removing the pinhole improves the detection efficiency as scattered fluorescence photons are not blocked from reaching the detector.

Since longer wavelengths are used for excitation, the optical resolution of a multiphoton microscope could be expected to be worse compared to confocal microscopy (Zipfel, Williams & Webb, 2003). However, since two-photon excitation has a square dependence on excitation intensity, the effective PSF is the square of the conventional PSF. Therefore, the optical resolution for a two-photon

microscope is the square of the intensity point spread function, $IPSF^2$. This volume of the $IPSF^2$ is less than a femtolitre (Murphy & Davidson, 2012). The resolution for two-photon excitation 1/e widths are estimated by the following formula (Zipfel, Williams & Webb, 2003);

$$d_{2PE\_xy} \approx \frac{0.320 \cdot \lambda}{\sqrt{2} \times NA} \approx \frac{0.23 \cdot \lambda}{NA} \; for \; NA \leq 0.7 \qquad \text{Equation 2.11}$$

$$d_{2PE\_xy} \approx \frac{0.325 \cdot \lambda}{\sqrt{2} \times NA^{0.95}} \; for \; NA \geq 0.7 \qquad \text{Equation 2.12}$$

$$d_{2PE_z} \approx \frac{0.532 \cdot \lambda}{\sqrt{2}} \left[\frac{1}{n - \sqrt{n^2 - NA^2}}\right] \qquad \text{Equation 2.13}$$

The IPSF^2 have been calculated based on the work presented by Richards and Wolf (Richards, Wolf & Gabor, 1959). The above estimates come from gaussian fits of the lateral and axial intensity squared profiles from the calculated IPSF^2 (Zipfel, Williams & Webb, 2003). Important to note these are the 1/e widths and the equations given above are for the FWHM. In principle, the achievable resolution of a multiphoton microscope is the same as an ideal confocal microscope but will use longer wavelengths.

Since the excitation wavelength is longer, the resolution achievable is slightly worse compared to confocal microscopy when imaging the same fluorophore. Multiphoton microscopy has a much lower photon efficiency, meaning that the number of excitation photons is much higher than the number of emission photons, than confocal microscopy and so imaging is usually slower.

2.5.5 TIRF Microscopy

TIRF (total internal reflection fluorescence) microscopy uses evanescent waves to excite fluorescence in fluorophores situated within ~100 nm into the sample above the coverslip (Murphy & Davidson, 2012). TIRF microscopy makes use of total internal reflection (TIR). TIR can occur when light in a higher refractive index medium is incident at an interface with a lower refractive index medium. If the angle of incidence exceeds the “critical angle”, then the light will be totally reflected at the interface. However, although the light is reflected at the interface between the different refractive index media, there is an evanescent wave formed along the interface. The electric field of

this evanescent wave decays exponentially with perpendicular distance away from the surface over a scale of ~100 nm (Axelrod, Burghardt & Thompson, 1984) and can excite fluorophores situated sufficiently close to the interface. Since TIRF microscopy does not excite fluorophores further than ~100 nm into the sample, it provides wide-field optical sectioning with an axial extent below the diffraction limited depth of field.

As illustrated in Figure 2.3, TIRF is commonly achieved by focusing an excitation laser beam to the edge of the back aperture of a high NA TIRF objective lens – usually an oil immersion lens. This means the collimated beam transmitted by the objective lens is highly inclined at the coverslip and will undergo TIR if the angle of incidence is greater than the critical angle defined by Snell's law

$$n_1 \sin\theta_1 = n_2 \sin\theta_2 \qquad \text{Equation 2.14}$$

$$\theta_C = \sin^{-1}\left(\frac{n_2}{n_1}\right) \; where \; n_2 < n_1 \qquad \text{Equation 2.15}$$

Where θ_C is the critical angle, 1 and 2 refer to the first and second media either side of the interface and n is refractive index. For a glass water interface, the critical angle of incidence in the glass is:

$$\theta_C = \sin^{-1}\left(\frac{n_2}{n_1}\right) = \sin^{-1}\left(\frac{1.333}{1.518}\right) \approx 1.07\, rad \; \approx 62^o \qquad \text{Equation 2.16}$$

However, the sample refractive index can range from ~1.33 –1.38. Before entering the glass coverslip, the excitation beam passes through the objective lens and the immersion fluid (n_3), positioned between the objective and the coverslip, and must satisfy the condition $n_3 > n_2$. Snell's law states that:

$$n_1 \sin\theta_C = \; n_2 = n_3 \sin\theta_T \qquad \text{Equation 2.17}$$

Hence to achieve TIRFM,

$$n_3 > n_2 \qquad \text{Equation 2.18}$$

Where $n_3 \sin\theta_T$ is the NA of the TIRF objective lens.

Therefore, an objective lens with NA higher than n_2 is needed for TIRF. The cytosol in cells has a refractive index of n_1 ~1.38 and the NA of the TIRF objective lens needs to be larger than this to

accommodate the angular divergence of the excitation beam. Immersion oil is commonly used as the immersion media because it typically has a refractive index of 1.52 and matches that of the glass coverslips. Oil objectives therefore permit a higher NA to be achieved compared to water or silicone oil immersion objectives and this provides a larger annular area at the back focal plane of the objective that can be used couple excitation in to achieve TIR. A minimum practical NA for a TIRF objective lens is approximately 1.45.

The internally reflected beam propagates back through the objective lens but the evanescent wave at the glass/aqueous sample interface can excite fluorophores near the coverslip. TIRF can provide a high signal to background ratio because there is no out-of-focus fluorescence to contribute to the background signal and this has been exploited for single molecule imaging. In addition, there is low phototoxicity as so little of the sample is exposed to the excitation radiation. However, TIRF can only be used to image structures very close to the coverslip and TIRF objective lenses are usually expensive, so it is a specialised form of microscopy.

A related technique is called highly inclined and laminated optical sheet (HILO) microscopy (Tokunaga, Imamoto & Sakata-Sogawa, 2008), for which the excitation beam is incident at the coverslip at a large angle of incidence (i.e., highly inclined) but at an angle below the critical angle. The collimated beam from the objective lens refracts at the interface with the lower refractive index (aqueous) sample and propagates at a shallow angle to the coverslip through the focal plane of the objective lens. This produces a thin sheet of excitation across the field of view. Thus, HILO can improve SNR compared to conventional widefield fluorescence microscopy by only illuminating part of the sample near the focal plane. It has the advantages that it can be used with lower NA (and therefore lower cost) objective lenses than TIRF and it can be used to image fluorophores further from the coverslip. Unlike TIRF, which provides optical sectioning beyond the diffraction limit, the thickness of the optical section is limited by diffraction.

2.5.7 Light sheet Microscopy

Optical sectioning of a sample can be achieved without scanning by using a thin light sheet to selectively illuminate a section of the sample: Selective plane illumination microscopy (SPIM) (Huisken et al., 2004), is typically implemented by focusing a collimated Gaussian excitation laser beam in one direction using a cylindrical lens to produce an optical sheet to illuminate a sample and imaging with a separate objective lens along a different (orthogonal) direction. A simple configuration of SPIM is shown in Figure 2.2b. Unlike widefield and confocal fluorescence microscopy where the illumination and detection paths coincide and use the same objective lens, the selective illumination of a thin sheet through the sample (arranged to be in the focal plane of the detection objective lens) means that optical sectioning can be achieved with minimal out-of-focus fluorescence or photobleaching. Furthermore, the use of widefield detection in SPIM means that the imaging rate can be much faster than for laser scanning techniques such as confocal or multiphoton microscopy. The sample can then be scanned axially through the excitation light sheet to image the sample in three dimensions. A disadvantage of SPIM is that the illumination optics (e.g., cylindrical lens) needs to be mounted in the same plane as the sample, which is not compatible with

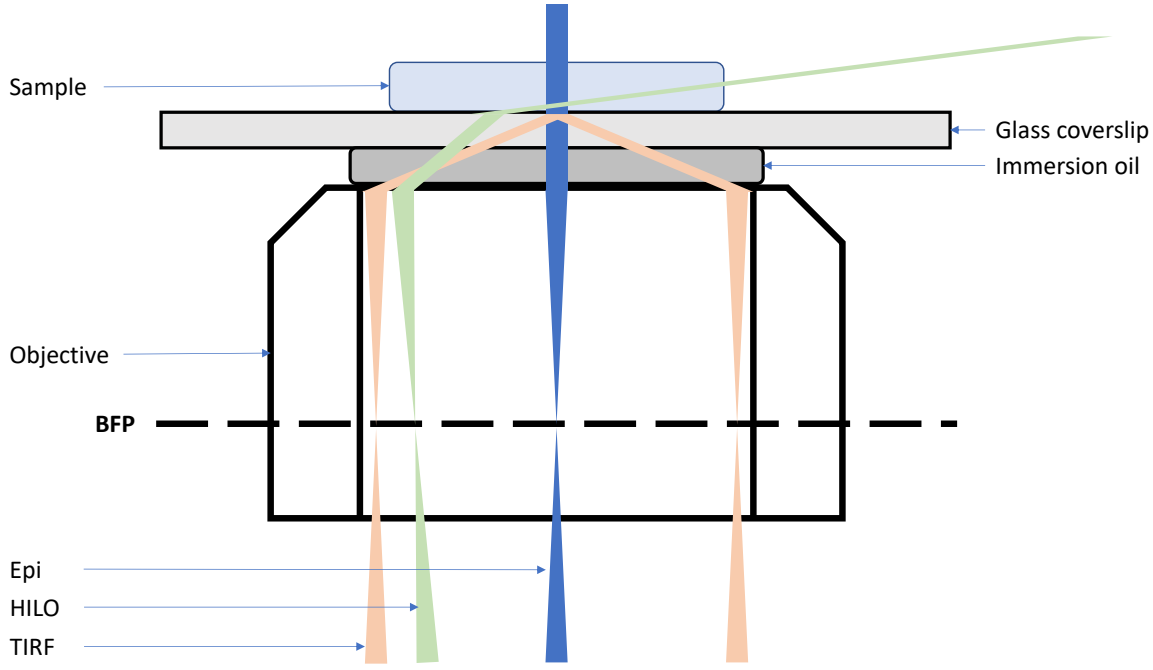

Figure 2.3. Diagram showing TIRF illumination (orange), HILO illumination (green) and widefield epi-illumination (blue) for a high numerical aperture oil immersion objective (NA≈1.45). An evanescent field extends for a few hundred nanometres above the interface between the coverslip (n≈1.518) and the sample media (n≈1.33-1.38) for TIRF illumination. The HILO illumination excitation beam is introduced at a smaller radial distance from the centre of the back focal plane compared to TIRF. HILO can illuminate to greater depths than TIRF.

conventional epifluorescence microscope designs or standard mounting of samples on microscope coverslips or in multiwell plates.

Besides SPIM, there are other approaches that realise optical sectioning by illuminating a section within a sample with a thin sheet of excitation light and imaging from a different direction to the axis of excitation. These techniques are described as light sheet fluorescence microscopy (LSFM, of which SPIM is an example). The earliest report of LSFM was in 1903 (Siedentopf & Zsigmondy, 1903), in which the technique was described as ultramicroscopy. An important variation of LSFM is oblique plane microscopy (OPM) (Dunsby, 2008) where, unlike SPIM, the sample is illuminated and imaged using the same objective lens. In OPM a light sheet emerging at a high angle from a high NA objective lens illuminates the sample with an oblique light sheet (similar to HILO microscopy) and the fluorescence from the sample is collected using the same objective lens with the imaging axis at 90 degrees angle to the excitation light sheet. Since OPM illuminates and images a sample using the same objective lens, it can be implemented on a conventional microscope frame using standard sample mounting techniques, including coverslips and multiwell plates. Recently, OPM has been extended to dual view OPM (dOPM) (Sparks et al., 2020), where two orthogonal views of the sample can be acquired using the same objective lens.

2.5.8 Optical projection Tomography

Optical projection tomography (OPT) (Sharpe et al., 2002; Sharpe, 2003) is often described as being an optical analogue of x-ray computerized tomography (CT) (Davis et al., 2018). In OPT, a sample is rotated through 360 degrees and widefield 2D projection images are acquired at different rotation angles. The illumination technique for fluorescent OPT is shown in Figure 2.2c. As in computerized tomography, the 3D structure of the sample is reconstructed from these projection images, usually using a filtered back projection algorithm (Sharpe et al., 2002; Sharpe, 2003; McGinty et al., 2008). This assumes parallel ray projection and requires the depth of field (DOF) of the imaging system to extend at least halfway through the sample (allowing the full volume to be reconstructed from a complete rotation). OPT can be used with transmitted light, using absorption, or scattering as a contrast mechanism, or can be a fluorescence imaging technique. In order, to acquire projection images throughout the sample, it needs to be transparent and so the sample may need to be chemically cleared to reduce optical scattering. To reconstruct the 3D structure without undersampling artefacts, hundreds of projection images typically need to be acquired when using filtered back projection. It is also imperative that the sample is static during the acquisition of the

projections through the full rotation to avoid motion blurred artefacts. OPT can image a range of sample sizes (by adjusting the depth of field of the imaging system) and is widely used for 3D imaging of (~1 -10 mm thick) mesoscopic (semi-transparent) samples such as chemically cleared animal organs (Sharpe et al., 2002; Bryson-Richardson et al., 2007) or in-vivo studies of small organisms such as Drosophila (Vinegoni et al., 2008) or zebrafish (McGinty et al., 2011; Kumar et al., 2016).

When imaging in vivo samples, the animal needs to be anaesthetised during imaging to reduce motion. It is important to minimise the amount of time that an animal is anaesthetised to reduce any side effects involved in the anaesthesia and reduce the risk of motion during the acquisition. Also, when reducing the imaging time, the light dose to the sample is also reduced which decreases photodamage and photobleaching. Therefore, it is advantageous to reconstruct the structure from fewer projections. However, if the number of projections is reduced significantly below the Shannon-Nyquist minimum sampling requirement, streak artifacts are introduced into a filtered back projection reconstruction (Davis et al., 2018). The effects of using fewer projections can mitigated by using compressed sensing techniques (Correia et al., 2015) although these iterative reconstruction techniques are slow and introduce significant computational cost. Convolutional neural network (CNN) reconstruction techniques have also been shown to produce streak free reconstructions of under sampled OPT data (Davis et al., 2018). Recently, low-cost single-shot OPT imaging of in vivo swimming zebrafish embryos has been demonstrated (Darling et al., 2022) using 4 cameras to capture 8 simultaneous projections of a 1 mm diameter volume at the camera frame rate. Here the sample no-longer needs to rotate as the cameras are arranged surrounding the sample and the undersampled OPT data can be reconstructed using either iterative compressive sensing algorithms or machine learning.

2.6 Super resolution modalities

As described previously by Abbe, the achievable resolution of a microscope is classically limited by the diffraction limit $d_{Abbe} = \lambda/(2 \cdot NA)$. This limits the lateral resolution of a widefield fluorescent microscope to about 200 nm and the axial resolution to about 500 nm, depending on the NA of the system and the emitted wavelength. Even for point scanning techniques using high NA oil objectives (NA ≥ 1.4), the diffraction limited spot will have an area on the order of 200-300 nm^2 (Murphy & Davidson, 2012). This means that all the fluorophores within the diffraction limited PSF of the excitation spot will be excited simultaneously and will all emit fluorescence. This limits the distance

over which two fluorophores can be resolved to on the order of 200 nm. However, research into super resolution light microscopy modalities has allowed the resolution of microscopy techniques to overcome the diffraction limit. In this section, some of the most common super-resolved microscopy imaging modalities are presented.

2.6.1 Structured illumination microscopy

Structured illumination microscopy (SIM) (Gustafsson, 2000) is described as a super-resolution imaging technique and can achieve lateral resolutions of up to 100 nm and axial resolutions on the order of 300 nm. SIM is able to achieve a maximum of a 2-fold increase of resolution compared to diffraction limited wide-field microscopy (Murphy & Davidson, 2012) by extending the spatial frequencies that can be collected by a given microscope objective lens beyond the normal region of support.

In SIM a high spatial frequency sinusoidal excitation pattern is projected onto the sample. This can be done in a variety of ways that include projecting the first order (and sometimes also zero order) diffracted beams from a grating onto the Fourier plane of the objective lens or by using a spatial light modulator (SLM) (Kner et al., 2009).

In frequency space in 2D, the edge of the region of support of the objective can be represented by a circle, with the lowest spatial frequencies near the origin and higher spatial frequency components further from the origin. The radius of the region of support is given by Abbe's spatial frequency diffraction limit

$$K_0 = \frac{2 \cdot NA}{\lambda} \qquad \text{Equation 2.19}$$

Where K_0 describes the highest spatial frequency component that can be transmitted by an objective.

Within the region of support, the transmission of each spatial frequency is modulated by the optical transfer function (OTF).

In SIM, the high spatial frequencies introduced by the structured illumination mix with the spatial frequencies in the sample. One consequence of this is that the high frequency components in the sample that are usually outside the region of support will mix with the projected grating spatial

frequencies to produce new spatial frequency components that are within the region of support and

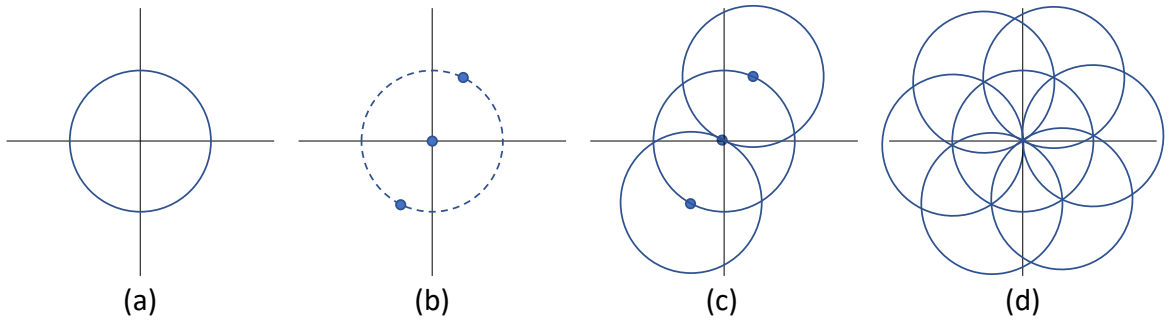

Figure 2.4. The concept of Gustafsson's method for SIM. (a) Region of support for the microscope. Low spatial frequencies are at the origin and higher spatial frequencies are further from the origin. The edge of the region of support is given by Abbe's limit and represents the maximum spatial frequency that can be resolved by the microscope. (b) Fourier transform of a coherently illuminated sinusoidal grating with the $\pm 1^{st}$ orders positioned at the edge of the back aperture of the objective (c) the extended observable region with two offset regions demonstrating frequencies that have been shifted by Moiré fringes (d) The extended OTF formed from three rotations of (c) formed by using different orientation and phase of the illuminated pattern, it is possible to recover spatial frequencies up to twice that defined by Abbe's diffraction limit. (Images recreated from those presented by (Gustafsson, 2000))

therefore detectable as lower spatial frequency structures contributing to the recorded image. This effect is referred to as Moiré fringes. Since the frequency of the projected grating sinusoidal pattern is known, it is possible to extract the information about the sample's spatial frequency components outside the region of support from the recorded Moiré fringes. Because the maximum spatial frequency of the grating that can be projected onto the sample is itself limited by the region of support of the objective lens, this technique allows access to higher resolution information for spatial frequencies up to twice the cut-off frequency, thereby doubling the diffraction limited resolution.

The concept of SIM is shown in Figure 2.4 demonstrating the increase in spatial frequency space which is accessible in the observable region and the increased resolution. SIM is still a diffraction limited imaging technique but provides resolution beyond the Abbe limit established for wide-field microscopy.

A recorded SIM image is the sum of the Moiré fringes and the normal diffraction limited image. In order to separate out and extract the higher spatial frequency components and reconstruct a "super-resolved" imaging of the sample, it is necessary to acquire multiple images with different phases of the grating projected onto the sample. This will only improve the spatial resolution along the direction perpendicular to the projected grating fringes and so this procedure should be applied with at least three grating orientations/angles to obtain a complete super-resolved SIM image. It is

possible to access the spatial frequency up to twice the original limit defined by Abbe's diffraction limit. If the grating illumination pattern is formed by the two first order diffracted beams from a grating, then three images are required to be recorded at different grating phases in each direction (i.e., 9 images in total for three grating orientations). This will provide a super-resolved SIM image but not optical sectioning. If three beams (i.e., zero and two first order beams) are used to project the grating pattern on the sample, then the grating will have spatial frequency components in the axial as well as the lateral directions. It is then necessary to acquire 5 images at different grating phases in each direction (i.e., 15 images in total) to reconstruct an optically section super-resolved SIM image. Thus, SIM potentially provides faster imaging than laser scanning confocal microscopy and better resolution, but is slower than wide-field imaging with more photobleaching/phototoxicity.

2.6.2 Stimulated emission depletion microscopy

The first demonstrated super-resolved microscopy technique was stimulated emission depletion (STED) microscopy (Hell & Wichmann, 1994) – a technique that utilises the concept of reversible saturable (or switchable) optical fluorescent transitions (RESOLFT). This concept was originally presented by Stefan Hell and exploits the ability to reversibly switch fluorophores between "on" and "off" states in order to achieve super resolved imaging far beyond the diffraction limit. An "on" state is a fluorescent state and an "off" state is a long-lived stable dark state. For STED microscopy, the fluorophore ground state is the "off" state and the excited singlet state is the "on" state. Fluorophores are switched off by stimulated emission back to their ground state.

STED can be considered an extension of laser scanning fluorescence microscopy that reduces the excitation PSF below the diffraction limit to improve the spatial resolution. The super-resolved image is acquired pixel by pixel. STED makes use of co-aligned laser beams at wavelengths appropriate for excitation and stimulated emission of the sample fluorophores, with the depletion beam having a hollow ("doughnut-shaped") profile in the focal plane. The power of the depletion beam is set to induce stimulated emission of excited fluorophores from the excited singlet state with a higher probability than de-excitation by fluorescence, such that it effectively switches off the fluorescence. The centre of the doughnut shaped depletion beam is aligned to overlap with the central peak of the (Gaussian profile) excitation beam and so stimulated emission depletes the outer rim of the excitation beam but not the central region. This results in a narrower excitation PSF – the width of which depends on the power in the depletion beam. Usually, the two laser beams are pulsed to

provide high peak power at much lower average power and the sample is excited first with the excitation pulse and then the depletion pulse. The excitation pulse is shorter than the depletion pulse, so that the excited fluorophores in the depletion region undergo stimulated emission back to the ground state before they get a chance to relax via fluorescence.

The size of the STED excitation PSF scales with the power in the depletion laser beam. As the depletion beam's intensity increases, the achievable resolution increases but there is also increased photodamage and photobleaching to the sample. Lateral resolutions on the order of 50 nm can be achieved with typical (organic dye or fluorescent protein) fluorophores. It is also possible to achieve axial super resolution using an appropriate depletion beam profile (Klar et al., 2000). As a laser scanning microscopy technique, STED is slower than SIM but can achieve better spatial resolution than SIM and since it can be implemented with confocal or multiphoton microscopy, it can provide optical sectioning to a deeper depth in biological tissue than other super-resolved microscopy techniques and has been demonstrated in vivo (Rankin et al., 2011).

2.6.3 Single molecule Localisation microscopy

Today the most widely used (and arguably easiest) super resolution approach is the family of techniques called single molecule localisation microscopy (SMLM), which can be implemented on a standard widefield epi-fluorescence microscope. SMLM works on the principle that the position of a single emitting fluorophore can be determined to a greater precision than the width of the PSF if its emission can be assumed to be from a single fluorophore. Typically, this can be done by fitting the recorded image ("PSF") of each emitter to an Airy function or Gaussian model. The precision to

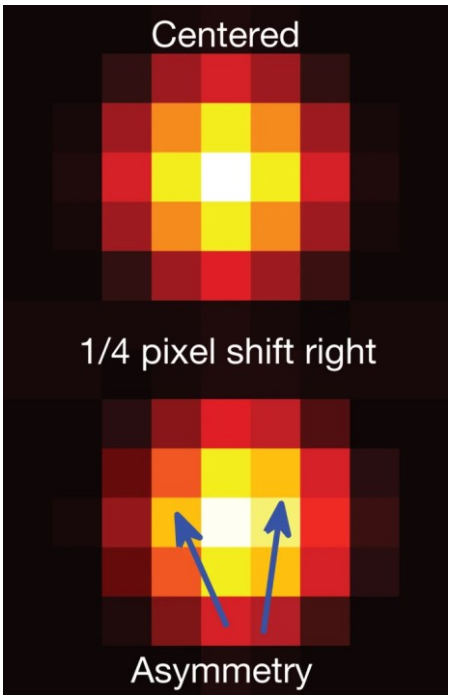

Figure 2.5. Image of a PSF distribution from a single fluorescent emitter recorded by a pixelated sensor. A small shift in the emitter's lateral position results in a noticeable asymmetry in the measured pixel digital number values. A Gaussian can be fitted to these distributions to give a prediction of the localisation to sub-pixel precision. Image from Small et al. (Small & Stahlheber, 2014)

which the centre of the PSF can be determined is limited by the size of the PSF and the number of photons collected. Therefore, if the emission PSF from the many fluorophores in a sample can be detected separately, e.g., by temporally distinguishing overlapping PSF, the resolution of the whole image can be improved by at least an order of magnitude, i.e., down to ~20-50 nm (Murphy & Davidson, 2012). The emission from different fluorophores is separated in SMLM by causing the fluorophores to emit stochastically (i.e., "blink"), such that there is a low probability that fluorophores located within the size of the PSF do not emit at the same time. The desired sparse blinking can be provided by putting all the fluorophores into a dark (non-emitting) state and stochastically switching them on using light of an appropriate wavelength and intensity. In SMLM, many thousands of frames of sparse fluorescence PSF are acquired and the fluorophores in each frame are localised such that a full image can be reconstructed from the co-ordinates of all the individual PSF - in a manner similar to the artistic painting technique called "pointillism".

SMLM was first demonstrated to provide super resolved imaging of cells by Eric Betzig et al. in 2006 using a technique called photo-activated localisation microscopy (PALM) (Betzig et al., 2006). In the same year Hess et al. also published a fluorescence photoactivation localization microscopy technique (Hess, Girirajan & Mason, 2006) and a different SMLM technique called Stochastic Optical

Reconstruction microscopy (STORM) (Rust, Bates & Zhuang, 2006) was developed by Rust et al., which used photo-switchable dyes to stochastically switch the fluorophore emission. Many SMLM techniques have been subsequently demonstrated with most of the innovation around the mechanism of inducing the stochastic switching of the fluorophore emission. Three of the most common SMLM techniques in current use are outlined below. Since SMLM can be implemented in a simple epifluorescence microscope, it currently provides the simplest, lowest cost and most widespread approaches to super-resolved microscopy.

PALM can be implemented with photoactivable or photoconvertible fluorophores. Photoactivatable fluorophores are irreversibly switched from a dark "off" state to a fluorescent "on" state (Lelek et al., 2021), usually using a high photon energy UV activation laser (e.g., at 405 nm). Before being activated, the fluorophores are all in a stable dark state and a random subset of the fluorophores is activated upon irradiation with a short pulse of UV excitation. The fluorophores can then be excited using a longer wavelength laser source and their emission localised to determine their spatial co-ordinates. Once this subset of fluorophores has been localised, they are photobleached using the excitation laser source and then another subset of fluorophores can be activated. This process is repeated for thousands of frames until all the fluorophores have been activated, localised, and bleached. The co-ordinates of the individually localised fluorophores are then used to reconstruct a super-resolved image of the sample by convolving a model PSF with the co-ordinate map obtained from the thousands of acquired frames. PALM was originally demonstrated using photoactivatable fluorescent proteins like PA-GFP (Lukyanov et al., 2005) which uses a $\lambda_{off\rightarrow on} = 405nm$ and $\lambda_{on\rightarrow off} = 488nm$. There are also photoactivatable fluorescent dyes include photochromic rhodamine amides (Bossi et al., 2008) and the silicon rhodamine PA Janelia Fluor dyes (Grimm et al., 2016).

The same approach is used for photoconvertible fluorophores, such as photoconvertible fluorescent proteins which can irreversibly switch between from one spectral state to another under irradiation (Lelek et al., 2021). Eos is a photoconvertible protein which can be switched from green emission to red emission by illumination with a $\lambda_{G\rightarrow R} = 405nm$ laser source. These Eos protein spectral states are respectively excited at 488 nm and 561 nm. The shorter wavelength can be used to first focus the sample and then acquire a widefield fluorescence image before the protein is photoconverted to enable the PALM acquisition. Once again, the proteins need to be bleached after imaging for localisation before another subset of proteins are activated.

STORM makes use of reversible photo-switching to provide temporal separation of emission from individual fluorophores. STORM was first demonstrated by Rust et al. (Rust, Bates & Zhuang, 2006)

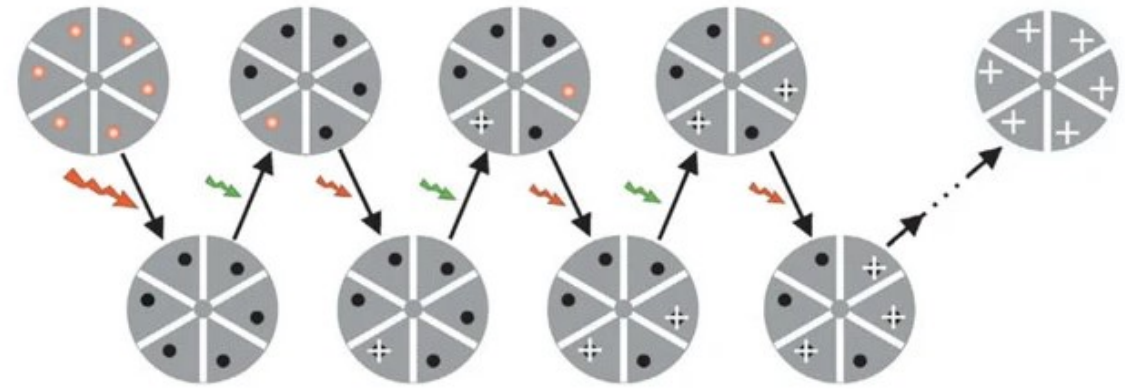

Figure 2.6. Schematic of first implementation of STORM. Cy5-Cy3 dye switch pairs are used to label a sample. The Cy5 dye is all initially switched to a stable dark state using a high power 633nm pulse. A random subset of fluorophores are switched to the on-state after illumination by a 532nm source. The sample is then re-excited by a continuous 633nm source exciting fluorescence before the cy5 dye returns to the dark state. The fluorophores that have emitted are localised. Then another subset of fluorophores is switched to the "on" fluorescent state by the 532nm source. This cycle repeats until all the fluorophores have been localised. Figure adapted from Rust el al. (Rust, Bates & Zhuang, 2006)

using photo-switchable cyanine dyes (Bates, Blosser & Zhuang, 2005; Heilemann et al., 2005). Cy5 dye molecules can be switched reversibly between a fluorescent "on" state and a dark "off" state using two different wavelength lasers. A red laser source at 633 nm, which excites fluorescence from the Cy5 dye, switches the Cy5 dye to a stable dark state and a green, 532 nm laser source can reversibly switch the Cy5 back into a fluorescent "on" state. The recovery rate to switch the dye back into the fluorescent state is dependent on the proximity of a Cy3 dye (Bates, Blosser & Zhuang, 2005). Therefore, a Cy3-Cy5 dye pair are used in combination as a photo-switch between the "on" and "off" states. In Rust et al.'s first implementation of STORM, the dyes are all initially switched into the dark state using a high-power pulse of the 633 nm laser source. Then the green, 532nm, laser is used to switch "on" a random small subset of fluorophores whose PSF have low probability to overlap. These fluorophores are then irradiated at 633 nm until they have switched off again. The emission from the "on" fluorophores is used to localise their positions. This process is then repeated thousands of times for different random subsets of fluorophores before the dye is permanently photobleached. The process is illustrated in Figure 2.6.

Another implementation of STORM is direct STORM or "dSTORM", which was presented by Heilemann et al (Heilemann et al., 2008) and also by Fölling et al., who described in as "ground-state depletion and single-molecule return" (GSDIM) (Fölling et al., 2008). dSTORM makes use of only a single photo-switchable dye, in the presence of chemical reducing agents, and a single laser source rather than the dye pair and multiple sources described above. Some common classes of dyes used

for dSTORM include carbocyanines (Dempsey et al., 2009), rhodamines and oxazines (Heilemann et al., 2009). The labelling strategies that are commonly used in dSTORM include immunolabelling, where a primary antibody targets a specific antigen and a secondary antibody, which has the fluorophore attached, targets the primary antibody and the use of chemical tags. Examples of chemical tags used for dSTORM include SNAP-tags (Keppler et al., 2003) and Halo-Tags (Los et al., 2008).

The process involved in the redox induced photo-switching of dyes into a dark state during dSTORM is shown in the Jablonski diagram in Figure 2.7. A fluorophore is excited from the ground state, S_0 into one of the higher energy excited states. The fluorophore will then de-excite, through internal conversion and vibrational relaxation, back to the lowest vibrational energy level of the first excited state S_1. From here the fluorophore can either undergo fluorescence or a non-radiative de-excitation and return to the ground state, or through the non-radiative process of intersystem crossing, the fluorophores can cross into a long-lived triplet-state (Endesfelder & Heilemann, 2015). In dSTORM, reducing agents are introduced which match the redox potential of the fluorophores and make it possible for an electron transfer to happen. When the fluorophore is in the presence of a thiol group, a reducing agent, the fluorophores are reduced from the triplet state to form a radical anion, $F^{\bullet -}$ (van de Linde et al., 2011). This is the "off" state used in the dSTORM process. The fluorophore is stable in this state, in aqueous solution, for up to potentially hours. The fluorophore can return to the ground state either through reaction with oxygen or irradiance with high energy UV excitation. Some fluorophores, like Atto 655, are able to be fully reduced to the leuco-form of the fluorophore, FH (Kottke et al., 2010). From here, they can return to the ground state through reaction with oxygen.

In order to control the number of fluorophores in the fluorescent "on" state and those in the dark "off" state, the concentrations of reducing agent and oxygen needs to be carefully adjusted. This is done by using a STORM buffer solution. In order to have a long-lived dark state, the oxygen concentration needs to be controlled using an oxygen scavenging agent such as the oxyrase enzyme. Otherwise, if there is a high oxygen concentration, the fluorophore will quickly de-excite from the dark state back to the ground state. The return of the fluorophore from the dark state is a random stochastic process. Therefore, provided the conditions have been optimised, under irradiance from the excitation laser, a subset of the fluorophore emitters will be in the fluorescent "on" state and the rest will be in the dark stable "off" state.

Another commonly used SMLM technique is "points accumulation for imaging in nanoscale tomography" (PAINT) (Sharonov & Hochstrasser, 2006). Here the sample sits in a solution of

fluorophores that are able to transiently bind and unbind to the target protein. This can be combined with DNA origami to enable reversible specific binding of labelled oligonucleotides to DNA nanostructures (DNA-PAINT) (Jungmann et al., 2010). In DNA-PAINT a docking strand is immunolabelled to a biological target and an imager strand is conjugated with an organic dye. The imager strand is able to freely diffuse within the imaging buffer. The imager strand and docking strand are single-stranded DNA oligomers (Schnitzbauer et al., 2017). The unbound imager strands generally do not appear in the imaged frames because they diffuse freely over multiple camera pixels during a single frame. When the imager strands transiently bind with the docker strands, they become temporarily stationary and will appear as single emitter in the image, which can then be localised. The time the imager strand is bound is dependent on the stability of the formed DNA duplex between the strands. The emitter will stop emitting fluorescence to be imaged by the sensor when it photobleaches. The fluorophores still emit if the strands transiently unbind, but it is moving faster than the exposure time of the camera and hence is not localised to a fixed position. The influx rate of new imager strands will determine the frequency of new binding events. Since the fluorophores can be repeatedly replaced from the buffer, the maximum achievable number of photons received from a target is not limited by photobleaching in DNA-PAINT.

SMLM performance can be compromised by several factors. There are many different algorithms that are used for the fitting of single fluorophore localisation data, e.g., (Sage et al., 2019, 2015; Small & Stahlheber, 2014) and the accuracy of these localisation algorithms can be affected by the amount of noise in the CMOS or EMCCD sensors being used and by the effects of dipole orientation of the fluorophores (Engelhardt et al., 2011). In order to localise a single emitter, the PSF needs to be sampled with at least twice its spatial frequency width to satisfy the Nyquist criterion (Sauer, 2013; Legant et al., 2016), which requires that the size of the detection pixels in the camera cannot exceed half of the FWHM of the magnified PSF. In the absence of noise, a single emitter being imaged by either a sCMOS or EMCCD sensor would appear as a continuous distribution, with the greatest digital number being recorded near the centre of the fluorescence intensity distribution. The fact that the PSF is being sampled by the camera pixels will result in a pixelated distribution as shown in Figure 2.5. However, it is still possible to fit a Gaussian to the pixel values and give a prediction of the emitter position to less than the size of a pixel. The detected photons in the fluorophore images will have shot noise and may be distributed within the recorded PSFs over multiple frames according to a normal distribution that will limit the precision of the localisation algorithm to determine the emitter's spatial co-ordinates. The standard deviation of the estimates of the fluorophore position across multiple frames gives a measure of the precision of localisation (Deschout et al., 2014).

A further factor that can degrade the localisation precision is the amount of background fluorescence contributed by out-of-focus fluorophores, which will add further noise to the recorded PSF images. A non-uniform fluorescence background may shift the predicted positions of some fluorophores towards brighter regions of the frame (Small & Stahlheber, 2014). Most single molecule localisation algorithms can account for uniform background, although it will reduce the SNR and the accuracy of the localisation prediction, but accounting for a non-uniform distribution is more difficult. Another challenge for SMLM is that the assumption only a single fluorophore is "on" in its local vicinity may not be valid. Some localisation algorithms aim to address overlapping fluorophore PSF but generally the precision will be worse than if the fluorophore PSF are well separated. A final consideration is that aberrations in the optical system can change the shape of the PSF. If the aberrated PSF is significantly distorted, then fitting to a Gaussian model PSF will be compromised.

The achievable resolution, R, of a SMLM is hard to determine, however it cannot be better than the Cramér–Rao lower bound (CRLB) (Kay, 1993). An approximation for the CRLB limit to resolution, R_{loc}, is described below (Lelek et al., 2021).

$$R_{loc} = 2\sqrt{2\ln 2}\,\sigma_{loc} \approx 2.355\sigma_{loc} \qquad \text{Equation 2.20}$$

Where σ_{loc} is the localisation precision where the system is shot noise limited. The R_{loc} is the FWHM value of a gaussian fit calculated from the σ_{loc} as the standard deviation. The CRLB is a way to estimate the localisation precision, but it generally overestimates the actual precision. The CRLB can be calculated in terms of σ_0, the standard deviation of a Gaussian fit to the PSF and N, the number of photons collected by the camera, whilst assuming that the camera noise and camera pixelation can be neglected (Lelek et al., 2021):

$$\sigma_{loc} \geq \frac{\sigma_0}{\sqrt{N}} \qquad \text{Equation 2.21}$$

$$FWHM = 2\sqrt{2\ln 2}\,\sigma_0 = \frac{0.51\lambda}{NA} \qquad \text{Equation 2.22}$$

This means that the achievable resolution is dependent on the NA of the objective lens, the wavelength of the light used and most importantly the number of photons collected from a specific

fluorophore. For typical wavelengths and fluorophores, σ_0 is on the order of 100 nm and N = 10^2-10^4 photons (Lelek et al., 2021).

$$\sigma_{loc} \geq 1 - 10nm \qquad \text{Equation 2.23}$$

However, this is an over-estimate on the achievable precision for a SLM technique. This does not take into account the effects from using a Gaussian fit for the PSF, read noise, background fluorescence, pixelization and dipole orientation. A more accurate description of the localisation precision is given by (Mortensen et al., 2010)

$$\sigma_{loc} \geq \sqrt{\left(\frac{{\sigma_0}^2 + \left(\frac{a^2}{12}\right)}{N}\right)\left(\frac{16}{9} + \frac{8\pi {\sigma_0}^2 b^2}{a^2 N^2}\right)} \qquad \text{Equation 2.24}$$

Where a is the pixel size and b is the background intensity. The CRLB provides the maximum achievable resolution for localisation algorithms.

In order to localise the position of a fluorophore, most localisation algorithms fit the recorded fluorophore PSF to a Gaussian model. These algorithms will usually use an iterative process to determine the fitting parameters and need a metric of the quality of the fit. The most common techniques to quantify the goodness of fit are least squares criterion (LS) and maximum likelihood estimation (MLE) (Small & Stahlheber, 2014). LS estimations are able to fit to the PSF without any knowledge of the camera's noise and the error is calculated in the following manner (Small & Stahlheber, 2014):

$$Sum\ of\ squared\ errors = \sum_{pixels} \frac{(data - predicted\ fit)^2}{expected\ variance\ of\ data} \qquad \text{Equation 2.25}$$

The parameters of the fit are varied to minimise the sum of squared errors.

MLE (Kay, 1993) is less biased for low numbers of detected photons but is computationally more demanding and is able to approach the limit of CRLB when a sufficiently high SNR is achieved (Small & Stahlheber, 2014).

ThunderSTORM (Ovesný et al., 2014), *WindSTORM* (Ma, Xu & Liu, 2022) and *Picasso* (Schnitzbauer et al., 2017) are examples of single molecule localisation algorithms.

ThunderSTORM is implemented as an open-source plug-in for ImageJ and offers a variety of different processing and post-processing techniques. The approximate molecular positions are determined by applying low pass and band pass filters to the recorded PSF image data. The sub-diffraction and pixel localisation is performed by either computing the centroid of the local neighbourhoods, by a radial symmetry technique or by fitting a function to the PSF. The lateral drift of the sample during the acquisition can be corrected for by either tracking fiducial markers (Balinovic, Albrecht & Endesfelder, 2019) or using cross-correlation of different time segments (Mlodzianoski et al., 2011). *ThunderSTORM* is implemented on the CPU. This means it is slower than some newer GPU-based techniques but the throughput of SMLM localisation can be increased via a parallelized implementation of *ThunderSTORM* on a high-performance computing cluster (HPC) (Munro et al., 2019). This is important if SMLM is to be scaled to an HCA modality.

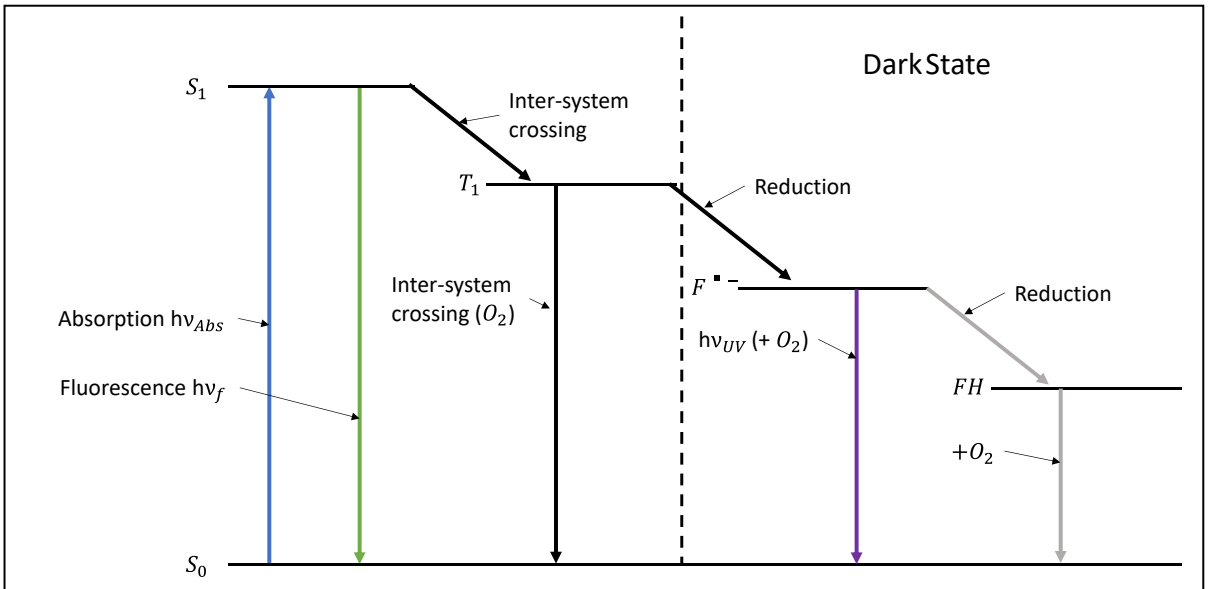

Figure 2.7. Jablonski diagram showing the energy levels involved in dSTORM. A fluorophore is excited to the first singlet state S_1 from the ground state S_0, under excitation from a single laser source. Then it can either fluoresce or undergo intersystem crossing into a triplet state T_1. In the presence of a reducing agent, e.g., a thiol, the triplet state can be reduced to a radical anion $F^{\bullet -}$. This is the very long lived dark "off" state of the dye used in dSTORM. The fluorophore can then return to the ground state through either irradiance by UV light or interaction with oxygen. Some dyes can be fully reduced from the radical anion state to the leuco-form of the fluorophore (FH). From here they can react with oxygen to return to the ground state S_0

WindSTORM uses a non-iterative linear deconvolution fitting approach that can achieve high density and high-speed emitter localisation (Ma, Xu & Liu, 2022) while minimising image artifacts and improving the localisation accuracy by using a background subtraction method based on extreme value-based emitter recovery. *WindSTORM* also applies an inverse deconvolution and frequency truncation step to remove noise frequencies above the PSF limit of the microscope and identifies

overlapping fluorophore PSF by finding their local maxima. *WindSTORM* can be implemented using a CPU or a GPU.

Picasso is a GPU implemented localisation algorithm which was developed in Python. It is available as an integrated downloadable software package composed of standalone modular components with graphical user interfaces (Schnitzbauer et al., 2017). The components are called “Localize”, “Filter”, “Render, “Average”, “Design” and “Simulate”. The Localize component uses a spot identification algorithm that uses image gradient. This is done to reduce the impact of non-uniform background. The local maxima are first detected by finding the pixels with the highest count for the local vicinity. The local vicinity is defined by a square box with a user defined pixel side length. The net gradient is calculated around the local maximum for each box. The net gradient of a localisation is the sum of intensity flow toward the centre of the spot (Schnitzbauer et al., 2017). This is approximately proportional to the signal photons. Then there is a user defined threshold for the net gradient which decides which spots will be further considered for fitting or be disregarded. After the boxes have been determined, they are the inputs for a maximum likelihood fitting procedure. After fitting, the localisations can be filtered using the “Filter” component and rendered using the “Render” component software.

There are also 3D localisation algorithms that make use of axially varying PSF. Traditionally the required axial variation is induced by adding astigmatism to the microscope PSF using a cylindrical lens positioned in front of the camera (Huang et al., 2008) . By first imaging a z-stack of fluorescent sub diffraction limited beads, it is possible to provide a calibration of the axial variation of the PSF and predict the axial localisation of fluorophores from the shape of their recorded PSF. Alternatively a spatial light modulator can be used to engineer an axially varying PSF such as the double helix PSF (Pavani et al., 2009) .

2.7 Conclusion

In this chapter, there was a brief overview of the history of optical microscopy, followed by a presentation of the photophysics involved in fluorescence and the classical diffraction limit definition for resolution. Some commonly used microscopy illumination and imaging modalities were briefly described, including conventional widefield epifluorescence, confocal, light-sheet microscopy, multiphoton microscopy, and OPT. Some commonly used super resolution modalities were also presented, including SIM, STED and SMLM (focusing mainly on STORM). There are many

more imaging modalities that are not included in this introductory chapter, which provide further scope for development, including MinFlux (Gwosch et al., 2020) and correlative imaging approaches.

3. EasySTORM

This chapter describes *easySTORM* (Kwakwa et al., 2016), a low-cost implementation of dSTORM (Heilemann et al., 2008; Fölling et al., 2008) that was developed in our laboratory at Imperial and which I used throughout my PhD project. *easySTORM* utilises multimode laser diodes and multimode optical fibres and provides uniform high power (~1 W) illumination across a large FOV (~125 x125 µm). Taking fuller advantage of large sCMOS or CMOS camera sensors, this enables many more cells to be imaged in a single FOV than is possible in many commercial microscopes, which is convenient for high content analysis. *easySTORM* can be implemented for wide-field epifluorescence, HILO or TIRF microscopy. This chapter outlines the experimental configurations used at the start of my project and presents the demonstration of super-resolved imaging of nuclear pore complexes (NPC) - confirming a lateral resolution below 40 nm – and also describes *histoSTORM,* the application of *easySTORM* to histological samples for pathology, illustrating the potential to be used in the clinical diagnosis of kidney disease.

3.1 Implementation of *easySTORM* on commercial microscope frames

dSTORM was adopted in our laboratory as we found it to be the most convenient and flexible SMLM technique in terms of sample preparation and image data acquisition. It can be implemented on most widefield capable fluorescence microscopes using just one excitation laser wavelength to provide the required stochastic fluorophore blinking. The only requirement for the laser illumination is sufficient high (typically > ≈ 1-3 kW/cm^2 (Lelek et al., 2021)) intensity across the field of view, which should be as uniform as possible.

The use of multimode laser diodes provides excitation power levels in the range of ~0.7- 2 W at discrete wavelengths (e.g., 405, 462, 470, 525, 635 nm) that are well matched to commonly used fluorophores including fluorescent proteins and small molecule dyes. This radiation can be coupled into multimode optical fibres with high (>90%) efficiency using low-cost optical components. As discussed below, the use of multimode diode laser radiation propagating through a vibrating multimode optical fibre can provide a relatively uniform flat-top illumination excitation intensity distribution when the output beam from the optical fibre is focussed to the back focal plane of the microscope objective lens. While a low-cost dSTORM microscope had previously been reported

(Holm et al., 2014), *easySTORM* (Kwakwa et al., 2016) was the first demonstration of the potential to use multimode laser diodes for SMLM and the first demonstration of SMLM with FOV >100 x100 µm.

By propagating multiple collimated multimode diode laser beams, which provide different excitation wavelengths, into a single multimode optical fibre, it is possible to perform multi-labelled STORM acquisitions on samples labelled with multiple appropriate fluorophores sequentially or simultaneously, e.g., (Bossi et al., 2008). *easySTORM* has been implemented using Vectashield (Olivier et al., 2013) to mount the samples or using chemical STORM (oxygen scavenging) buffers as described in chapter 2. For the results described in this thesis, a chemical STORM buffer was used to mount the nuclear pore complex samples.

easySTORM was designed so that it could be easily implemented on a standard (commercial) microscope frame without any input required from the manufacturer. Figure 3.1 shows a schematic of the experimental configuration for *easySTORM* implemented with laser illumination introduced via the back port of the microscope frame. Collimated beams from the multimode diode lasers are coupled into a multimode optical fibre (previously shown to be useful for STORM with single mode lasers (Křížek, Raška & Hagen, 2011)) by a 12.5 mm focal length lens inside the laserbank (Comar Optics 12 DQ 06) and the output from the optical fibre is collimated by lens L1 of 100 mm focal length (Thorlabs, AC254-100-A). An advantage of using multimode optical fibres rather than single mode optical fibres is that it is easier to deliver the excitation laser radiation to the microscope sample with high (>90%) coupling efficiency. Since the core size of the multimode optical fibres used is typically 50 to 100 µm for our STORM systems, the coupling efficiency – and therefore the excitation power at the sample - is also more robust to misalignment and optical beam drift (e.g., due to laboratory temperature variation or the mechanical relaxation of optomechanical components) compared to when using single mode optical fibres, which typically have a core diameter of ~5 µm.

Lasertack multimode diode laser modules are used as the excitation sources for our implementation of *easySTORM*. These laser diode modules make use of anamorphic prism pairs to produce a more circular collimated beam profile. This helps to maximise the coupling efficiency of the lasers into the multimode optical fibres. Propagating laser radiation through a multimode optical fibre will typically introduce a speckle pattern (Goodman, 2007) at the output. This speckle pattern would produce inhomogeneities in the illumination across the FOV. The resulting variation in power density could lead to varying SMLM resolution across the FOV. However, it is possible to time average the speckle pattern over the camera exposure to achieve an effectively uniform illumination across the FOV. This

can be done by vibrating the multimode optical fibre at a sufficiently high frequency to scramble the propagating modes within the exposure time of the camera.

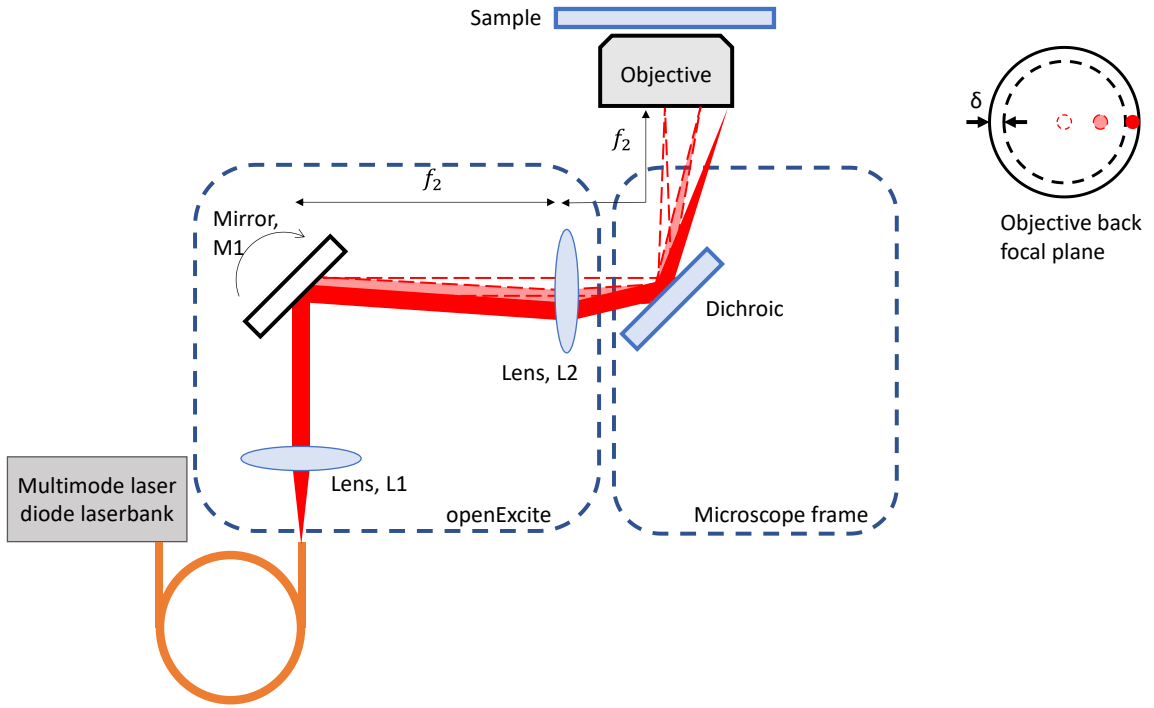

Figure 3.1. Diagram of optical configuration of *easySTORM* implemented on a standard inverted fluorescence microscope frame using an *openExcite* laser excitation module. By adjusting the tip and or tilt of the mirror (M1) in the *openExcite* module, the position where the beam focusses in the back aperture of the objective lens can be adjusted (see inset top right) to switch between epi-illumination (dashed line), HILO (shaded), or TIRF (solid) if supported by the objective lens. To realise TIRF, it is necessary to focus the excitation laser within the indicated annular region, δ. See Figure 4.6 for diagram of multimode laser diode laserbank.

A basic implementation of *easySTORM* on a standard fluorescence microscope frame (Zeiss Axiovert 200) is shown in Figure 3.1. The laserbank comprises an array of multimode laser diodes and mirrors and beam splitters arranged to combine their respective output beams into a single beam that is coupled into a multimode optical fibre (0.1 NA, 100 µm core diameter) using a 12.5 mm focal length lens (Comar Optics 12 DQ 06). The multimode optical fibre is vibrated using a despeckler motor (Cairn Research Ltd, Despeckler) clamped to the outside jacket of the fibre. The output of the multimode optical fibre is connected to an *openExcite* module mounted at the back port of the microscope frame. This essentially collimates the laser beam from the multimode optical fibre and steers it using an adjustable mirror (M1) to a lens (L2) that focuses it to the back aperture of the microscope objective lens via the fluorescence microscope dichroic beam splitter.

3.1.1. *openExcite* module

The *openExcite* module can be assembled from generic components and Figure 3.2 shows a CAD rendition of the configuration I used that is based on components from Thorlabs costing less than £700. The list of these *openExcite* components is publicly available on the Imperial photonics group website for *easySTORM* (Kwakwa et al., 2016):

https://www.imperial.ac.uk/photonics/research/biophotonics/instruments--software/super-resolved-microscopy/easystorm/.

A copy of the components list is also shown in Appendix A2.

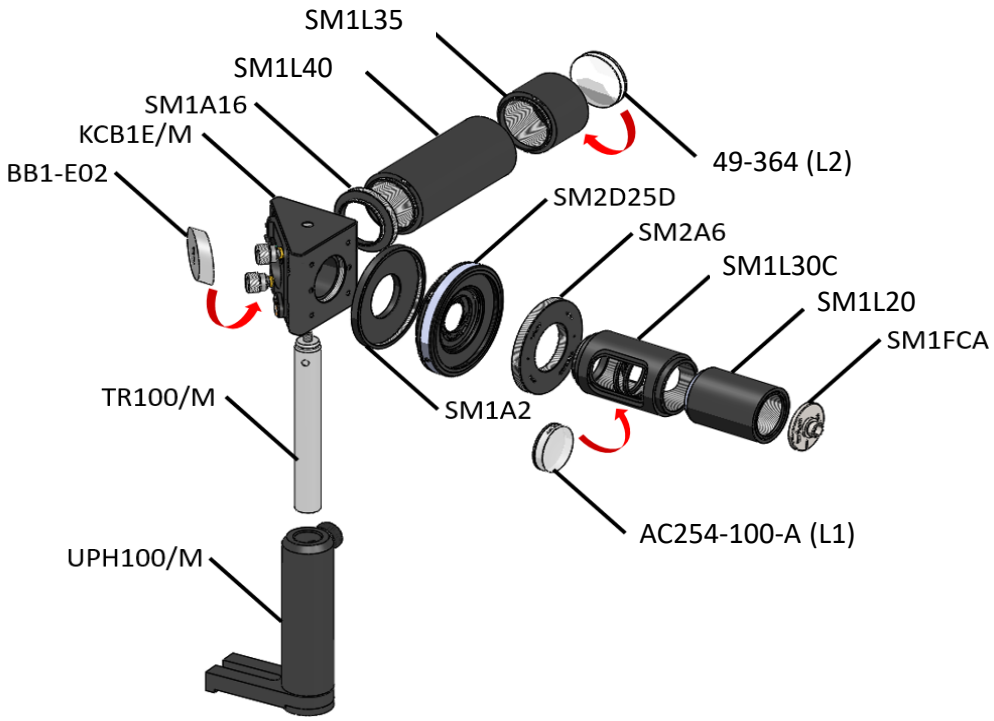

Figure 3.2. *openExcite* CAD rendition (Thorlabs and Edmund Optics component part numbers indicated)

The laser beam emerging from the optical fibre is collimated by a lens of 100 mm focal length (L1 in Figure 3.1), and then reflected by an adjustable mirror (M1 in Figure 3.1) positioned in the back Fourier plane of the excitation tube lens of 200 mm focal length (L2 in Figure 3.1), which focuses the laser beam to back focal plane of the objective lens to provide reasonably uniform “top-hat" widefield illumination of the sample. With this combination of multimode optical fibre and lenses L1

and L2, the illumination extends over a field of view exceeding 120 µm in diameter when using a 100x 1.4NA objective.

Item	**Supplier**	**Part #**
Fibre connector [FC-APC]	Thorlabs	SM1FCA
1-inch lens tube	Thorlabs	SM1L20
Slotted 1 inch lens tube	Thorlabs	SM1L30C
Fibre collimating lens [100mm]	Thorlabs	AC254-100-A
1-inch to 2-inch adapter	Thorlabs	SM2A6
25mm clear aperture iris	Thorlabs	SM2D25D
SM2 to SM1 adapter	Thorlabs	SM1A2
90-degree kinematic mount (elliptical hole)	Thorlabs	KCB1E/M
1" elliptical mirror (EO2 coating)	Thorlabs	BBE1-E02
100mm post holder	Thorlabs	UPH100/M
100mm post	Thorlabs	TR100/M
1-inch lens tube	Thorlabs	SM1L40
1-inch tube lens tube	Thorlabs	SM1L35
Tube lens [200mm]	Edmund Optics	49-364

Table 3.1. Components list and part numbers used to build openExcite module

The steering mirror, M1, positioned in the back Fourier plane of lens L2, can be used to change the angle of the excitation beam to implement epifluorescence (when the beam is on the optical axis), total internal reflection fluorescence (TIRF), or highly inclined and laminar optical sheet (HILO) microscopy (Tokunaga, Imamoto & Sakata-Sogawa, 2008).

There is a commercial alternative to the low-cost *openExcite* module that can be provided by Cairn Research Ltd; the OptoTIRF V2 provides similar functionality to the *openExcite* module but is motorised to enable electronic control of the steering of the focussed excitation laser beam in the back aperture of the objective lens. We have an OptoTIRF V2 unit in our laboratory and sometimes use this instead of an openExcite module.

3.1.2 TIRF and HILO microscopy

The mirror M1 inside the *openExcite* module (or the equivalent mirror in the OptoTIRF V2) can be set to enable total internal reflection fluorescence (TIRF) microscopy when using a TIRF objective lens by steering the focussed beam to the outer edge of the back aperture of the TIRF objective lens. TIRF requires that the angle of incidence of the excitation beam at the coverslip-sample interface should be greater than the critical angle of incidence such that excitation is confined to an evanescent field in the lower refractive index medium of the PBS STORM buffer solution. This limits the fluorescence to a few hundred nanometres above the coverslip, avoiding any background due to out of focus fluorescence.

To achieve TIRF illumination, the incidence angle at the interface between the sample media and the glass coverslip needs to exceed the critical angle

$$\sin \phi_C = \frac{n_{sample}}{n_{glass}} \qquad \text{Equation 3.1}$$

Where ϕ_C is the critical angle and n is the refractive index of the sample media or the glass coverslip respectively. Thus, the excitation radiation should be confined outside a circle in the back aperture of the objective lens with a radius exceeding (Kwakwa et al., 2016):

$$r \geq f \times n_{glass} \times \sin \phi_C = f \times n_{sample} \qquad \text{Equation 3.2}$$

Where the back focal length of the lens f can be estimated by dividing the magnification of the objective lens by the focal length of the standard tube lens.

The outer radius of the back aperture of the objective lens is given by (Juskaitis, 2006):

$$r = f \times NA \qquad \text{Equation 3.3}$$

Where r is the radius, f is the back focal length of the objective lens and NA is its numerical aperture.

This means the excitation radiation should be confined to an annulus in the back aperture between the limiting aperture radius and the minimum radius required for TIRF. This width, δr, of this annulus is described by the following equation:

$$\delta r = f(NA - n_{sample}) \qquad \text{Equation 3.4}$$

TIRF *easySTORM* has previously been implemented with an oil immersion TIRF objective lens (Zeiss, α Plan-apochromat 100x/1.46 oil DIC Vis) with NA of 1.46. Since the refractive index of PBS is ~1.335 and the back focal length of this objective lens is 1.65 mm, the width of the annulus can be calculated:

$$\delta r = 1.65(1.46 - 1.335) = 0.206\ \text{mm}$$ Equation 3.5

This annulus is shown by the dotted region in the back aperture of Figure 3.1. Therefore, if the focussed excitation spot size is ~200 µm, then all the laser power can contribute to the *easySTORM* TIRF excitation (Kwakwa et al., 2016).

Highly inclined and laminar optical sheet (HILO) microscopy entails illuminating the fluorescent sample with an inclined beam to increase the signal to background ratio compared to that obtained using epi-illumination. While HILO microscopy does not provide the sub-diffraction limit optical sectioning or background-free fluorescence imaging of TIRF microscopy, it has the advantage that it does not require a TIRF objective lens (which are expensive) and can image objects further than ~200 nm from the microscope coverslip. To implement HILO illumination, the excitation beam is focused near the edge of the objective lens' back aperture – but inside the circle beyond which TIRF would be implemented if a TIRF objective lens was used. The off-axis excitation beam is then collimated by the objective lens to be incident at the coverslip at a highly inclined angle such that only a thin section of the sample is illuminated. This provides optical sectioning of the sample and reduces the background fluorescence compared to what would be observed when using widefield epi-fluorescence illumination. The increase in signal to noise ratio (SNR) is important for SMLM since it improves the localisation precision and hence the achievable resolution of the microscope. When using a multimode optical fibre (with a core diameter of 100 µm), the excitation beam is not perfectly collimated but still provides close to uniform illumination over the HILO FOV.

Figure 3.4 in the following section illustrates the imaging performance achievable with TIRF and HILO microscopy, compared to epi-illuminated easySTORM.

3.2 easySTORM images of Nuclear Pore Complexes

To quantify the achievable resolution of *easySTORM*, I imaged cells expressing SNAPtag-labelled nuclear pore complexes (NPCs) (Thevathasan et al., 2019), derived from a cell line (Cell Line Services GMBH, U-2 OS-Nup96-SNAP clone no.33 cells, Catalogue No. 300444) that is becoming a *de facto* standard in STORM resolution measurements. In this cell line, Nucleoporin Nup96 is expressed in U-2OS cells labelled with a SNAP-tag (Keppler et al., 2004) to which the dye AF647 can be linked. There are 32 copies of Nup96 in each NPC and these form two (cytoplasmic and nucleoplasmic) "rings" that are separated axially by 50 nm. The rings each have 16 copies of Nup96 arranged with 8 corners, each containing two Nup96 proteins separated by 12 nm. The corners of the two rings are

vertically aligned with each other and the distance between Nup96 proteins in neighbouring corners of the nuclear pore complex is 42 nm, while the diameter of the rings between opposite corners is 107 nm. The prior knowledge of these reproducible biological structures (well-characterised using electron microscopy) makes them a useful reference sample to quantify the achievable resolution. For example, if the individual corners of the nuclear pore complex are clearly resolved, then the resolution is better than 42 nm. A useful feature of U-2OS cells on a microscope coverslip is that the lower nuclear envelope containing the NPC is flat, enabling hundreds of complexes to be imaged in a single TIRF FOV.

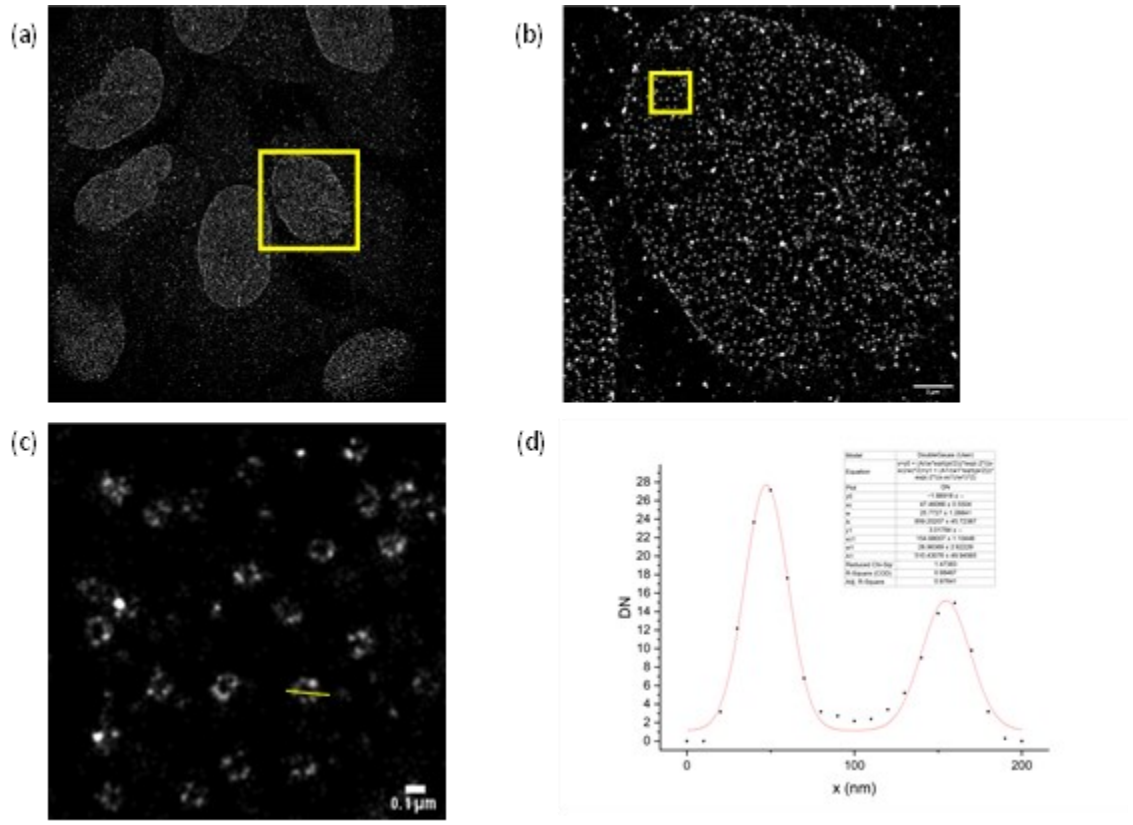

Figure 3.3. (a) image of U-2OS nuclei showing Nup96 proteins in nuclear pore complexes endogenously labelled with a SNAP-tag AF647; (b) magnified region of interest from (a) containing a nucleus; (c) magnified region of interest of nuclear pore complexes within the nucleus shown in (b). A line profile across the diameter of one of the nuclear pore complexes is shown. A double Gaussian fit has been plotted to the line profile (d), where the amplitudes, stand deviations and central positions of the two Gaussians are used as fit parameters together with a global offset to account for the background intensity level

Figure 3.3 shows *easySTORM* image data of these nuclear pore complexes expressed in U-2OS cells that were acquired with TIRF illumination (using the OptoTIRF V2 to couple the multimode diode laser excitation into the Zeiss Axiovert 200 microscope fitted with a 100x, 1.46 NA Zeiss TIRF objective lens) and imaged using a (Photometrics Prime 95B) sCMOS camera. The optical autofocus

module described in Chapter 5 was used to maintain the sample in focus during the TIRF *easySTORM* image data acquisitions that comprised 20,000 frames with an 80 ms exposure per frame for each FOV.

All widefield images shown in this thesis were acquired as a single seperate acquisition prior to the acquisition of the STORM frames. The STORM images in this thesis were rendered using ThunderSTORM. There are a number of common visualisation techniques (Baddeley, Cannell & Soeller, 2010; Ovesný et al., 2014). The simplest visualisation approach is to just present the localisations as a scatter plot. This presents the image as a binary image with pixel values set to 1 at the localisation positions. All other pixel values are set to zero. This however does not provide high quality reconstructed images. Another approach is gaussian rendering. Here, for every localisation a 2D or 3D Gaussian function is integrated over the voxel volume. The standard deviation for each gaussian is the respective localisation uncertainty. The render is the sum of these gaussians centred at their respective localisation positions. The disadvantage of the gaussian rendering approach is that it is slow.

SMLM data can also be visualised as a 2D histogram counting the number of the localisation positions within a bin size chosen as the final pixel size in the super-resolved reconstructed image. The histogram can be "jittered". Here, a random number is chosen from the normal distribution with a standard deviation matching the localisation uncertainty. This number is added to the co-ordinates of all the localisations before making the histogram. This is repeated multiple times until and all the generated histograms are then averaged. As the number of jitters increases, the reconstruction approaches the gaussian rendering. An alternative approach to visualisation is "average shifted histograms" with jittering (Scott, 1985; Ovesný et al., 2014). Here, n^d multidimensional histograms of the same bin width are averaged. The histograms are created by shifting the original histogram for "n" times in each of its "d" dimensions. The bin width for the histogram is chosen to be the equal to the number of shifts, n, multiplied by the chosen pixel size for the reconstructed super-resolved image. The average shifted histogram method is fast orders of magnitude faster than the gaussian rendering and gives a reconstruction that approaches the gaussian rendering with a constant standard deviation for each localisation. The renders used in this thesis use the average shifted histogram approach.

There is a trade-off between imaging speed and quality of SMLM reconstruction (Diekmann et al., 2020). Lower power densities at the sample enable more individual pores to be localised at the cost of greater total image data acquisition times. I empirically found 80 mW average laser power (measured at the sample plane, corresponding to a power density of 0.60kW/cm^2 over the 130 µm

FOV) with 80 ms exposure time to be a reasonable compromise. The transverse drift during each image data acquisition was corrected in post processing using 100 nm diameter TetraSpeck fluorescent beads (T7279) as fiduciary markers, which were added to the sample within the FOV. The *easySTORM* image data were processed using Picasso (Schnitzbauer et al., 2017), which has the capability to track the drift of the fiducial markers embedded in the sample and hence correct for any transverse drift during acquisition. The reconstructions shown in Figure 3.3 are rendered with 10 nm resolution. Figure 3.3(d) shows that neighbouring corners within the NPC were resolved in the reconstructed images and that the measured separation of opposite proteins within an NPC was consistent with the expected value of 107 nm. A double gaussian was fitted, using Origin Pro 2022, to the line profile between the opposite pores within the NPC, see yellow line in Figure 3.3(c). The locations of the peaks were found to be at 47.5±0.6nm and at 154.7±1.1nm, as shown by the table in Figure 3.3(d). The errors quoted are those returned by the non-linear Origin fitting algorithm for a double gaussian. This gave a measured separation of 107.2±1.7nm and agreed with the expected value.

The same NPC sample was imaged under the same conditions using the OptoTIRF V2 unit to switch the excitation modality between widefield epi-illumination, HILO (Tokunaga, Imamoto & Sakata-Sogawa, 2008) and TIRF (Funatsu et al., 1995; Tokunaga et al., 1997) by moving the position of the focused spot on the back aperture as shown in Figure 3.1. Representative results are shown in Figure 3.4 to illustrate the relative performances of the different modalities. The top row shows rendered easySTORM images of individual nuclei and the second row shows the corresponding magnified ROIs for each modality, presenting the reconstructions of individual NPCs. The background fluorescent signal is lowest for TIRF illumination, with only on the order of 100 nm penetration of the evanescent field into the sample (Almada, Culley & Henriques, 2015). HILO provides some background reduction, as fluorescence is only excited within the thin optical sheet of excitation radiation, while widefield epi-illumination results in out of focus fluorescence within the sample that contributes to a significant background. This means that the signal to background ratio in the raw data will be significantly reduced for the epi illumination in comparison to TIRF and HILO. Background fluorescence can reduce the localisation precision and hence the achievable image quality and resolution. The extent to which this impacts the SMLM image data, e.g., through artifacts in the reconstructed SMLM images, will depend on the labelling of the sample and the specific SMLM software used.

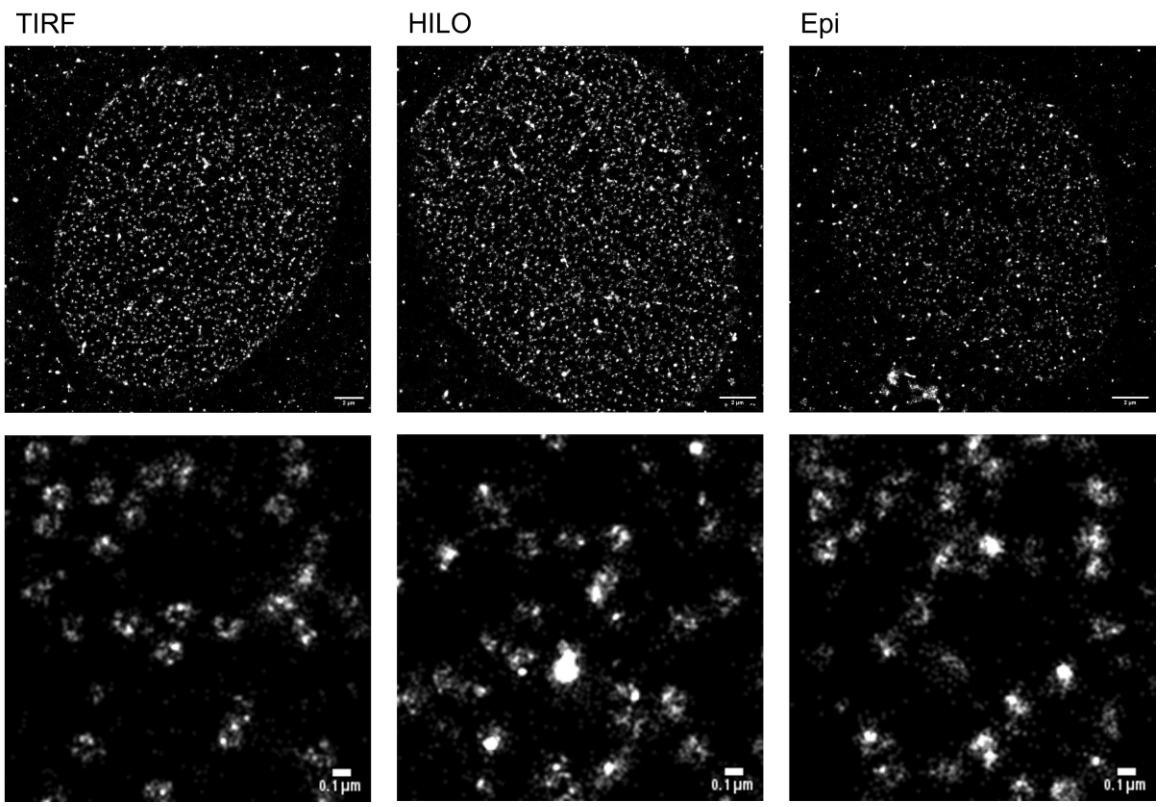

Figure 3.4. (Top) Rendered *easySTORM* images of U-2OS nuclei acquired on the Zeiss Axiovert 200 microscope frame under TIRF, HILO and epi-illumination. Each FOV was acquired using the Photometrics Prime 95B sCMOS camera with 20,000 frames of 80 ms exposure. (Bottom) Corresponding magnified ROIs showing individual nuclear pore complexes for the respective illumination modalities.

Figure 3.4 illustrates how TIRF illumination provides the best reconstructed images of the NPC, resolving most of the NPC proteins, HILO provided an intermediate SMLM image quality, resolving proteins in many NPC but with more artefacts present and some NPC not resolved, while epi-illumination provided the worst reconstructed image - with few NPC protein being resolved and the characteristic NPC ring structure being difficult to discern. For the different illumination modalities, the power measured at the sample plane was kept constant.

3.3 histoSTORM

We were motivated to explore potential clinical applications of easySTORM, particularly where electron microscopy (EM) is used for diagnostic pathology. In the UK, EM is routinely used in the diagnosis of kidney disease, particularly human glomerular diseases (Haas, 1997; Shore & Moss, 2002). EM can be helpful to image structural abnormalities of the basement membrane and is also

used to investigate the shape, sub-structure, and location of immune complexes relative to the glomerular basement membrane. It may also be applied to diseases that involve fibrils and rare genetic diseases like Fabry's disease.

However, clinical EM is expensive and requires specialist staff. It is currently limited to a few NHS facilities, the number of which has decreased in recent years. Outside the UK, most countries do not include EM in their standard clinical diagnoses (Kurien et al., 2016). We were therefore interested to investigate whether cost-effective super-resolved SMLM microscopy, e.g., *easySTORM,* could be used to image ultracellular structure to aid in clinical diagnosis and thereby augment or replace EM in the diagnosis of kidney disease, partly in the hope that it could provide clinical benefit to patients in countries with no access to clinical EM. We therefore developed protocols to apply *easySTORM* to clinical histological sections that have been stained for immunofluorescence using clinically approved antibodies on human kidney biopsy samples (Garcia et al., 2021). Edwin Garcia developed the staining protocol and I developed the imaging protocol. We termed the approach of applying *easySTORM* to clinical histological samples to acquire super-resolved immunofluorescent images using clinically approved antibodies as "*histoSTORM*" (Garcia et al., 2021).

For *histoSTORM*, the kidney samples were either frozen or formalin-fixed paraffin-embedded (FFPE) sections. Silicon (Polycraft ZA22 Mould RTV Addition Cure Mould Making Silicone Rubber; MBFibreglass, Newtownabbey, Northern Ireland) was added to the frozen kidney biopsy samples and then the sample was polymerised at room temperature to provide a "rubber" consistency (Garcia et al., 2021). The biopsy samples had a thickness of 3 microns. For the FFPE samples, xylene was used to remove the paraffin in two 5-minute treatments followed by five 2-minute ethanol washes with decreasing ethanol concentration (100%, 75%, 50%, 25% and 0% dilution in water). The FFPE and frozen samples were then dried before being fixed with acetone. The kidney tissue was labelled with primary antibodies (laminin MAB1920 and IgG or Rabbit isotype X0936). The samples were then washed and then treated with the secondary antibodies (goat anti-mouse IgG H+L, goat anti-rabbit IgG H+L). Then the secondary antibodies were conjugated with fluorescent dyes (Alexa Fluor 555 or iFluor 647). Finally, the samples were washed and fixed with acetone. The samples were also cleared by immersing them in a PBS solution with 70% thiodiethanol (TDE). The samples were then mounted in a PBS STORM buffer. The STORM buffer used was composed of 50 mM of mercaptoethylamine, 10 mM D-lactate, 60% TDE in a PBS solution and 0.75 U/mL of an Oxyrase-EC enzyme (SAE0010; Sigma-Aldrich).

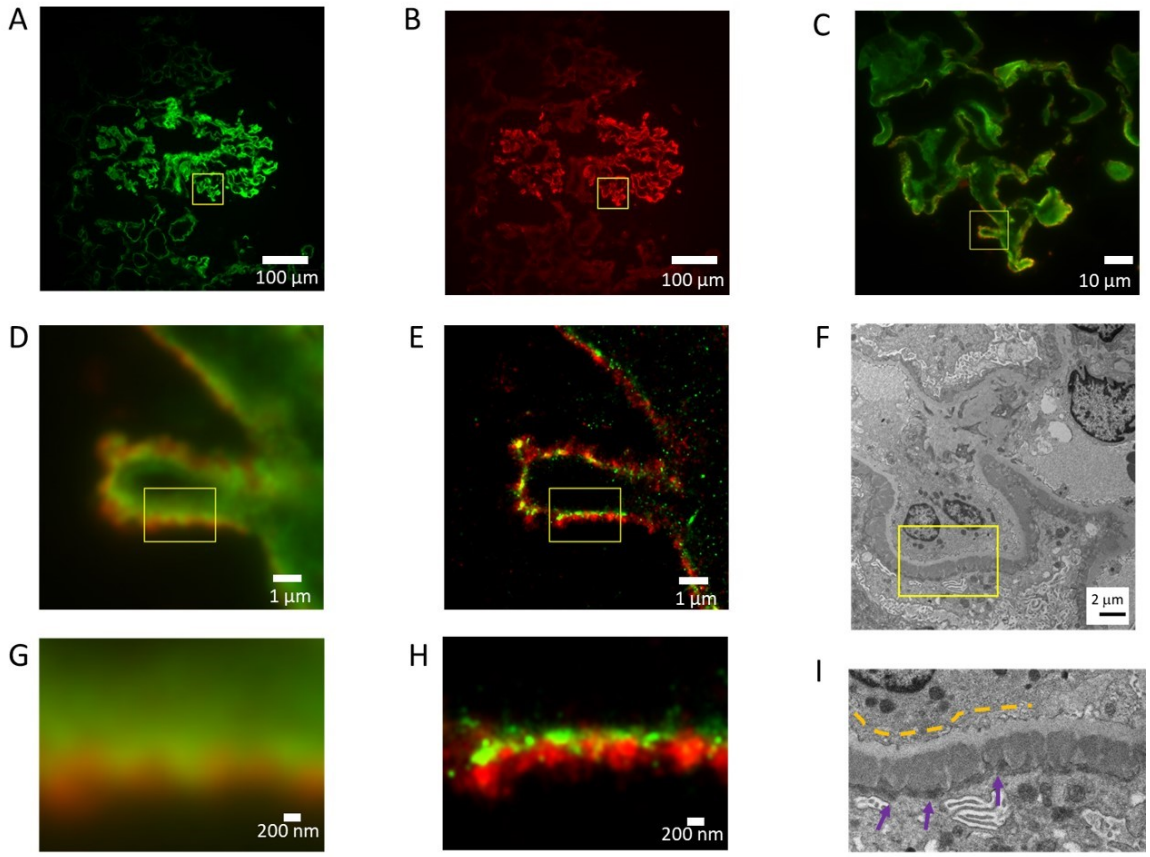

Figure 3.5. (a-b) Widefield immunofluorescence images of frozen membranous glomerulonephritis biopsy samples with (a) the laminin labelled with Alexa Fluor 555 (green) and (b) IgG deposits labelled with iFluor 647 (red). (c) shows a two colour merged image of the ROI indicated in (a, b). (d, e) show the widefield IF image and corresponding *histoSTORM* image of the ROI indicated in (c). (e) has been rendered at 25 nm resolution. (f) shows an EM image acquired at 5500x magnification of a similar structure as (e) from the same biopsy. (g, h) show magnified widefield and *easySTORM* images of the 3.2 µm x 2.4 µm ROI indicated in (d, e). (i) shows the magnified EM ROI indicated in (f), in which the yellow dashed line indicates the location of the GBM (light grey), and the purple arrows point to the dark grey regions indicating the immune complexes that contain IgG on the subepithelial side. Reproduced from (Garcia et al., 2021)

The kidney tissue sections were imaged using the Zeiss Axiovert 200 microscope frame with the OptoTIRF V1 unit and a multimode diode laser bank provided by Cairn Research Ltd. No autofocus was available on the microscope when these easySTORM image data were acquired using a 100x, 1.46 NA TIRF oil objective lens (Zeiss, α Plan-apochromat 100x/1.46 oil DIC Vis) and the Photometrics Prime95B sCMOS camera. Since the tissue sections were so thin, the easySTORM image data were acquired with epifluorescence illumination. The two fluorescent dyes (AF 555 or iFluor 647) were imaged sequentially, with iFluor 647 being imaged first to avoid it being bleached by the shorter wavelength excitation radiation before being imaged. The AF 555 was excited using a 520 nm laser diode (Lasertack LDM-520-1000-C) and the iFluor 647 was excited using a 638 nm laser diode

(Lasertack LDM-638-700-C). The exposure time of the sCMOS camera used to acquire the *easySTORM* image data was 30 ms and the power density at the sample was initially at 1.045 kW/cm^2 for the 520 nm excitation and 2.5kW/cm^2 for the 638 nm excitation. The sample was excited at these power densities for 5-10 s before the power density was reduced by approximately 50%. The *easySTORM* images were reconstructed using ThunderSTORM (Ovesný et al., 2014) and lateral drift correction (without fiduciary markers) was performed for both spectral channels. The two spectral channel images were registered using cross correlation with software developed by Yuriy Alexandrov that is available at the following address https://github.com/yalexand/Imperial-ClusDoC.

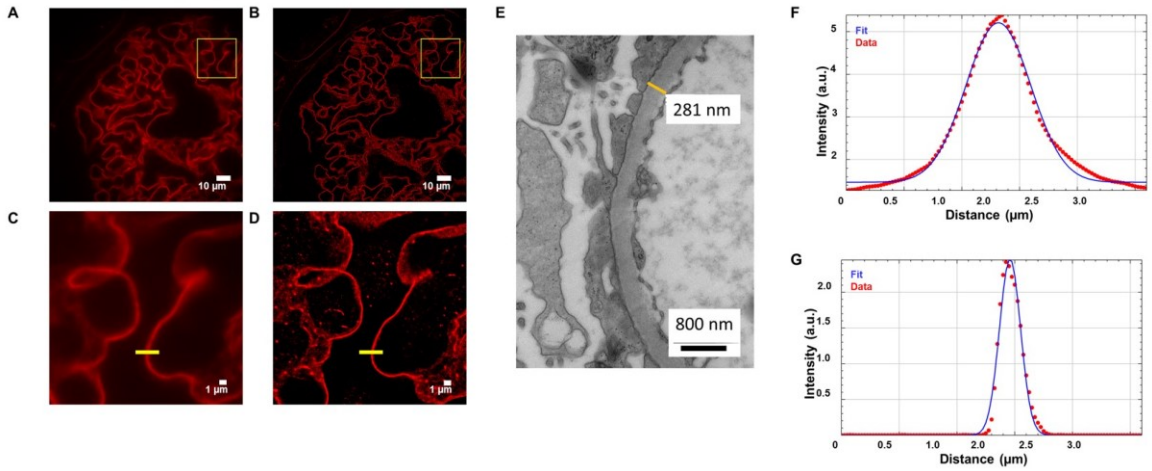

Figure 3.6. Widefield (a, c) and easySTORM (b, d) images of minimal change disease in FFPE section from a biopsy. (c) and (d) show enlarged ROIs indicated by the yellow boxes in (a) and (b). Laminin present in the GBM is labelled with iFluor 647. (e) shows an EM image of the GBM from a different section within the same biopsy imaged with a magnification of 15,500x. The GBM thickness was measured using EM to be 281 nm. The FWHM of the line profile of the yellow lines in (c) and (d) measure the thickness of the GBM from the widefield and STORM reconstruction. The widefield gives a measured thickness of 657 nm and the STORM gives a measured thickness of 212 nm. Reproduced from (Garcia et al., 2021)

For this initial study, both the frozen and FFPE samples were labelled using clinically approved antibodies. Figure 3.5 shows widefield epifluorescence, STORM and EM images of kidney tissue sections presenting membranous glomerulonephritis, which is characterised by subepithelial immune complex deposits containing IgG, in the glomerular basement membrane (GBM). Membranous glomerulonephritis also results in a thickening of the GBM (Lai et al., 2015). Figure 3.5 (a, b) show the two separate colour epifluorescence images, with an anti-human laminin probe labelled with AF 555 (green) and the GBM and IgG deposits labelled with iFluor 647 (red). Figure 3.5 (c) shows a magnified view of the indicated ROI with the two colours superimposed. Figure 3.5 (d) shows a magnified epifluorescence image of the indicated ROI in Figure 3.5(c) that contains a

capillary loop and Figure 3.5 (e,h) show the corresponding *histoSTORM* images of the same ROI rendered at 25 nm resolution. The *histoSTORM* images clearly show the IgG subepithelial deposits in context of the laminin-labelled GBM ultrastructure. By comparing the results with the EM equivalents of a similar region within the same biopsy, Figure 3.5 (f, i), it can be seen that the location of the IgG is consistent between the different imaging modalities, providing some confidence that *histoSTORM* could be used for clinical diagnosis.

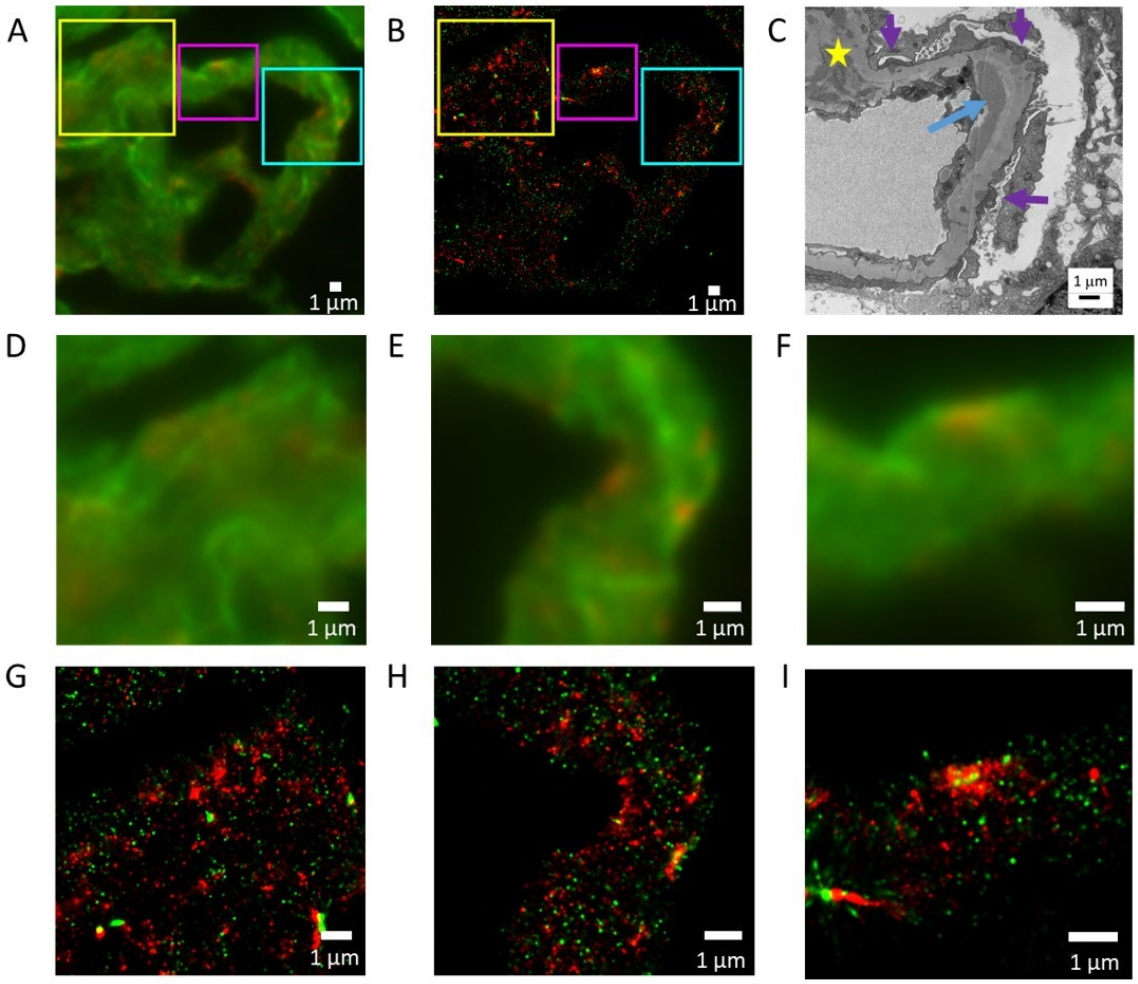

Figure 3.7. Widefield (a, d, e, f) and dSTORM (b, g, h, i) images of Lupus nephritis type IV in frozen sections. The basement membrane is labelled by staining of the laminin using Alexa Fluor 555 (green) and the IgG deposits are stained with ifluor 647 (red). The yellow box indicates the expanded regions in (d) and (g) showing Lupus Nephritis presenting mesangial deposits. The blue boxes indicate the expanded regions in (e) and (h), and present regions with subendothelial deposits. The purple boxes indicate the expanded regions as shown in (f) and (i) presenting regions with subepithelial deposits. (c) shows an EM of a similar structure from within the same sample imaged at 8000x magnification. The dark grey regions represent electron dense deposits that contain IgG. The purple arrows indicate deposits on the subepithelial side of the GBM. The blue arrows show deposits on the subendothelial side of the GBM, and the yellow star indicates mesangial deposits. Reproduced from (Garcia et al., 2021)

As described earlier, the thickness of the GBM is measured using EM as part of the diagnosis of glomerular disease. This can be addressed using *histoSTORM*, as shown in Figure 3.6, which compares *histoSTORM* and EM images of FFPE sections of a kidney biopsy. The thickness across the GBM measured by EM was 281 nm (Figure 3.6 e). Widefield immunofluorescence images do not allow measurement of the GBM thickness below the diffraction limit and a line intensity profile across the GBM has a FWHM of 657 nm (Figure 3.6 c,f). However, the *histoSTORM* images, rendered at 25 nm per pixel, present a thickness of 212 nm (measured in a different tissue section, Figure 3.6 d, g). This value is credible and indicates that histoSTORM could be used to measure the GBM thickness as clinical diagnostic tool.

Lupus Nephritis (LN) is another glomerular disease that is commonly diagnosed using clinical EM. The glomerular deposits that characterise LN usually contain polyclonal IgG and can be detected by immunofluorescence (Weening et al., 2004; Haas et al., 2020). These deposits are distributed in various regions across the glomerulus as shown for subendothelial, subepithelial and mesangial deposits in a glomerular capillary of stage IV LN. The IgG has again been labelled with iFluor 647 and the basement membrane laminin was labelled with AF 555. The *histoSTORM* images are reconstructed with a 25 nm resolution and demonstrate that the IgG deposits can be localised and have a similar distribution as presented by the EM image shown in Figure 3.7 (c) (Garcia et al., 2021).

The work developing *histoSTORM* demonstrated that *easySTORM* (and other SMLM techniques) can be applied to both FFPE and frozen biopsy sections, e.g., to indicate the positions of subendothelial, subepithelial and mesangial immune complex deposits, or to measure the thickness of the GBM. Thus, *histoSTORM* provides more information than is available from standard widefield immunofluorescence and may be useful as part of clinical diagnosis of glomerulonephritis. Because *histoSTORM* is much cheaper to implement than EM and can be undertaken by staff trained for immunofluorescence, it can be used much more widely. *histoSTORM* cannot achieve resolutions matching EM but since it is a lower cost to implement, it could find particular use for clinical applications in low resource settings, where expensive EM facilities are not as readily available. Further research is required before the technique can be fully use in clinical applications. *histoSTORM* may also provide higher throughput, due to the larger FOVs that can be imaged using *easySTORM* (Garcia et al., 2021) compared to EM.

3.4 Conclusion

In this chapter, easySTORM was presented as a low-cost implementation of dSTORM, including how by using low-cost multimode diode laser sources coupled into a vibrated multimode optical fibre to provide uniform illumination over large FOVs that can be imaged by CMOS and sCMOS sensors. The application of easySTORM was verified by resolving the neighbouring pore structures within NPC in U-2OS nuclei. This verifies that the resolution achievable exceeds 40nm. These NPCs were imaged using three different easySTORM illumination modalities, namely widefield epifluorescence, HILO and TIRF. EasySTORM was also applied to image the ultrastructure in renal pathology for histological kidney samples. The application of easySTORM to histological samples is referred to as "histoSTORM". HistoSTORM was used to image both frozen and paraffin embedded kidney samples and the position of IgG deposits were found to be consistent with that observed with EM. The aim is to continue to apply histoSTORM to other histological samples and see if it can be used as a cost-effective alternative to EM for clinical diagnosis.

4. Low-cost, modular, sustainable open-source microscopy

Optical microscopy has provided powerful tools to study cell biology and automated imaging workflows have potential to accelerate discovery but access to many advanced microscopy modalities has been limited by the cost of the instruments and components (e.g. microscope frames, cameras, excitation sources, computing resources) and automated imaging/high content analysis (HCA) instruments are typically too expensive for lower-resource research settings (e.g., low and middle income countries), and in some medical, industry or teaching contexts. This is being addressed within the microscopy community by open-source approaches with the free exchange of ideas, technology, and capabilities. This has predominantly involved the open-source access to software tools (as exemplified by ImageJ). There is increasing interest, however, in open microscopy hardware (Hohlbein et al., 2022) to reduce cost and widen access to a range of microscopy techniques. The development of open-source hardware for microscopy has been accelerating over the last few years (Hohlbein et al., 2022), partly to enable lower resourced researchers around the world to freely replicate imaging modalities elsewhere but also for leading microscopy laboratories to more easily implement and prototype new microscopy approaches. A further benefit of open-source-based instruments is that they may be more easily maintained, upgraded or adapted to new modalities than proprietary commercial microscopes.

When implementing or developing new imaging modalities, microscopists generally have to modify a commercially available microscope or build a custom microscope from generic optical and optomechanical components. Commercially available microscope frames are typically designed to provide stability and robustness and optimise optical performance (e.g., minimising aberrations) and offer ease of use. Unfortunately, the development and optimisation of hardware and software is expensive, resulting in advanced instruments costing >>$100,000 to purchase and >>$1000/year for service agreements. Commercial instruments can also be limiting because it can be difficult to add additional excitation sources, optical systems and detectors as there is typically a limited number of ports on the microscope frame. In addition, it can be difficult to access important imaging and Fourier planes when they are located inside the microscope frame (Fölling et al., 2008). It is usually difficult to modify the proprietary control software or change/upgrade the hardware components and so the instruments are typically limited to their specifications at the time of purchase and become obsolete over time as microscope technologies and techniques develop.

These considerations have motivated the work described in this chapter developing an open source, modular, low-cost, robust and sustainable microscope platform (www.openScopes.com), including a

cost-effective modular microscope frame ("*openFrame*"), new low-cost cooled CMOS cameras, a low-cost Arduino-controlled laser engine for fluorescence microscopy including easySTORM (Kwakwa et al., 2016) (a low-cost implementation of dSTORM (Heilemann et al., 2008; Fölling et al., 2008)), and the optical autofocus approaches described in Chapters 5-6. These open microscope hardware components are controlled using the open-source software *µManager* 2.0 and associated plug-ins. These components can be utilised to develop open-source microscope systems including for SMLM, for HCA and for pathology. In this thesis a prototype super-resolved HCA system utilising easySTORM of samples arrayed in multiwell plates is demonstrated.

4.1 Exemplar open microscope systems

There are several open hardware microscopes that have been developed over the past few years, ranging from optical microscopes that can increase the access and availability of microscopy, e.g. for educational purposes, to much more complex instruments for specialist applications. One of the simplest concepts for an open microscope is the Foldscope (Cybulski, Clements & Prakash, 2014) - an origami-based microscope that can be used to perform multiple different imaging modalities including brightfield, darkfield and fluorescent microscopy. Samples can be viewed by eye or can be imaged using a small ball lens and a smartphone. The sample can be focused and scanned positionally by using the folded origami structure. This design lends itself particularly well to scientific communication and for educational outreach.

The recent wide availability of 3D printing has allowed for the creation of 3D printed microscope frames that can be easily shared to provide open hardware. The OpenFlexure (Collins et al., 2020) microscope is a 3D printed open hardware microscope frame with a flexure mechanism that provides a 3D positioning capability that provides the ability to scan the sample transversely and offers a focusing capability. A Raspberry Pi camera V2 (8MP CMOS camera, Sony IMX219 sensor) is used for image capture. The OpenFlexure z and xy stages are controlled using actuator gears which can be driven by stepper motors for automated imaging with a range of 12x12x4mm of travel with a vertical step interval of 50nm and a transverse step interval of 70nm (Collins et al., 2020). This travel range is smaller than that of standard commercial microscopes with a more limited step interval size than commonly used commercial XYZ stages. There are optional electronics including stepper motor controllers and a Raspberry Pi which can control the automation. The OpenFlexure is provided with software that includes two software based autofocus algorithms for imaging thin samples.

The OpenFlexure was designed to provide access to microscopy in lower resource settings where not just the cost of a commercial microscope, but also the maintenance, is prohibitive. Since it is 3D printed, replacement parts can be printed locally and there is no need for an engineer to visit the laboratory to install the components. However, the system is somewhat limited as it cannot be directly adapted to more complex designs, e.g., utilising multiple excitation and emission paths, and the Raspberry Pi camera can limit the sampling performance and bit depth of the acquired images. Nevertheless, it is sufficient to perform multiple imaging modalities including, epifluorescence, brightfield and polarisation contrast.

Other examples of 3D printed microscopes include the Flypi (Maia Chagas et al., 2017), UC2 (Diederich et al., 2020), µCube (Delmans & Haseloff, 2018) and Octopi (Li et al., 2019). These systems are all able to be produced for less than $500 and can be maintained or replaced without the need for service engineers. They allow access to internal imaging and Fourier planes and are able to perform multiple imaging modalities including epifluorescence, automated slide scanning. These systems can often be automated using Raspberry Pi controllers and open-source GUI hardware control. However, it may not be practical to extend them beyond their initially designed functionality. They may also be relatively low mass, which could impact their stability.

As an alternative to these 3D printed microscopes, there has also been development of more robust (metal-based) approaches that are designed to provide similar performance and stability to conventional commercial microscopes – and to work with standard microscope components. They can be designed to give more flexibility and many of the designs include modularity - allowing for the easy introduction of multiple excitation and imaging lines. This means that more imaging modalities can be added to a microscope frame, or the use of the frame can be altered easily.

Some of these platforms have been used to implement low-cost SMLM. One of these platforms is the liteTIRF (Auer et al., 2018), which is built from custom-made and generic optomechanical components on a breadboard and was designed specifically for SMLM and used to acquire super resolved images using DNA-PAINT. The performance of liteTIRF was assessed using DNA-origami (Rothemund, 2006) structures with known fluorescent structures arrayed in 10 nm intervals. An alternative modular open microscopy platform is “Squid” (Li et al., 2020). Implementing microscope frames with many generic commercial optomechanical components can be relatively expensive, due to the cost of the individual components required, and these designs may not support rapid switching of imaging modalities.

A more cost-effective example of an open microscope frame is the miCube (Martens et al., 2019), which utilises an aluminium cube for its basic structure and with additional generic optomechanical

or 3D printed components. The aluminium central body, which can be Computerized Numerical Control (CNC) milled in most standard mechanical workshops, provides stability of the microscope frame and it has been applied to SMLM. Other open microscope frames have been used to implement a range of specific imaging modalities, including “LSFM” (Prakash, 2021), “smfBox” (Ambrose et al., 2020), “OpenSPIM” (Pitrone et al., 2013) and SIM (Sandmeyer et al., 2021).

This range of recently developed microscope frames demonstrates the growing interest for low-cost optical microscopes. Most have been designed for a specific microscope application. We were interested to develop a fully modular low-cost but robust and stable microscope platform that could be applied to a wide range of applications and would be straightforward to assemble and could be as flexible as standard commercial microscopes with respect to switching or combining microscope modalities without rebuilding the microscope. Thus, as well as enabling research microscopy at low cost, we wanted a platform that would be the approach of choice to prototype and apply new microscopy techniques.

The Optic’s workshop at Imperial fabricated our own miCube-based instrument to explore its potential but found it limited in terms of functionality and difficult to switch filter cubes – which required partly dismantling the microscope. We therefore designed our own modular microscope frame, basing it on a cylindrical layered structure with the idea that functionality could be switched by just modifying one layer and not dismantling or adapting the whole microscope frame. Our “*openFrame*” was designed to be used for a variety of different imaging modalities and to be of comparable mass to standard commercial research microscopes, making it sufficiently robust and stable to allow long image data acquisition times, e.g., for super-resolution imaging, high content analysis and slide-scanning. Because of its inherent compatibility with a wide range of 3rd party microscope components, and its applicability to almost any microscope modality, the potential for commercially available and user-friendly open-source microscopes was indicated and our laboratory at Imperial started collaborating with Cairn Research Ltd to refine the design for ease of use. The basic *openFrame* CAD files of the basic modules (layers) are freely shared at https://www.imperial.ac.uk/photonics/research/biophotonics/instruments--software/fluorescence-microscopy/openframe/ (and in Appendix A3) to allow anyone to fabricate their own openFrame microscope, e.g. using parts lists accessible via www.openScopes.com or https://www.imperial.ac.uk/photonics/research/biophotonics/instruments--software/. These basic *openFrame* components are also commercially available at low cost from Cairn Research Ltd, who also sell more advanced modules.

4.2 Design and implementation of *openFrame* microscopes

The aim of the *openFrame* was to develop an open-hardware microscope frame that was modular, could be upgraded easily and rapidly and could be maintained without the need for experts or service engineers. Unlike the cubic block structure of the miCube, the *openFrame* was designed to have a cylindrical core shape around the primary optical axis with cylindrical layers carrying the required optical components such as the main dichroic beamsplitter and excitation path, the objective lens, the tube lens and stackable ports for cameras and other detectors. This concept and the implementation are illustrated in Figure 4.1. The inherent rotational symmetry makes the manufacturing of the modular layers convenient using lathes, and the well-defined optical axis (in which it is easy to centre apertures and circular components) provides a reference to which optical subsystems can be aligned. The core microscope frame's capabilities can be enhanced with the addition of add-on modules which can be attached to these modular layers or incorporated in a new layer module. These add-on modules included fibre coupled excitation modules ("*openExcite*" – see Figure 4.3) and imaging layers with ports for cameras or other detectors.

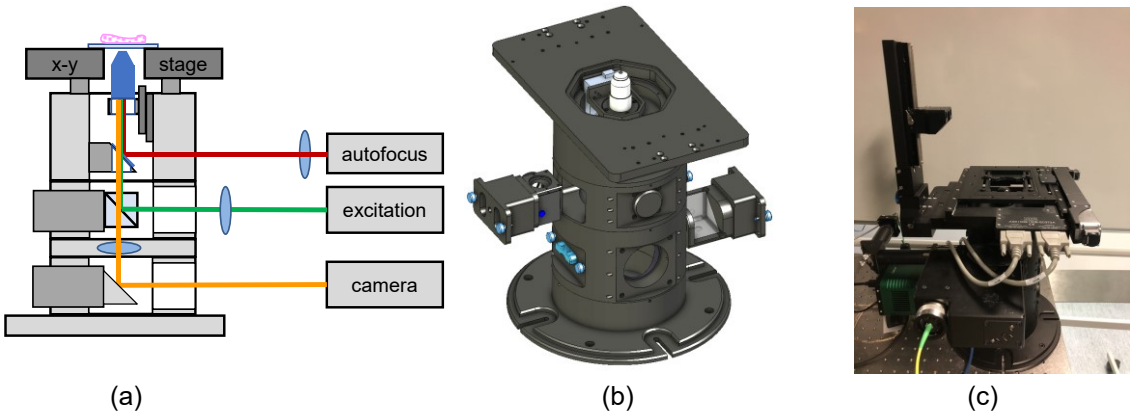

Figure 4.1. (a) shows a schematic of a simple arrangement of an openFrame for automated easySTORM (Kwakwa et al., 2016). The top layer contains a short pass dichroic and has the objective mounted on a L-shaped bracket attached to an encoded linear Z-stage. There is an automated XY stage with a sample above. The excitation source is introduced from the layer below the autofocus layer. The excitation beams are reflected by a multiline dichroic and fluorescence is transmitted by the dichroic. The fluorescence is then focused by the tube lens mounted horizontally inside the openFrame and forms an image on the camera after the signal is reflected by a mounted mirror. (b) shows a CAD of the openFrame showing the different layers, stage adaptor plate, and base plate with mounting slots and countersunk holes. (c) shows the openFrame arranged for HCA STORM imaging. There is a vertical transilluminator, the openExcite module which provides the multiline excitation via a multimode fibre source. There is an automated XY stage and an automated piezo Z-stage.

The *openFrame* was conceived by Paul French and initially developed within the Photonics group at Imperial College London. Significant development of the first prototype was performed by Simon Johnson and Martin Kehoe in the Optomechanical Instrumentation workshop within the Optics

(a) (b)

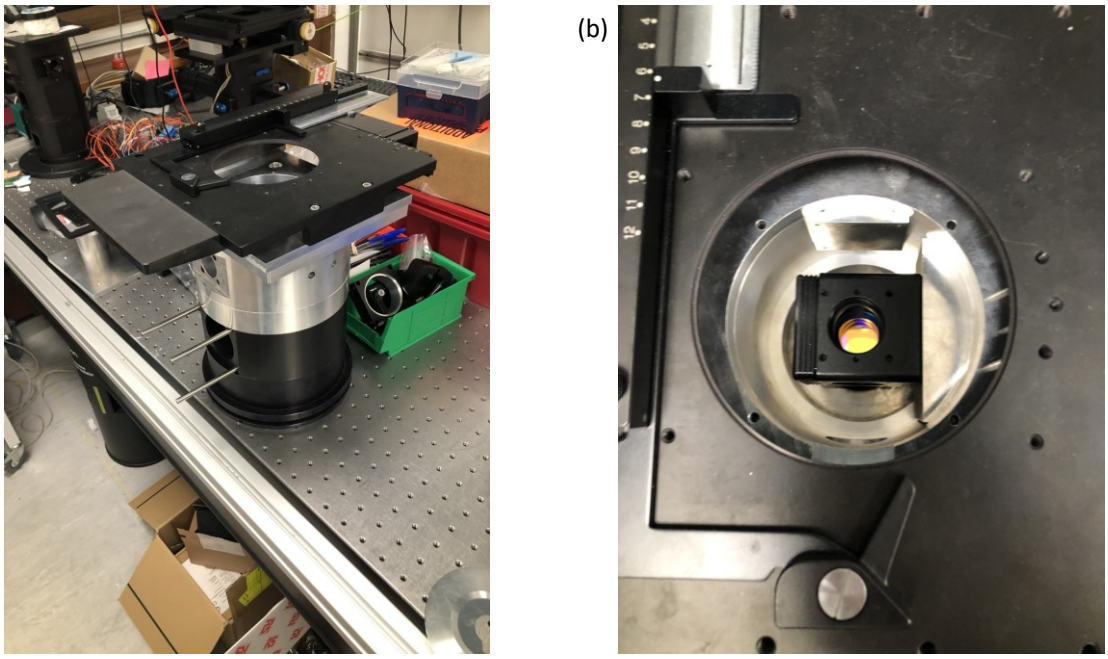

Figure 4.2. (a) shows a photo of the original prototype *openFrame*. This version was built in Imperial Photonics group's Optomechanical Instrumentation Workshop. The layers were machined using a lathe and CNC milling machine. The setup above shows the frame arranged with an Olympus manual XY stage mounted on a stage adaptor top layer plate. Beneath the stage layer is the excitation layer with a Thorlabs dichroic cube mounted and a 30mm input for the excitation laser source. Below the excitation layer is a layer housing the tube lens. Below the tube lens is the camera layer with a 60mm smooth bore output to the camera and 60mm spaced Thorlabs cage system. And finally, at the bottom of the frame is a base layer which can be fixed to an optical bench using L-shaped brackets and M6 screws. (b) shows a view looking down the centre of the frame along the optical axis defined by the objective and the centred tube lens. The dichroic cube containing the dichroic, excitation filter and emission filter can be seen mounted and positioned in the centre of the optical axis. Beside the dichroic is the mounting bracket that a piezo linear Z-stage could be mounted to, and the objective is attached to the stage using an L-shaped bracket

Section with contributions from members of the Photonics Group. The CAD design was then refined by Frederik Görlitz of the Photonics Group in collaboration with Cairn Research Ltd ("Cairn") and subsequently developed in partnership, with Cairn, who are also developing their own commercial modules that are compatible with *openFrame*.

The initial *openFrame* prototype is illustrated in Figure 4.2. It comprised layers machined using a lathe and milling machine. The module layers had channels drilled through them so that they could be located on rods fed through the layers to help maintain the relative angular orientation of the layers. These rods were externally threaded, and a nut was screwed downwards on each of the four

rods to provide stability and hold the layers together. The imaging layer had a 2-inch side port opening for the camera and Thorlabs cage rods could also be mounted into pre-drilled holes in a 60mm spacing format. The tube lens (Nikon MXA20696) was positioned in a separate layer, mounted horizontally, and centred on the optical axis. The frame was designed to have an inner circular channel running through the middle of the frame of sufficient width to mount (Thorlabs DFM1/M) dichroic beamsplitter cubes and associated mounting plate. An image of this first prototype *openFrame* with a manual XY microscope stage is shown in Figure 4.2. The stage was designed to have enough space to incorporate a low-cost (~£3000 including controller) piezo inertia drive Z-stage (with encoder) that was mounted vertically on the inside circular channel and the objective lens was attached to this via an L-shaped bracket. The piezo inertial drive (PI, Q-545.140) uses a single piezoelectric actuator, controlled with a modified sawtooth voltage. As the actuator explands, it moves the runner. The runner has an associated inertia so doesn't follow the same fast contractions of the actuator and hence remains in its current position as the actuator retracts. This first *openFrame* prototype presented some significant challenges. Although the vertical retaining rods created a stable microscope frame, they made it time-consuming to add new layers and precluded changing the dichroic filter cube while the frame was assembled.

Figure 4.1 shows an optical schematic and CAD drawing of the next iteration of the *openFrame*, developed in collaboration with Cairn. The design maintained the rotational symmetry but the retaining posts through the layers were eliminated. Instead, each layer now has a dovetail base shape and is locked in position using set screws. There were also 8 angularly equidistant small locater metal pins (25 mm long), between sequential layers that prevent the layers rotating relative to each other, other than allowing the possibility for adjacent layers being rotated by 45 degrees with respect to one another. The outer diameter of the frame was reduced, which helped reduce the cost of the frame (requiring less aluminium) and the Thorlabs dichroic filter cube mounts were replaced with smaller filter cube mounts (fabricated by Cairn) held in place with magnets. Cairn developed two cube holders: one to incorporate a 25 mm long dichroic beamsplitter and the other to incorporate a 32mm long dichroic beamsplitter. A mount was built to allow fine positioning of the dichroic filter cube to align it with the central optical axis of the microscope frame. The design could also accommodate smaller Thorlabs dichroic filter cube mounts (CM1-DCH/M) instead of Cairn's dichroic filter cubes cube mount, although these cannot be used with the magnetic coupling but can be held in position using an M4 screw. A significant improvement in the openFrame design was the introduction of ports on the side of the dichroic filter cube layers which allowed the dichroic cubes to be removed and switched without the need for the frame to be disassembled.

The top “focussing” layer housing the objective lens is similar to that of the first *openFrame* prototype, incorporating the same vertical piezoelectric z-stage (PI, Q-545.140) with objective lens on L-bracket in the central channel, but also incorporates a beamsplitter cube and SM30/Thorlabs 30 mm cage system port to support an optical autofocus module. This autofocus beamsplitter is a short pass dichroic that transmits the excitation and fluorescence radiation and reflects an infrared autofocus laser beam. Two optical autofocus designs are discussed in detail in chapters 5 and 6.

After the focussing top layer, the *openFrame* is designed to be formed from standard layers of 65 mm or 80 mm height. There is a 2-inch clear aperture running through the layers that can be fitted with alignment pinhole tools at the top and the bottom of layers to align laser beams onto the optical axis. On the bottom of each layer, there is a thread to which a 30 mm diameter horizontal tube lens (e.g., a large FOV tube lens from Nikon, Olympus or Thorlabs) can be attached. The tube lens suspended below the layer can be housed inside a 30 mm height spacer layer.

The standard 65 mm high layer has two 30 mm smooth bore (SM30) output ports opposite each other with 30 mm (Thorlabs) cage rod mounting holes around each SM30 opening. This layer can be used to mount the dichroic filter cube and to introduce an epifluorescence excitation source.

The 80 mm camera layers have two output ports that incorporate C-mount camera adaptors on sliders to enable adjustment of the camera position relative to the tube lens or SM60 output ports with mounting holes for 60 mm Thorlabs cage system. This camera port layer is generally positioned immediately after the tube lens spacer layer and typically includes a mirror mounted at 45 degrees to direct the light from the tube lens to the camera. This mirror has fine adjustment to adjust the position of the image on the camera.

Below the camera layer, there is a base layer that has slots and countersunk holes for screws to attach the *openFrame* to an optical breadboard or bench.

The cost of a standard *openFrame* (composed from a base layer, camera layer, 65mm standard layer, a focusing layer and stage layer) is ~£3,200. The cost of a piezoelectric z-stage and controller was £3,600. The breakdown in costs can be found in the components list, on the *openFrame* webpage and in Appendix A3.

https://www.imperial.ac.uk/photonics/research/biophotonics/instruments--software/fluorescence-microscopy/openframe/

This refined openFrame can be used with a range of microscope accessories. Above the top focussing/autofocus layer there is a stage adaptor plate that has sets of tapped holes to allow mounting of the most common commercial XY-microscope stages. An important aim of the

openFrame is to be manufacturer-agnostic, meaning that components from multiple companies can be installed and so users are not limited to only buying components from a single commercial source. The microscope stage can be manual or automatic. Since we aimed to develop an automated high content analysis capable system, an automated Zaber stage (Zaber, ASR100B120B-T3) was mounted to the stage adaptor. The stage adaptor plate also has mounting points for a transillumination arm to mount an LED source above the sample on the optical axis to provide transillumination through the objective lens. The Zaber ASR100B120B-T3 stage costs in the region of £7,500.

All of the motorised components and cameras discussed in this work were controlled using *µManager* 2.0 software. However, an *openFrame*-based microscope could be implemented with other software and the basic *openFrame* layers can be replaced with other commercial or open source or self-built alternatives. For example, Cairn now provides an 80 mm camera layer with a 2-mirror switching unit that can direct the image to one of two cameras mounted on the ports. This module can be manual or motorised and allows imaging of the same FOV with different detection functionality, e.g., different spectral channels or different imaging modalities. Cairn can also now provide a 65 mm layer with a unit to switch (manually or automatically) between different dichroic filter cubes and different (input) ports.

4.2.1. *openExcite*

To introduce the excitation laser beam into the excitation layer, which houses the main microscope dichroic beamsplitter (e.g., the multiline dichroic used for the *easySTORM* (Kwakwa et al., 2016) implementation) Dr Sunil Kumar and I have developed the *openExcite* module, which can be assembled from generic components (from Thorlabs) at a cost of less than £700. The list of *openExcite* components is available on the Imperial photonics group website for *easySTORM* (Kwakwa et al., 2016) and in Appendix A2:

https://www.imperial.ac.uk/photonics/research/biophotonics/instruments--software/super-resolved-microscopy/easystorm/.

Figure 4.3 shows a CAD rendition of the *openExcite* module. It has an optical fibre adapter port to couple the excitation sources via a multimode optical fibre. The laser beam emerging from the optical fibre is collimated by lens L1 and then reflected by a mirror positioned in the Fourier plane of the excitation tube lens L2, which focuses the laser beam to the back focal plane of the objective

lens to provide widefield illumination of the sample. A fibre-vibrator is applied to the multimode optical fibre to time-average laser speckle and the result is a uniform excitation intensity over field of view. If the focal lengths of L1 and L2 are 45 cm (Thorlabs, AC254-045-A) and 150 cm (Edmund optics, 32-502), the illumination enables imaging over a field of view exceeding 120 µm when using a 50 µm diameter core, 0.22 NA fibre. The choice of focal length for the collimating and tube lens can be altered depending on the size of FOV that requires illumination, the NA of the optical fibre used and depending on the type of illumination modality that is being used.

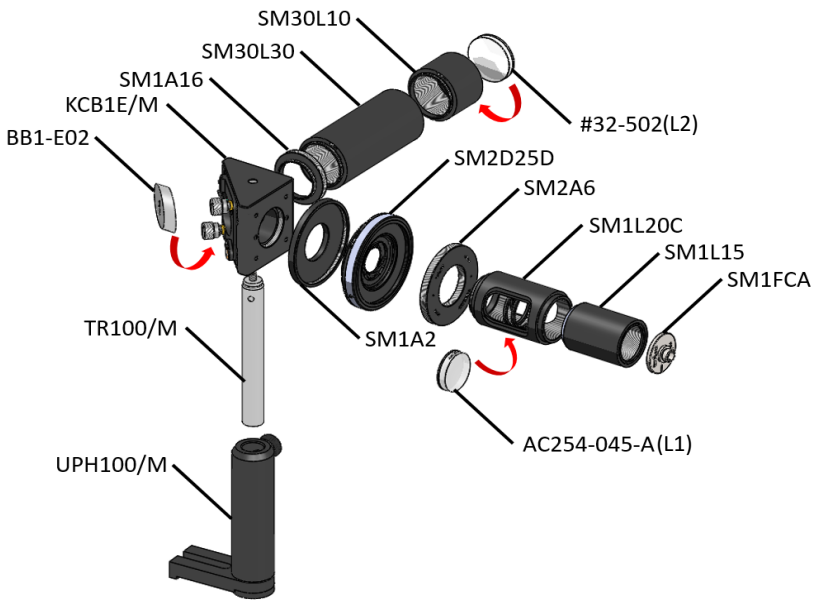

Figure 4.3. *openExcite* CAD rendition (Thorlabs and Edmund Optics component part numbers indicated)

The steering mirror can be used to change the angle of the beam to enable highly inclined and laminar optical sheet (HILO) microscopy (Tokunaga, Imamoto & Sakata-Sogawa, 2008) or total internal reflection fluorescence (TIRF) microscopy. For HILO illumination, the beam is no longer focused on the optical axis of the objective lens but is focused near the edge of the objective's back aperture. This is the position just before total internal reflection would occur if a TIRF objective was used. The resulting excitation beam is then collimated by the objective lens at a highly inclined angle such that only a thin section of the sample is illuminated. This reduces the background fluorescence that occurs in epifluorescence and increases the signal to noise ratio (SNR), which is important for SMLM where it improves the localisation precision and hence the achievable resolution of the microscope. HILO does not require an (expensive) TIRF objective lens but provides some optical sectioning. The openExcite components cost in the region of ~£665.

4.3. Cost-effective multiline laserbank

A key component of a fluorescence microscope for SMLM and many other applications is a laser excitation source. The group previously demonstrated the efficacy of multimode diode lasers for *easySTORM* (Kwakwa et al., 2016) and I set out to design a low-cost sustainable multiline laserbank that would be a suitable excitation source for automated *easySTORM*. The lasers should be automatically controllable using µ*Manager* 2.0, and so low-cost laser driver controllers were developed using Arduinos to interface between the computer and the laser.

4.3.1 Low-cost laser drivers

The multiline laserbank is based on high-power multimode laser diodes from Lasertack (www.lasertack.com), which provide approximately 1W of continuous wave power at their respective visible wavelength. Lasertack provide low-cost laser diode driver modules (iLD series diode high power laser diode driver with TEC controller) to be used with the laser diodes that, depending on the model, can output a maximum drive current of 0.5A, 2.5A or 4.5A. These controllers can monitor and maintain the temperature of the laser diode using a negative temperature coefficient thermistor (NTC) and thermoelectric cooling (TEC). The temperature controller is designed to be used with a 10 kΩ NTC (NTCAFLEX05103HH) and the temperature is set using a potentiometer on the chip. The resistance is measured across two pins on the controller using a multimeter and the resistance values measured can be compared to the datasheet to match with the corresponding required temperature when using the NTCAFLEX05103HH thermistor. The diodes were set to operate at a nominal temperature of 25°C corresponding to 18,0488 Ω.

The driver circuit boards have connections for a power supply, external modulation signal and an interlock connection. An Arduino Uno was used to provide the required analogue modulation signal for the controller and also communicate with µ*Manager* 2.0 via a USB connection. The power supply to the diode controller could be between 5V and 24V. A 12V, 3.34 A power supply was used for each of the controllers (Mean Well GST40A12-P1J).

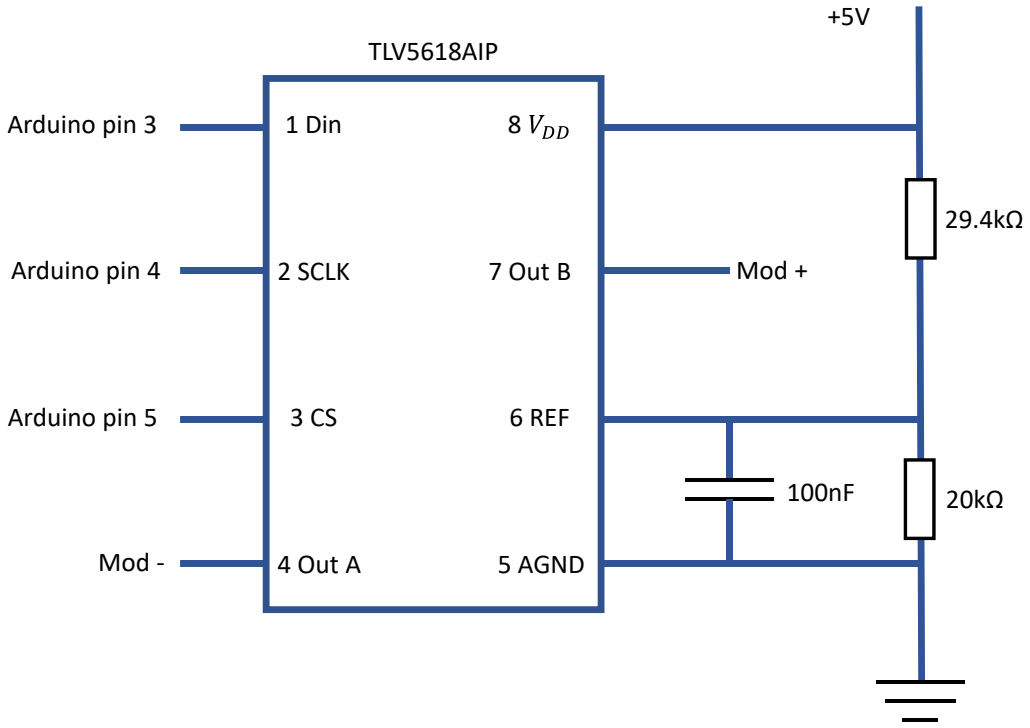

Figure 4.4. A schematic showing the wiring for the TLV5618AIP DAC to convert the digital output signal to an analogue modulation signal for the Lasertack iLD series laser diode drivers.

Din: Digital serial data input, SCLK: Digital Serial clock input, CS: chip select, AGND: Ground, REF: analogue reference, V_{DD}: Positive power supply, Out A & B: DAC A & B analog outputs connected to the negative and positive modulation terminals on the driver

A device adaptor for the Arduino Uno was provided for µ*Manager* 2.0, as part of the *µManager* installation, with firmware to enable analogue control of the diode laser output modulation by a programmable signal output from a digital-to-analogue converter (DAC) on a daughterboard of the Arduino (which normally only outputs a digital signal). The firmware was downloadable from the *µManager* documentation for Arduinos. The DAC was a Texas Instrument TLV5618AIP, which is a 12-bit voltage output DAC with dual channels that can output a voltage range of 0-5.1 V and can accept a 5.5 V input. The Arduino firmware can communicate natively with the DAC through a built-in SPI protocol. The wiring of the TLV5618AIP DAC is shown in Figure 4.4. The DAC requires a reference voltage of 2.04 V between pins 5 and 6. The 5 V output from the Arduino Uno pin is connected to pin 8, V_{DD}, and two resistors connected in series are used to split the voltage and match the required reference voltage for the DAC. Pin 5 of the DAC is connected to the ground pin on the Arduino to ensure there is a shared ground connection. A 100 nF capacitor is connected between pins 5 and 6 to act as a decoupling capacitor, which is used to decouple the two circuits connecting the reference and ground pins to the V_{DD} pin. The SCLK, pin 2, is the serial clock and is the connection that carries

the clock pulse from the Arduino (master device) via the Arduino digital pin 4. The CS connection, pin 3 on the DAC, is connected to the Arduino digital pin 5, and is the slave chip select connection, through which the Arduino, acting as the master device, informs the slave device that it will send or receive data. When the Arduino is sending or receiving data, the chip select pin is set to Low, otherwise it is set to High. When the reference voltage is set correctly, the response time of the DAC to a trigger is 50 µs.

The DAC output pins A and B are connected to the negative and positive modulation inputs on the laser driver. The voltage signal for the modulation of the laser driver is varied between 0 and +5 V. The driver is set such that when the modulation voltage is set to 0.2-0.3 V, the drive current to the laser results in the laser just reaching lasing threshold. A modulation voltage of 5V modulation provides the maximum drive current for the laser. There is a shunt resistor as part of the iLD series driver that will be 1 Ω, 0.2 Ω or 0.1 Ω, to output a maximum of 500 mA, 2500 mA or 4500 mA, depending on the model of the driver. The driver board has potentiometers for the bias and gain levels on the board which are adjusted using a flatheaded screwdriver. Initially both the bias and gain potentiometers are set to zero by rotating the screw 25 times anti-clockwise. Then, with the interlock connected and the laser diode connected, the modulation signal is set to 0.2V. The bias potentiometer is adjusted until the point where the laser diode has just begun to lase. Then, with the laser output enclosed, the modulation voltage is set to the maximum 5 V, and the gain potentiometer is adjusted, by rotating the screw clockwise, until the operating maximum laser drive current is reached for that specific diode. This is measured by monitoring the voltage across the shunt resistor and calculating the drive current accordingly.

For example, if the diode driver is the 4500 mA series, then the resistor will have a resistance of 0.1 Ω. For the Lasertack multimode 638 nm, 700 mW laser diode (LDM-638-700-C), the operating current is 1000 mA and hence the voltage measured across the shunt resistor at this current will be 0.1 V.

$$V = IR = 1000mA \times 0.1\Omega = 0.1V \qquad \text{Equation 4.1}$$

After the maximum current has been set, the bias level should be checked again in case the gain has shifted the cut-on voltage level. If it needs to be adjusted, the voltage is set again to 0.2 V and the potentiometer is adjusted to the correct level. Similarly, the maximum level should be checked again, and the gain potentiometer adjusted accordingly.

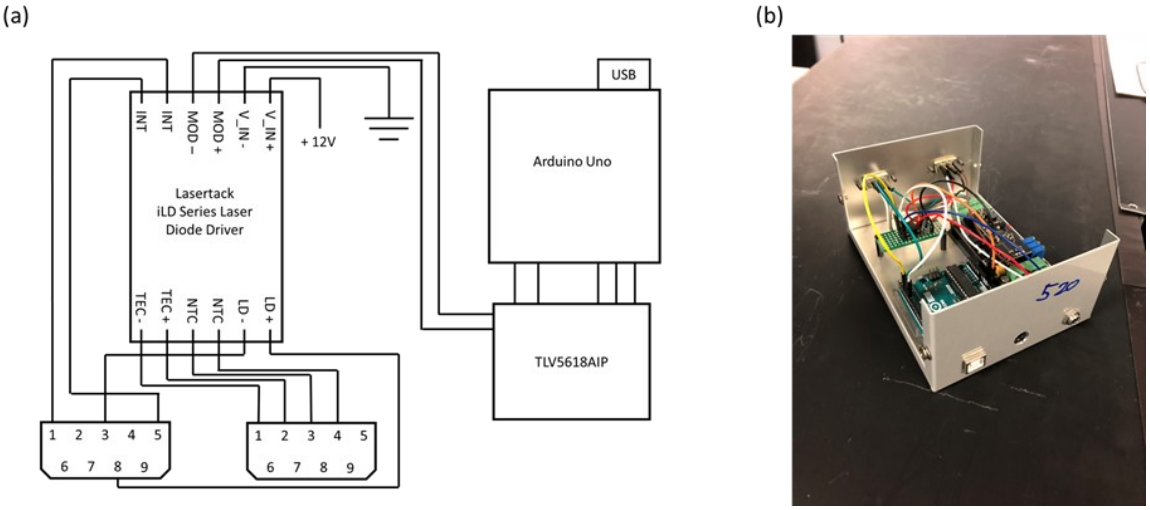

Figure 4.5. (a) Schematic of homebuilt laser driver and TEC controller built with a Lasertack iLD Series Laser diode driver, TLV5618AIP DAC and Arduino Uno (b) Photos of laser driver controller

As illustrated in Figure 4.5, the iLD series driver, the TLV5618AIP DAC and the Arduino are housed in an aluminium box (Takachi Electric industrial MB5) and the DAC is raised from the aluminium using nylon posts and screws. The DAC, capacitor, and resistors are soldered onto a breadboard (Roth Electronik RE941-S2) and the connections to the Arduino and driver are also soldered to the board. Holes are machined into the box for the 12 V power supply and the USB serial communication between the Arduino and *µManager*. The Arduino is powered by the USB connection. Holes are also added to the box so that two 9-pin D-sub connectors can be attached. One of the D-sub connectors has male connection pins and the other has female connection pins. The connections for the driver's interlock, laser diode positive and negative current connections are made to one of the 9-pin D-subs and the NTC, TEC+ and TEC- pins are connected to the other 9-pin D-sub. This is to match the pin configuration used by Thorlabs for their laser diode driver and temperature controller units respectively. This enabled these home-built drivers to be used interchangeably with a Thorlabs laser diode controller such as the LDC220C, which would be used with a Thorlabs temperature controller such as the TED200 (together these Thorlabs units cost ~£1800). The LDC220C has the interlock connections on pins 1 and 5. It also has pin 3 as the laser diode ground and for cathode grounded laser diodes it has the laser diode anode connected to pin 8. The TED200 temperature controller has connections to pins 1 and 2 for the TEC- and TEC+ respectively and the NTC thermistor is connected to pins 3 and 4. The connections inside our Lasertack diode laser driver are shown in the schematic in Figure 4.5, which also shows a photograph of the home-built laser diode driver and TEC. The total cost to build this driver is ~£102 and the breakdown of the costs is available on the .csv file on the Imperial Photonics website and in Appendix A3.

https://www.imperial.ac.uk/photonics/research/biophotonics/instruments--software/fluorescence-microscopy/openframe/

These low-cost laser diodes controllers have been designed to control only a single diode laser. Since our multiline laserbank typically includes 4 diode lasers (e.g., at 405, 470, 520 and 630 nm) four homebuilt drivers are therefore required.

4.3.2 Low-cost multiline laserbank

EasySTORM is an implementation of *dSTORM* that uses multimode diode lasers coupled into a multimode optical fibre to provide excitation of the fluorescence samples. We use diode lasers from Lasertack and are all OEM modules. The laser diodes used are the 405 nm (LDM-405-350-C, 350 mW), 462 nm (LDM-462-1400-C, 1400 mW), 520 nm (LDM-520-1000-C, 1000mW) and the 638 nm (LDM-638-700-C, 700mW). These multimode diode lasers output elliptical beam profiles. In order to improve the coupling efficiency into the optical fibre, the diode laser beams are collimated by an aspheric lens and then the collimated beam profiles are corrected using an anamorphic prism pair, which magnifies the laser beam along one transverse axis. Thus, the diode laser beam can be corrected from an elliptical to a circular beam profile. Before the prism pair, the collimated beams have an elliptical profile with a long axis diameter of 4 mm and short axis diameter of 1 mm (4 mm×1 mm). After the optical correction by the prism pair, the beam has a circular profile with a (4 mm×4 mm) diameter. The diode lasers and their collimating/beam-shaping optics are supplied incorporated into OEM modules by Lasertack, onto which the NTC and TEC connections are attached.

In our multiline laserbank, these diode laser modules are heatsinked to machined copper blocks that have countersunk holes to allow them to be screwed directly down onto an aluminium breadboard. These laser modules and copper heatsink blocks are enclosed within black die-cast aluminium boxes (RS PRO 146-5333) in which a hole is machined to provide an output aperture for the collimated laser beam. Two holes are machined in the box to attach the 9-pin D-sub connectors to connect with the laser driver diode and temperature controls. The LD+ and LD- pins on the iLD laser driver module are connected to the laser diode, the NTC pins are connected to the NTC (which is attached by heatsink paste to the OEM module) and the TEC+ and TEC- connectors are connected to the laser diode OEM unit. A further hole is machined in the box so that a RS PRO 3.5 mm Chassis Mount Mono Socket can be connected for the interlock.

The external laser safety interlock connections are soldered onto a 3.5 mm jack socket pin that completes the circuit between pins 1 and 5 on the 9-pin D-sub and the interlock on the driver board when inserted into the socket. If the external interlock is turned off, the laser diode driver will not send a drive current to the diode laser.

A Thorlabs smooth bored half inch cage plate is mounted on the outside of each die cast box centred on the laser output aperture. This is used to mount 12.5 mm diameter, OD4 emission filters, which are fixed in place by a grub screw. These emission filters used are: 405 nm/10 nm (Edmund Optics 65072), 467 nm/10 nm (Edmund Optics 39308), 520 nm/10 nm (Edmund Optics 65093) and 636 nm/10 nm (Edmund Optics 65106).

These enclosed laser modules are mounted on a Thorlabs optical breadboard and the whole laserbank is enclosed with aluminium composite shielding. As shown in Figure 4.6, the 4 laser modules are positioned parallel to each other and the output beam from each laser module is steered by a set of 2 half inch mirrors and beamsplitters mounted on tip/tilt controllable kinematic mirror mounts (Thorlabs KM05/M) on posts (Thorlabs TR30/M). The posts are held in pedestal post holders (Thorlabs PH20E/M) and clamped into position on the breadboard using clamping forks (Thorlabs CF125C/M). The mirrors/beamsplitters are orientated at 45 degrees to the beam. Via a mirror (Thorlabs BB05-E02) and 25 mm diameter longpass dichroic beamsplitters – a 613 nm long pass filter (Edmund Optics 86394), a 482 nm longpass filter (Edmund Optics 86324) and a 427 nm longpass filter (Edmund Optics 86389) mounted in 1-inch fixed mounts (Thorlabs FMP1/M) – the 4 laser beams were steered to be collinear on the optical axis before being reflected by a final 1-inch kinematic mirror (Thorlabs KM100-E02). All the mirrors have a visible wavelength anti-reflection coating from 400nm to 700nm.

The collinear laser beams are then focused into a multimode optical fibre (Thorlabs FG105LVA 105nm 0.1NA) by a half inch diameter bi-convex lens of 15 mm focal length (Thorlabs LB1092-A-ML) – chosen to fill the numerical aperture of the optical fibre and hence to maximise the number of laser modes that are be coupled into the optical fibre. The fibre had an APC connector fibre and was connected into an angled fibre adaptor plate (Thorlabs SM1FCA) mounted in a XY translating mount (Thorlabs CXY1) that was connected to a half-inch Thorlabs cage plate holding the lens by 4 Thorlabs cage rods. The 4 laser beams, already aligned to a common axis, could be coupled into the optical fibre by adjusting the XY mount holding the fibre adaptor and the final 1-inch mirror. The axial position of the lens relative to the fibre could be adjusted by sliding the lens cage plate along the Thorlabs cage rods. The coupling efficiency of the individual laser beams into the multimode optical fibre all exceeded 80%.

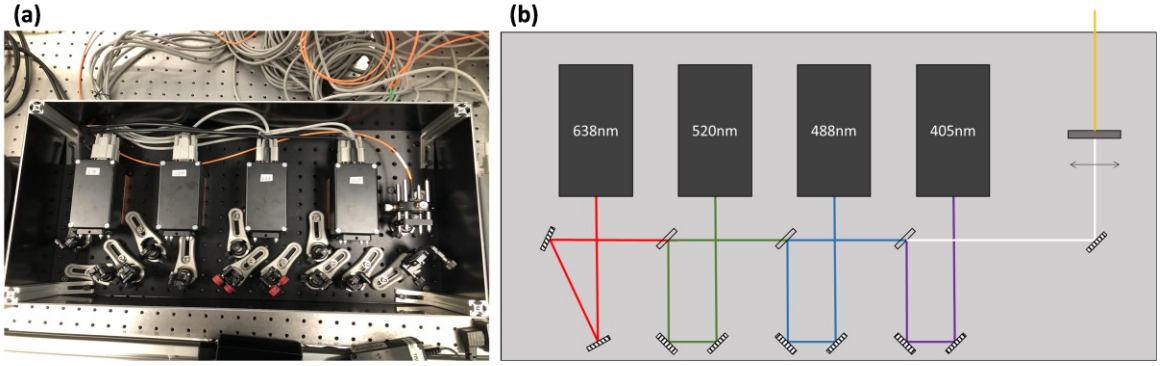

Figure 4.6. Home-bult multiline laserbank for *easySTORM* excitation using high power multimode diode lasers.

The assembled multiline laserbank is shown in Figure 4.6. The whole assembly was enclosed by a light-tight aluminium enclosure mounted on posts at the corners of the breadboard. A lid for the laserbank was made of an aluminium/plastic composite material and could be locked into position using M6 screws into the posts. A slot just above the breadboard was cut into the side of the laserbank shielding to accommodate the cables connecting to the diode driver units, interlock cables and the optical fibre. The total cost for a 4-line excitation source presented above, with drivers, is ~£4,500. A commercial laser engine costs in the region of ~£35,000.

4.3.3 Uniformity of excitation using multimode diode lasers and optical fibres

The use of a multimode optical fibre (MMF) to deliver the excitation laser radiation to the microscope (*openExcite* module) provided high coupling efficiency and insensitivity to small changes in alignment of the laser beams compared to using a single mode optical fibre (SMF). The MMF also provides a much more uniform intensity distribution across the field of view compared to using a SMF, although the use of multimode diode lasers and multimode propagation along the MMF will produce a speckle pattern. However, if the fibre is vibrated, any speckle in the excited fluorescence images will time-average as long as the image integration time is longer than the timescale of the vibration (Fujimaki & Taniguchi, 2014). The typical exposure time used for *easySTORM* is 30 ms (e.g., for a camera frame rate of ~33 fps, requiring the fibre to be vibrated at a frequency greater than 330 Hz.

In SMLM, and for most quantitative microscopy techniques, it is important to maintain a homogenous illumination field across the sample whilst maintaining a suitably high intensity, which

is challenging for SMF-delivered excitation light – where it is often necessary to overfill the FOV to achieve a reasonably uniform intensity. Exploiting the "flat-top" field output from a MMF (Almada, Culley & Henriques, 2015) in which the radiation is coupled into a large number of modes provides a reasonably homogeneous Illumination across the FOV, while also benefitting from the high coupling efficiency and insensitivity to alignment drift of the MMF. To maximise the homogeneity of the illumination, it is helpful to make the NA of the laser coupling lens as large as the NA of the MMF – and the number of modes is further increased by the use of multimode diode lasers. If the NA of the coupling lens is higher than the NA of the MMF, however, the power coupling efficiency into the fibre will be lower.

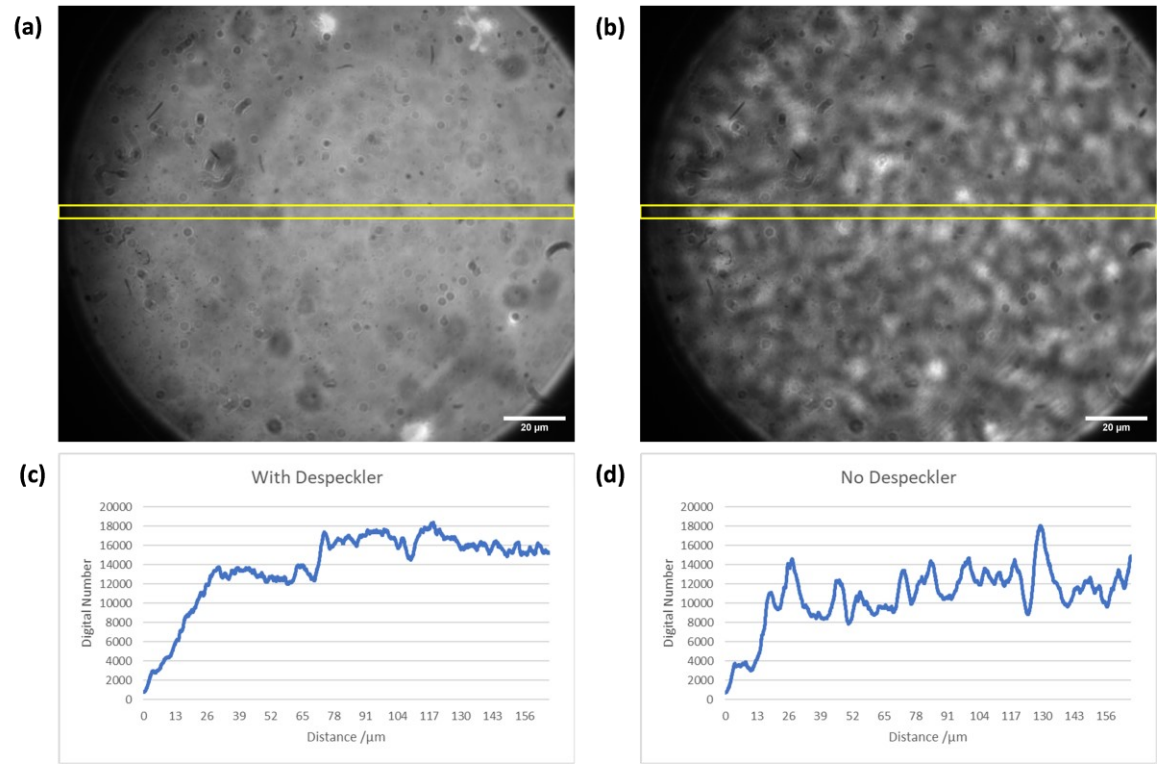

Figure 4.7. Improvement in field homogeneity through the vibration of a multimode fibre. Figures (a, b) show images acquired by an Andor Zyla 5.5 when imaging a thin film of fluorescent highlighter pen fluid illuminated by a 635nm Lasertack multimode diode via a multimode fibre. Left (a, c): shows the FOV when the fibre is vibrated using a CAIRN despeckler unit. Right (b, d): The fibre is not vibrated and there is a speckle pattern in the illumination. The yellow lines in (a) and (b) indicate where the line profiles shown in (c) and (d) are taken from.

Figure 4.7 illustrates the improved image homogeneity obtained when vibrating a MMF delivering 635 nm multimode diode laser excitation. The sample used was a fluorescent highlighter fluid that has been wiped onto a coverslip to produce a "thin" film. The fluorescence from the highlighter was imaged using a Andor Zyla 5.5 sCMOS camera on an *easySTORM* microscope with a 30 ms exposure. Figure 4.7 (a) shows the image recorded of the highlighter across the full FOV of the sensor when the

MMF is vibrated, and Figure 4.7(b) shows the same FOV imaged when illuminated by the non-vibrating MMF. There is an obvious laser speckle pattern observable in Figure 4.7 (b). By vibrating the MMF, the laser speckle pattern is time averaged to produce a more uniform illumination. Figure 4.7 (c, d) show the average line profile from the yellow boxes indicated in Figure 4.7 (a, b) respectively. There is greater percentage variation in digital number for the non-vibrating MMF illumination in the illuminated region on the sensor.

4.4 Low-cost cameras for fluorescence microscopy and SMLM

Another key component for any microscope, including HCA instruments, is a sensitive low noise camera. SMLM requires sufficient sensitivity to detect the fluorescence signal from single fluorophores, and historically this was provided by Electron-Multiplying Charge Coupled Device (EMCCD) cameras that can provide high quantum efficiency (up to 95%) and the fast readout speeds (>~70 frames per second) required for STORM (Huang et al., 2013). In our laboratory we use a high-end back-illuminated EMCCD (Andor iXon 897) that has a 11.6 mm diagonal sensor size of 512x512 pixels with a square pixel size of 16 µm and a maximum frame rate of 56 fps at full FOV. However, due to the high gain, the noise is amplified in EMCCD sensors if each pixel detects more than one photon on average per frame (Chao et al., 2013) and this can reduce the signal to noise by a factor of approximately $\sqrt{2}$, which results in the effective quantum efficiency being halved (Mortensen et al., 2010).

The more recently developed scientific complementary metal-oxide semiconductor (sCMOS) sensors provide a cost-effective alternative to EMCCD and typically have more pixels, (e.g., >2000x2000 pixels) and a high quantum efficiency (~60-70% for front-illuminated sensors). For example, the Andor Zyla 5.5 sCMOS camera has a maximum quantum efficiency of 64% at 600 nm, and a full FOV frame rate of 40 fps that is sufficient for STORM of the Alexa Fluor dyes. It has a pixel sensor size of 2560x2160 with square pixel size of 6.5 µm, giving a diagonal sensor size of 21.8 mm. This larger area is important for HCA since it increases the FOV and therefore the number of cells that can be imaged per frame, thereby increasing the throughput of the system. The larger imaging FOV makes the impact of non-uniform (e.g. Gaussian) illumination intensity profiles more significant but this can be mitigated by delivering the excitation light via a vibrating MMF, as discussed above. The smaller pixel size means a smaller magnification objective lens is needed to achieve Nyquist sampling of the sample in imaging space – for which the maximum resolvable intensity spatial frequency of the optical system should be sampled at twice per period. Numerically this is approximately the same as

sampling the FWHM of the point spread function (PSF) of the fluorescence emission of a single molecule with at least 2 camera pixels. Ideally, the pixel size sampling the wide field image should be 2.3 times smaller than the diffraction limited resolution of the microscope (Almada, Culley & Henriques, 2015). For fluorescence emission at 668 nm (e.g., for peak of emission spectra for Alexa Fluor 647 dye) when using a 1.4 NA, oil immersion objective lens, the FWHM definition for resolution of the diffraction-limited system is given by:

$$\sigma = \frac{0.51 \times \lambda}{NA} = \frac{0.51 \times 668nm}{1.4} = 243.3nm \qquad \text{Equation 4.2}$$

This would mean that a pixel size of less than 105.8 nm (243.3/2.3 = 105.8nm) is needed for Nyquist sampling (in the image plane).

Camera (approximate cost)	Peak Quantum Efficiency (%)	Full FOV frame rate (fps)	Pixel size (µm)	Sensor Size (mm)	Number of pixels	Full Well Capacity (e^-)	Read Noise (e^-)	Bit depth	Cooling TE = Thermo-electric
Andor Ixon life 897-BV (Back illuminated) (~£26,000)	>95	56	16 x 16	8.2 x 8.2	512 x 512	180000 (800000 for gain register depth)	< 1 With EM Gain	16bit	Air cooled Or Liquid cooled
Photometrics Prime 95B (~£15,000)	95	40	11	13.2 x 13.2	1200 x 1200	80000	1.6	16bit	Air Cooled TE
Andor Zyla 5.5 (~£8000)	64	30	6.5	16.6 x 16.6	2560 x 2160	30000	0.9	16bit	Air cooled TE
CellCam Kikker (~£2000)	90	35 @ 8-bit, 17 @ 14-bit)	4.63 (can be 2.315)	13 x 19	4128 x 2808	66000 in LCG 7500 in HCG	<1.5	8-bit and 14-bit	Air-cooled TE
CellCam Centro (~£900)	>80	17 @ 8-Bit, 9 @ 12-Bit	2.4	13.2 x 8.8	5440x3648	15000	<1.5	8bit or 12bit	Air-cooled (fan, no TE)

Table 4.1. Camera Specifications for sCMOS and CMOS sensors used for *easySTORM* at Imperial

sCMOS cameras are cheaper than EMCCD cameras and have become more commonly used for STORM but they are still relatively expensive (£10000-£20000) for a low-cost microscope system. Recently, there has been significant development of new, high performance CMOS sensors. Historically CMOS sensors have been used for industrial applications like machine vision and are much cheaper than EMCCD or sCMOS cameras, but they have been limited to inferior signal to noise levels and presented fixed pattern noise. However, CMOS sensors have been developed over time (partly driven by smart phone camera priorities) to improve their QE, read noise and performance for low photon count settings. This new generation of CMOS cameras are much lower cost compared to sCMOS cameras and recently have become available with cooling. This makes them

interesting for fluorescence microscopy and SMLM acquisitions. Table 4.1 compares sCMOS and newly available cooled CMOS cameras in use in our *easySTORM* microscopes.

The new generation CMOS sensors are back illuminated and can be thermoelectrically cooled to reduce the noise level of the sensor. They have peak quantum efficiencies exceeding 80% and, as discussed below, can be incorporated in low-cost cameras that appear to offer comparable performance to sCMOS cameras. Like the sCMOS sensors, they have a faster read frame rate than the EMCCD sensors as each pixel in a CMOS has an individual capacitor and amplifier and there is an analogue-to-digital converter (ADC) for the readout of each column. In contrast, an EMCCD has a single ADC and amplifier which is used to read out all the pixels of the sensor. For the CMOS and sCMOS sensors, the pixel readout can be parallelised and a rolling shutter across the sensor can be implemented, which provides faster readouts–- and therefore faster frame rates–- than a global shutter.

I have worked with two new low-cost cameras utilising this new generation of CMOS–- specifically the Sony IMX 183 sensor incorporated in a camera (Cairn Research Ltd, CellCam Centro 200MR) that utilises fan-cooling and the Sony IMX 492 sensor incorporated in a camera (Cairn Research Ltd, CellCam Kikker 100MT) that utilises thermoelectric-cooling. The CellCam Centro camera costs ~£900 and the CellCam Kikker camera costs ~£2000. Thus, these “CellCam” CMOS-based cameras are much cheaper than the nearest equivalent sCMOS camera.

The main limitation of these new CMOS sensors compared to sCMOS is the relatively low frame rates: 9 fps for 12-bit depth acquisitions for the CellCam Centro and 17 fps for 14-bit depth acquisitions for the CellCam Kikker. This arises because of the large number of image pixels relative to the total image data rate from the cameras. These frame rates are relatively low for SMLM and would lead to long image data acquisition times – particulate for automated “high throughput” STORM. For dSTORM, the fluorophore photoswitching rate depends on the laser power density at the sample (Lin et al., 2015) and an on-state lifetime of 5-30 ms is typically used in our laboratory. We would like to acquire STORM image data at a frame rate of at least 33 fps to minimise image data acquisition times (and photobleaching if the excitation laser is on continuously).

In order to achieve a STORM frame rate >30 fps, the FOV could be electronically cropped by reading out fewer pixels of the sensor per frame and so the frame rate could be increased. Normally this would reduce the FOV and hence reduce the number of cells imaged and therefore the throughput for HCA. Further, the illuminated sample outside the cropped FOV would undergo photobleaching without being imaged, which would be a particular problem if image tiling was to be used for STORM of large samples. Therefore, instead of electronically cropping the FOV on the CMOS sensor, the

image formed on the sensor was optically demagnified (using a Motic microscope c-mount adaptor) such that it illuminated a smaller region on the sensor. A 0.5X or 0.35X adaptor was used to demagnify the image onto the CellCam Kikker and the 0.35X Motic adaptor was used with the CellCam Centro. These demagnification factors reduced the active area on the CMOS sensor such that the cropped region could be read out to achieve frame rates in excess of 33 fps.

The pixel size of the two respective CellCams (2.4 µm for the CellCam Centro and 4.63 µm for the CellCam Kikker) were sufficiently small to still reach Nyquist sampling of the demagnified images. A 1951 USAF resolution test chart was used to calculate the magnification and hence calculate the size of the pixels in imaging space when using the respective Motic adaptors. The pixel size in image space for the CellCam Centro with a 0.35x Motic adaptor was 85.8 nm and the pixel size for the CellCam Kikker was 90.8 nm when using a 0.5X motic and 115.0nm when using the 0.35X motic. Thus, Nyquist sampling was achieved since the FWHM of the PSF of the fluorophores was ~220 – 250 nm. The overall magnification of the STORM microscope using a 100X objective lens was changed by the Motic adapters to be ~28 when using the CellCam Centro (2.4µm/85.8nm = 27.97) and to be ~51 when using the CellCam Kikker with the 0.5X motic (4.63µm/90.8nm = 50.99) and ~40 when using the CellCam Kikker with the 0.35X motic (4.63µm/115.0nm =40.26).

To compare the performance of the new CellCam CMOS cameras with an sCMOS camera, three cameras listed in Table 4.1 were used to acquire *easySTORM* data of the same sample of FRTL5 Rat Follicular thyroid cells in which the tubulin was decorated with AF488. The reconstructed wide-field and STORM images are shown in Figure 4.8. It is apparent that the CellCam CMOS cameras can both be used for STORM and that the quality of the super-resolved images of tubulin obtained with the CellCam Kikker, using the 0.5X Motic adaptor here, is comparable to that obtained with the (Andor Zyla 5.5) sCMOS camera were able to produce super-resolved reconstructions of the tubulin.

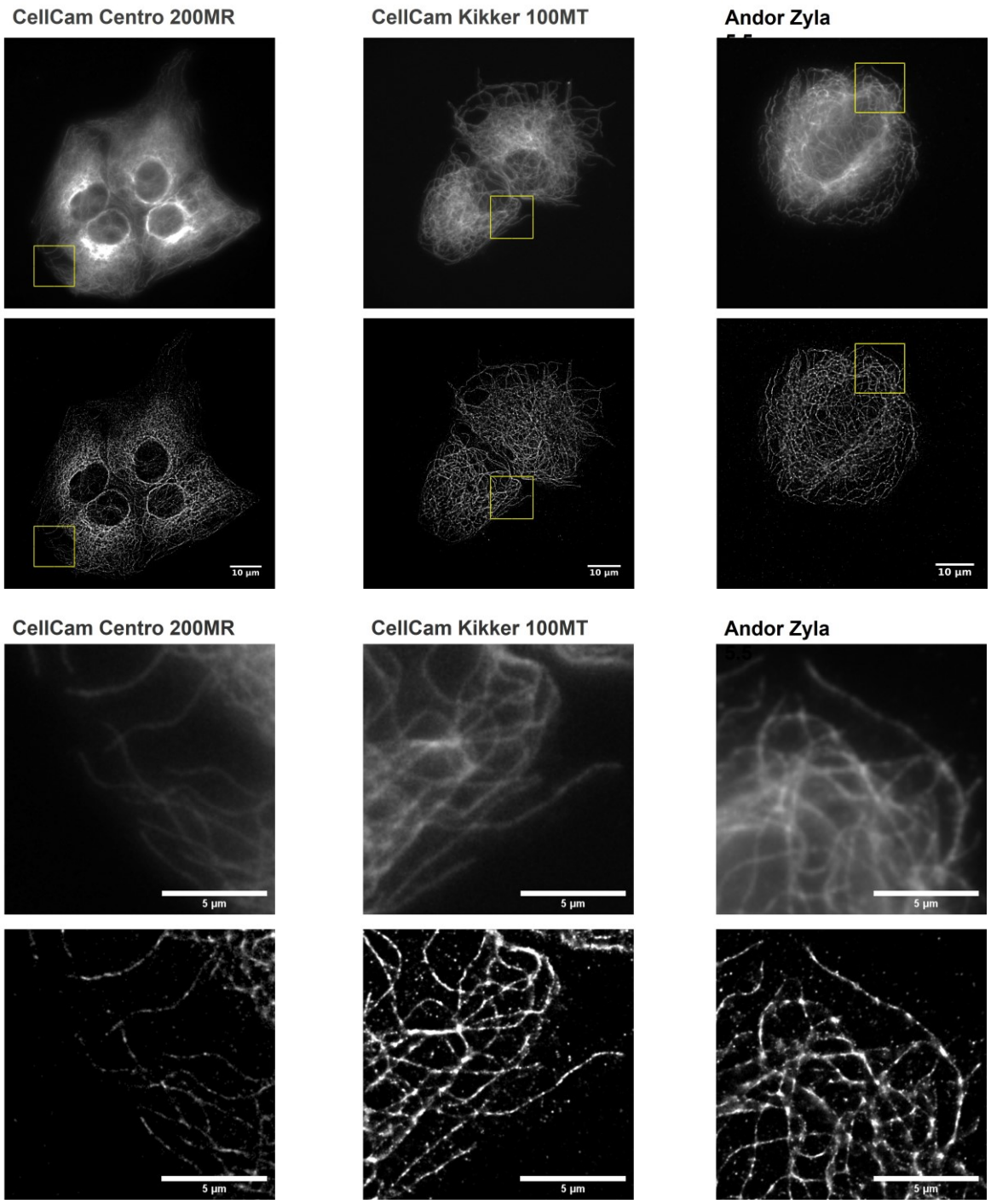

Figure 4.8. Top images: Widefield and *easySTORM* reconstructions of tubulin in a FRTL5 Rat Follicular thyroid cell line decorated with AF488 for the CellCam Centro, CellCam Kikker and Andor Zyla 5.5 camera. All images acquired on the same day and reconstructed from 10000 frames with 30ms exposure.

To further compare the SMLM performance of these different cameras, I used the SMLM image analysis software SQUIRREL (Culley et al., 2018), which is part of the NanoJ (Laine et al., 2019) imageJ plugin for SMLM. SQUIRREL compares widefield epifluorescence images of the sample with

pseudo-widefield images reconstructed from the super-resolved image data (by convolution with a resolution scaling factor derived from the data) for the same FOV and can output an error map and Fourier Ring Correlation (FRC) map across the FOV. Figure 4.9 shows the NanoJ-SQUIRREL error maps (purple and yellow plots) for the same FOVs presented in Figure 4.8. In regions that do not have sufficient localisations, Squirrel will automatically colour code the region based on neighbouring regions.

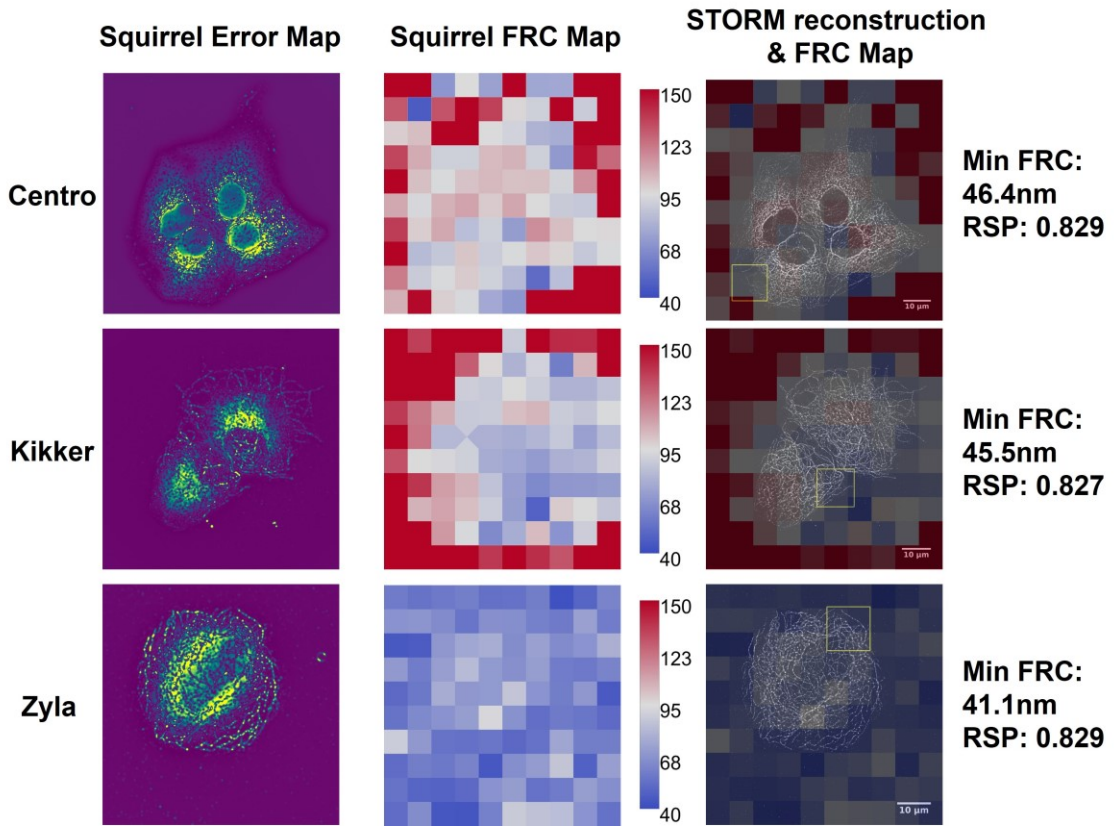

Figure 4.9. NanoJ-SQUIRREL SMLM reconstruction analysis of cameras and FOVs as shown in Figure 4.8. Images on the left show an error map from comparing the super-resolved reconstructions with the widefield images. Regions with a low error are shown in purple, regions with higher error are shown in yellow. The middle column images show Fourier ring correlation (FRC) maps of the same FOVs. The localisations were split into odd and even frames and used to create two reconstructions. The images were segmented into 100 regions and FRC analysis was then performed on each region. The minimum FRC value in each image is given and the resolution scaled Pearson-correlation (RSP) is provided for each error map. Images on the right show an overlap image of the STORM reconstruction and the FRC map to highlight the FRC regions containing localisations.

The error map is generated by calculating the pixel-wise absolute difference between the actual widefield image and the scaled-up super-resolution image. The error map can also yield the Resolution scaled Pearson coefficient (RSP) for the entire FOV. The RSP is a metric that gives an indication of the correlation between the two image datasets and can be used to compare the

performance of STORM with the different cameras. The RSP coefficient varies between -1 and +1 with a greater value indicating a higher correlation. For the images shown in Figure 4.8, the corresponding error maps shown in Figure 4.9 (lefthand column) indicate that the three cameras provide a similar performance in terms of the RSP calculation.

The Fourier Ring Correlation (FRC) is a way to estimate the resolution of a SMLM dataset (Nieuwenhuizen et al., 2013). To calculate the FRC, the STORM localisation tables are split in half to produce two distinct tables, e.g., of the even-numbered frames and the odd-numbered frames. Two super-resolved images of the same FOV are then reconstructed from these two tables. The FRC is a statistical correlation between the Fourier transforms of the two reconstructed super-resolved images and entails calculating the correlation coefficient for rings of constant spatial frequency in frequency space. For low spatial frequencies, the correlation will be high, approaching 1, but at higher spatial frequencies, the correlation will be increasingly degraded by noise, eventually tending to 0.

The FRC is formally calculated using the following equation for two images, $f_1(\vec{r})$ and $f_2(\vec{r})$, where $\vec{r}$ denotes the spatial coordinates. Their respective Fourier transforms are given by $\widehat{f_1}(\vec{q})$ and $\widehat{f_2}(\vec{q})$, where $\vec{q}$ is the spatial frequency coordinates. The magnitude of the ring used to describe the radius of the Fourier ring is given as $q = |\vec{q}|$.

$$FRC(q) = \frac{\sum_{\vec{q} \in circle} \widehat{f_1}(\vec{q})\widehat{f_2}(\vec{q})^*}{\sqrt{\sum_{\vec{q} \in circle} \left|\widehat{f_1}(\vec{q})\right|^2} \sqrt{\sum_{\vec{q} \in circle} \left|\widehat{f_2}(\vec{q})\right|^2}} \qquad \text{Equation 4.3}$$

A figure of merit for the FRC is provided by determining the spatial frequency at which the correlation falls to a predefined threshold, which is commonly taken to be $\frac{1}{7} \approx 0.143$. (Nieuwenhuizen et al., 2013) The reciprocal of this FRC spatial frequency gives the estimation of the resolution in spatial coordinates.

The FRC analysis may be applied to the entire FOV to give a single value, but it can also be useful to sub-divide the FOV into smaller regions to see how the resolution varies across the SMLM image – provided that these regions are sufficiently large that there are sufficient correlations for the FRC to be calculated. Thus, a colour coded heat map of the FRC-derived resolution can be generated. If there are insufficient correlations in a particular region, that region can be colour coded according to a natural neighbour interpolation). For the data presented in Figure 4.9 and Figure 4.11, the easySTORM images were divided into 100 spatial regions and the FRC value is calculated for each region. Taking the minimum FRC value across the FOV ("Min FRC") provides an overall indication of the resolution of the easySTORM images. It is important to note that this will be systematically

overestimating the achievable resolution in the images. It is also worth noting that the FRC values returned in the regions in which there are no cells, do not provide a meaningful resolution estimate as they are determined purely by noise.

Figure 4.9 (middle column) shows the FRC plots of the super-resolved images obtained using the CellCam Centro and Kikker CMOS cameras and the Andor Zyla 5.5 sCMOS camera. The images on the left show column show the error map that was calculated by comparing the super-resolved reconstructions and the widefield images. The error map is colour scaled with regions with low error shown in purple and regions with higher error in yellow. The middle column of figures show the FRC maps corresponding to the same FOVs. In order to create this the localisations were split into odd and even frames to create two separate localisation tables used to reconstruct the images. The images were then segmented into 100 smaller square regions and then FRC was calculated for each respective region. This demonstrates the variation in FRC values across the FOV. The minimum FRC region value and the scaled Pearson correlation was calculated for each error map. The minimum FRC region values are similar with the sCMOS camera providing slightly better performance in this experiment, but the FRC maps clearly show the inferior performance of the fan-cooled CellCam Centro compared to the two thermoelectric-cooled cameras. In the regions which overlap with the cells , right-hand column of Figure 4.9, (i.e not the background), the CellCam Centro camera STORM image data yields FRC values ranging between 50 nm and 110 nm and the CellCam Kikker has FRC values ranging between 45.5 nm and 100 nm with more of the regions shaded blue compared to the Centro, indicating a superior performance for the Kikker camera. The outer edge of the FOV for the Kikker presents poor FRC values but this is in regions without any cells, suggesting this may be due to noise in the images. The Andor Zyla 5.5 camera produces FRC values ranging between 41.1 nm and 95 nm, but these FRC values are generally more uniform across the entire FOV, including in the outer regions away from the cells.

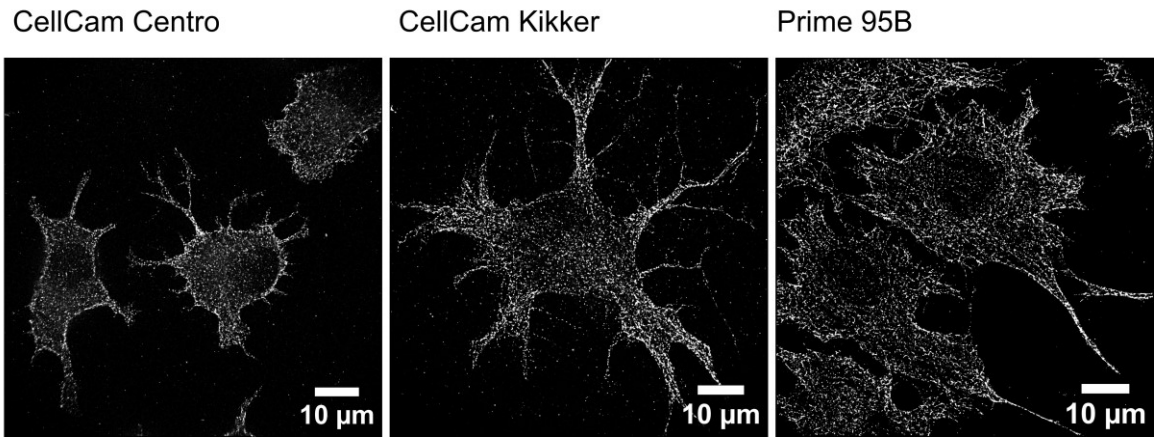

Figure 4.10. *easySTORM* reconstructions of tubulin in a FRTL5 Rat Follicular thyroid cell line decorated with AF647 acquired using the CellCam Centro, CellCam Kikker and Photometrics Prime 95B cameras. All images reconstructed from 10000 frames with 30 ms exposure.

In a further easySTORM experiment imaging tubulin labelled with AF647 in a FRTL5 Rat Follicular thyroid cell line, the CellCam Centro and Kikker CMOS cameras were compared against a high end sCMOS camera – the Photometrics Prime 95B. Figure 4.10 presents the easySTORM images acquired using the CellCams and the Prime 95B and Figure 4.11 shows the corresponding error and FRC maps.

In this experiment, the CellCam Kikker, using the 0.5X Motic adaptor here, provided a slightly higher RSP value, but these were similar for all cameras. The FRC values were more uniform across the FOVs for the Prime 95B sCMOS camera and the CellCam Kikker and all cameras yielded an FRC value below 30 nm for this experiment.

Overall, it is likely that the easySTORM images acquired using the CellCam Centro are more impacted by noise than the CellCam Kikker or the two sCMOS cameras, which is understandable because only the CellCam Centro utilises fan-cooling rather than thermoelectric cooling, and the Centro also has a slightly lower QE compared to the CellCam Kikker and the Prime 95B. However, all the cameras were able to achieve low FRC values and can be used for SMLM image data acquisition. Furthermore, the difference in performance between the CellCam Kikker and sCMOS cameras is sufficiently small to support the use of the CellCam Kikker as a useful low-cost alternative to sCMOS cameras.

4.5 Implementation of *easySTORM* on *openFrame* microscope

As discussed in Chapter 3, *easySTORM* (Kwakwa et al., 2016) is a low-cost implementation of dSTORM (Heilemann et al., 2008) utilising multimode diode lasers coupled into multimode optical

fibres to provide the high excitation power needed for the photoswitching of the fluorescent dyes for dSTORM and other SMLM techniques. While it is possible to implement *easySTORM* on a standard microscope frame, we are particularly interested to develop low-cost SMLM and HCA instrumentation and so I implemented it on an *openFrame*-based microscope, for which the experimental configuration is depicted in Figure 4.12.

The multimode diode lasers used were from Lasertack (LDM-405-350-C, LDM-462-1400-C, LDM-520-1000-C, LDM-638-700-C, 700mW) and were mounted inside the homebuilt laserbank described above. The lasers were aligned onto the same optical axis and coupled into a 0.1 NA step-index multimode optical fibre (Thorlabs FG105LVA) using a 15 mm focal length lens (Thorlabs LB1092-A-ML). The output end of the optical fibre connected to the input fibre face-plate of the *openExcite* module mounted on the *openFrame*. A fibre vibrator (Cairn Research Ltd, Despeckler, P1350/DES/000) oscillating at ~230 Hz was attached to the multimode optical fibre to increase the coupling into higher order modes and to time-average the speckle pattern to achieve a reasonably uniform intensity illumination of the sample.

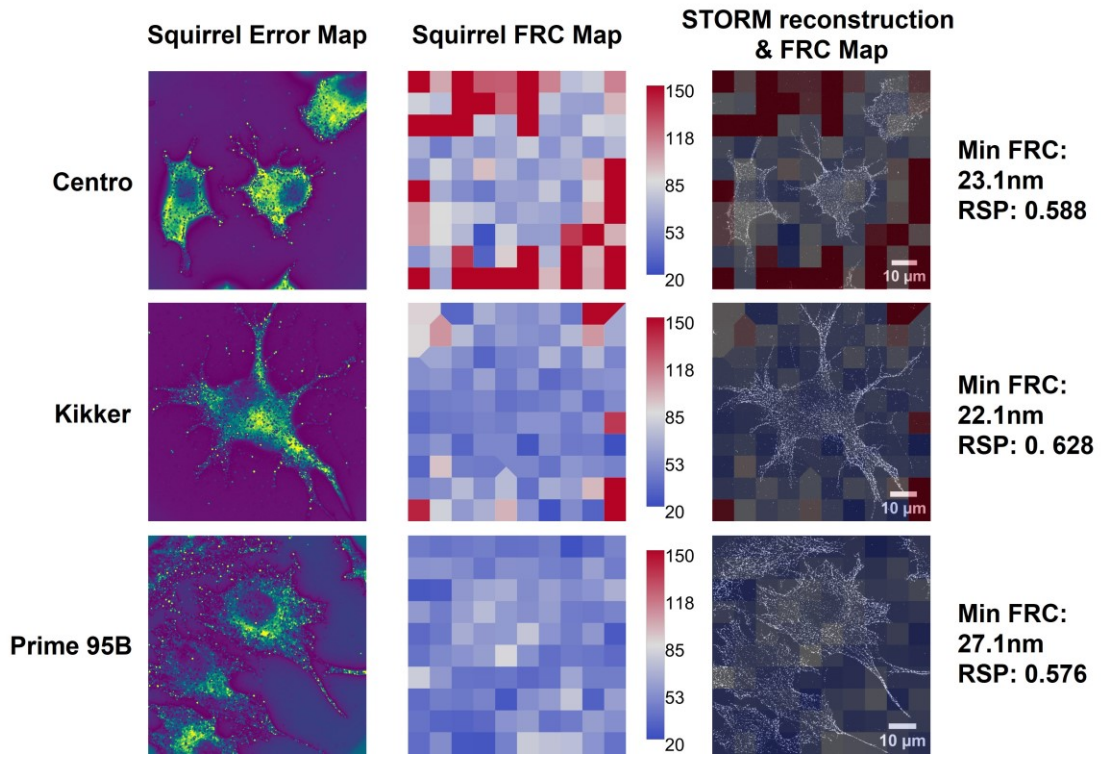

Figure 4.11. NanoJ-SQUIRREL SMLM reconstruction analysis of cameras and FOVs as shown in Figure 4.10. Images on the left show an error map from comparing the super-resolved reconstructions with the widefield images. Regions with a low error are shown in purple, regions with higher error are shown in yellow. The middle column images show Fourier ring correlation (FRC) maps of the same FOVs. The minimum FRC value in each image is given and the resolution scaled Pearson-correlation (RSP) is provided for each error map. Images on the right show an overlap image of the STORM reconstruction and the FRC map to highlight the FRC regions containing localisations.

The output of the multimode optical fibre was collimated by a 100 mm focal length lens, L1, (Thorlabs AC254-100-A) and the collimated beam was reflected by an elliptical mirror in a mount (Thorlabs KCB1E/M and Thorlabs BBE1-E02) with tip and tilt controls for steering the beam that is focussed by a tube lens (L2) of 200 mm focal length (Edmund Optics 49-377) to the back focal plane of the objective lens. This enabled the excitation to be switched between epifluorescence, HILO (Tokunaga, Imamoto & Sakata-Sogawa, 2008) illumination and total internal reflection fluorescence (TIRF) if a suitable TIRF objective lens is available. The multimode optical fibre has a core diameter of 100 µm and this is imaged with a 2x magnification to a focal spot size of 200 µm at the back aperture of the objective lens. For epifluorescence illumination, this spot is steered to the optical axis. Due to the size of this focal spot, the illumination is not perfectly collimated but still provides uniform illumination over a FOV exceeding 130 µm.

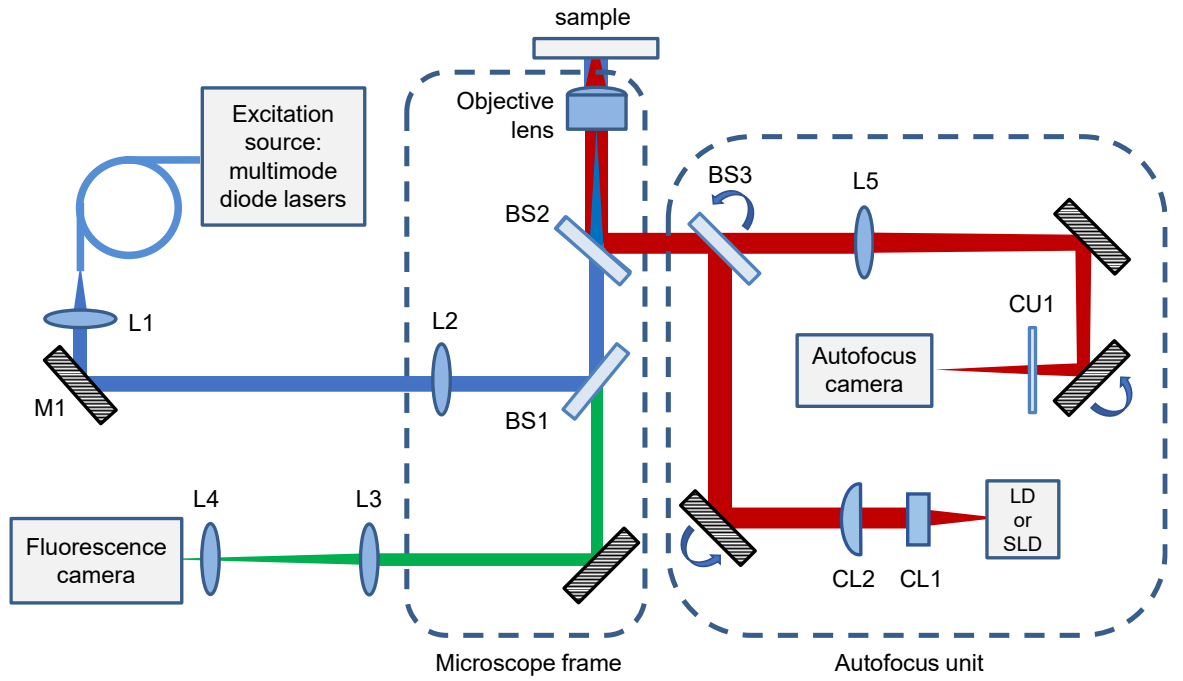

Figure 4.12. *easySTORM* implementation on the openFrame using the *openExcite* module

Exemplar *easySTORM* image data acquired using the *openFrame* microscope to image tubulin in HeLa cells immunolabelled with ifluor647 are shown in Figure 4.13. The primary antibody used was the T8203 anti-alpha tubulin (https://www.sigmaaldrich.com/GB/en/product/sigma/t8203) and the secondary antibody was goat-anti mouse label (https://www.aatbio.com/products/ifluor-647-goat-anti-mouse-igg-h-l?unit=16482). These cells were imaged with a Photometrics Iris 9 sCMOS camera.

Another exemplar *easySTORM* image is shown in Figure 4.14 for a formalin fixed paraffin embedded histological histological section of kidney tissue from a biopsy of a patient presenting Lupus Nephritis. The laminin in the glomerular basement membrane (GBM) was labelled with iFluor647. The section was prepared according to the same "*histoSTORM"* (Garcia et al., 2021) protocol discussed in Chapter 3. Figure 4.14 demonstrates the *openFrame's* ability to acquire super resolved *easySTORM* reconstructions of kidney tissue. Figure 4.14(d) shows the line profile indicated in Figure 4.14(c), with a recorded FWHM thickness of the GBM of 89nm. This was on the same order of magnitude as expected from measurements using electron microscopy (EM).

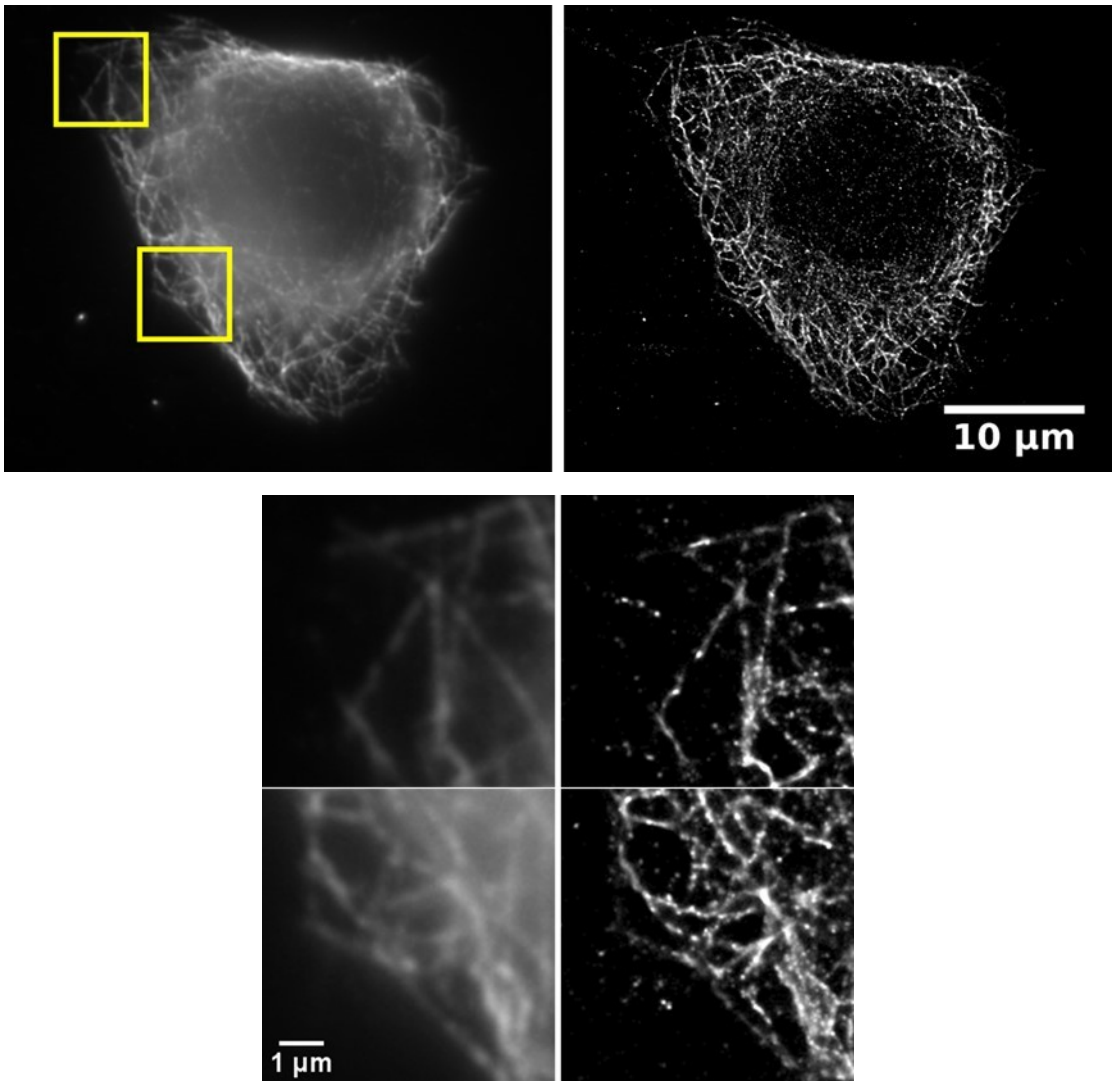

Figure 4.13. Widefield (left) and *easySTORM* (right) images of HeLa cells with tubulin immunolabelled with iFluor 647 and acquired on the openFrame using a Photometrics Iris 9 camera. Top row shows whole FOV imaged, and centre and bottom rows show zoomed in views of the top and bottom regions respectively indicated by the yellow squares in the top left panel.

To quantify the achievable resolution of *easySTORM* on the *openFrame*, I imaged samples with labelled nuclear pore complexes (NPCs), which are becoming a *de facto* standard in STORM resolution measurements (Thevathasan et al., 2019). Here, Nucleoporin Nup96 was endogenously labelled using SNAP-tags labelled with iFluor647 in a U-2OS-CRISPR-NUP96-SNAP cell line clone (Thevathasan et al., 2019) (distributed by CLS Cell lines Services GmbH). There are 32 copies of Nup96 in each nuclear pore complex and these form two (cytoplasmic and nucleoplasmic) "rings" that are separated axially by 50 nm. The rings each have 16 copies arranged with 8 corners, where each corners contain two Nup96 proteins separated by 12 nm. The corners of the two rings are vertically aligned with each other and the distance between Nup96 proteins in neighbouring corners of the nuclear pore complex is 42 nm, while the diameter of the rings between opposite corners is

107 nm. This prior knowledge of these well-characterised biological structures makes them a useful test sample to quantify the achievable resolution. For example, if the individual corners of the nuclear pore complex are resolved, then the resolution exceeds 40nm.

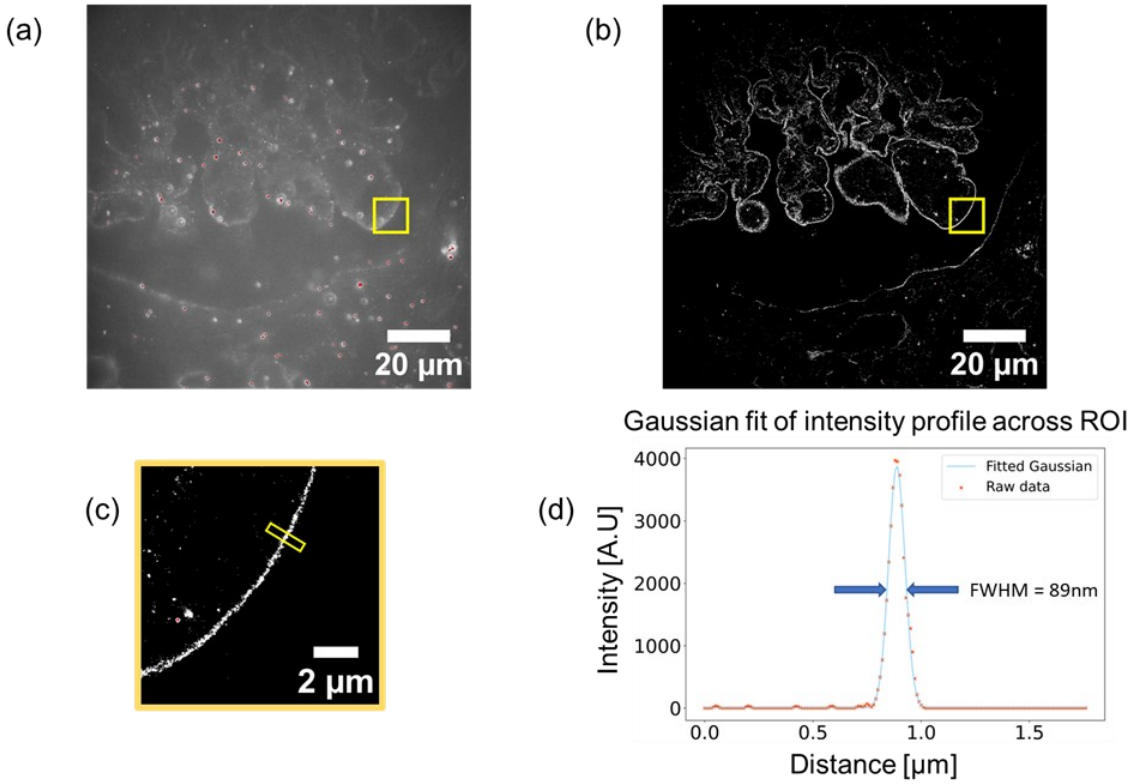

Figure 4.14. Whole FOV (a) epifluorescence widefield and (b) *easySTORM* images of a FFPE section presenting with Lupus nephritis imaged on the *openFrame* using a CellCam Kikker, with a 0.35X Motic adaptor. (c) shows a zoomed Roi indicated in (b) by the yellow box. (d) shows a line profile section through the GBM, with an indicated FWHM thickness of 89nm.

Figure 4.15 shows *easySTORM* image data of these nuclear pore complexes expressed in the U-2OS-CRISPR-NUP96-SNAP-iFluor647 cell line that were acquired using HILO illumination on the *openFrame* microscope and imaged using the CellCam113ickerr camera using the 0.35X Motic adaptor and a 100x 1.4NA Olympus objective. The U-2OS cells are a useful cell line for this measurement because the lower nuclear envelope is flat, enabling hundreds of complexes to be imaged in a single FOV since the nuclear pore complexes lie on the nuclear envelope.

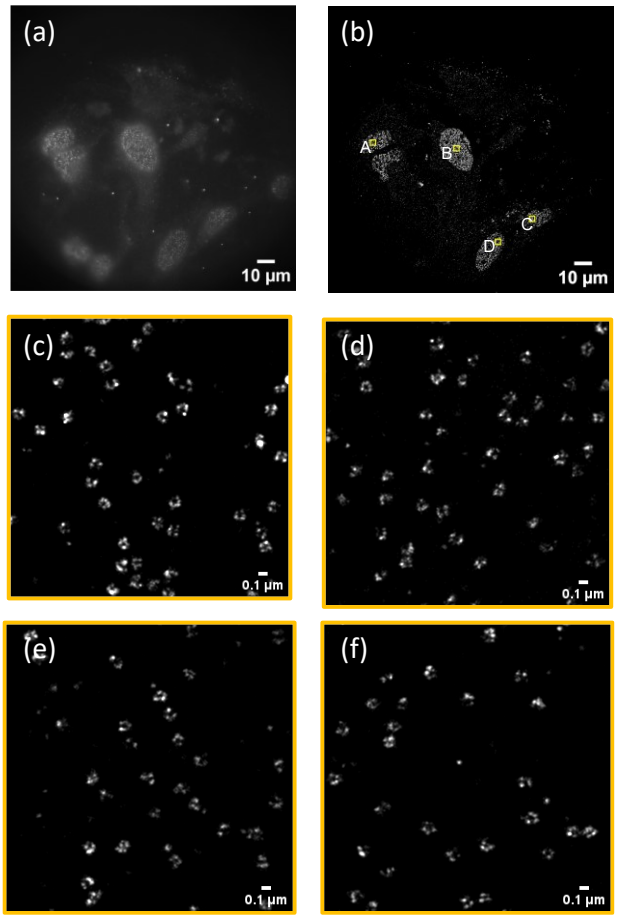

Figure 4.15. HILO illuminated whole FOV (a) widefield and (b) *easySTORM* reconstruction of fixed U-2OS-CRISPR-NUP96-SNAP-iFluor647 cells from 80000 frames at 60ms exposure. (c-f) show zoomed ROIs indicated in (b). The expanded ROIs show the sub-units are resolved within the nuclear pore complexes. Images were acquired on an *openFrame* microscope and imaged using a CellCam Kikker, using a 0.35X Motic adaptor. Axial drift was continuously corrected using the closed loop autofocus presented in Chapter 5.

The axial drift during this *easySTORM* image data acquisition was corrected using the hardware autofocus described in Chapter 5. 80,000 frames were acquired with a 60 ms exposure per frame. The transverse drift was corrected in post processing using fiduciary markers, for which 100 nm diameter Tetraspeck fluorescent beads were added to the sample and were imaged during the acquisition. The STORM image data were processed using Picasso (Schnitzbauer et al., 2017), which has the capability to track the drift of the fiducial markers embedded in the sample and hence correct for any transverse drift during acquisition. Figure 4.15 shows that neighbouring corners within the nuclear pore complex, for a number of ROIs across the FOV, were successfully reconstructed, demonstrating that *easySTORM* can achieve resolutions exceeding at least 42 nm across a large FOV.

4.6 Conclusion

In this chapter, I have presented the work involved developing a low-cost open-source microscopy platform, that can be used for multiple imaging modalities including SMLM. The components of the platform include, the development of a modular, low-cost open hardware microscope frame, the "*openframe*", a low-cost but high-power multimode diode laserbank with low-cost drivers and the *openExcite* module. This chapter also introduces a description of the next generation CMOS sensor based, low-cost and cooled cameras, called CellCams. I demonstrated that these CellCams can be used for easySTORM acquisitions with comparable performance to commercial sCMOS cameras that are typically used for STORM. These components were used in combination to acquire *easySTORM* acquisitions of nuclear pore complexes (NPCs), Kidney histological kidney biopsy samples and a FRTL5 Rat Follicular thyroid cell line. The *openframe* is now being developed by other PhD students within the Biophotonics group at Imperial College for other imaging modalities.

An open hardware HCA microscopy platform, capable of performing automated SMLM acquisitions, can be assembled utilising the openFrame, the home-built excitation source laserbank presented, a piezoelectric z-stage with an autofocusing module (described in chapter 5), the openExcite module, a dichroic layer and a motorised XY stage for <£25000 (see https://www.imperial.ac.uk/photonics/research/biophotonics/instruments--software/fluorescence-microscopy/openframe/ or Appendix A3 for a full breakdown of costs). A commercial motorized epi-fluorescence microscope, including an LED illuminator, filter sets, software, cameras etc. costs in the region of ~£100,000. An automated SMLM HCA capable commercial microscope, with a laser engine and cameras would cost up to £250,000. Therefore, the cost of building the SMLM HCA capable system presented in this chapter is approximately 5-10x less than the cost of a commercial equivalent depending on the configuration.

5. Development of an optical autofocus module

This chapter presents the development of a hardware based autofocus, which can enable automated imaging, on both the *openFrame* and commercial microscope frames, and provides continuous closed-loop focus correction. The autofocus makes use of orthogonally orientated cylindrical lenses to collimate a fibre coupled infrared super luminescent diode (SLD) source. This provided an elliptical beam profile with differing confocal parameters, for its two respective orthogonal axes. The differing confocal parameters provided both a long-range, but less precise metric, and a short-range, more accurate metric, to be used near to the focus. The autofocus was used to provide closed-loop continuous correction during *easySTORM* acquisitions.

5.1 Motivation for high-throughput microscopy

Fluorescence microscopy is a powerful tool to investigate cell dynamics and structure with subcellular resolution that can be applied to in vivo imaging as well as fixed samples. Since the labelling of the fluorophores is highly specific, spectrally-resolved imaging can follow multiple biological entities or processes in parallel. This is often not possible for structural techniques such as electron microscopy, which can achieve significantly higher resolution than the optical diffraction limit but usually are not able to follow biological function. The diffraction limitation of classical optical microscopy has been addressed by the development of techniques aiming to provide super-resolution. Examples of these imaging modalities include SIM, RESOLFT, STED, SMLM, as described in in chapter 2.6.

One challenge encountered when using these super-resolved methods is that they require long image data acquisition times. SMLM techniques like DNA-PAINT, STORM and PALM, require thousands of individual frames to be acquired to reconstruct a super-resolved image of a single FOV. As the image acquisition timescales increase, the number of samples that can be practically imaged using manual microscopy is limited. Automated high-throughput microscopy aims to increase the amount of image data that can be acquired and analysed within a single experiment, without decreasing the image quality (Oheim, 2011). In order to decrease the acquisition time and hence increase the throughput of a microscopy experiment, automation needs to be introduced for the cell preparation, the focusing of the system during acquisition, the image analysis and data storage. Such

automation also reduces or eliminates operator bias and the increased number of samples imaged within an experiment confers significantly improved statistical robustness of an experiment.

For drug discovery research in the pharmaceutical industry, high content analysis entails imaging with subcellular resolution at throughputs compatible with screening compound or gene libraries. This requires automation of sample preparation, imaging and data storage with parallelisation of procedures where possible. The use of multiwell plates enables cell biology experiments to be parallelised with consistent preparation of arrays of different samples with repeated conditions in multiple wells. It is then important to make the imaging of the sample arrays as consistent as possible and this requires that all image data is taken under the appropriate focussing conditions. This can be challenging because the distance from objective lens to sample can vary laterally between wells across a multiwell plate. In addition, for techniques like STORM that require long (> 1 minute) acquisition times, samples can move out of focus due to thermal or mechanical drift. The focus position can drift by an amount that is significant compared to the DOF of the imaging system and Shen et al. have measured it to be on the order of 1 micron per 1^{o}C fluctuation (Shen, Hodgson & Hahn, 2006) and a single FOV being imaged using 2 channel STORM typically requires a minimum of 5 minutes (5000 frames with a 30ms exposure for each channel). Thus, a "focus-lock" – or autofocus - mechanism is required to ensure that every FOV is imaged with the same focus conditions, e.g., acquiring every FOV image in a plane at the same distance from the coverslip. Thus, a critical component of automated microscopy is the autofocusing capability. In this chapter, the work developing a hardware based optical autofocus will be presented.

5.2 Introduction to autofocus techniques

Autofocus methods fall into two main categories: software and hardware-based techniques. These all typically determine the current defocus (i.e., the distance by which the separation between the objective lens and the sample (coverslip) needs to change to bring the system back into focus). Once the current defocus is quantified, a correction can be applied, usually by axially translating the objective lens or the microscope stage.

Software autofocus (also described as "image-based autofocus") techniques calculate image metrics that are chosen to be minimised or maximised at focus from the acquired images. This typically requires acquiring multiple images of the same FOV at different axial planes. Software-based autofocus techniques do not require any additional optical components in the system, but the need

to acquire multiple images can slow the imaging throughput and increase phototoxicity. Their performance can be sample-dependent, and they may not work with thick (i.e., axially extended) samples.

Hardware-based autofocus techniques (often described as “optical autofocus” approaches) do require additional components to be incorporated in the instrument that are used to measure the degree of defocus – typically by measuring the separation between the objective lens and the coverslip (LIRON et al., 2006) using a separate (auxiliary) illumination and imaging system. They can be implemented using lower phototoxicity near infrared radiation and can often operate in parallel with the acquisition of microscope images, thereby not decreasing the imaging throughput, and their performance can be largely sample-independent.

5.2.1 Software-based autofocus techniques

Software or image-based autofocus techniques calculate the current defocus in the optical system by analysing the images acquired by the microscope’s usual camera. The image data can be brightfield or fluorescence images. The image-based methods calculate an image metric that varies with defocus (either maximised or minimised at focus). An ideal image metric would change rapidly with axial position and should be monotonic either side of a single peak (or trough) at focus since multiple peaks could result in the autofocus locking onto a local maximum (minimum) that does not correspond to the true focal plane. A range of different image metrics can be used as a measure of defocus, as reviewed by Sun et al. (Sun, Duthaler & Nelson, 2004). These include image contrast, variance, entropy, standard deviation and Brenner gradient (Yazdanfar et al., 2008).

The first commonly used metric is *image contrast*. For a thin sample, there will be maximum image contrast (with sharper edges and larger intensity variations) when the image is in focus. This metric is quantified using the difference between the maximum and minimum pixel values in an image.

$$C = \frac{I_{max} - I_{min}}{I_{max} + I_{min}} \qquad \text{Equation 5.1}$$

Where C is the image contrast, and I is the pixel intensity value.

A second image metric is the *image variance*:

$$V = \frac{1}{N \times M} \sum_{i=1}^{N} \sum_{j=1}^{M} [I(i,j) - \mu]^2 \qquad \text{Equation 5.2}$$

Where V is the image variance, μ is the mean pixel value in the image, I is the pixel value at coordinates i and j. N and M are the maximum number of pixels along the x and y axes respectively of the sensor.

The *standard deviation* can also be used as an image metric, this is the square root of the variance of the image

$$\sigma = \sqrt{V} \qquad \text{Equation 5.3}$$

Where σ is the image standard deviation.

The *entropy* of an image can be calculated by making a histogram of pixel intensity values in the image and determining the probability that a pixel has an intensity within a certain bin in the histogram:

$$H = \sum_{i=1}^{N} p_i \log(p_i) \qquad \text{Equation 5.4}$$

Where H is the entropy, i is the histogram bin number and p_i is the probability that a pixel has an intensity value within histogram bin i.

Another image metric is the *Brenner gradient* (Brenner et al., 1976) . The Brenner gradient is an edge detection metric that looks at the difference between a pixel value and another pixel at set distance away (typically 2 pixels). As the image becomes better focused, it becomes sharper with more defined edges, hence the difference between neighbouring pixels at an edge should increase.

$$B = \sum_{i=1}^{N} \sum_{j=1}^{M} [I(i,j) - I(i+m,j)]^2 \qquad \text{Equation } 5.5$$

Where B is the Brenner gradient, I is pixel value, (i,j) are the pixel coordinates and m is the separation between neighbouring pixels.

Yazdanfar (Yazdanfar et al., 2008) performed a comparison of the four metrics presented above and found the best performing metric was the Brenner gradient with the worst being entropy. The Brenner gradient had the most symmetric and monotonic of the curves through focus with the steepest gradient. This meant a more defined focus position can be determined. In contrast, the entropy-based metric did not vary symmetrically either side of focus and the variation in entropy values was smaller.

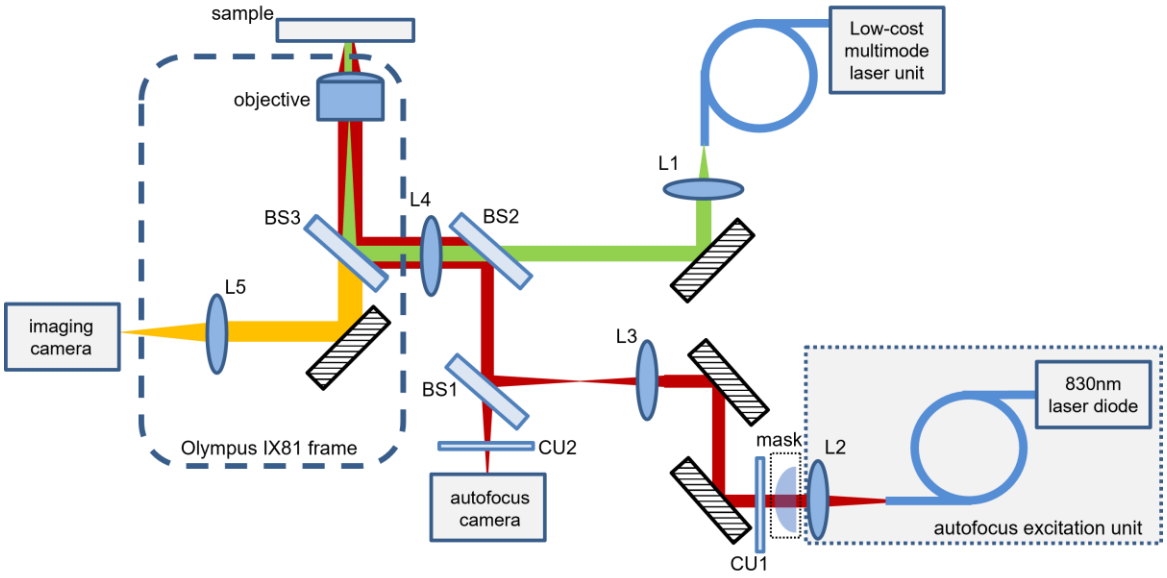

Figure 5.1. showing the optical setup for a knife-edge-based centroid autofocus using an infrared, 830 nm, fibre coupled source implemented on an Olympus IX81. The path of the autofocus beam is represented by the red line. The output from the fibre is collimated by an 18.4 mm focal length aspheric lens, (Thorlabs C280TMD-B), and bisected by a knife-edge mask. The beam then passes an excitation filter, CU1 (Edmund 65-119), and is steered by a pair of mirrors. The beam is reflected by a 50:50 beamsplitter, BS1 (Edmund 47-026), a short pass dichroic, BS2 (Edmund 69-220) and a custom multiline dichroic, BS3 (Chroma ZT405_465_625_825rpc-UF2). An image of the knife-edge is formed on the back focal plane of the objective (Olympus UplanFL 100x, NA 1.3, oil) using a 100 mm focal length lens L3 (Thorlabs AC254-100-B-ML) and a 200 mm focal length Lens L4 (Edmund 49-364). The bisected beam is reflected at the interface between the coverslip and the sample before propagating back through the system. Here it is transmitted by the 50:50 beam splitter, BS1, and a clean-up bandpass filter, CU2 (Edmund 65-180), before being imaged onto a secondary autofocus USB camera (FLIR CM3-U3-31S4M-CS).

This order of metric performance was in agreement with the analysis by Sun et al. (Sun, Duthaler & Nelson, 2004) who compared the performance of 18 different image metrics using 5 different performance criteria (accuracy, range, number of false maxima, width and the noise level). The authors combined these results to determine an overall score for the 18 metrics presented. The best

performing metric when applied to brightfield, phase contrast and DIC imaging modalities was the *normalised variance*:

$$V_{norm} = \frac{1}{N \times M \times \mu} \sum_{i=1}^{N} \sum_{j=1}^{M} [I(i,j) - \mu]^2 \qquad \textit{Equation 5.6}$$

Where V_{norm} is the normalised variance, N is the image pixel height, M is the image pixel width.

For all of these metrics to be used to determine focus, multiple images needed to be acquired at different axial positions through focus with interpolation between the measured metric values being used to quantify the defocus. It is preferable to minimise the number of image acquisitions that are required to determine the optimal focus position. A minimum of 3 images acquired through focus are required to fit a Gaussian if the defocus curve is a single peak and monotonic either side. However, measuring at more axial positions will improve the performance at the expense of increased measurement time per FOV.

The disadvantage of image-based autofocus methods is that they are inherently slow, as they require multiple frames to be acquired for each FOV, during which time the sample should be static, which can be a problem for imaging live samples. In addition, the acquisition of multiple images per FOV for the autofocus can increase the light dose on the sample and increase the probability of the sample suffering from photobleaching or phototoxicity. Another limitation for image-based autofocuses, is they typically work over a limited narrow axial range close to the DOF of the microscope objective. This would not be adequate to accommodate large axial focus variations such as those encountered when moving between wells across a multiwell plate which can be as much as ~250 µm for a 96 well plate. A further significant limitation is that image-based autofocus techniques may not work with thick samples such as biological tissue where there may be features that contribute to image-based metrics at multiple axial planes in the sample.

5.2.2 Hardware-based autofocus techniques

In these techniques, additional optical components are introduced into the system to measure the separation between the coverslip or the sample and the objective lens. In general, hardware-based techniques use a separate detector to the primary microscope camera and can operate faster than software-based techniques and in parallel with the primary imaging modality - typically requiring only one or two auxiliary “autofocus measurements” and often being able to operate in “closed loop” mode to lock on the focus condition. In addition, the optical system of the autofocus can be

designed to optimise the autofocus readout without compromising the primary microscope function and this can make the signal (image) processing simpler. The performance of optical autofocus systems is much less dependent on the sample, and they will usually work with thick samples. However, implementing an optical autofocus requires either a new design of the microscope frame or the integration of additional hardware components and this adds cost and complexity to the instrument.

Optical autofocus techniques have been implemented using a range of different principles to measure the coverslip objective lens separation. These include *confocality* (LIRON et al., 2006), where the intensity of a laser beam, focused onto and reflected from the coverslip, is monitored through a pinhole located in a conjugate plane to the coverslip. When the coverslip is in the focal plane of the objective lens, the light transmitted through the pinhole will be at maximum intensity and this signal will decrease with defocus. Alternatively, the light reflected from the coverslip can be imaged on an auxiliary camera (with no detection pinhole required), as discussed later in this chapter. For other autofocus techniques, *fiducial markers* (such as gold beads (Coelho et al., 2023)) are introduced into the sample and are imaged on an auxiliary camera using a variety of imaging modalities including intensity or phase imaging or using a wavefront sensing device (Bon et al., 2015). Defocus can be determined from the auxiliary camera images using a range of metrics such as measuring the displacement of an image (Liao et al., 2016) or by calculating a centroid value from the optical signal being monitored from the sample (Liu et al., 2010). As well as using light reflected from the coverslip, this approach can also be implemented using fluorescent emission (Silvestri et al., 2021) (as long as it originates from a single plane in the sample) or light scattered from fiduciary markers (Bon et al., 2015).

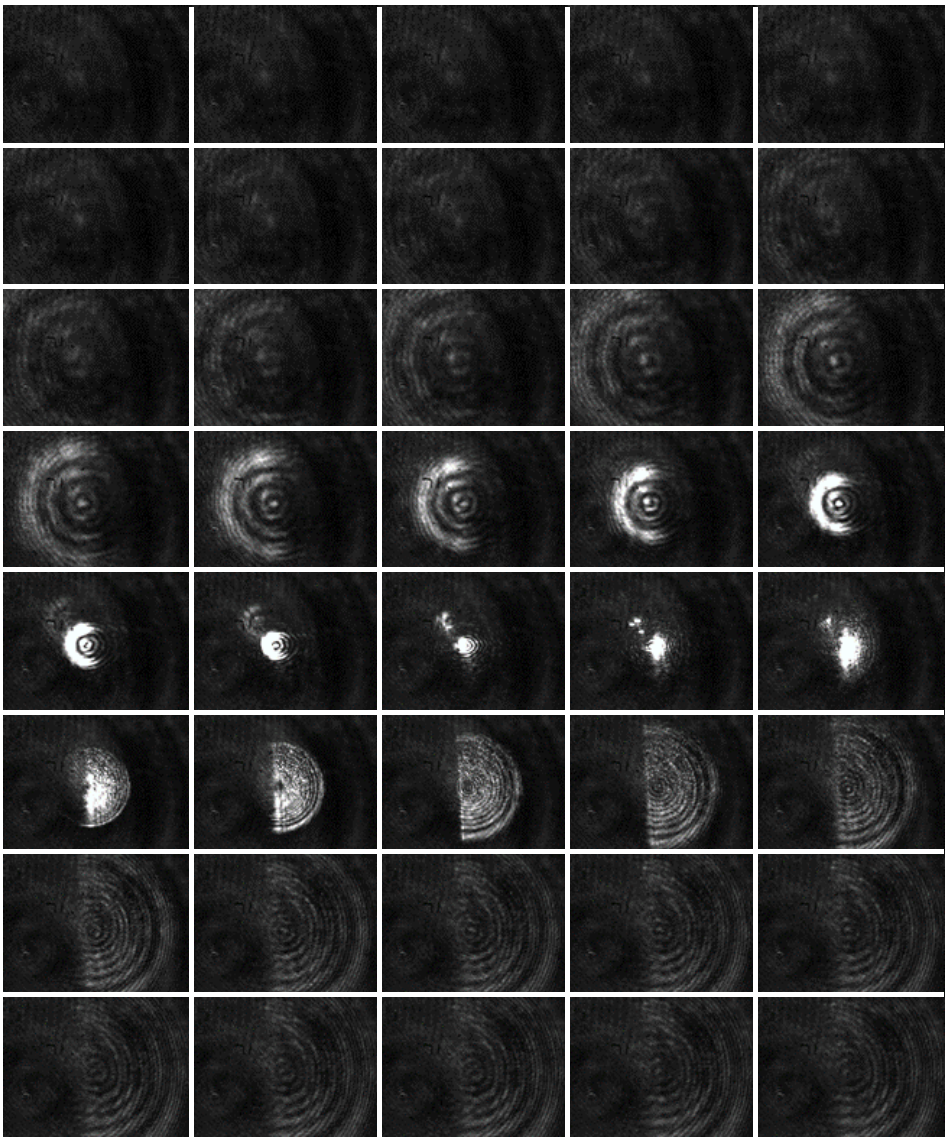

Figure 5.2. showing the image formed on the full FLIR CM3-U3-31S4M-CS camera sensor (2048x1536 pixels) of the bisected autofocus beam as the sample is passed axially through focus. The images were acquired every 5 microns. The defocus in the images increase in axial height scanning from left to right along each row from -110µm (top left) to +90µm (bottom right) through focus. A 6.4mm focal length lens was used to collimate the beam out of the fibre.

A disadvantage of these optical techniques can be that they are limited by diffraction. If the optical autofocus illumination is through the objective lens, then the short confocal parameter may limit the range of the autofocus such that it cannot accommodate large defocussing experienced with multiwell plates or slide scanning.

5.3 Knife-edge centroid autofocus

The initial implementation of an optical autofocus system was based on a centroiding measurement of a laser beam that is focussed by the objective lens on the sample coverslip and reflected back to an auxiliary (autofocus) camera, as illustrated in Figure 5.1. A knife-edge was used to bisect a laser beam after collimation from an optical fibre to form a semi-circular collimated illumination beam incident on the back aperture of the objective lens. This design, which was originally presented by Liu et al. (Liu et al., 2010), was implemented on an Olympus IX81 microscope frame with a motorised sample stage. An infrared beam from a laser diode at 830 nm (Ushio HL8337MG), was coupled into a single mode optical fibre (FS-SN-4224) fibre and collimated using an 18.4 mm focal length lens (Thorlabs C280TMD-B) to provide a collimated TEM_{00} illumination beam with a Gaussian intensity profile. This beam was coupled into the microscope via the main (multiline) dichroic beamsplitter and was aligned with the optical axis of the microscope using two steering mirrors. A knife-edge was placed before the steering mirrors to bisect the collimated illumination beam which was then reflected by a 50:50 beamsplitter (Edmund 47-026). The beam was then reflected by a short pass dichroic beamsplitter, BS2 (Edmund 69-220), before being reflected by the microscope dichroic beamsplitter, BS3, to be collinear with the optical axis of the microscope. The short pass dichroic beamsplitter was used to introduce an excitation laser beam into the microscope (e.g., for easySTORM). The 50/50 beamsplitter transmitted part of the reflected infrared laser beam. Lens L4 (Edmund 49-364) of 200 mm focal length effectively imaged the autofocus laser spatial profile at the coverslip onto the autofocus camera (FLIR CM3-U3-31S4M-CS).

Figure 5.2 shows frames from an “axial fly-through” movie acquired by the autofocus camera as the microscope sample stage was translated through focus, where the optical fibre aspheric collimating lens here was changed to a focal length of 6.4 mm, to increase the operating range, giving a beam diameter on the order of 12.8 mm at the back aperture of the objective lens. The choice of collimating lens focal length impacts the confocal parameter of the system. The shorter the confocal parameter, the more accurate the focus prediction will be but the shorter the operating range. The knife-edge bisecting the collimated illumination laser beam produces an asymmetric intensity distribution that changes size and shape and moves across the autofocus camera sensor as the objective lens is translated through focus. When the coverslip is in focus, the image on the autofocus camera will be a focussed spot, and this grows as an approximately semi-circular intensity distribution when the sample stage is translated either side of focus. Figure 5.2 illustrates how the direction of defocus is indicated by the lateral position of the intensity distribution on the autofocus camera.

Liu et al. (Liu et al., 2010) used an approach based on the centroid of the intensity distribution on the autofocus camera, using a ray optics description to establish a linear relationship between the degree of defocus (quantified by the sample stage position) and the radius and centroid position of the intensity distribution on the sensor. By fitting the image data acquired from an axial scan of the objective or sample stage to their ray optics model, they could use that relationship to predict the current defocus from the acquired autofocus camera image after appropriate image processing.

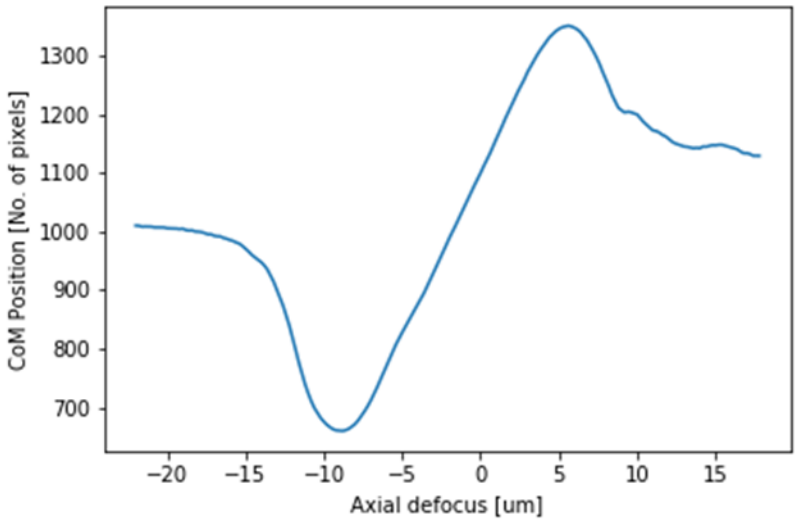

Figure 5.3. Centre of mass (CoM) position of the distribution of light on the camera as a function of sample defocus for the knife-edge-based autofocus system shown in Figure 5.2. This calibration data was used as a look-up table for the image data shown in Figure 5.4. The linear range is approx. 13 µm. The raw image data was acquired in 200 nm step intervals.

For my implementation of this knife-edge autofocus system, I acquired a “calibration” axial scan of autofocus camera images, calculated the centroid position of each frame and stored these values in a look-up table of centroid position and axial stage position. This allows the defocus (i.e., the stage translation required to bring the microscope back into focus) to be determined from a single autofocus image by calculating the intensity centroid position and comparing it to the look-up table. The nearest value in the table could be found and hence the current defocus could be predicted.

This approach can avoid artefacts that could arise if the relationship between centroid position and defocus is nonlinear. However, it requires an up-to-date calibration z-stack of autofocus camera images acquired during an axial scan through focus as the relationship between centroid position and defocus may change if the alignment is perturbed or drifts over time.

I found the useful axial range of this knife-edge autofocus approach to be limited because the intensity distribution on the autofocus camera expands with defocus such that its diameter exceeds the size of the camera sensor and then the calculated centroid position no longer increases linearly

with defocus but flattens off and then starts decreasing, as illustrated in Figure 5.3. This stack was acquired when using the 18.4 mm focal length aspheric collimating lens. Therefore, outside the

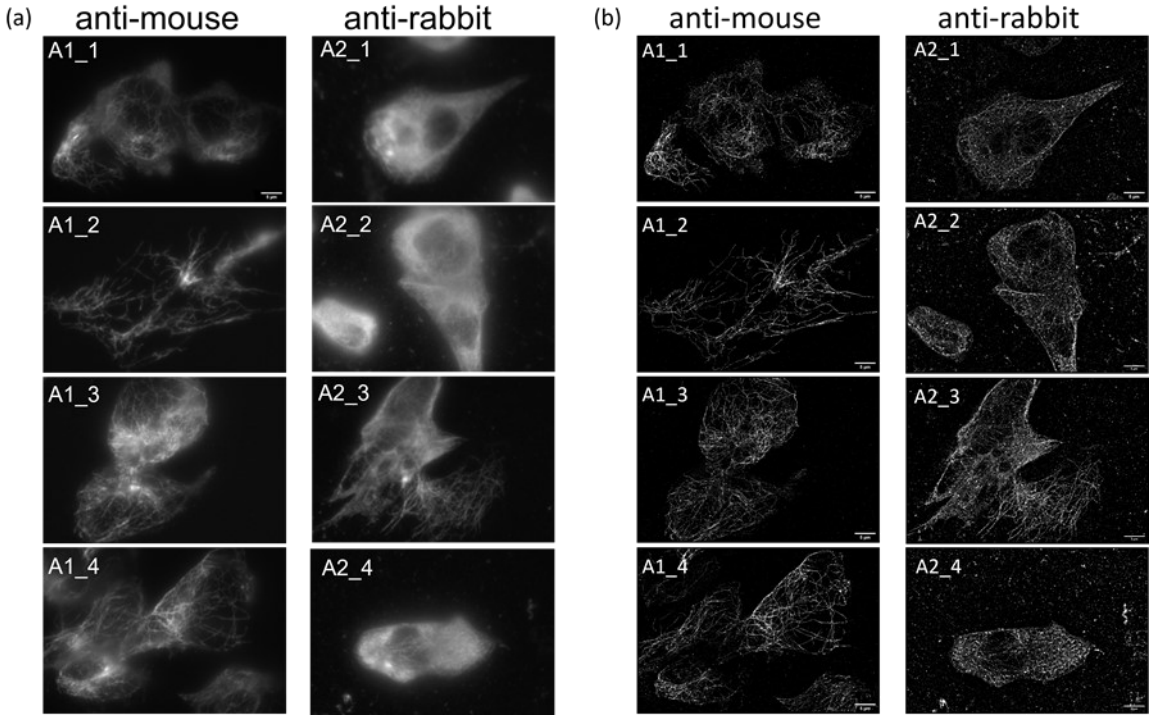

Figure 5.4 A figure showing automatically acquired HCA acquisition of HEK293 cells arrayed in two wells of an 8 well chamber slide. 4 FOV's were acquired in each well. The cells in A1 were labelled with a mouse primary antibody (Sigma Aldrich T8203 clone AA13, Lot:013M4788V, 1:1000) and the secondary antibody was a donkey anti-mouse conjugated with Alexa Fluor 647 (ThermoFisher Scientific catalogue A31571, Lot:1692912). The cells in A2 were labelled with a rabbit primary polyclonal antibody (Abcam ab18251, Lot:GR275948-1, 1:1000) and a goat anti-rabbit secondary antibody (ThermoFisher Scientific A-21244) conjugated with Alexa Fluor 647. (a) shows the automatically acquired widefield images of the same super-resolved reconstructed FOV's shown in figure (b). The focus was maintained using the knife-edge centroid autofocus technique.

approximately linear regions, the autofocus is no longer able to reliably determine the defocus. The signal to noise ratio of the images acquired on the autofocus camera also decrease with defocus and ultimately this prevents any useful calculation of the centroid position in a single step, but rather it must move back to the linear region first and then jump to focus.

If the defocus is outside the linear range but the images still present sufficient signal to noise for useful image processing, it is possible to implement a multistep approach to return to focus. The sign of defocus can still be determined from the autofocus camera images and so the stage can be moved in the direction towards focus to search for the linear region, from where the system can then move to focus with a single step. However, this iterative process can be slow.

5.3.1 HCA STORM using knife-edge autofocus

To demonstrate the efficacy of this knife-edge autofocus system, I used it when imaging samples arrayed in a multiwell chamber slide with STORM. Having acquired a calibration autofocus z-stack, I applied the autofocus every 200 frames during the STORM acquisitions to correct for any axial drift. Figure 5.4 shows representative images of HEK293 cells from an easySTORM experiment where the cells were arrayed in 2 wells of an 8-well chamber slide and 4 FOV's were acquired in each of the wells. In the first well the tubulin in the cells were labelled with a donkey anti-mouse secondary antibody (ThermoFisher Scientific A31571, Lot:1692912) conjugated with Alexa Fluor 647 and a mouse primary antibody (Sigma Aldrich T8203 clone AA13, Lot:013M4788V) in 1:1000 concentration. The cells in the second well were labelled with a goat anti-rabbit secondary antibody (ThermoFisher Scientific A-21244) conjugated with Alexa Fluor 647 and a rabbit primary polyclonal antibody (*Abcam ab18251, Lot:GR275948-1*) in 1:1000 concentration. Each FOV was acquired with 20,000 frames and the exposure was set at 30 ms. The widefield epifluorescence and super-resolved image reconstructions are shown in Figure 5.4. The cross-section of a feature interpreted to be a single isolated microtubule structure was measured to be 56 nm for the reconstructed STORM images compared to 289 nm in the widefield epifluorescence images. The measured cross section of the microtubule is increased from the expected 25nm when using primary and secondary antibodies since the secondary antibody is located up to 20nm from the target after labelling. Therefore, the FWHM is increased to an expected ~50nm (Leduc et al., 2018).

I observed that, while this autofocus technique worked well for short image acquisitions of less than 2 hours, it could fail during longer experiments such as multiwell plate image data acquisitions. This is because the optical autofocus system can be subject to environmental perturbations over time in a similar manner to the microscope itself. While thermally induced drift in the microscope can lead to the defocus that the autofocus is intended to correct, the optical system for the autofocus itself can be affected by thermal or mechanical drift that can change the optical alignment. If such drift leads to lateral displacement of the autofocus laser beam relative to the knife edge or the camera sensor, this can have a strong impact on the defocus measurement. This would be an issue for any optical autofocus technique that uses a metric based on position of an image on the autofocus camera sensor. It is therefore desirable to base the defocus measurement on an autofocus image metric that will not be as sensitive to perturbations of the alignment of the autofocus laser beam. I therefore explored designs that determined defocus from the shape of the intensity distribution on the autofocus camera sensor, rather than its position.

5.4 Slit-based autofocus

Figure 5.5 shows the schematic of an optical autofocus design that utilises a rectangular slit to aperture the autofocus illuminating laser beam profile, thereby creating a collimated rectangular beam that is aligned to propagate through the optical system to the back focal plane of the objective lens centred on the optical axis. The aspect ratio of the slit used was approximately 3:1. The defocus is then determined by the width of the intensity distribution on the autofocus camera sensor, rather than its position. The mask was located in the back focal plane of the collimating lens after the optical fibre and this plane was designed to be conjugate with the back focal plane of the objective lens. The slit leads to different beam diameters along the two orthogonal axes parallel and perpendicular to the slit. In turn, this leads to stronger or weaker focussing of the autofocus laser beam on the coverslip relative to the orientation of the slit, which means that the autofocus provides different precision and range when measuring the width of the intensity distribution on the autofocus camera sensor in orthogonal directions.

The defocus measurements are made by averaging the intensity along either the rows and columns of the autofocus image to provide two respective intensity "projections" along the horizontal and vertical axes of the sensor, i.e., parallel, or perpendicular to the slit. The defocus can then be calculated from a measure of the width of these intensity projections. Initially I used the numerical standard deviation of the averaged intensity values along each projection, which peaks at focus, as the defocus metric to be used in the look-up table.

The range and precision of the autofocus is governed by the confocal parameter of the focussed autofocus illumination beam:

$$Confocal\ Parameter = 2 \times Z_R \qquad \textit{Equation 5.7}$$

$$Z_R = \frac{\pi {\omega_o}^2 n}{\lambda} \qquad \textit{Equation 5.8}$$

Where Z_R is the Rayleigh range, ω_o is the beam waist, n is refractive index and λ is the wavelength.

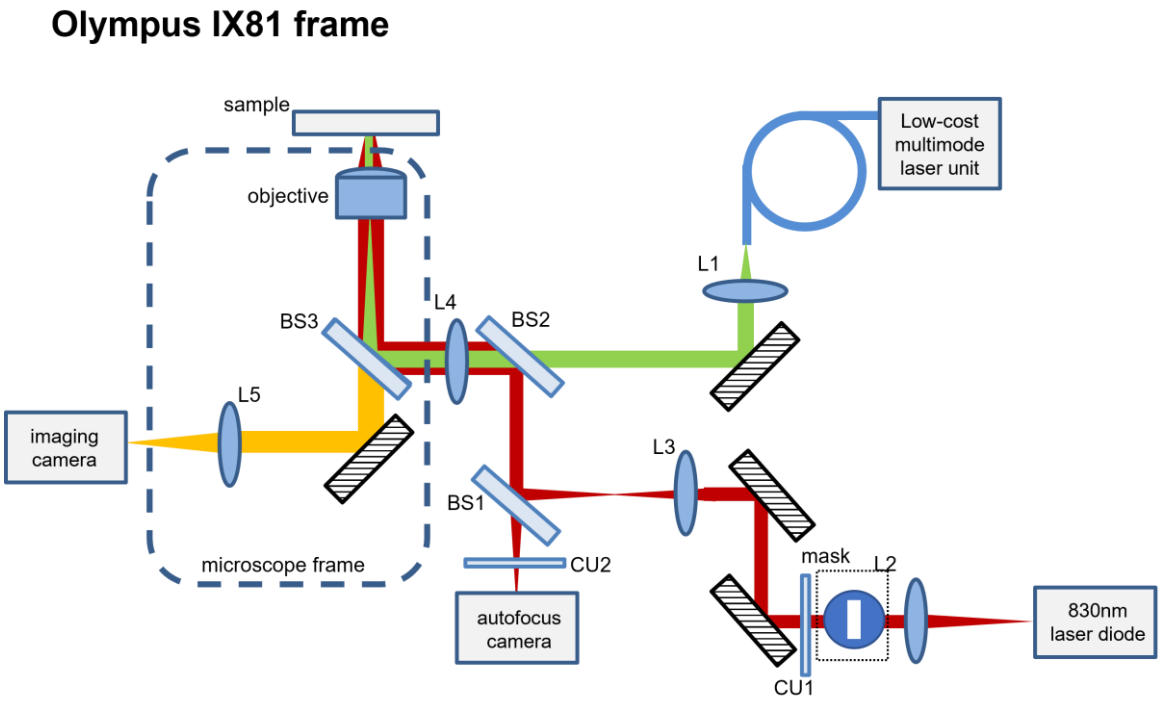

Figure 5.5. The optical system for the slit-based autofocus implemented on an Olympus IX81 frame. An 830 nm laser diode (Ushio HL8337MG), was coupled into a single mode fibre with a 0.1 NA and the output of the fibre was used as the source for the autofocus. The beam was collimated using an 18.4 mm aspheric lens (Thorlabs C280TMD-B). The collimated beam was masked using a rectangular slit with a slit size of 1.2 mm. This resulted in a collimated rectangular beam (3.6 mm and 1.2 mm respective diameters), propagating through the optical system. The beam diameter was magnified by a factor of 2 using a 100 mm focal length lens, lens L3 (Thorlabs AC254-100-B-ML), and a 200 mm focal length lens, L4 (Edmund 49-364). In between these lenses, the beam was reflected first by a 50:50 beamsplitter, BS1 (Edmund 47-026), and then by an 800 nm shortpass filter, BS2 (Edmund 69-220). The beam was then reflected by a purpose designed multiline dichroic for use with multi-channel STORM excitation, BS3 (Chroma ZT405_465_625_825rpc-UF2). The rectangular beam was then focused onto the sample by a 100x objective (Olympus UplanFL 100x, NA 1.3, oil) and reflected at the refractive index change between the coverslip and the sample's media. The reflected signal then propagated back through the system and was transmitted by the 50:50 beamsplitter, BS1, before being imaged by an auxiliary autofocus camera, Flir Chameleon3 (FLIR CM3-U3-31S4M-CS). CU1 (Edmund 65-110) and CU2 (Edmund 65-180) are clean up bandpass filters

The confocal parameter scales with the square of the laser beam waist, which is proportional to the diameter of the illumination beam at the back focal plane of the objective lens. It should be noted that the given formula is for a Gaussian beam, but the beam used here is a Gaussian subject to a top hat mask. The autofocus confocal parameter will be larger or smaller when measured parallel or perpendicular to the slit. The parallel projection presents a narrower beam waist in the back focal plane so that the beam reflected from the coverslip will expand faster with defocus, providing more sensitive measurements but also limiting the range of operation as the beam more quickly exceeds

the size of the sensor at the autofocus camera. Thus, by controlling the width of the illumination beam along these two orthogonal directions, we can simultaneously realise a high precision autofocus over a short operational range and a lower precision over a longer range. This is characterised in detail in Chapter 6.

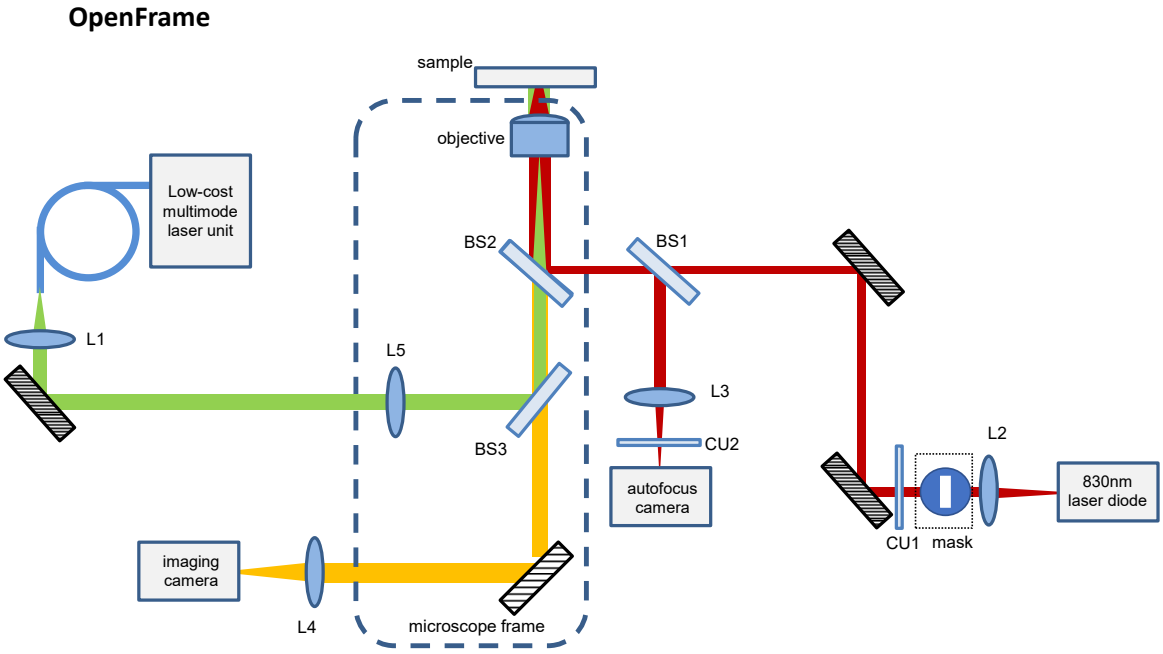

Figure 5.6 Implementation of the slit autofocus on the openFrame. An 830 nm laser diode (Ushio HL8337MG) was coupled into a single mode fibre with a 0.1 NA and the output of the fibre was used as the source for the autofocus. The beam was collimated using an 18.4 mm aspheric lens (Thorlabs C280TMD-B). The collimated beam was masked using a rectangular slit with a slit size of 1.2 mm. This resulted in a collimated rectangular beam (3.6 mm and 1.2 mm respective diameters), propagating through the optical system. The beam was transmitted first by a 50:50 beamsplitter, BS1 (Edmund 47-026), and then reflected by an 800 nm shortpass filter, BS2 (Edmund 69-220). The rectangular beam was then focused onto the sample by a 100x objective (Olympus UplanSApo 100x, NA 1.40, oil), and reflected at the refractive index change between the coverslip and the sample's media. The reflected signal then propagated back through the system and was reflected by the 50:50 beamsplitter, BS1, before being imaged by an auxiliary autofocus camera, Flir Chameleon3 (FLIR CM3-U3-31S4M-CS) using lens L3 (Thorlabs AC254-200-B-ML). CU1 (Edmund 65-110) and CU2 (Edmund 65-180) are clean up bandpass filters

Unfortunately, the expansion of the autofocus laser beam is approximately symmetric either side of focus and so it is not possible to determine the required correction from a single autofocus camera image. Instead, a 2-step approach can be adopted where the defocus metric is determined for autofocus camera images acquired at two sample stage positions separated by a 10 µm. By comparing these values, one can determine whether the sample stage needs to be moved in the positive or negative direction.

5.4.1 Implementation of slit-based optical autofocus on an *openFrame* microscope

The slit-based optical autofocus system was implemented and tested on the openFrame modular microscope discussed in Chapter 4, for which focussing is realised by axially translating the objective lens rather than the sample stage. The system design for the autofocus is shown in Figure 5.6. A single mode laser diode emitting at 830 nm was coupled into a single mode optical fibre and the output was collimated using an 18.4 mm focal length aspheric lens to provide the autofocus illumination beam with a radius of 1.84 mm. This collimated laser beam was then apertured using a rectangular slit with a short axis width of 1.2 mm and a long axis width which exceeded the diameter of the beam, which was approximately 3.68 mm, to provide a beam with an approximately 3:1 aspect ratio between the two axes. The beam was then steered using 2 elliptical mirrors to propagate through a 50:50 beam splitter and reflect off the microscope multiline dichroic beamsplitter to propagate along the optical axis to the back aperture of the Olympus 1.4 NA 100x objective lens, which focused it down onto the sample where it was partially reflected at the refractive index interface between the glass coverslip and the sample media. The reflected beam then propagated through the system where part was reflected at the 50:50 beam splitter and focused by a 100 mm focal length tube lens onto the autofocus camera. As the beam diameter differs by a factor of ~3 in the two orthogonal directions, the confocal parameter differs by a factor of ~9 between the two orthogonal directions, giving almost an order of magnitude difference in the precision and range of the autofocus operation using the orthogonal intensity projections.

5.4.2 Comparison of slit-based and knife-edge-based autofocus systems: temperature variations

The performance of the slit-based optical autofocus was compared to the knife-edge approach in two experiments designed to explore the impact of drift in the optical alignment, with the hypothesis that the slit-based approach would prove more resilient since the defocus measurement does not depend on the position of the reflected laser beam at the autofocus camera sensor. These comparisons were carried out on the *openFrame* microscope.

The first comparison was made by imaging 100 nm Tetraspeck fluorescent beads (T7279) arrayed in a 96-well plate over a timescale similar to that needed for STORM experiments, where 5000 frames with 30 ms exposure times would typically be acquired for each FOV, i.e., requiring >150 seconds per

FOV. Accordingly, a FOV of beads was imaged in each well 15 times at 10 second intervals. For the first 1hr20min of the experiment, both autofocus approaches were applied under normal laboratory conditions and then the air conditioning fans were turned off and the temperature in the lab was allowed to rise. 2hr40min into the experiment the temperature in the vicinity of the equipment was further increased using a portable fan heater and the room temperature was monitored using a temperature sensor (Teracom TCW210-TH controller and Teracom TSH300v2 Temperature sensor).

(a) (b)

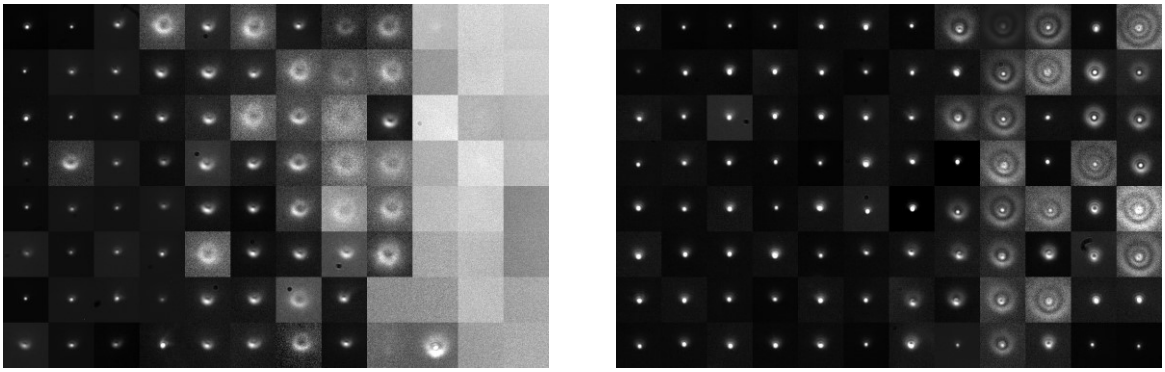

Figure 5.7. 96-well plate image acquisitions of one 100 nm tetraspeck bead in each well acquired using (a) centroid metric utilising a knife edge and (b) standard deviation of the mean projection intensity along the axes. Each sub-image shows the bead image acquired in a different well. The wells were acquired starting in the top left well (A1), moving straight down column 1, one well at a time until after imaging H1. After imaging H1, the image in H2 was acquired. Then the acquisition proceeded vertically up column 2. The wells were then accordingly acquired in this snake pattern down and up the columns. After 1hr20min into the experiment, the system was imaging well A4. After 2hr40min since experiment start, the system was imaging well A8.

Using each autofocus approach, the 96-well plate was traversed in a vertical snake-like pattern, starting in well A1 and initially moving down the plate, 1 well at a time, before reaching H1. Then the acquisition travelled back up column 2. The acquisition continued in this fashion progressing column by column. Figure 5.7 shows representative images of 100 nm Tetraspeck fluorescent beads acquired in each well using an sCMOS camera (Andor Zyla 5.5). Each FOV is represented by a single bead image The autofocus systems were applied before the image data acquisition at each new FOV. It took 4 hours for all 96 wells to be imaged. The 2 different autofocus approaches were tested on consecutive days.

As illustrated in Figure 5.7(a), when using the knife-edge autofocus approach, the beads were maintained in-focus for the initial 1hr20min during which time the temperature in the lab was steady (changing by less than 0.1^{o}C). After the air conditioning fans were switched off, the temperature increased by 1.1^{o}C over the next 1hr20min, during which time the defocus measurement acquired an offset with respect to the true value due to the beam position shifting

across the autofocus camera sensor. When the fan heater was switched on, the temperature in the vicinity of the experiment increased by 3.6°C during the final hour of the acquisition and the knife-edge autofocus failed such that the beads were too far from focus to be resolved.

Using the slit-based autofocus approach, it was possible to image beads in all of the wells throughout the 4-hour experiment. The laboratory temperature changed during the first 1hr20min of the experiment by only +0.1°C, whereas it increased by 1.3°C over the next 1hr20min with the air conditioning units switched off and then the local temperature increased further by 4.2°C in the final hour of the experiment. Figure 5.7 (b) illustrates how the beads were imaged in focus for the first 2hr40min of the experiment. However, as the temperature increased further when the fan heater was switched on, the collimated autofocus laser beam drifted relative to the slit, which changed the shape of the intensity profiles at the autofocus camera sensor. This change compromised the efficacy of the defocus look-up table such that the autofocus failed to maintain the correct focus for some of the FOVs.

Overall, it is clear that the slit-based autofocus was more resilient to thermal-induced drift than the knife-edge technique, but its performance was still compromised by a total temperature change of 5.2 °C. However, if the laboratory temperature is maintained within 2°C during an experiment, the slit-based optical autofocus may be a reasonable strategy for super-resolved microscopy and multiwell plate imaging or slide-scanning applications.

5.4.3 Comparison of slit-based and knife-edge-based autofocus systems: simulated system drift

The knife-edge autofocus can fail if the position of the reflected autofocus laser beam on the autofocus camera changes with respect to the position used when acquiring the calibration z-stack. This may be caused by thermal or mechanical drift in the alignment of the autofocus optical system. To demonstrate that the slit-based autofocus approach should be insensitive to such drifts in the position of the reflected laser beam, I simulated such drift computationally and physically and, having acquired the respective autofocus calibration image z-stacks (over a range of -25 µm to +25 µm in 200 nm step intervals) to build the respective defocus look-up tables for each autofocus approach, I then shifted the autofocus camera images to challenge the autofocus system and acquired a new autofocus camera image z-stack at each value of shift. This shift could be realised by physically moving the camera sensor (mounted on an x-y micrometer stage) or simulated by

cropping the autofocus camera images by 50 pixels from the outer perimeter and shifting the camera image horizontally with respect to the calibration defocus look-up table. Both the knife-edge autofocus and the slit-based autofocus were implemented on the openframe for the comparison.

Figure 5.8 shows the results of the simulated camera shifting in steps equal to half the focussed laser beam spot size (i.e., ω_{ac}) on the camera sensor, up to a maximum distance of 4.5 ω_{ac}. The focal spot size on the sensor was calculated, when using the following *Equation 5.9*.

$$\omega_f = \frac{\lambda f}{\pi \omega_0} = \frac{830 \times 10^{-9} \times 100 \times 10^{-3}}{\pi \times 1.84 \times 10^{-3}} = 14.4 \mu m \qquad \textit{Equation 5.9}$$

Where ω_f is the focal spot radius, λ is wavelength, f is the focal length of the tube lens, and ω_0 was the beam diameter of the collimated beam into the back focal plane of the tube lens.

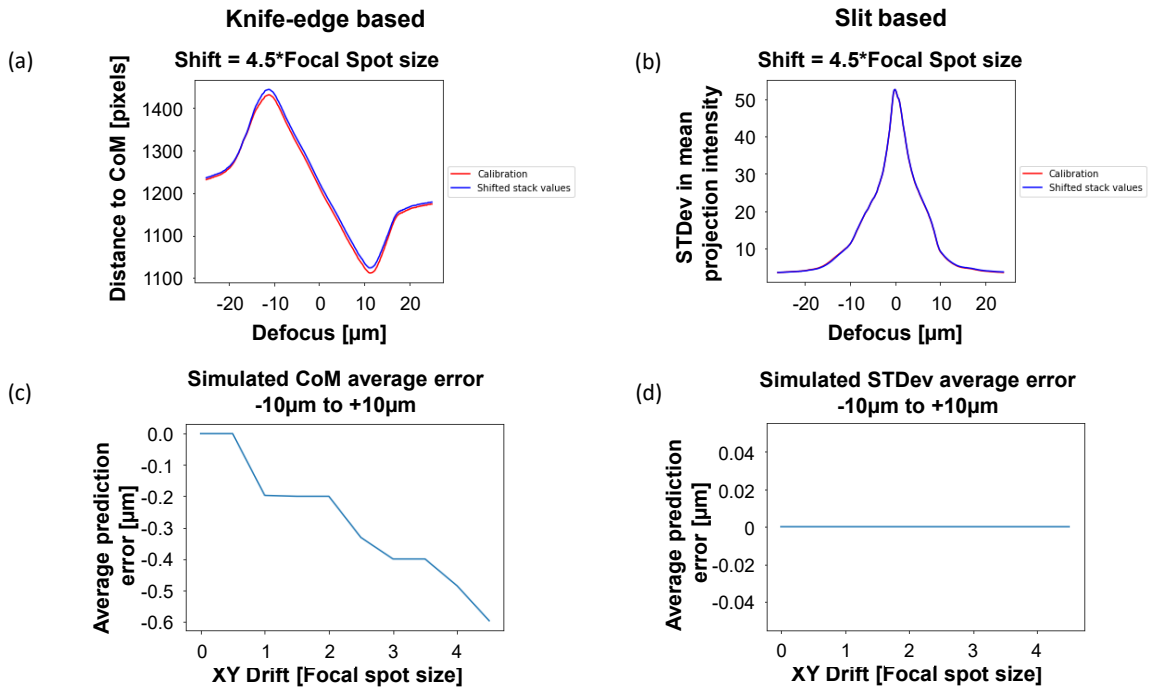

Figure 5.8. Simulated drift of translated cropped images from the autofocus camera. Images were shifted in half integer values of the focal spot size. The results for the knife-edge centroid based autofocus are shown on the left (a, c) and the slit-based standard deviation autofocus results on the right (b, d). As the drift was induced in the images, the current defocus was predicted from the original calibration stack. The induced drift caused the centroid values, associated with the knife-edge, to be shifted to larger values. This created an error when predicting the defocus with a constant offset. Whereas the standard deviation approach was able to correctly predict the defocus as the drift was introduced and the values did not shift from the calibration plot.

The pixel size of the FLIR Chameleon3 CMOS camera is 3.45 µm and the reflected laser beam has a

focal spot size radius of 4.16 pixels. For the simulated drift, the cropped image was translated by 4 pixels in the x direction and 1 pixel in the y direction, to give a shift of ω_{ac}. = 4.12 pixels.

Figure 5.8(a,b) shows plots of the calibration defocus look-up data for (a) the knife-edge and (b) slit-based autofocus techniques (in red) and the maximum shifted values (in blue) of the respective defocus metric (i.e. centroid position or standard deviation of intensity distribution of reflected laser beam on camera sensor) when using the computationally shifted autofocus camera images.

Figure 5.8(c, d) show the average defocus prediction error across the linear region in the calibration z-stack that was calculated at each simulated drift value of the autofocus camera images between 0 and 4.5 ω_{ac}. For the (c) knife-edge-based and (d) slit-based autofocus approaches: the knife-edge autofocus data shows an incorrect offset in the predicted defocus compared to the true defocus for that stack, which became worse with increasing camera image shift. In contrast, for the slit-based autofocus, there was no defocus prediction error for any of the autofocus camera image drift values.

This comparison was repeated by mounting the autofocus camera on an x-y micrometre stage and physically shifting the camera sensor. Figure 5.9(a,b) shows the plots of the calibration defocus look-up data (in red) and the maximum shifted values (in blue) of the respective (a) knife-edge-based and (b) slit-based defocus metric, and Figure 5.9(c,d) show the respective average defocus prediction error across the linear region in the calibration z-stack that was calculated at each simulated drift value of the autofocus camera images between 0 and 3.2 ω_{ac}. In this experiment, the maximum camera shift was limited to 3.2 ω_{ac} by the translation stage and the knife-edge was mounted in the opposite side of the illuminating autofocus laser beam so the plots in Figure 5.9(a) are horizontally flipped.

As was observed with the simulated autofocus camera shift, the knife-edge autofocus data shows an incorrect offset in the predicted defocus, which again increased with camera shift up to a maximum of 0.700 μm. There was also some error in the defocus prediction of the slit-based autofocus but the maximum error was lower (<0.125 μm) and is within the depth of field of the 1.4 NA objective lens in the microscope (~±300 nm for imaging with light at 647 nm). The increased prediction error compared to the simulated camera shift results may be due to variations in noise across the autofocus camera image stacks, or there may have been some drift of the relative alignment of the autofocus laser beam and slit between the acquisitions of the calibration and measurement z-stacks. However, these experiments demonstrate that the slit-based autofocus is more robust than the knife-edge-based autofocus with respect to optical drift that may be caused, e.g. by thermal variations or mechanical relaxation of components.

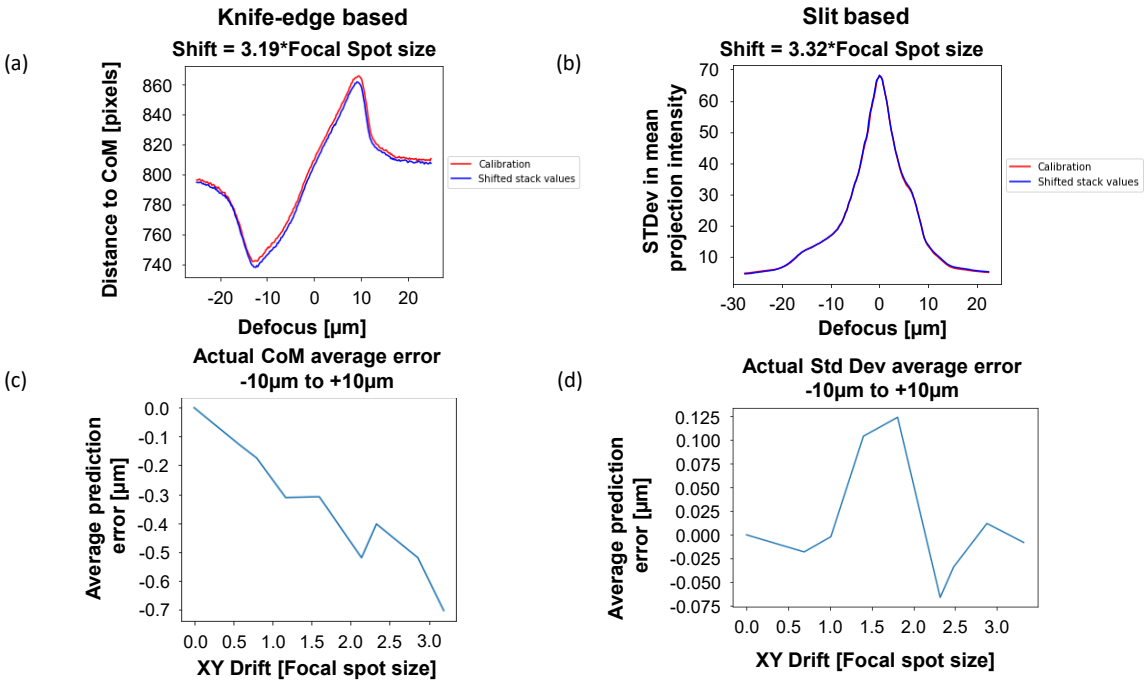

Figure 5.9 Induced drift of images acquired from the autofocus camera using a micrometre stage to shift the image position on the sensor. Images were shifted in half integer values of the focal spot size. The results for the knife-edge centroid based autofocus are shown on the left (a, b) and the slit-based standard deviation autofocus results on the right (b, d). As the drift was induced in the images, the current defocus was predicted from the original calibration stack. The induced drift caused the centroid values, associated with the knife-edge, to be shifted to larger values. This created an error when predicting the defocus in the form of a constant offset. In contrast, the standard deviation approach was able to perform better at predicting the defocus as the drift was introduced. The maximum error predicted from the knife-edge approach was 700 nm, compared with 125 nm for the standard deviation technique when considering an image drift up to three times the focal spot size.

5.5 Cylindrical lens autofocus

The slit based autofocus was shown to be more robust than the knife-edge approach and also provides both long-range/lower precision and short-range /higher precision readouts of defocus. However, it is still unable to determine the sign of defocus from a single autofocus camera acquisition and the defocus metric (standard deviation of the intensity distribution of the reflected laser beam at the autofocus camera) can be impacted by small changes in the relative alignment of the autofocus laser beam and the slit. To address the latter issue, it was proposed to use a pair of orthogonal cylindrical lenses of different focal lengths to collimate the autofocus laser beam from the optical fibre to generate the required (~3:1) difference in beam diameter in orthogonal directions rather than a slit. This would be less sensitive to small changes in alignment of the laser

beam with the optical axis (and therefore the slit). It was also proposed that, by slightly translating one of the cylindrical lenses from the position where it collimated the light from the optical fibre, the autofocus laser beam would provide slightly different defocus measurements parallel to each cylindrical lens and this would enable the sign of defocus to be determined from a single autofocus camera image.

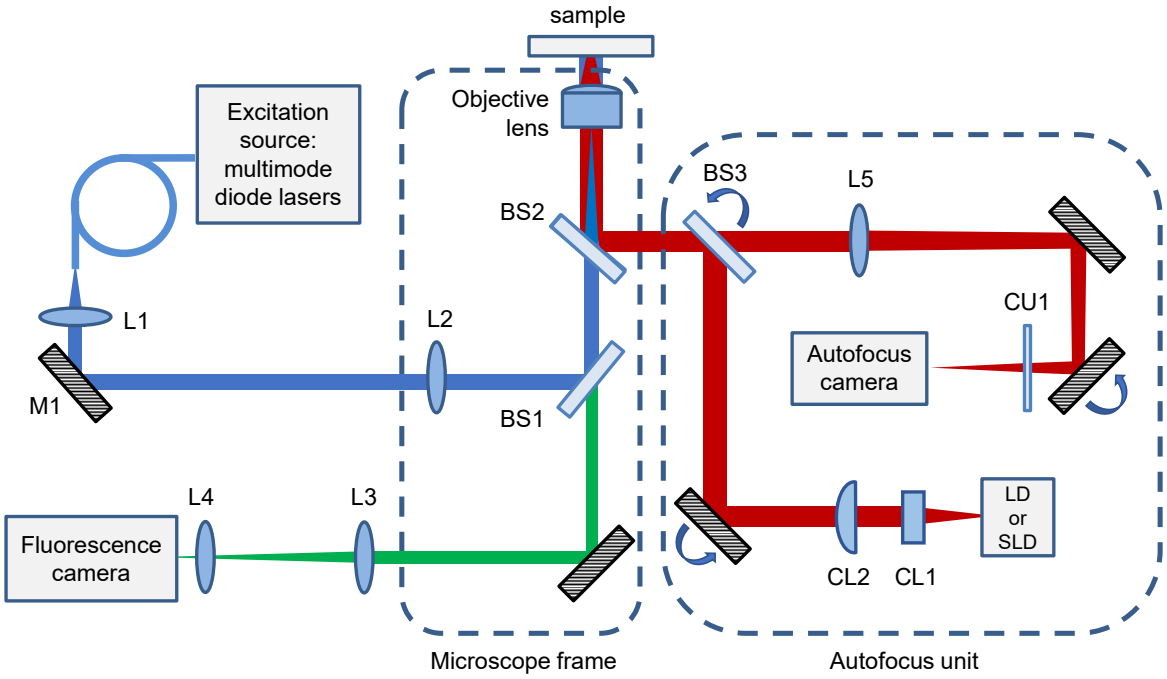

Figure 5.10. Implementation of the cylindrical lens autofocus on the openFrame. An 830 nm laser diode (Ushio HL8337MG), or an 840nm SLD (Superlum SLD-840F50P05S-TOSA9), is coupled into a single mode fibre with a 0.1 NA and the output of the fibre was used as the source for the autofocus. The beam is collimated in by a 6.4 mm focal length cylindrical lens, CL1 (Thorlabs LJ1227L1-B), and by a 20 mm focal length cylindrical lens, CL2 (Thorlabs LJ1960L1-B), which are orientated at 90^{O} to each other to produce an elliptical beam profile. CU1 (Edmund 65-180) is a clean-up long pass filter. The beam is steered using a mirror and a 50:50 beamsplitter, BS1 (Edmund 47-026), which it reflects off, and then is reflected by an 800 nm shortpass filter, BS2 (Edmund 69-220). The elliptical beam is then focused onto the sample by a 100x objective (Olympus UplanSApo 100x 1.40 oil) and reflected at the refractive index change between the coverslip and the sample's media. The reflected signal was then propagated back through the system and was transmitted by the 50:50 beamsplitter, BS1, before being imaged by an auxiliary autofocus camera (FLIR Chameleon3 CM3-U3-31S4M-CS) by a 200mm focal length lens L5 (Thorlabs AC254-200-B-ML). Reproduced from (Lightley et al., 2023)

Figure 5.10 shows the schematic of the experimental implementation of this new approach on an *openFrame*-based microscope. The first cylindrical lens had a focal length of 6.4 mm, and the second (orthogonal) cylindrical lens had a focal length of 20.0 mm – providing an aspect ratio of the beam of 3.125. These two cylindrical lenses collimated an infrared laser beam at 830 nm emerging from a single mode optical fibre with 0.10 NA. Initially a single mode diode laser was used as the autofocus

laser source, but this was later replaced later by superluminescent diode (SLD) at 840 nm. As before, the (elliptical) collimated laser beam was focused onto the coverslip by the microscope objective lens and the reflected laser beam intensity distribution was imaged onto the autofocus camera.

The orthogonally orientated cylindrical lenses create different confocal parameters in the long and short axes of the elliptical beam. Analogously to the slit-based autofocus discussed previously, this serves to increase defocus measurement precision when near focus when using intensity projections formed by summing the autofocus camera pixels in the orientation parallel to the larger autofocus laser beam diameter associated with the shorter confocal parameter. Summing the camera pixels in the orthogonal direction parallel to the smaller autofocus laser beam diameter provides less precise but longer-range operation of the autofocus associated with the longer confocal parameter.

5.5.1 Single shot autofocus

When one of the collimating cylindrical lenses is slightly offset from its focal length relative to the fibre output, the autofocus laser beam will focus at a different axial position in the plane associated with that cylindrical lens compared to the focusing of the beam in the orthogonal plane. By offsetting one of the cylindrical lenses so that it focuses a few microns axially separated from the focus for the orthogonal axis, it is possible to determine which side of focus the sample is positioned in a single acquisition. This is because the peaks of the two orthogonal autofocus metrics (e.g., a measure of the width of the respective intensity projections) are now offset in the autofocus calibration image z-stacks and the sign of the difference between the pair of defocus values returned from the respective look-up tables changes with the sign of defocus.

When implementing the cylindrical lens-based autofocus on the *openFrame* microscope, it was observed that there was an unwanted background signal on the autofocus camera due to a reflection from the microscope objective lens that led to a structured intensity distribution with interference fringes that changed as the objective lens was axially scanned. It was found that the superposition of this unwanted reflection with the reflected autofocus laser beam on the autofocus camera could lead to errors when taking the two orthogonal average projections of the back-reflected beam and calculating the standard deviation of each projection to use with the look up table, particularly if there was any drift in the alignment. It was found empirically that using the FWHM of the Fourier transform power spectrum of the projection, rather than the standard deviation, provided a more robust metric for the autofocus. This metric depends on the spatial

frequency content of the intensity projections and seemed to be less sensitive to perturbations in alignment and variations in intensity.

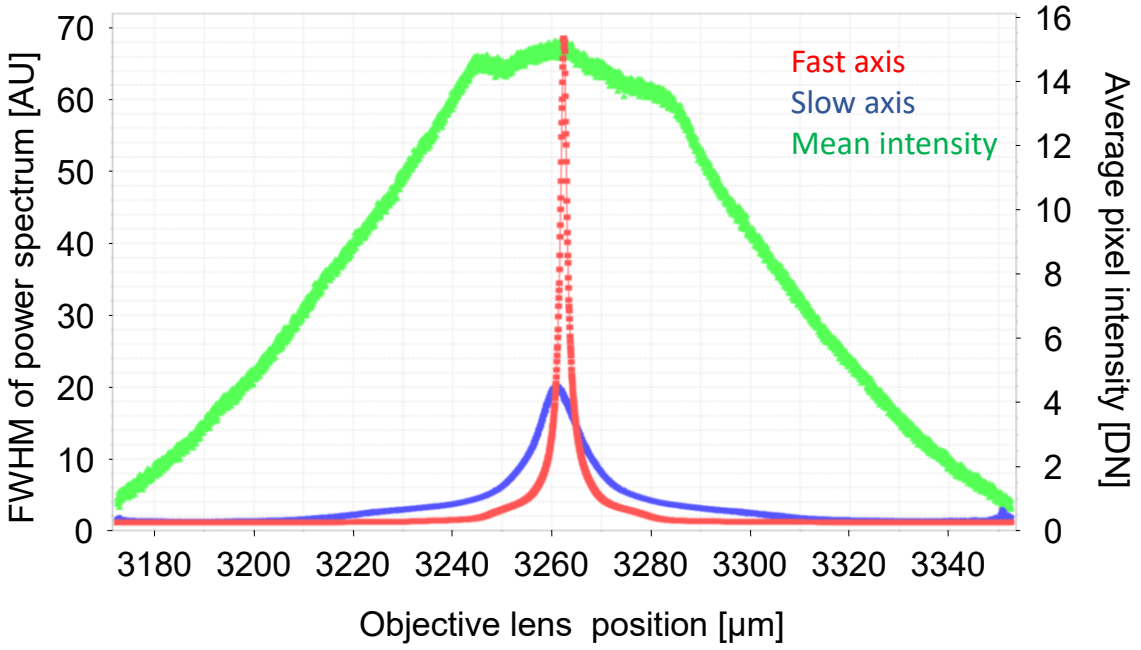

Figure 5.11. FWHM of the Fourier transform power spectrum of the two projections of average intensity along the horizontal and vertical axes of the sensor of the FLIR Chameleon3 CMOS camera. The red and blue peaks represent the autofocus metrics for the short confocal parameter and long confocal parameter respectively. The Green plot shows the average intensity in the image after a background subtraction. As the 20 mm focal length lens has been positioned slightly further away than its focal length from the fibre, it focuses onto the sample 2 microns axially above the blue peak. This enables closed loop single-shot autofocus

Figure 5.11 shows a plot of this Fourier transform power spectrum metric plotted against defocus (objective lens position) for the shorter (red) and longer (blue) confocal parameter for the calibration autofocus camera image z-stack used to build the look-up table, for which autofocus camera images were acquired every 50 nm over a range of ±90 µm translation of the objective lens. The offset collimation of the two orthogonal cylindrical lenses causes the peaks to occur at separate defocus positions, which removes the ambiguity about the sign of defocus. Also shown (green) is the average intensity of the whole autofocus camera image, after subtracting a background image recorded at a sufficiently far enough axial position from focus such that the autofocus signal was no longer detectable on the camera.

If the sample is close enough to focus (within ~37.5 µm) such that the reflected autofocus beam along the faster expanding axis is still contained within the camera sensor dimensions, the red curve (associated with the shorter confocal parameter) of this defocus metric starts to increase in value

and may be used to implement a single-shot autofocus, which can operate in either single-shot mode or in closed loop if continuous correction is required. Further away from focus, this (red) curve is flat, and the orthogonal defocus (blue curve corresponding to longer confocal parameter) can be applied for a lower resolution correction of defocus that will bring the microscope back to the regime where the higher precision focus correction can be used. This coarser autofocus using just the autofocus camera intensity projection corresponding to the longer confocal parameter is not able to determine the sign of defocus from a single autofocus camera image, and so two images are acquired with the objective lens separated by 10 µm (as discussed in section 5.4), followed by a 3rd autofocus camera image acquisition to apply the higher precision defocus correction.

The autofocus control software, written in Java for *µManager*, first determines whether the high precision autofocus metric (red curve in Figure 5.11) is above a threshold value to enable the single-shot autofocus to be used. If this is the case, the objective lens is translated to correct the defocus. If not, then a second autofocus camera image is acquired at an objective lens position separated by 10 µm from the first. These two images are used to bring the microscope close to focus, after which the higher precision single-shot autofocus is automatically applied.

The performance of this cylindrical lens-based autofocus system on the *openFrame* microscope was quantified by automatically imaging 100 nm fluorescent beads (Tetraspeck, T7279) plated in a glass-bottomed 96 well plate pre-coated with poly-L-lysine. The image acquisition was performed in a snake-like pattern moving row by row with microscope fluorescence image z-stacks of one FOV being acquired in each well over a range of ±4 µm with axial sampling of 100 nm. At each new well, the change in defocus was less than 37.5 µm such that the autofocus was applied in the single-shot, high precision mode to axially translate the objective lens and return the microscope to focus and then the microscope fluorescence image z-stacks were acquired. If the autofocus system performed perfectly, then the central image in the fluorescence image z-stack should be the in-focus image.

To quantify the performance, the z-stack image data was analysed using PSFj (Theer, Mongis & Knop, 2014), previously published software that analyses all the individual 100 nm bead images in the FOV and determines the slice in the z stack for which each specific bead is in focus. For each FOV, a histogram of the values of the offset of the bead in-focus plane relative to the central plane in the z-stack (i.e., the predicted in-focus plane) can be generated and quantified by the mean and standard deviation.

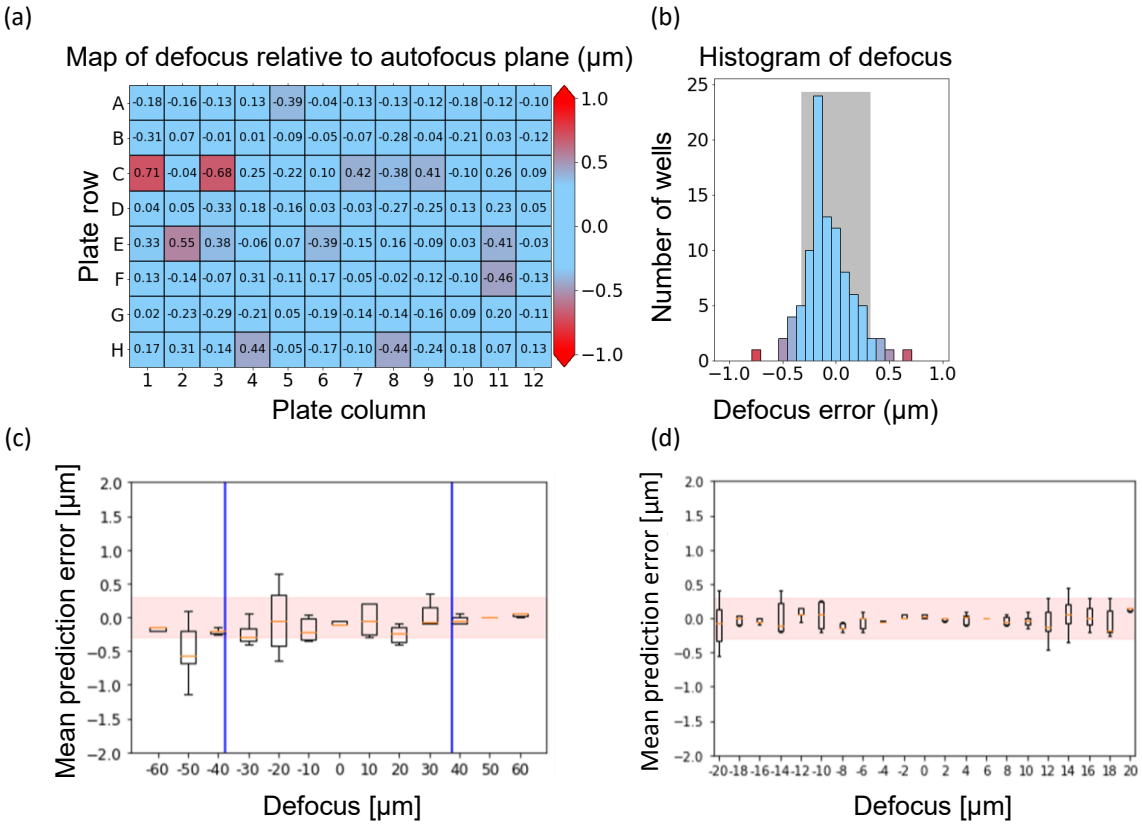

Figure 5.12. (a) shows a 96 well plate arrayed with 100 nm Tetraspeck beads that was scanned using autofocus with a z-stack acquired in each well. PSFJ was used to determine the in-focus axial plane for each bead and the mean offset from the centre image provided the error in the defocus for each well - shown with associated heatmap of defocus in microns. (b) shows a histogram of errors in defocus for the 96-wellplate. The grey region shows the depth of field. Figures (c, d), system was refocussed 10 times from range of known defocus offsets for the longer (c) and shorter (d) range autofocus prediction. Errors in predicted defocus are plotted (boxplots with mean error, interquartile range and outliers). Red highlighted region shows depth of field of microscope objective lens. The depth of field for this fluorescence microscope with 100x, 1.4 NA objective lens was ~0.65 µm for an emission wavelength of 680 nm. Reproduced from (Lightley et al., 2023)

Figure 5.12(a) presents the performance of the autofocus in each well as a colour map and is also displaying the mean error across each FOV of the error (i.e., the offset between the autofocus-predicted central plane of the z-stack and the actual in-focus plane as determined by PSFj for each bead). The colour map indicates the variation of this mean error from 0 µm (cyan) up to ±1 µm (red). Within the depth of field, the colour map is solid cyan and then varies on a continuous scale from cyan to red at ±1 µm. The depth of field for this fluorescence microscope with 100x, 1.4 NA objective lens was ~0.65 µm for an emission wavelength of 680 nm. The Figure 5.12(b) presents a histogram of these mean errors/FOV, for which the standard deviation for the 96-well plate is 230 nm and mean of the absolute prediction errors is 179 nm.

To further quantify the performance of the cylindrical lens-based autofocus approach, the accuracy of defocus correction from predetermined defocus values was measured. This was done using the shorter range (smaller confocal parameter) intensity projections, with initial defocus values ranging between ±20 µm of defocus in axial steps of 2 µm, and with the longer range (larger confocal parameter) intensity projections with initial defocus values ranging between ±60 µm in 10 µm steps.

From each pre-set defocus position, the autofocus was applied 10 times and the objective lens was moved to the predicted in-focus position for each of the 10 repeats. The actual in-focus position was determined by acquiring an autofocus camera z-stack and interpolating between frames to find the plane where the size of the focused laser beam was minimised in the fast (i.e., short confocal parameter) direction.

The differences (errors) between the known defocus offset and the autofocus predicted defocus correction were calculated for each repeat for each initial defocus offset value. Figure 5.12(c, d) show boxplots showing the mean error (orange line), interquartile range (boxplot) and any outliers for the longer range and shorter range autofocus predictions respectively. As the initial defocus value was decreased, the error in defocus prediction decreases as expected because the gradients of the autofocus metric curves (Figure 5.11) increase towards the peak.

5.5.2 Closed-loop autofocus

Within the range of the single-shot autofocus capability, it was possible to enable continuous closed-loop focus correction, which is desirable for time-lapse microscopy experiments or when acquiring long image data acquisitions, such as during STORM experiments. If the closed-loop autofocus can be implemented independently of the main microscopy imaging, then it will not increase the image data acquisition time. To illustrate the closed-loop autofocus functionality, Figure 5.13 presents results from 50,000 frame STORM image data acquisitions (over ~30 minutes at 30 frames/s) that was performed with and without continuous defocus correction to compensate for drift on the openframe microscope.

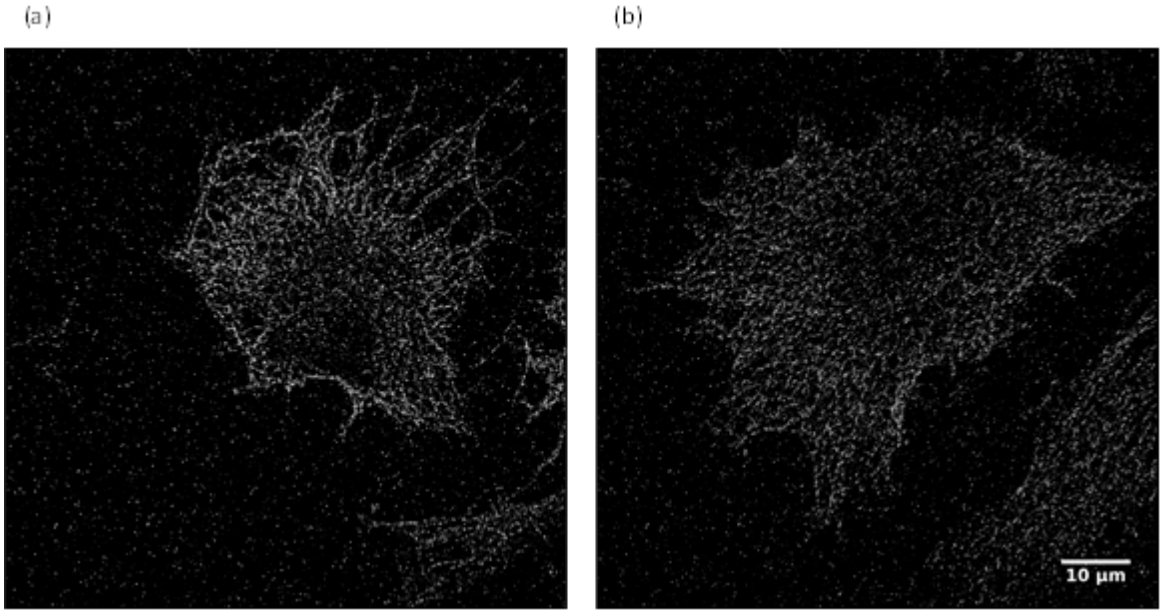

Figure 5.13. STORM reconstruction of thyroid cells with the tubulin labelled with ifluor647 acquired on the openframe using a CellCam kicker camera. (a) Continuous closed-loop autofocus correction was used (b) Continuous closed loop autofocus correction was not used

The sample was fixed thyroid cells in which tubulin was labelled with ifluor647 and the easySTORM images were reconstructed using a parallelised implementation of ThunderSTORM running on Imperial's HPC cluster (Munro et al., 2019). Figure 5.13(a) shows the super-resolved image reconstruction of the easySTORM data acquired when using the continuous closed loop autofocus whereas Figure 5.13(b) shows the reconstruction from the easySTORM acquisition starting from the microscope in focus but without the closed loop autofocus enabled. The tubulin filaments are more clearly discernible for the easySTORM acquisition using the closed loop autofocus.

The objective lens position was recorded before and after the STORM image data acquisition to quantify the net axial drift. Using the continuous closed loop autofocus, the objective lens stage position changed from 3132.3 µm to 3133.0 µm after the 50,000 frames. This axial change of 700 nm exceeds the ±300 nm DOF for this system when using a 635nm excitation source and so the microscope would have drifted out of focus within the STORM image data acquisition without the correction of defocus.

For the case where the autofocus was not used during the acquisition, the objective lens stage started in focus at 3133.3 µm. The autofocus was then applied after this uncorrected STORM image data acquisition and the in-focus objective stage position was determined to be 3132.9 µm. Thus,

the microscope exhibited a system drift of ~400 nm in the objective lens position during this STORM image data acquisition.

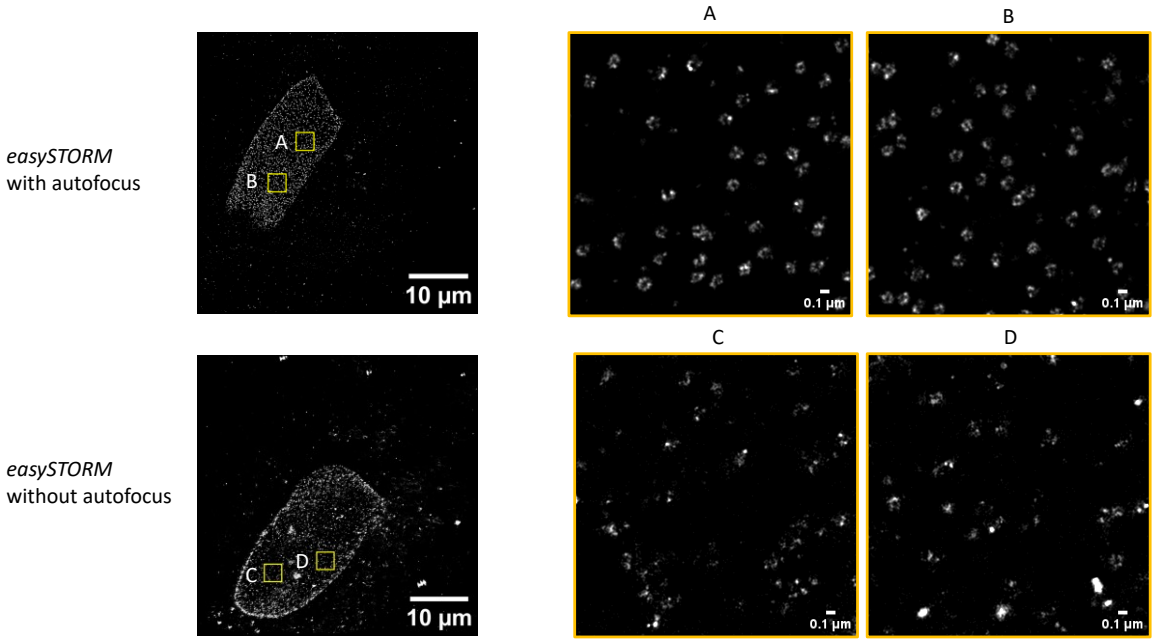

Figure 5.14. *easySTORM* reconstructions of fixed U-2OS-CRISPR-NUP96-SNAP-iFluor647 cells from 80000 frames at 30 ms exposure with HILO illumination acquired on the *openFrame* using the CellCam Kikker camera. Top row: frames were acquired with continuous autofocus correction. Bottom row: 80000 frames were acquired without autofocus correction. (A, B) show zoomed regions indicated in easySTORM reconstruction with continuous autofocus correction. (C, D) show zoomed regions indicated in easySTORM reconstruction without autofocus correction. The sub-units within the NPC are resolved when using the autofocus correction but are not without using the autofocus. Reconstructions performed using Picasso (Schnitzbauer et al., 2017).

To further demonstrate the closed-loop functionality, easySTORM images of U-2OS-CRISPR-NUP96-SNAP-iFluor647 cells were acquired with and without the continuous closed-loop autofocus, see Figure 5.14. The top row of figures in Figure 5.14 show the easySTORM reconstructions, each from 80,000 frames acquired with 30ms exposure using the Cellcam Kikker and implemented on the *openFrame.* The bottom row shows an easySTORM reconstruction of U-2OS-CRISPR-NUP96-SNAP-iFluor647 cells from the same sample acquired without continuous autofocus correction. Figure 5.14 (A-D) show the zoomed regions indicated in the full FOV easySTORM reconstructions. 100 nm Tetraspeck fluorescent beads (T7279) were used as fiducial markers to correct for lateral drift for both acquisitions. As can be seen in Figure 5.14 (A, B), the individual sub-units of the NPCs are distinguishable, whereas they are not distinguishable in (C, D). Therefore, the achieved resolution when using the continuous, closed loop autofocus correction exceeded 42 nm.

5.5.3 Incoherent light sources

One challenge in developing this autofocus system was the presence of back reflections from optical components in the system other than the sample coverslip. When the autofocus laser beam was provided by a collimated beam from a single mode laser diode, the high spatial and temporal coherence of the laser beam resulted in interference between the desired back reflected light from the sample coverslip and other spurious back reflections. The resulting interference fringes would change with defocus (due to changing optical path difference) and could not be addressed by simple background intensity subtraction because of the coherent addition of the signal and background light.

The main background signal occurred from one of the optical elements within the objective lens and so this back reflected beam was defocussed with respect to the autofocus beam back reflected from the coverslip. It was possible to adjust the position of the cylindrical lens that was slightly offset from collimation to maximise the spread of this unwanted reflected light while retaining the autofocus function to decrease the unwanted fringe modulation depth and, as discussed in section 5.5.1, it was found that using a defocus metric based on the Fourier transform power spectrum of the intensity projections was less compromised than using the standard deviation. However, it would be better to eliminate these unwanted interference fringes by using an autofocus light source of lower spatial and temporal coherence. I tried using an LED, but the divergence of the focussed LED radiation was too fast with defocus, and this limited the range of the autofocus to a few microns. Instead, I tried a super-luminescent diode (SLD) that provides low temporal coherence but high spatial coherence. This could directly replace the single mode diode laser and still couple efficiently into the single mode optical fibre.

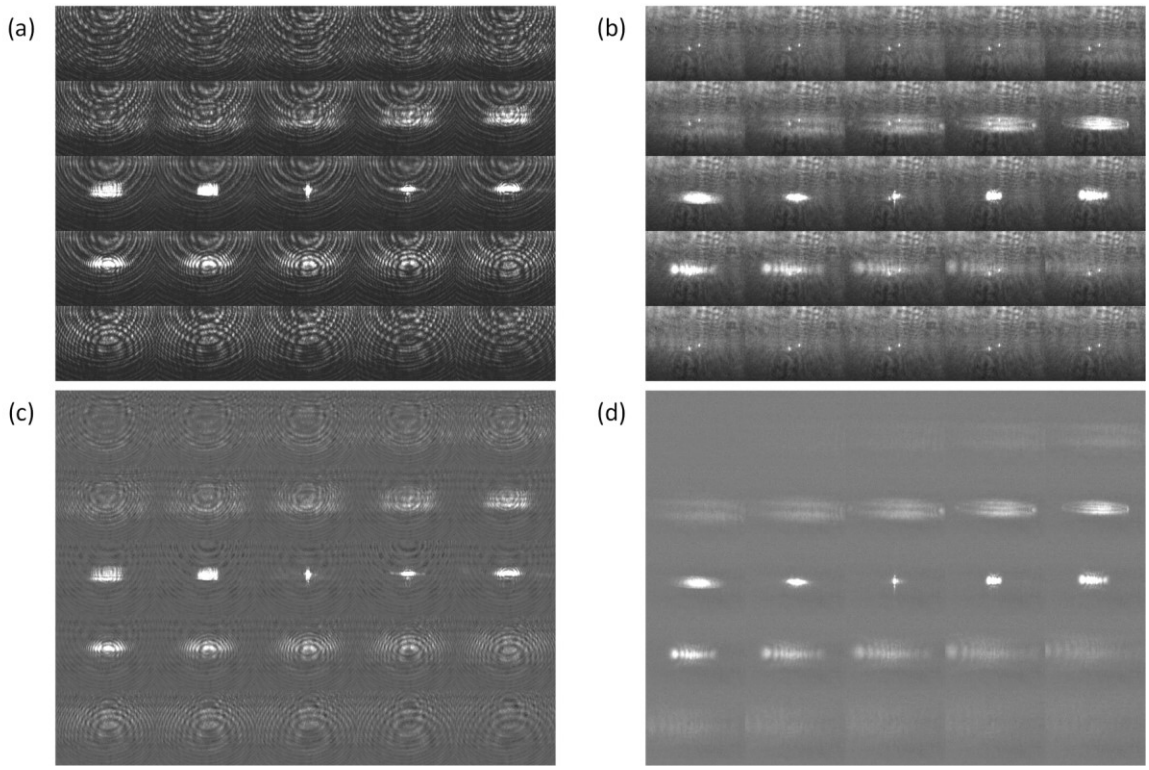

Figure 5.15. (a) and (b) show montages of images of an axial fly-through of focus of the cylindrical lens autofocus when using a laser diode and SLD source respectively. The montages show images every 5 µm over a range of ±60 µm. The top left image in each montage is acquired at -60 µm. The axial defocus increases from left to right along the columns and from top to bottom. The bottom right image in each montage is at +60 µm. Figures (c) and (d) show the same axial z-stacks but with a background subtraction for the laser diode and SLD sources. As can be seen in figures (a) and (c), the background subtraction couldn't remove all structured features from the background as the source is coherent. This meant the interference pattern changed with focus. This interference structures prevented the autofocus from working when using the Fourier transform metric. Whereas in figures (b) and (d), it can be seen that the background can be subtracted as it is a constant background from an incoherent source. This meant that there is a better signal, for the autofocus metric.

Using two SLD, either the Superlum sld-840f50p05s-tosa9 SLD with 4.5 µm coherence length, or the Superlum S-930 with 7.3 µm coherence length, I found that the interference between back reflections from the coverslip and other optical components was eliminated as the difference in path length was greater than the coherence length. This meant that the unwanted background did not vary with defocus and so a background autofocus camera image could be recorded sufficiently far from focus, and this could be subtracted from autofocus camera images before calculating the defocus metric. Figure 5.15(a, b) show representative images from the calibration autofocus camera image z-stacks acquired using (a) the single mode diode laser and (b) the SLD. The reduction in interference fringes is evident. Any fringes still present result from interference effects at the microscope sample coverslip, and these do not change with defocus so can be removed with the background subtraction. Figure 5.15(c, d) show the same autofocus camera image data after

background subtraction. Thus, while the single mode laser diode can provide a practical autofocus, the performance is improved by its direct replacement by an SLD at a similar wavelength.

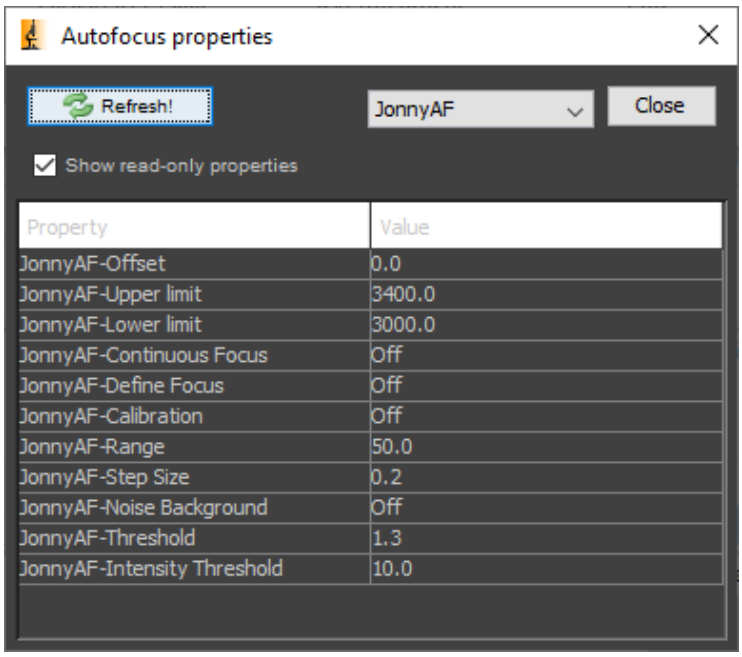

Figure 5.16. User interface of *µManager* 2.0 autofocus plug-in.

5.6 Autofocus control software

The software to control all the autofocus implementations reported in this thesis were written as a plugin for *µManager* 2.0, for which the interface of the cylindrical lens-based autofocus software is shown in Figure 5.16. The plugin was written in java using Netbeans as the IDE and controls the hardware to move the stage or objective into the correct defined focus plane. This *µManager* plug-in enables the user to define the desired in-focus plane and to activate or disable continuous closed-loop autofocus correction. Limits can be set to prevent the axial translation of the objective lens or sample beyond pre-determined safe positions if the autofocus system were to fail. The calibration controls can be used to create a look-up table to convert the measured autofocus metric value to defocus offset distance. This is carried out by the user selecting run from the drop-down control options within the plugin interface. A background image can be stored to be subtracted from the autofocus camera image if required. This provides a means to remove unwanted signals, e.g., from back reflections from components in the optical system. Threshold autofocus metric values can be set to define the regions in which the closed loop autofocus should be used and regions where the multistep autofocus correction should be used.

The plugin communicates via a socket connection to a Python script running simultaneously in an Anaconda environment. The socket is created in the Python script. Once connected, the Python script waits to receive a call for a new focus correction from the Java plugin. Once received, the Python scripts acquires an image on the autofocus camera (FLIR chameleon) and calculates the width of the power spectrums measured for the mean intensity projections of the sensor. The values are then sent via the socket to the *μManager* 2.0 to compare with the pre-recorded look-up table to determine the current defocus.

The *μManager* plugin is called openAF and is available at (https://github.com/ImperialCollegeLondon/openAF).

5.7 Conclusion

This chapter has presented the iterative work developing a hardware-based autofocus, beginning with the knife-edge-based approach using a centroiding metric, then progressing to the rectangular slit masked beam technique before finally reaching the design using orthogonally orientated cylindrical lenses. The cylindrical lens autofocus can operate in single-shot operation over a range of ±37.5μm and as a 2-step approach over a range of ±68μm. The accuracy of the autofocus was <230 nm. The autofocus was implemented on the openframe and used to acquire automated easySTORM acquisitions of FRTL5 Rat Follicular thyroid cells and fixed U-2OS-CRISPR-NUP96-SNAP-iFluor647 cells.

6. Neural network-enabled optical autofocus module

In the previous chapter, the development of a non-neural network-based autofocus has been discussed. This has the disadvantage that a new calibration measurement needs to be acquired every day and for long acquisitions there may be variation in lab conditions that could change the calibration values during the data acquisition, thereby introducing errors. This motivated us to develop a robust neural network-based autofocus that would not require daily calibration and would be resilient to changes in lab conditions. The work developing such a network is discussed in this chapter.

6.1 Introduction to neural networks

In recent years, deep learning neural networks (DNNs) have been applied to both the image acquisition, processing, and analysis of SMLM microscopy (Liu et al., 2022). A neural network (NN) is composed of neurons. These neurons are operators that receive multiple inputs to produce an output (Liu et al., 2022). A layer is formed by placing multiple neurons in parallel. The outputs of these neurons from one layer, form the inputs for the next layer of neurons. A NN is formed from multiple layers of neurons. A NN has associated parameters such as the number of layers, the number of neurons in each layer and the weights of the neurons. The weight of a connection between two neurons controls how much influence the input has on the output signal from that neuron. These parameters are adjusted and optimised through learning on a large amount of training data.

Deep learning (DL) is a subset of machine learning (ML). The motivation for DL is from the neuronal information processing structure of the human brain (Alzubaidi et al., 2021). DL can be further classified as being either supervised, semi-supervised or un-supervised (Alzubaidi et al., 2021; LeCun, Bengio & Hinton, 2015).

In supervised DL, the data involved has been labelled and is the most common form of DL (LeCun, Bengio & Hinton, 2015). This type of DL is very applicable to classification problems where there are a set of images which need to be classified into one of a discrete number of outputs each with a specific label. In supervised DL, the potential outputs are already known, and the model needs to iterate over the training datasets until it converges to the minimum prediction error (Liu et al.,

2022). Supervised learning is generally very accurate but requires knowledge of the outputs in advance to label the datasets. This can limit the applicability of supervised DL to certain problems.

Semi-supervised DL involves semi-labelled datasets. The advantage of this approach is that you do not require as large a labelled dataset for the training process but can lead to more incorrect decisions from the model (Alzubaidi et al., 2021).

Unsupervised DL does not need the training datasets to be labelled in advance. Here the model automatically finds and determines the significant features required to classify or identify relationships in the training data (Alzubaidi et al., 2021). This means that unsupervised learning is particularly applicable to problems like clustering analysis (Liu et al., 2022; Alzubaidi et al., 2021). A disadvantage to unsupervised DL is that it is generally computationally more demanding and complex.

There are multiple different types of network architectures for DL. Some of the most commonly used architecture types include fully connected neural networks (FCNNs), recursive neural networks (RvNNs), recurrent neural networks (RNNs), convolutional neural networks (CNNs) and generative adversarial networks (GANs) (Alzubaidi et al., 2021).

A CNN architecture is used for the work presented in this chapter. CNNs are constructed from multiple layers to form a deep network. The different types of layers involved in CNN's include convolutional layers, pooling layers, activation layers and fully connected dense layers.

Convolutional layers are the most significant layer involved in CNNs. Convolutional layers are composed from many different convolutional kernel filters and receive multi-dimensional matrices as the input. These kernels are convolved with the input image to produce the output feature maps (Alzubaidi et al., 2021). By adjusting the pixel sizes of the kernels, the amount of pixel padding added to the input image and the stride step used for sliding the kernel across the input image, the dimensionality of the output will be changed compared to the input. Some of the advantages of convolutional layers are that they have sparser connectivity than FCNN and have weight sharing. In FCNNs, every neuron is connected to all the neurons in the previous and following layers. Whereas, in CNNs there are only a few connections available between adjacent layers (Alzubaidi et al., 2021). This means that the number of connections is much smaller, and the network will have a much smaller memory footprint than a FCNN. The computation cost is reduced as CNNs make use of dot products rather than more complex matrix multiplication involved in FCNN.

Pooling layers perform sub-sampling of the output feature maps from convolutional layers. These pooling layers can reduce the size of the feature maps. Some common pooling layers include max-pooling, min pooling, global averaging pooling and average pooling.

The activation layer decides whether a neuron should fire by summing up all the weighted inputs to a neuron. Non-linear activation layers are always used after any learnable layer (layers with weights). There are many different activation layers but some of the most common are the Rectified Linear activation Unit (ReLU), Sigmoid and Tanh (Alzubaidi et al., 2021).

A fully connected layer can be positioned at the end of CNN to act as a classifier in some networks, in which every neuron in the final layer would be connected to all the neurons in the previous layer.

A detailed description of the roles and applications of these layers is presented by Alzubaidi et al. (Alzubaidi et al., 2021). They also review and compare many of the most popular CNN architectures. The authors also describe backpropagation, CNN regularization and optimiser selection. For an overall introduction to DL see the review paper by LeCun et al. (LeCun, Bengio & Hinton, 2015) and for a review of published deep learning applications for SMLM see Liu et al. (Liu et al., 2022).

6.2 Previous autofocus neural networks

There are several published neural network-based autofocuses that have been developed for microscopy. This section will introduce a few of them that are considered to be the most relevant to the work presented in this chapter.

Luo et al. developed an offline single-shot autofocusing technique that created a virtual in-focus image from a single out of focus acquired image using a GAN architecture (Luo et al., 2021). The network is trained with axially defocused z-stacks of the sample paired with the in-focus image as a pair. The GAN generates a synthetic in focus image for the out of focus inputs. This technique is arguably “single shot”, but it isn’t truly correcting the focus but trying to remove aberrations from the defocused image. Therefore, it can be difficult to be confident on how accurate the synthetically reconstructed images are compared to the ground truth in focus image. However, this technique does not require any additional hardware components and is faster than conventional software based autofocus approaches.

Several autofocus approaches have been applied to whole-slide imaging previously. Some of these techniques make use of colour multiplexing to encode defocus for brightfield illumination by trans-

illuminating the sample with red and green LEDs at different off axis angles (Jiang et al., 2019). This results in two images being formed on the imaging camera. When at focus these images overlap, but when defocus is introduced, there is a translational shift between these images. This shift can be used to measure the defocus. This is normally quantified by either using a cross-correlation calculation between the two channels recorded on the colour camera, which peaks at focus or to maximise the mutual information (joint entropy) between the channels (Jiang et al., 2019). Xin et al. used the colour multiplexing approach to train a neural network (Xin et al., 2021). Here once again they illuminated the sample with partially coherent illumination from off axis red and green LEDs. They then acquired an axial through-focus stack. They also acquired an incoherent brightfield illumination axial stack of the same FOV. They used the Brenner gradient to determine the ground truth for the "in-focus" plane and used that to label the in-focus image in the coherently illuminated axial stack. Since the axial step size between the images in the stack is known, the other images in the stack can be labelled accordingly with their respective defocus labels. These labelled images are used as the input to the network. The architecture the authors used was the lightweight version of the MobileNetV3-small architecture CNN (Howard et al., 2019).

Another whole-slide imaging system (Rai Dastidar & Ethirajan, 2020) uses an autofocus trained using a MobileNetV2 CNN architecture (Sandler et al., 2018). This approach required the acquisition of two axially separated images. A pixelwise difference image was calculated from these images and used as the input for the network to predict the current defocus. The images were acquired at a separation of 2µm using a 20x 0.75NA objective. Unlike the previous approaches, Dastidar and Ethirajan used white light trans-illumination instead of colour multiplexing and the difference image, calculated from the subtraction of one of the axially separated images from the other, was chosen as the input for the CNN to remove some of the coarse colour information in the image which helped prevent overfitting (Rai Dastidar & Ethirajan, 2020).

The above autofocus techniques have been applied to trans-illumination widefield imaging, but neural-network-based autofocuses have also been applied to other imaging modalities. Li et al. developed a CNN for use in light-sheet microscopes (Li et al., 2021). Here, the authors used a network to classify the defocus of an image into 13 output defocus bins with widths of ±3µm. These bins were centred on defocus values of -36 µm to +36 µm in 6 µm step intervals. Another autofocus presented by Ding et al. has been applied to quantitative phase imaging (Ding et al., 2021).

Another autofocusing technique, by Pinkard et al., presented a single-shot NN-based autofocus that uses one or a few off-axis illumination LED sources (Pinkard et al., 2019). The premise of their autofocus is that a neural network can be trained to predict the defocus from a single image when

illuminated by spatially coherent illumination. Their approach can be implemented on standard commercial microscope frames. The authors showed that they could apply their autofocus system to general microscopes that utilise either incoherent or coherent illumination. The authors argued that even when the sample is out of focus, and when illuminated with coherent illumination, the system can still yield an image with sharp enough features such that an appropriate NN can be trained such that it can learn a function that can map these features to the current defocus position. They argued that there should be sufficient information for the network to predict the current defocus regardless of the structural features themselves within the sample. This means that the network's prediction ability could be robust to different samples. The authors chose to use a fully connected Fourier neural network (FCFNN) for the architecture.

To train their network, (Pinkard et al., 2019) acquired axial z-stacks over a range of -30 µm to +30 µm through focus, in 1 µm step intervals, on a Zeiss Axio observer microscope using a 20x 0.5NA objective. At each lateral position in their sample, they collected 2 distinct axial, through-focus stacks, illuminated with either spatially coherent (a single LED) or a spatially incoherent (multiple simultaneous LEDs) illumination. The authors used the incoherent illumination stack to provide the ground truth in focus position because the coherence length is far shorter and hence the image will defocus faster than the coherently illuminated stack. The sharpness of the images, in the incoherently illuminated stacks, were quantified by summing the high frequency content of its radially averaged power spectrum. This sharpness metric is maximised at focus and used to provide the ground truth focal position in the axial stack. Once the ground truth image in the coherently illuminated stack is determined, the other images in the stack can be labelled with their respective defocus value accordingly and every image is used as an input for the training of the network.

A single image is used as the input and a Fourier transform is performed on the image before the magnitude of the complex valued central pixels of the transform are reshaped into a single vector which is the input to the FCFNN. The training of the network was done using 440 focal stacks for a period of 1.5 hours on a desktop CPU with a Nvidia GeForce GTX 1080 GPU. After training the FCFNN could predict defocus from a single acquired image. The root mean squared error (RMSE) of the network after training, when applied to validation data of the same sample type was within the 5µm thickness of the sample. However, the performance of the network was significantly worse when applied to unseen data of a different cell type. The performance was regained by including a hybrid dataset of the 2 cell types into the training datasets. This highlights the importance of increasing the size of training datasets to better generalise to unseen data and help prevent overfitting of the model.

Pinkard et al.'s FCFNN provided evidence that NNs could be used to predict defocus from a single image. However, their approach is not applicable to high throughput SMLM of thicker tissues with high NA objectives, as it requires to use the imaging camera to acquire images for the autofocus. However, since there are localisations at different planes within the sample, when using epi-fluorescent or HILO illumination, there would still be high frequency, in focus, localisations with axial drift. It also requires the modulation of the excitation laser, and additional off-axis LEDs, on and off, to acquire the autofocus image. Therefore, by having an auxiliary separate imaging camera for the autofocus, the acquisition doesn't need to be interleaved and the throughput is increased.

6.3 MobileNetV2 Autofocus

In this chapter, the work developing a convolutional neural network (CNN) based hardware autofocus will be presented. The CNN autofocus was developed to enable automated high content analysis, (HCA) capabilities with several different imaging modalities but with a particular implementation on automated single molecule localisation microscopy (SMLM). The CNN was developed to have a small memory footprint so that it has the potential to be implemented on low memory devices in the future. The work in this chapter is largely presented in the published article (Lightley et al., 2022).

6.3.1 Network architecture

The CNN uses the MobileNetV2 (Sandler et al., 2018) architecture as the base model, which introduced some new layers to those that were previously implemented in the MobileNetV1 architecture (Howard et al., 2017). In the V1 architecture, the concept of depthwise separable convolutions were introduced. These depthwise separable convolutions split the function of a standard convolutional layer into two distinct layers. The first layer is referred to as a depthwise convolution and, for each input channel, it applies a single convolutional filter. This lightweight filter results in spatial filtering. The second layer is a pointwise convolutional layer that builds new features through linear combination of the input channels.

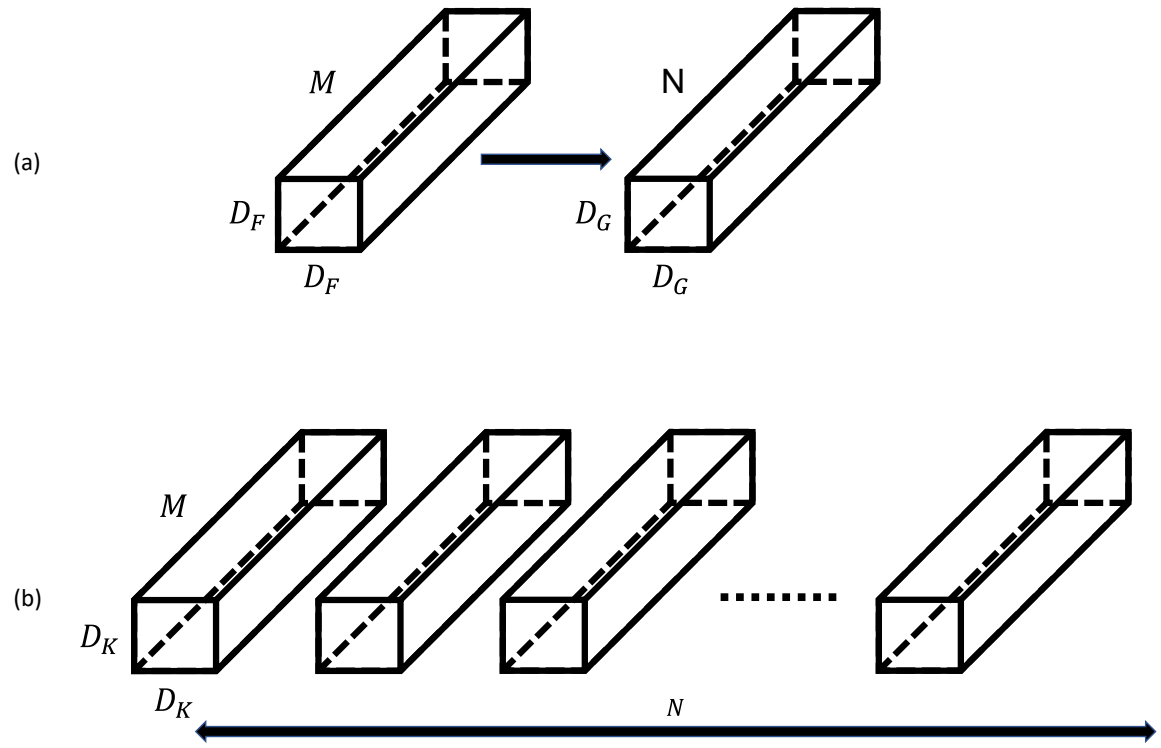

Figure 6.1. Figure showing the function of a standard convolutional layer: (a) shows an input feature map with shape $F = D_F \times D_F \times M$ into a convolutional layer to produce an output feature map with shape $G = D_G \times D_G \times N$; (b) shows the N standard convolutional kernel filters with shape $D_K \times D_K \times M$

In a standard convolutional layer, the input feature map, $F = D_F \times D_F \times M$, is converted into an output feature map, G, of shape, $G = D_G \times D_G \times N$, where D_F is the height and width of a square input feature map, M is the number of input channels, D_G is the output feature map's height and width and N is the number of channels for the output feature map. As shown in Figure 6.1(b), a set of convolutional kernel filters are scanned across the feature map. The inner product of the kernel with the overlapping section of the feature map is calculated to produce a single value before the kernel moves to the next position of the feature map. This is repeated for the set of N filters.

The structure of the depthwise separable convolution kernel filters are shown in Figure 6.2(b, c). Here, the convolution filters are split into two steps. Figure 6.2(b) shows the depthwise convolutional filters. These depthwise convolutions apply a single filter to each input channel. Then the pointwise convolutions shown in Figure 6.2(c) are 1x1 filters that perform linear combination of the output channels from the depthwise layer. The pointwise convolutions can build new features. The whole procedure of a depthwise convolutional layer is shown in Figure 6.3.

The depthwise convolutional layer can be a drop-in direct replacement for a standard convolutional layer. The advantage of using a depthwise convolutional layer is that they have a reduced

computational cost when compared to a standard convolutional layer. The standard layer computational cost is given by Equation 6.1.

$$Cost = D_K \times D_K \times M \times N \times D_F \times D_F \qquad \text{Equation 6.1}$$

Whereas the computational cost of the depthwise separable convolutional layer is given by Equation 6.2.

$$Cost = (D_K \times D_K \times M \times D_F \times D_F) + (M \times N \times D_F \times D_F) \qquad \text{Equation 6.2}$$

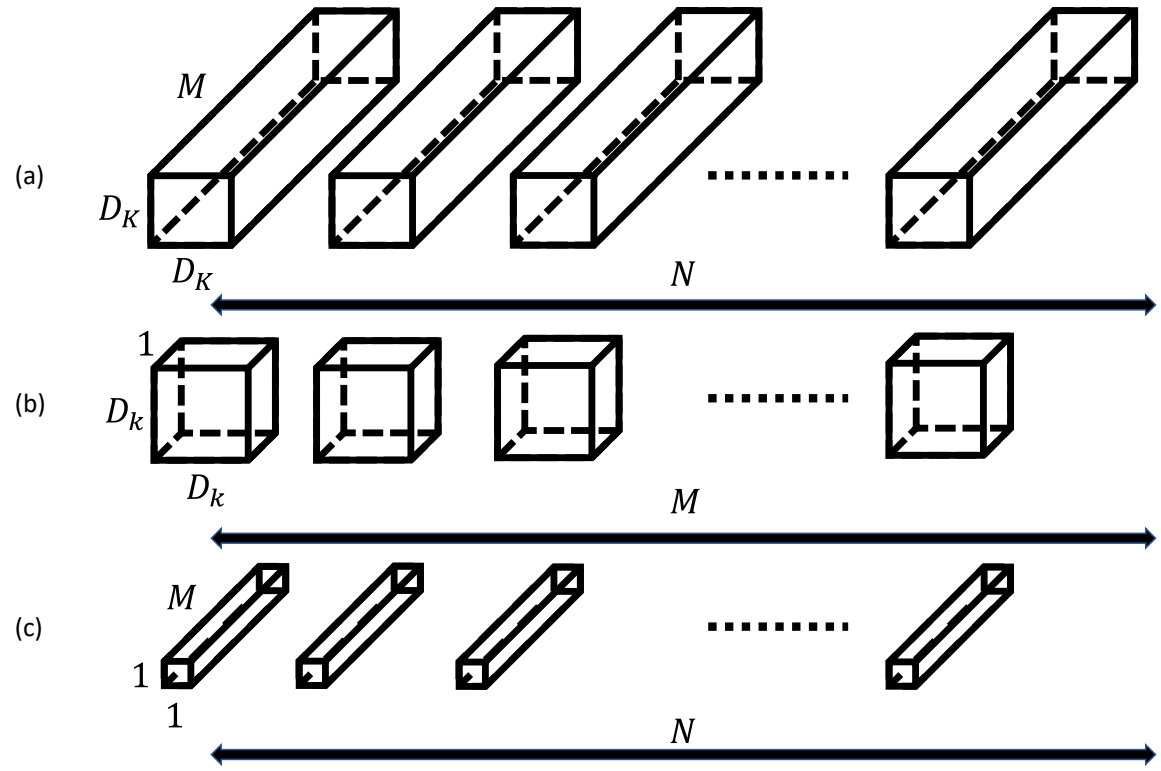

Figure 6.2. A figure demonstrating how a standard convolutional layer can be replaced by a depthwise convolutional filters followed by pointwise convolutional figures. (a) shows a set of standard convolutional filters (b) shows a set of depthwise convolutional layers and (c) shows a set of pointwise convolutional layers

The first term in the above Equation 6.2 is the cost of the depthwise convolution step and the second term is the cost of the pointwise convolution. If we take the ratio of the computational cost of the depthwise separable layer compared to a standard convolutional layer, it is possible to see the computational saving when using the drop-in replacement layer.

$$Ratio = \frac{(D_K \times D_K \times M \times D_F \times D_F) + (M \times N \times D_F \times D_F)}{D_K \times D_K \times M \times N \times D_F \times D_F} \qquad \text{Equation 6.3}$$

$$Ratio = \frac{1}{N} + \frac{1}{{D_K}^2} \approx \frac{1}{{D_K}^2} \qquad \text{Equation 6.4}$$

In most cases N will be much greater than ${D_K}^2$, so the ratio approximates to only $\frac{1}{{D_K}^2}$. So, for example a 3x3 kernel is used the computational saving will by 9 times. This is advantageous to the autofocus application presented in this section as it reduces the computational cost of the network, potentially enabling it to be implemented on lower memory devices.

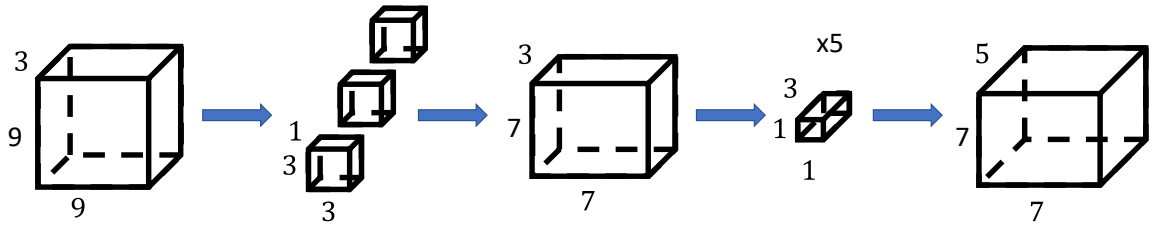

Figure 6.3. Diagram showing the function of the 2 step depthwise convolutional layer on an example 9x9x3 input feature map. The 3x3x1 depthwise kernel filters are used to produce an intermediate feature map of shape 7x7x3. The pointwise convolutions, with shape 1x1x3, are then used on the intermediate feature maps to produce the final output feature map. 5 pointwise filters are used to achieve 5 output channels. The output is the same as would be achieved with a standard convolutional layer with 5 kernel filters, each with a shape of 3x3x3, using a stride of 1 and zero padding

The MobileNetV2 architecture improves on the MobileNetV1 structure discussed so far by introducing the concepts of inverted residual and linear bottleneck layers (Sandler et al., 2018). The inverted residual bottleneck layers are designed to limit the number of feature maps included in the network. This is achieved by having fewer output neurons than inputs.

The input to an inverted residual layer blocks is a tensor with low dimensionality. The layer block is composed of 3 separate layers. The first of these layers is a pointwise convolution. This layer expands the feature map to a high dimensional space. The reason for this is that nonlinear activation layers, although they can increase the representational complexity by increasing the number of channels, result in information loss due to their nonlinearity. However, nonlinear activations are better performing when being used in higher dimensionality. After the pointwise layer has expanded the feature map to higher dimensionality, a rectified linear unit (ReLU) activation function is used. Although when the activation function is applied to a channel, some of the information in that channel is lost, if there are many channels, in a high dimensional space, that lost information might be preserved in the other channels.

The number of pointwise convolutional filters that are applied determine the expansion factor to the higher dimensional representation. The next layer that is applied in the bottleneck block is a depthwise convolution layer using a 3x3 kernel. This layer performs spatial filtering of the higher dimensionality space. A ReLU activation function is applied after the depthwise convolution layer. Finally, a pointwise convolution layer is used to reduce the output from the depthwise convolution layer back down to a smaller dimensionality subspace. This reduction in dimensionality does introduce some loss of information and so a linear activation is used to reduce information loss. If a stride of 1 is used for the intermediate depthwise convolution, then the input and output channels can have the same dimensions and a residual connection can be made between the input and output low dimensionality spaces. This residual connection is important as it helps during backpropagation to maintain gradient flow. The structure of the inverted bottleneck is shown in Figure 6.4(a).

The advantage of having the residual connections being between low dimensional spaces is that it leads to a faster training of the weights when training. By introducing many bottleneck layers, the number of parameters in the model can be limited by reducing the number of output layers compared to inputs. This means a very deep network can be achieved without the introduction of too many parameters. By limiting the number of available parameters, the model is encouraged to generalise its prediction and improve the robustness of the model to unseen data.

The structure of the network used is shown in Figure 6.4(a). There are two alternative implementations of the bottleneck layer as shown in Figure 6.4(b). The main difference between the layers is that either a stride length of 1 or 2 is used in the depthwise convolution layer. The stride length is the number of pixels that the kernel is moved as it scans across the input feature map's pixels. If a stride length of 2 is used, the dimensionality of the subspace is halved. As can be seen in Figure 6.4(a), the bottleneck layers are repeated multiple times in each row of the table. The first of these repeated bottleneck layers in a new bottleneck block will apply the stride length given in the final column in the table, either 1 or 2. All the other repeated bottlenecks for that block will have a stride length of 1. Zero padding is used to ensure that the dimensionality is not changed when using a stride length of 1. The expansion factor introduced by the pointwise convolution used in that layer is also represented.

(a) Network Architecture

Input	Operator	Expansion factor	Output Channels	Repeats	First Lay Stri
96x96x1	Conv 2D	-	32	1	
48x48x32	Bottleneck	1	16	1	
48x48x16	Bottleneck	6	24	2	
24x24x24	Bottleneck	6	32	3	
12x12x32	Bottleneck	6	64	4	
6x6x64	Bottleneck	6	96	3	
6x6x96	Bottleneck	6	160	3	
3x3x160	Bottleneck	6	320	1	
3x3x320	Conv 2D	-	1280	1	
3x3x1280	Global Averaging pooling 2D	-	1280	1	
1x1x1280	Dense	-	1	-	

(b) Bottleneck layer structure

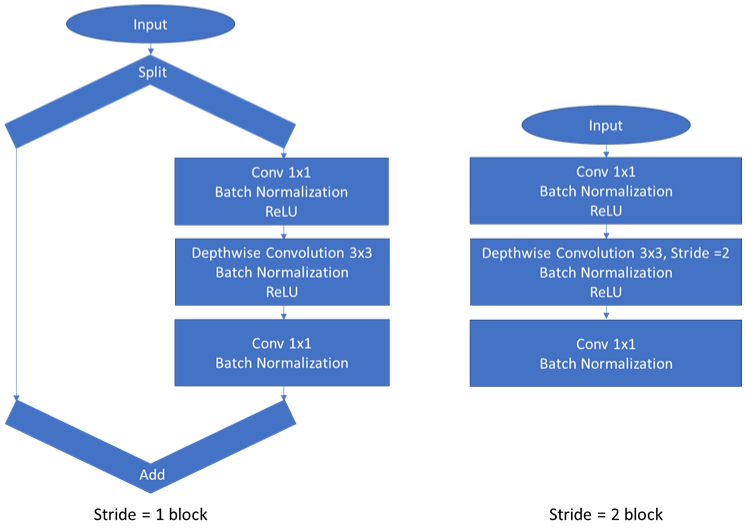

Figure 6.4. (a) table of the MobileNetV2 architecture used. Every row represents a sequence of layers, and these are repeated by the number indicated in the repeats column. For each sequence, the first layer uses the stride length indicated in the final column and a stride length of 1 is used for the remaining layers. This maintains the number of output channels for each repeat within each sequence of repeated bottleneck layers. When a stride of 2 is used, the dimensionality for the input of the next row of the table is halved. (b) shows the different architectures of the stride = 1 and stride = 2 bottleneck blocks in the model. Figure reproduced from (Lightley et al., 2022)

The input for the architecture was a 96x96x1 tensor and, in order for the model to provide a regression prediction of the current defocus, the output of the MobileNetV2 architecture was changed to a dense fully connected layer giving a scalar output.

Our laboratory had explored alternative CNN models prior to using the MobileNetV2 architecture. These CNN models were made up from convolutional layers in combination with batch normalisation and ReLU activation functions. Weight regularization using L2 regularization was used

to try to prevent overfitting of the training data. A max pooling layer was used to flatten the model to provide input to a series of fully connected dense layers. These dense layers finally provided a scalar prediction as an output. However, these models suffered from overfitting and, although were able to learn well on the training data, they performed poorly for unseen data and required large amounts of memory that exceeded what was available on the MSI GeForce RTX 2080 SUPER VENTUS XS OC GPU (8Gb RAM) in our desktop laboratory computer.

The MobileNetV2 architecture has a lower memory footprint than the other CNN models, meaning it could be implemented on the GPU. The efficiency and low memory requirements for the MobileNetV2 architecture also provided the possibility to implement the model on a low memory mobile device in the future, e.g., a Raspberry Pi, after training. Due to the MobileNetV2's structure reducing the parameters of the model whilst allowing for a deep architecture, the model was more robust to overfitting of the training data and was able to perform better on unseen data than the previous models. Adam (Kingma & Ba, 2014) was used as the optimization algorithm and a learning rate of 0.0001 was used during training. The mean squared error was used as the loss function.

6.3.2 Optical setup

The autofocus was initially implemented on an inverted epifluorescence microscope frame (Olympus IX81) that had been adapted to be used as an automated easySTORM (Kwakwa et al., 2016) multiwell capable imaging system and used a motorised x-y stage (Marzhauser SCAN IM 112x74 that was controlled using a Marzhauser TANGO controller). The optical system implementation of the autofocus is shown in Figure 6.5.

The infrared laser source used for the autofocus beam was introduced into the Olympus IX81 frame via the rear lamp port. The autofocus laser beam source was a 5.6 mm TO-CAN single-mode laser diode (HL8338MG). The output from the laser diode was collimated using a 4.51 mm focal length aspheric lens (Thorlabs, CMETME-B) and coupled into a 0.1 NA single mode optical fibre (FS-SN-4224) using 2 steering mirrors to adjust the tip and tilt of the beam incident on a 10x objective lens. The laser diode was mounted in a TE-cooled laser mount (Thorlabs, TCLDM9) and driven using a laser diode controller (Thorlabs, LDC500) with a temperature controller (Thorlabs, TED200C).

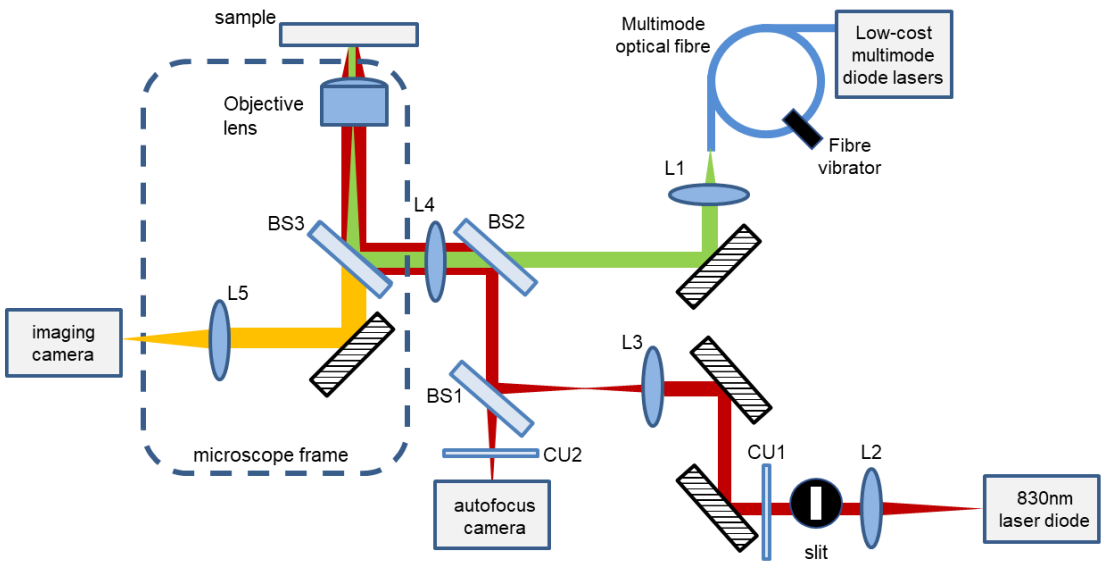

Figure 6.5. Schematic of the optical autofocus implemented on an Olympus IX81 microscope frame used for HCA easySTORM (Kwakwa et al., 2016). The objective lens was an oil immersion 1.3 NA 100x lens (Olympus, UplanFl 100x, NA 1.3, oil) with a depth of field of ~600 nm. The focal lengths of the other lenses were L1: 50mm (Thorlabs, AC254-050-A-ML), L2: 18.4mm (Thorlabs C280TMD-B), L3: 100mm (Thorlabs, AC254-100-B-ML), L4: 200mm (Edmund Optics 49-364), L5: 180mm (Olympus tube lens). Figure reproduced from (Lightley et al., 2022)

The output from the single mode optical fibre was connected using a FC/PC adaptor plate (Thorlabs, SM1FC) into a 30 mm (Thorlabs) cage rod system to provide a spatially coherent beam for the autofocus system. This beam emerging from the single mode optical fibre was collimated using an 18.4 mm focal length aspheric lens (L2 in Figure 6.5, C280TMD-B). The diameter of this collimated beam was 3.68 mm. An adjustable slit (Thorlabs VA100C/M) was positioned in the Fourier plane of the aspheric lens and conjugate to the back focal plane of the objective lens and adjusted to produce a quasi-rectangular collimated beam. The slit width was set at 1.2 mm, and this resulted in a beam profile with an aspect ratio of 1:3 between the two orthogonal axes.

The collimated beam then passed through a 10 nm bandpass filter (Edmund Optics, 55-119) to clean up the beam's spectrum and then steered by 2 mirrors to align the beam along the optical axis of the objective lens. Before reaching the objective lens, the collimated beam first reflects off a 50:50 beamsplitter BS1 (Edmund Optics, 47-026) and a shortpass dichroic beamsplitter BS2 (Edmund Optics, 69-220) that is used to introduce the high power visible multimode laser excitation radiation for the implementation of easySTORM. The collimated beam is also expanded using a 2x magnification telescope, made using two achromatic doublets L3 and L4, to double the beam diameter at the back focal plane of the objective lens. L3 is a 100 mm focal length lens (Thorlabs, AC254-100-B-ML) with anti-reflection coating in the infrared (650-1050nm) and lens L4 is a 200 mm

focal length lens (Edmund Optics 49-364) with a long-range anti-reflection coating between 400 nm and 1000 nm.

The collimated autofocus laser beam reflects off a custom-made multi-line dichroic beamsplitter, BS3 (Chroma, ZT405/462/635/830rpc-UF2), with reflection bands centred on 405, 462, 635 and 830 nm, into the back aperture of the Olympus 100x objective lens (Olympus, UplanFl 100x, NA 1.3, oil). The beam is then focused onto the sample by the objective lens and reflected at the refractive index interface between the immersion medium of the sample and the glass coverslip. The glass coverslip had a refractive index of ~1.518 and the refractive index of PBS STORM buffer is ~1.33 since it is water based. The reflected beam is then recollimated by the objective lens and is reflected back along its original path by BS3 to be focussed by L2 onto the autofocus camera (FLIR, Chameleon3, cm3-U3-31S4M via a reflection at the shortpass beamsplitter dichroic BS2 and transmission through the 50:50 beamsplitter BS1. Thus, when the microscope is in focus, the autofocus laser beam will be focussed on the autofocus camera and any defocus of the microscope will defocus the beam at the autofocus camera, changing the recorded autofocus image.

The precision of determining the focus position is dependent on the confocal parameter of the infrared autofocus laser beam at the coverslip, which depends on the focal length of the objective lens and the diameter of the incident collimated beam. Thus, a larger collimated beam diameter will increase the accuracy of defocus determination as there will be a greater variation of the autofocus image size with defocus. However, this faster expansion of the autofocus camera image will decrease the defocus range over which the autofocus camera is able to record useful images. Thus, there is a trade-off between precision and range of the defocus measurement. By imposing a rectangular beam profile on the collimated autofocus beam, however, two distinct confocal parameters for the two orthogonal axes of the beam can be realised. The larger collimated beam diameter gives a shorter confocal parameter for increased accuracy of defocus measurement while the smaller collimated beam diameter gives a longer confocal parameter for increased range.

6.2.3 Implementation

The MobileNetV2 architecture has been implemented using the TensorFlow (Abadi et al., 2016) 2.1 package installation on Python. Anaconda was used as the Python distribution platform and Spyder was used as the Python development environment. The model was trained using a MSI GeForce RTX

2080 SUPER VENTUS XS OC GPU graphics card installed on a desktop PC. The GPU had 8 GB RAM and the memory footprint for the MobileNetV2 architecture was 3.5 GB.

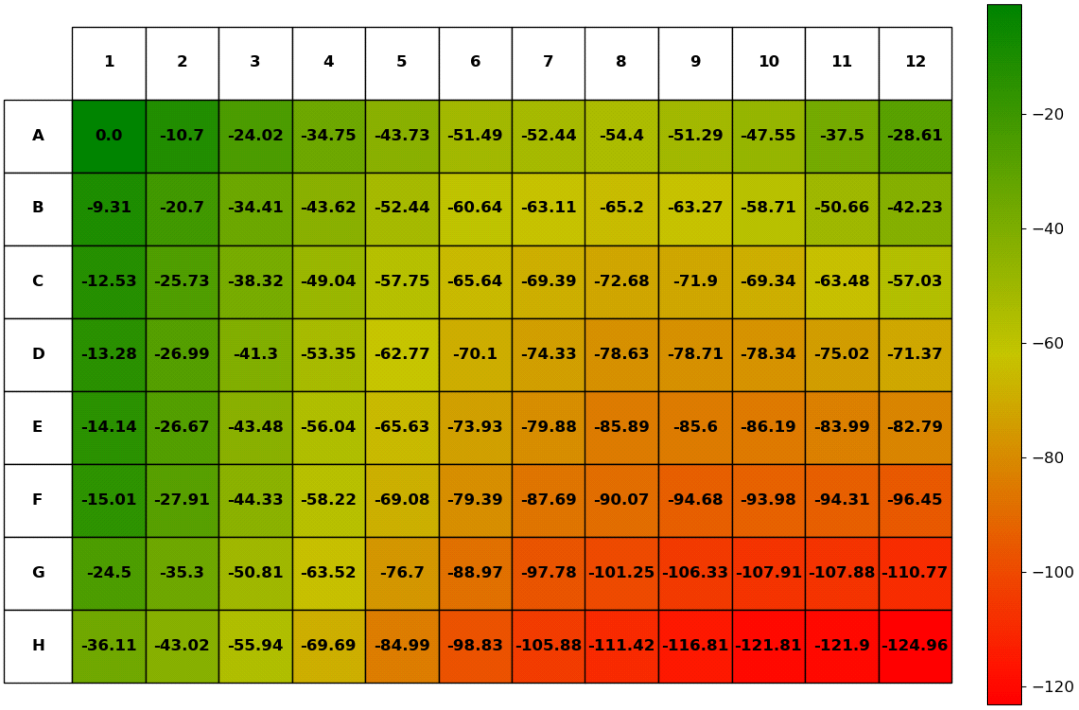

	1	2	3	4	5	6	7	8	9	10	11	12
A	0.0	-10.7	-24.02	-34.75	-43.73	-51.49	-52.44	-54.4	-51.29	-47.55	-37.5	-28.61
B	-9.31	-20.7	-34.41	-43.62	-52.44	-60.64	-63.11	-65.2	-63.27	-58.71	-50.66	-42.23
C	-12.53	-25.73	-38.32	-49.04	-57.75	-65.64	-69.39	-72.68	-71.9	-69.34	-63.48	-57.03
D	-13.28	-26.99	-41.3	-53.35	-62.77	-70.1	-74.33	-78.63	-78.71	-78.34	-75.02	-71.37
E	-14.14	-26.67	-43.48	-56.04	-65.63	-73.93	-79.88	-85.89	-85.6	-86.19	-83.99	-82.79
F	-15.01	-27.91	-44.33	-58.22	-69.08	-79.39	-87.69	-90.07	-94.68	-93.98	-94.31	-96.45
G	-24.5	-35.3	-50.81	-63.52	-76.7	-88.97	-97.78	-101.25	-106.33	-107.91	-107.88	-110.77
H	-36.11	-43.02	-55.94	-69.69	-84.99	-98.83	-105.88	-111.42	-116.81	-121.81	-121.9	-124.96

Figure 6.6. Map of variation of axial focus position of bottom of glass 96-well plate in µm relative to the focus at the centre of well A1 (Brooks life Science Systems, MGB096-1-2-LG-L). Figure reproduced from (Lightley et al., 2022).

The autofocus was initially implemented as part of a custom *µManager* 2.0 plugin for automated HCA STORM acquisitions of multiwell plate acquisitions called “STORMhelper”. The *µManager* plugin, which is written in Java using NetBeans as the IDE, controls the hardware to move the Z-stage to correct for the defocus. A Python script running in parallel is used to implement the autofocus, with the two software programs communicating using a socket connection. The Python script creates the socket and then uses a socket listener, within a while loop, to wait for a call to calculate the current defocus. The Java plugin connects to the socket created by the Python script. When the Java plugin calls for the current defocus to be calculated, a message is sent to the socket which is read by Python script that then uses the trained neural network to determine the current defocus from the image on the autofocus camera, which is controlled from within the Python script. The Python script then writes the current defocus value to the socket and the value is read by the *µManager* Java plugin, which is then able to move the Z-stage to the correct focus position. An arbitrary target focus position can be set within the *µManager* plugin and the Python script will move the Z-stage to the appropriate position. The actual defocus value returned by the Python script is stored as the defined focus position for the image acquisition.

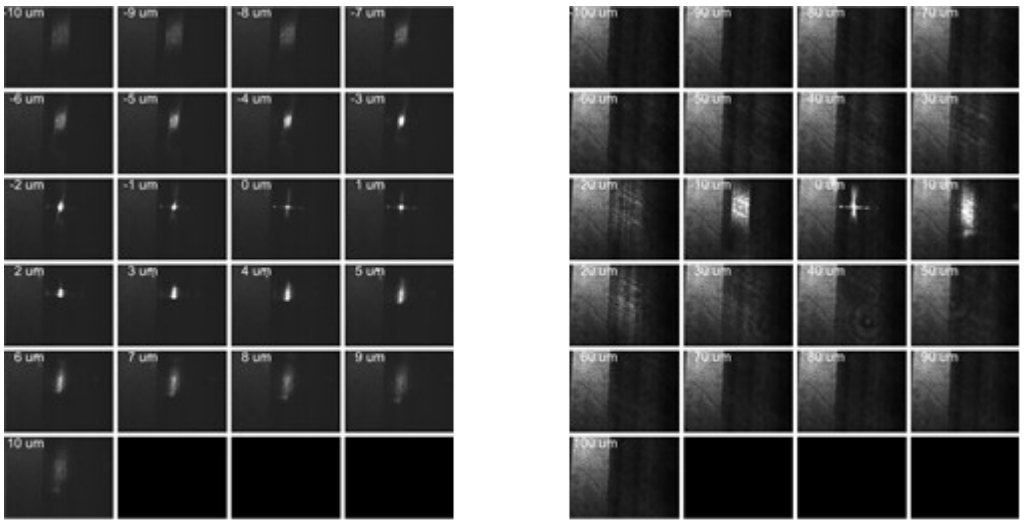

Figure 6.7. Images of exemplar image z-stacks acquired on the autofocus camera as the sample coverslip is translated through the focus of the microscope objective lens: (a) shows a z-stack used to train the "short-range" model over a range of -10 µm to +10 µm acquired in 50 nm step intervals. An image is shown every 1 µm in the stack. (b) shows a z-stack stack used to train the "long-range" model over a range of -100 µm to +100 µm acquired in 1 µm step intervals. An image is shown every 10 µm in the stack. The grey feature visible on the left-hand side of the FOV is a back-reflection from the excitation lens, L4 in Figure 6.5.

The system allows a two-step autofocus to be implemented utilising a long-range training data set that can be used over a range of $\pm 100\ \mu m$ and a higher accuracy short range training data set applicable over a range of $\pm 10\ \mu m$. When the defocus is larger than 10 µm, e.g., when moving between wells of a multiwell plate, the autofocus acts in 2-steps: First the *µManager* plugin requests a focus correction using the long-range CNN training set and then it moves the stage the calculated defocus value. The defocus will then be within the range of the more accurate short range training data set, with which the autofocus procedure can be repeated. During a STORM acquisition of a single field of view, any axial drift typically will not exceed the range of the near focus model and so the autofocus can be implemented using only a single step correction. This reduces the time needed to perform the focus correction and hence increases the throughput of the acquisition.

6.3.4 Data Acquisition and Preparation

The CNN training datasets were acquired as 100 axial "through-focus" z-stacks acquired using *µManager* and saved in the OME TIF data format. The z-stacks used to train the CNN for the long-range autofocus were acquired over a range of $\pm 100\ \mu m$ with $1\ \mu m$ step increments and the short-

range training data set was acquired over a range of ± 10 μm with a sampling increment of 50 nm. The ± 100 μm range was found to be sufficient to image samples arrayed in a multiwell plate using a snakelike pattern to move between neighboring wells. The typical inter-well axial variation in focus is shown in Figure 6.6, showing that the maximum variation between wells across the whole plate was less than 125 μm. This was within the 200 μm total operating range of the autofocus system and the inter-well axial variation between neighboring wells was less than 100 μm. The acquisition of the 100 axial training stacks took approximately 3 hours. Figure 6.7(a) and Figure 6.7(b) shows exemplar images from the training stacks. The grey feature visible on the left-hand side of the FOVs, is from a back reflected signal from Lens L4 in Figure 6.5.

The images in each training stack were processed before being used as inputs for the CNN training model. Each individual image was rescaled and binned using OpenCV package in Python to produce a (96x96x1) shaped Python NumPy array. The data in the arrays was then normalized using a Euclidean 2-norm process. These arrays were converted to a tensor format to be used as the input for the MobileNetV2 network.

During the acquisition of the autofocus camera image training data, there was axial drift of the focus position such that the in-focus image (described as the *zero-defocus image*) in the z-stack was typically not the central stack image. Hence, all the z-stacks needed to be aligned with respect to the focal plane before training the CNN. Since the sampling interval of the z-stacks acquired for the training data is known, all the other images in the stack can be labelled according to their respective defocus offsets once the zero-defocus image in the stack is determined. In order to determine the zero-defocus position in each axial z-stack, an image metric was calculated that is minimized at focus: the intensity values were averaged along the pixel rows of the camera to produce a one dimensional intensity projection of the image and a Savitsky filter was applied to these projections to smooth them without altering their overall shape. The power spectrum of these 1D projections was calculated by taking the square of the of the absolute value of the Fourier transform and the standard deviation of the power spectrum for each image's projection was then calculated and was plotted as a function of axial position within the z-stack. The function produced a smooth curve with a minimum at focus, corresponding to the zero-defocus position. Figure 6.8 shows exemplar functions plotted against normalised axial position (i.e. defocus value) for the short range and long range autofocus camera image training data.

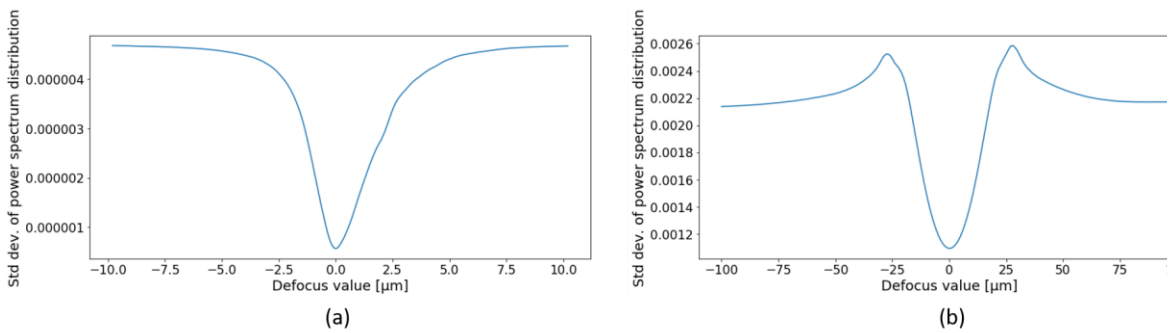

Figure 6.8. Exemplar through-focus plots, used for determining and labelling the in-focus plane of the training stacks, of the standard deviation of the power spectrum of the autofocus camera intensity distribution averaged (a) across the pixel rows for the short-range autofocus training data and (b) across the pixel columns for the long-range autofocus data. The graphs are plotted as a function of defocus for the images in a z-stack. A Savitzky-Golay filter was passed along these distributions of (averaged) intensities to produce a smoothly varying function. Figure reproduced from (Lightley et al., 2022)

The determined defocus offset values of the autofocus camera images were then normalized for each z-stack. This was done by centering on the mean and dividing by half the total range. These normalized defocus labels were then used as the “ground truth” values for training. This process was repeated for every acquired z-stack.

In order to produce a validation dataset, 10% of the stacks were removed from each day’s training dataset. During training the validation loss was calculated after each epoch and, if the accuracy of the model improved, the weights were recorded. This meant that only the best performing model’s weights were recorded to produce the final model. This allowed the model to perform early stopping during training to prevent over fitting to the training datasets. This training of the CNN models took approximately 3 hours. After the CNN model had been trained, the defocus offset can be determined by the CNN from a single autofocus camera acquisition. The procedure for the data preparation and training is shown in Figure 6.9.

6.4 Autofocus performance using a single-day training dataset

Every 10th stack of the 100 axial z-stacks were removed from the training dataset and used for validation during training. A learning rate of 0.0001 was used during training and Adam (Kingma & Ba, 2014) was used as the optimization algorithm. The mean squared error was used as the loss metric and the loss was

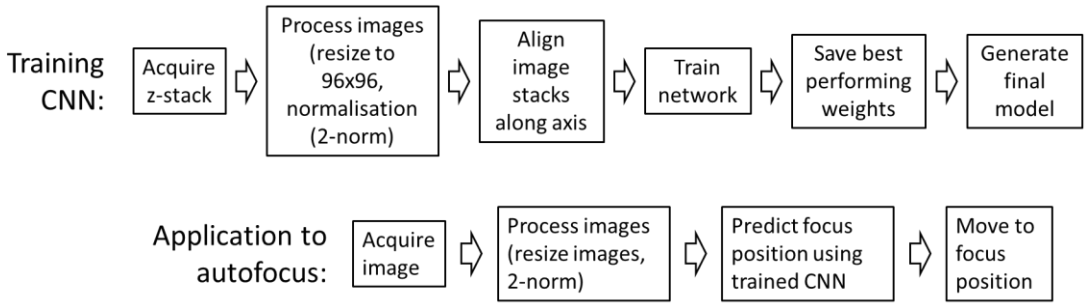

Figure 6.9. Schematic of workflow process to train and apply CNN for optical autofocus. Figure reproduced from (Lightley et al., 2022)

calculated in the normalized space. In order to determine the performance of the model during training, the validation dataset was tested, and the validation loss was recorded after each epoch. If the validation loss decreased the weights of the model were saved.

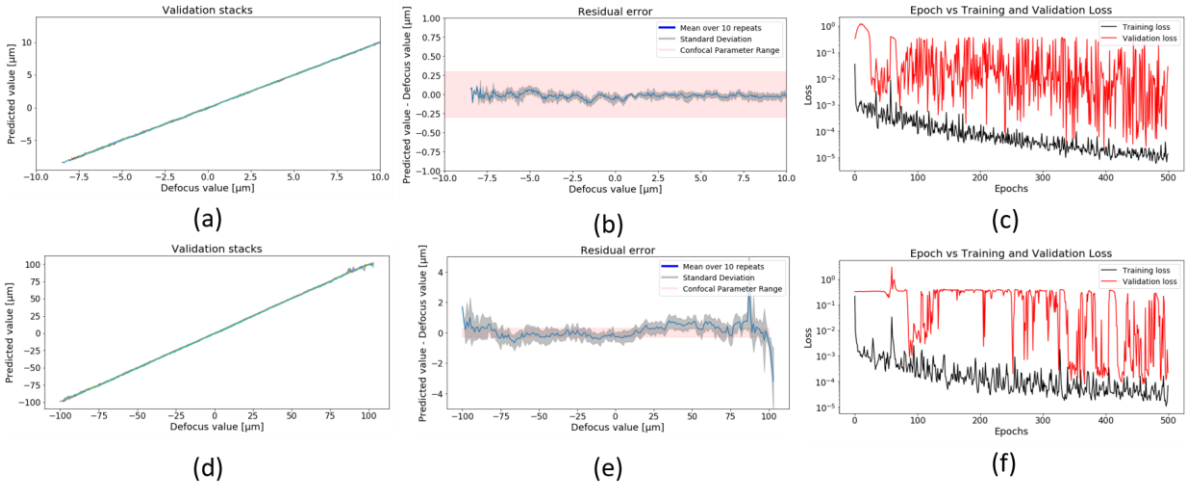

Figure 6.10. Plots of predicted vs actual defocus for 10 through-focus axial z-stacks. Each stack is plotted in a different colour in (a, d) for both the short range and long-range models respectively. The corresponding mean of the residual errors are shown in (b, e) resulting when using the short-range and long-range CNN training sets acquired and validated on data acquired on the same day. Figures (c, f) show plots of the changing training and validation loss with increasing epochs during training for the short range and long-range CNN training sets respectively. Figure reproduced from (Lightley et al., 2022)

During the testing of the model's performance, it was noted that the accuracy of the prediction of current defocus offset by the network was limited by the axial sampling rate that was used when acquiring the training data. For the optical set-up described earlier, the depth of field (DOF) for the STORM imaging system was $\approx 600\ nm$. In order to realise an autofocus accuracy well within half the DOF, an axial sampling rate of every 50 nm was chosen for the short-range training data, noting that the axial stage was able to provide readouts at intervals down to 10 nm. However, if this sampling rate was used for the long-range training data, the data volume would be prohibitive, and the

training time would be unnecessarily long. Therefore, the long-range training data was acquired with a sampling interval of 1 µm to reduce the data volume and training time. The short range autofocus camera image training data with 50 nm sampling was processed to average the pixels across the pixel rows perpendicular to the slit, in order to produce the rapidly changing defocus metric shown in Figure 6.8(a). Beyond the ±10 µm range, the beam expanded to overfill the sensor of the camera such that the signal to noise ratio (SNR) was no longer sufficient to provide a reasonable prediction of defocus.

The long-range autofocus camera image training data with 1 µm sampling interval over a range of ±100 µm was processed to average the pixels across the pixel rows parallel to the slit, in order to produce the slower changing defocus metric shown in Figure 6.8(b).

Figure 6.10(c, f) show the training and validation loss for the short-range and long-range training data models respectively. The training loss is plotted in black, and the validation loss is plotted in red as a function of epoch number. They were each trained over 500 epochs and then the weights were recorded for the epoch with the smallest validation loss. 90 of the 100 respective stacks were used to separately train the two models and 10 stacks were used for the validation.

Figure 6.10 shows the performance of the autofocus – plotting the defocus values predicted from the model after training had been completed against the "true" defocus values. Figure 6.10(a,b,c) show the performance for the short-range training data model and Figure 6.10(d,e,f) show the performance corresponding to the long range training data model. The ground truth defocus for each z-stack was obtained by finding the minimum of the standard deviation of the power spectrum distribution of the autofocus camera image intensity projections averaged across the pixel rows, as discussed above. This is shown for all 10 validation stacks in Figure 6.10(a, d) for the short-range and long-range models respectively, presenting a linear relationship for the 10 repeated stacks for both models.

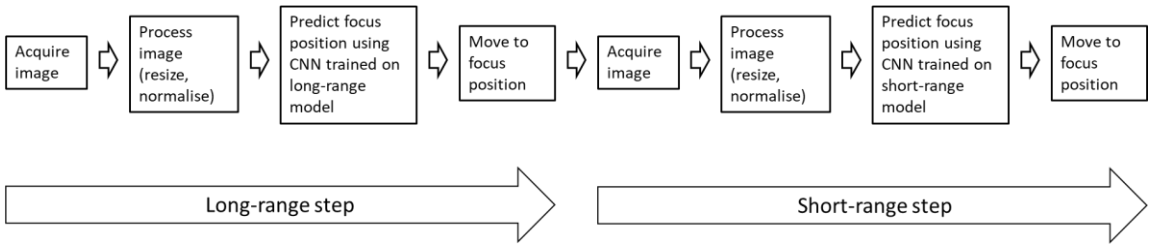

Figure 6.11. Diagram of data process workflow and use for two-step CNN autofocus. Figure reproduced from (Lightley et al., 2022)

The mean of the residual errors for the 10 axial stacks are shown in Figure 6.10(b, e). The residual error is defined as the predicted defocus minus the true defocus. The mean residual error is

indicated by the blue line with the standard deviation of the 10 repeats represented by the grey shaded region. The confocal parameter of the 100x microscope objective lens (Olympus, UplanFl 100x, NA 1.3, oil) is shown in the shaded orange region. Figure 6.10(b) shows that a prediction accuracy better than 100 nm was achieved for the short-range model across the ±10 µm training range, which was within the DOF for the objective lens. The prediction precision using the long-range model was better than 1 µm over most of the training range of ±100 µm. By using these two models sequentially, the long-range CNN can bring the optical system within the ±10 µm training range of the short-range CNN model. Then the short-range model can be applied to correct the focus to be within the confocal parameter of the system. This procedure is shown in Figure 6.11.

However, when the autofocus was tested on subsequent days following the day the training data was acquired, the performance was significantly degraded. Thermal variations and other perturbations to the microscope over time, such as mechanical drift, can result in the defocusing of the microscope, which the autofocus system should ideally correct. Unfortunately, these perturbations can also impact the optical autofocus system itself. In some commercial microscopes, these effects are minimised by positioning the optical autofocus components very close to the objective lens of the microscope to minimise the optical path length and therefore the impact of system drift. However, for microscopes utilising a more extended external autofocus unit, optical system drift can cause a problem. The performance of the CNN autofocus when tested on subsequent days following training is shown in Figure 6.12. In Figure 6.12(a, c), the predicted defocus vs true defocus value is plotted for each day up to 4 days after training. For each day, 10 axial stacks were acquired, and the defocus was calculated using the previously acquired CNN training data model. The relationship between predicted and actual defocus is no longer linear for both the short-range and the long-range models. Likewise, the residual error plotted for the subsequent days are significantly larger and the autofocus system is not sufficiently accurate to be useful. The mean residual error for the short-range model exceeds 2 µm and the mean residual error for the long-range model exceeds 100 µm.

Using this autofocus system would therefore require the acquisition and training of a new CNN model each day, which Is not practical, as this would take more than 3 hours. In addition, the aspiration to use this autofocus in an HCA STORM platform with acquisitions of multiwell plate STORM data lasting many hours could be compromised by the errors induced by the optical autofocus system drift occurring within a single experiment. Therefore, it was decided to extend the acquisition of the CNN training data over multiple days to capture the impact of laboratory perturbations within the CNN training data model.

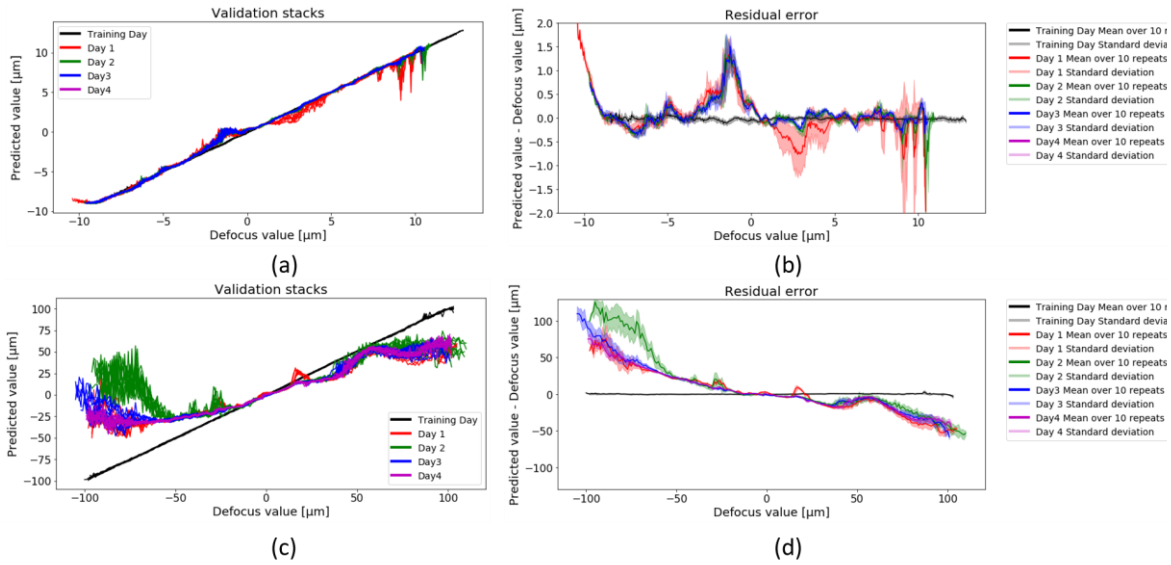

Figure 6.12. Plot of predicted vs actual defocus (a, c) and the corresponding mean of the residual errors (b, d) when using the short-range and long-range CNN training sets acquired (separately and sequentially) on a single day and applied to data stacks acquired on different subsequent days. Figures (a) and (c) show data acquired from multiple days with 10 repeated stacks plotted for each day, with all data from a single day plotted in the same colour. Figure reproduced from (Lightley et al., 2022)

6.5 Autofocus performance using a multiple-day training dataset

In order to mitigate for the optical system drift induced by thermal variations in the laboratory over time, a training dataset of 100 axial z-stacks was acquired on each of 6 days within a 10-day period. It was found empirically that a 10-day period was sufficient to capture the day-to-day variation in optical autofocus training datasets, such that the resulting composite model could be applied to subsequently acquired data. Figure 6.13 shows the performance of the autofocus system utilising this composite training data set with data acquired on the subsequent 11th day. As shown in Figure 6.13(a, c), the linear relationship between predicted defocus and true defocus has been regained for both the short-range model and the long-range model. Furthermore, Figure 6.13(b) shows that the short-range model is able to determine the defocus with a mean error within the microscope objective lens depth of field range of 600 nm. For the majority of the autofocus training range, the prediction accuracy is within 200 nm. The performance of the long-range model, shown in Figure 6.13(d), is not within 1 µm (as was the case in Figure 6.10(e) but it does have a prediction accuracy within the ±10 µm training range of the short-range model. Thus, when the autofocus system is run

as a 2-step process, it is still able to correct defocus over the ±100 µm within a final accuracy of 200 nm.

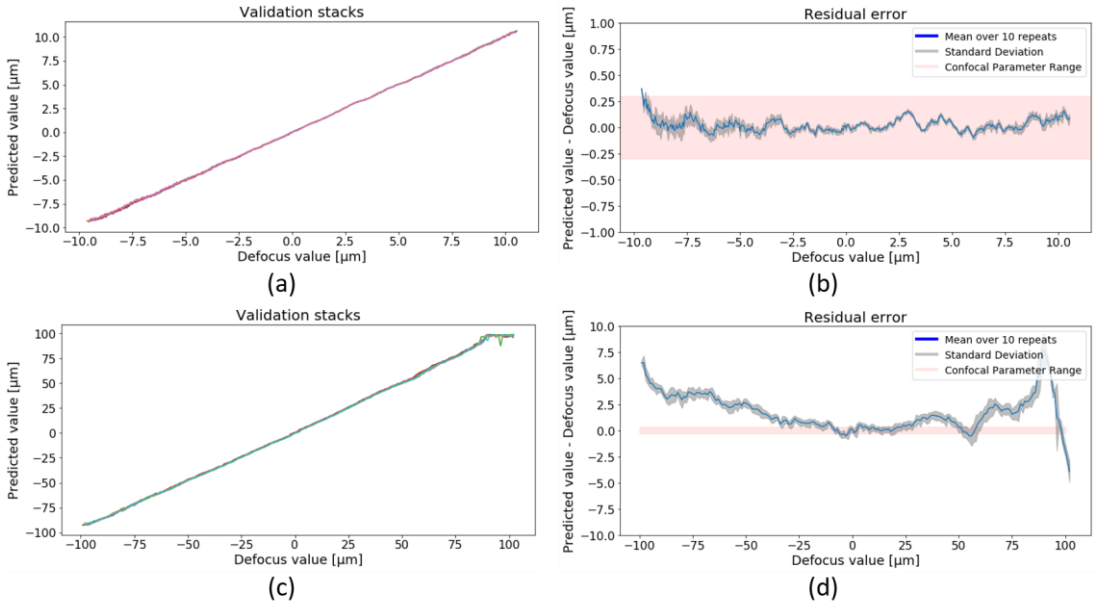

Figure 6.13. Plot of predicted vs actual defocus for 10 through focus axial z-stacks, with each z stack plotted in a different colour (a, c), and the corresponding mean of the residual errors (b, d) when using the aggregate CNN training sets, acquired over a period of 10 days and applied to measurements undertaken on a subsequent day for the short-range and long-range models respectively. Figure reproduced from (Lightley et al., 2022)

6.6 Performance of Autofocus

In order to further quantify the accuracy of the autofocus, two different studies were undertaken. First, the error in focus correction was systematically studied for a range of known initial defocus values. The defocus was determined using the composite training data model acquired over the 10-day period. From each initial defocus position, the autofocus was set to correct focus 10 times. for each measurement, a Z-stack was subsequently acquired, and the power spectrum intensity metric described early was used to determine the true focus. Thus, a mean error in focus correction could be calculated for each initial defocus position. To evaluate the performance of the short-range autofocus only, the initial defocus values were set at 2-micron intervals over the range of ±16 µm. To evaluate the performance of the long-range autofocus only, the initial defocus values were set at 20 µm intervals over the range of ±80 µm. To evaluate the 2-step autofocus, the initial defocus values were again set at 20 µm intervals over the range of ±80 µm. This autofocus performance is presented in Figure 6.14. The figures in the left-hand column show the same data as is presented in

the right column but with a larger range for the error axis. The figures show a boxplot of the results obtained for the 10 repeat measurements for each initial defocus. The orange line shows the mean error, the box shows the inter-quartile range, and the whiskers show the outliers. As can be seen in Figure 6.14(a), the short-range model was able to reproducibly correct the defocus and move the sample within the depth of field (~600 nm) of the microscope over the ±10 µm training range. As shown in Figure 6.14(b), outside of its training range, the CNN model is not able to correct to within the objective lens DOF but is able to correct the defocus to a mean error of 3 µm across the training range. However, the maximum error was still within the operating range for the short-range CNN model. Furthermore, within the range of ±40 µm, the long-range autofocus had a mean error within the 600 nm DOF of the microscope and a maximum mean error did not exceed 2 µm. As previously shown in Figure 6.6, the maximum axial variation between neighbouring wells does not exceed 20 µm and so a range of ±40 µm is sufficient to correct for axial focus variation when traversing a 96 wellplate in a snake-like pattern. Figure 6.14(c) shows the performance of the two-step autofocus, where the long-range and the short-range models are used sequentially. The autofocus is able to correct to +/-200 nm of focus, within the 600 nm DOF over the range of ±80 µm. This demonstrates that the 2-step CNN-based autofocus with the composite 10-day training data model can correct the defocus over a long-range whilst maintaining a high accuracy. This provided confidence that the autofocus system would enable automated multiwell plate image acquisitions for HCA-STORM.

A second study demonstrated the ability of the optical CNN-based autofocus system to automatically image across a 96-well multiwell plate. The methodology used can be applied to any automated multiwell plate microscope platform to measure the performance of the autofocus system. This study entailed automated imaging of sub-resolution, 100 nm diameter fluorescent beads (TetraSpeck, T7279), that were arrayed on the coverslip at the bottom of each well of a 96 wellplate (Brooks life Science Systems, MGB096-1-2-LG-L). When moving to image in a new well, the autofocus system was applied and then a subsequent axial Z-stack was recorded. Using previously published software, PSFj (Theer, Mongis & Knop, 2014), the image of the beads (and therefore the coverslip) in focus within the Z-stack could be calculated to give an indication of the true defocus. The plate was traversed in both a vertical and horizontal snake pattern around the 96 wells - either travelling along the columns vertically before moving across the plate to the next column or stepping horizontally across the rows before moving down the plate to the next row.

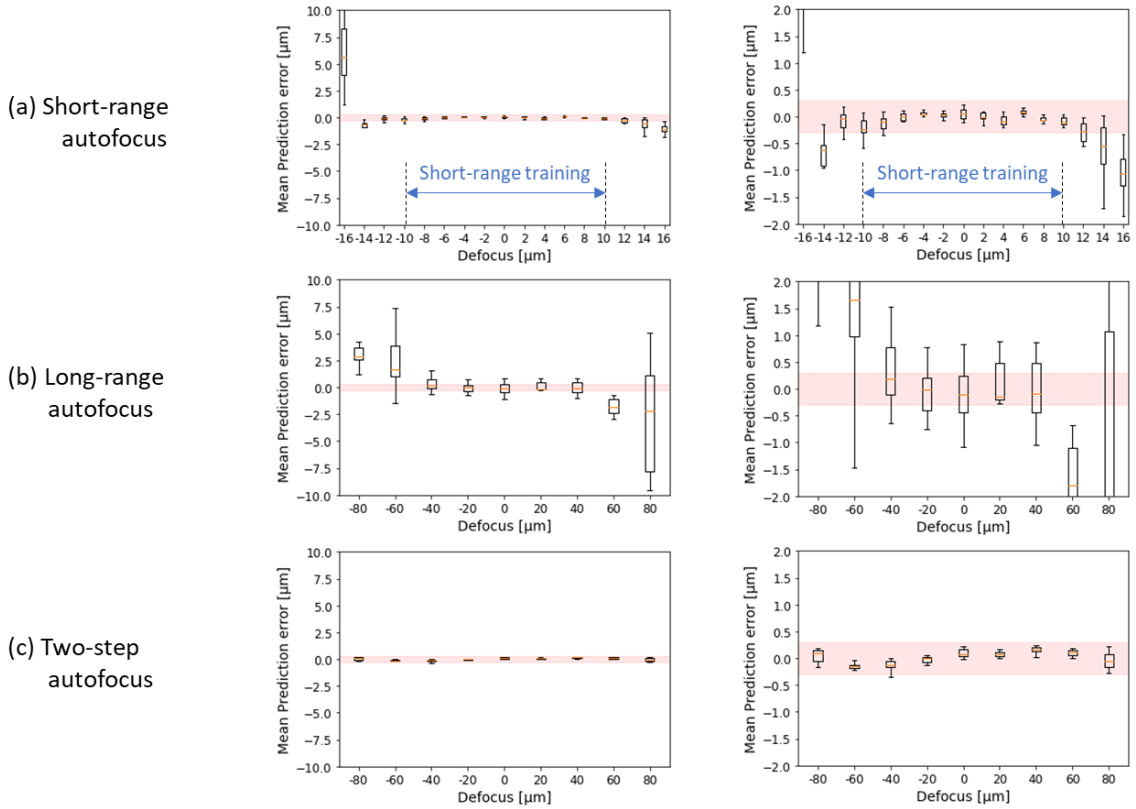

Figure 6.14. Plots of the prediction error vs known initial defocus for 10 measurements at each defocus position. The right-hand column shows same data as left-hand column on expanded vertical scale. (a) shows data for applying only the short-range model, (b) shows data for only applying the long-range model and (c) shows the data for sequentially applying the long-range and then the short-range CNN training models trained with data acquired over 10 previous days. The red band corresponds to the ~600 nm depth of field of the fluorescence microscope. Box plot shows the interquartile range of the prediction errors, the orange line shows the mean prediction error, and the whiskers show any outlier predictions for each of the 10 repeats at the known defocus offsets. Figure reproduced from (Lightley et al., 2022)

The performance of the autofocus was tested when using the short-range model only, the long-range model only and the two-step autofocus. For the short-range model and the two-step model, the subsequent axial Z-stacks were recorded over a range of ±2 µm in 100 nm intervals. For the long-range only dataset, the range was increased to ±4 µm in 100 nm step intervals to account for the lower accuracy of the long-range model. *PSFj* (Theer, Mongis & Knop, 2014) was able to automatically segment the individual beads arrayed within the field of view in each axial z-stack and determined the axial co-ordinate when each bead was in focus. Then, *PSFj* outputs a csv file which includes the focus plane positions of all the beads. The average of these bead positions was calculated for each well and was used to calculate the mean offset from the image plane that the autofocus system determined to be in focus. Histograms of the mean bead position defocus for each of the 96 well measurements were plotted for each of the three autofocus procedures. From these histograms, the mean overall defocus could be calculated from the distribution and the standard

deviation could be calculated as an error. These results are shown in Figure 6.15 and Figure 6.16 for the data acquired in a horizontal and vertical snake pattern respectively.

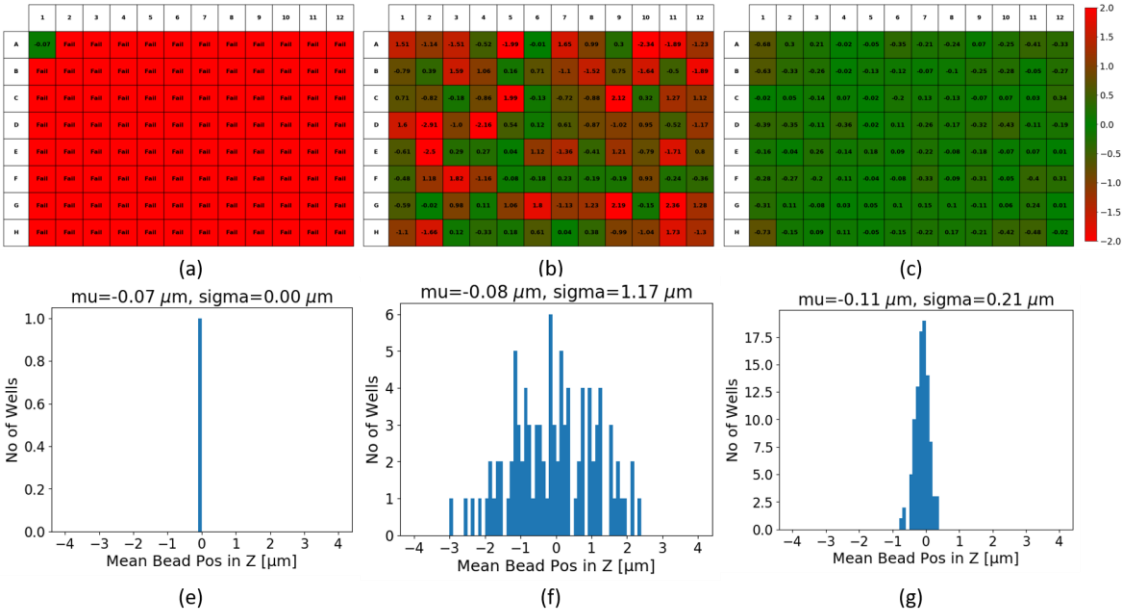

Figure 6.15. Results obtained when automatically imaging 100 nm diameter fluorescent beads (TetraSpeck, T7279) arrayed in a 96-well plate (Brooks life Science Systems, MGB096-1-2-LG-L), for which a through-focus image axial z-stack was automatically recorded in each well. The plate was traversed following a horizontal (row-by-row) snake pattern. (a-c) show heat maps of the mean defocus of the beads imaged in each well calculated using *PSFj*. In the top row, the heatmaps summarize the results for when (a) only the short-range autofocus, (b) only the long-range autofocus and (c) the combined 2-step autofocus were employed. The amount of defocus error in each well is encoded in a colour scale in µm, with red indicating that the autofocus failed to locate within +/- 2 µm. Where *PSFj* was unable to determine the defocus of the bead images, or where the mean defocus was outside the +/-2 µm range, the heat map presents a red coloured well with either "Fail" or the mean (out-of-range) defocus value. In the bottom row (e-g), histograms of the mean defocus for each well, with bin widths of 100 nm, are displayed for the bead image z-stacks for which *PSFj* could determine the defocus. Figure reproduced from(Lightley et al., 2022)

The data is represented by heatmaps showing the mean defocus of the 100 nm fluorescent beads within the axial z-stack of each well of the 96 wellplate. The heatmap colour scale ranges from green when there is zero defocus error up to red at ±2 µm error in defocus. If the defocus error exceeded ±2 µm, the colour of the well was set to red, and if *PSFj* could not determine any bead focus within the range due to the autofocus failing, the well is indicated with the text "Fail." When considering the results shown in Figure 6.15 (a) and Figure 6.16 (a), it is likely that the plate is tilted, mainly along the longer dimension of the plate, causing the short-range autofocus to fail after the first well in Figure 6.15(a) when the plate is imaged in the horizontal snake mode. The system successfully images the first well and then moves horizontally and fails to reach focus in the next and all remaining wells because the defocus offset exceeds the ±10 µm training range. This is visible by

considering Figure 6.6, which shows the variation in axial focus position across a 96 well plate acquired on the same system. The change in focus from A1 to A2 has a magnitude of 10.7 μm, which is more than the training range for the short-range model. Also, the difference in focal positions between A1 and B1 is within the training range at 9.31 μm.

For the vertical snake mode, where the vertical tilt is postulated to be less steep, Figure 6.16(a) shows that the short-range autofocus is able to correct the defocus for the majority of the wells. However, it does fail for one of the wells, A3, and the error in some of the wells exceeds the DOF of the system. Overall, however, Figure 6.16(e) shows that it achieved an average error of -0.02 μm ± 0.26 μm, where the error is given by the standard deviation of the mean error of the bead positions within the axial stacks across all the 96 wells. In Figure 6.15(b) and Figure 6.16(b), the long-range autofocus was successfully able to traverse the whole multiwell plate such that the *PSFj* software was able to determine the bead position within the axial z-stack of each well for the horizontal and vertical acquisition paths respectively.

The long-range autofocus results presented in Figure 6.15(f) and Figure 6.16(f) show that the mean error in position across the 96 wells is -0.08 μm ± 1.17 μm when acquired in a horizontal snake movement pattern and 0.11 μm ± 0.98 μm when moving in a vertical snake pattern. The standard deviation in the autofocus error is on the order of the sampling rate of the training data for the long-range model.

When the 2-step autofocus method is used, the autofocus successfully traverses the plate in both the horizontal and vertical snake acquisition patterns and achieves an mean error of -0.11 μm ± 0.21 μm and -0.07μm ± 0.16 μm respectively. The standard deviation accuracy measurements both improve on the accuracy achieved when solely using the short-range model in a vertical snake pattern. This is because the autofocus is not acting at the extremity of its training range since the long-range model has already moved the coverslip to be near focus. The performance is better for all cases when using a vertical snake pattern as the average inter well axial variation is reduced because the plate was tilted along the longer dimension.

The models were able to be used for periods of months without needing to be retrained. The aggregate models, presented in Figure 6.13, were trained on 18/06/2020 and 20/06/2020 for the short-range and long-range models respectively. These models were used without the need for retraining to image the mulitwell plate HCA easySTORM experiments, of THP1 and WM2664 Melanoma cells, presented in Chapter 7.2. These experiments were undertaken on 27/08/2020 and 07/12/2020 respectively, demonstrating the robustness of the model to operate over 5 months after initial training.

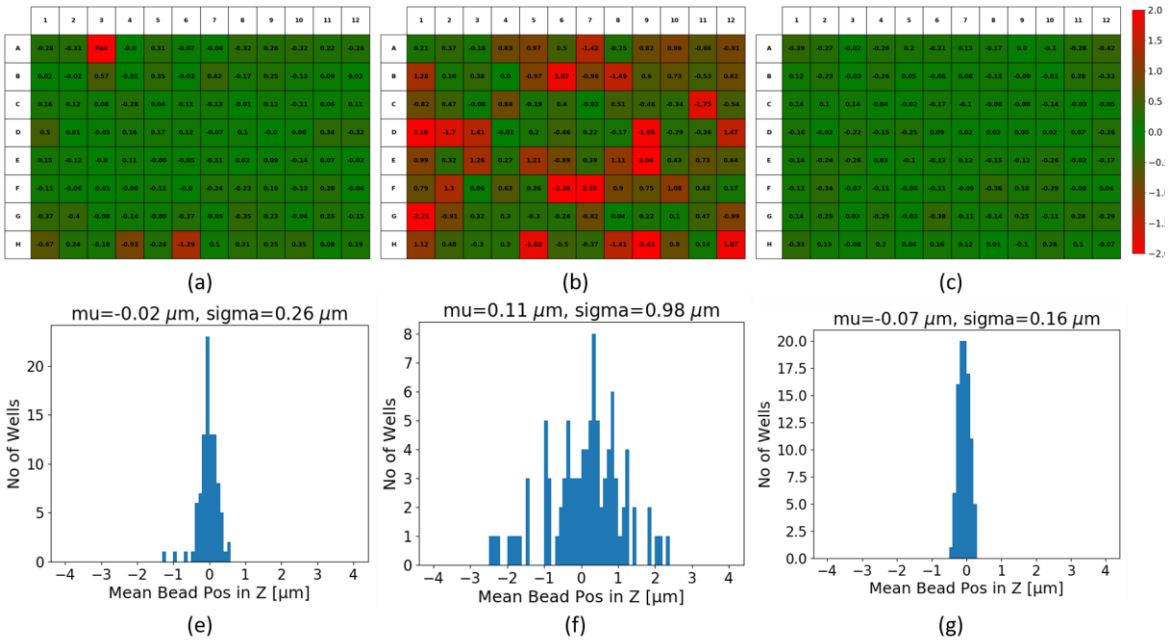

Figure 6.16. Results obtained when automatically imaging 100 nm diameter fluorescent beads (TetraSpeck, T7279) arrayed in a 96-well plate (Brooks life Science Systems, MGB096-1-2-LG-L), for which a through-focus image axial z-stack was automatically recorded in each well. The plate was traversed following a vertical (column-by-column) snake pattern. (a-c) show heat maps of the mean defocus of the beads imaged in each well calculated using *PSFj*. In the top row, the heatmaps summarize the results for when (a) only the short-range autofocus, (b) only the long-range autofocus and (c) the combined 2-step autofocus were employed. The amount of defocus error in each well is encoded in a colour scale in µm, with red indicating that the autofocus failed to locate within +/- 2 µm. Where *PSFj* was unable to determine the defocus of the bead images, or where the mean defocus was outside the +/-2 µm range, the heat map presents a red coloured well with either "Fail" or the mean (out-of-range) defocus value. In the bottom row (e-g), histograms of the mean defocus for each well, with bin widths of 100 nm, are displayed for the bead image z-stacks for which *PSFj* could determine the defocus. Figure reproduced from (Lightley et al., 2022)

6.7 Conclusion

In this chapter, the work developing a CNN-based autofocus has been presented. It has been demonstrated that the hardware-based optical autofocus is able to enable automated imaging of a multiwell plate. The autofocus is able to operate over a range of ±100 µm with an accuracy better than 200 nm. For robust operation, the training data for the networ k was acquired over a period of 10 days and the training of the CNN model took 3 hours. This aggregate model, acquired over the 10-day period, was able to incorporate for thermal variations within the lab into to the dataset. However, once trained the network was able to be applied and correct defocus in only 300 ms. The models were able to be used for periods of months without needing to be retrained. The

performances of the models were characterized by imaging a 96 wellplate arrayed with 100nm Tetraspeck fluorescent beads in each well. For each well after an autofocus correction had been performed, an axial stack of the fluorescent beads was acquired. PSFj was used to determine the error of the autofocus correction for each well. When applied as a 1-step correction, the long-range model was able to traverse the plate when travelling in either a horizontal or vertical snake pattern. The short-range model when operated as a 1-step correction, was not able to traverse the plate when using a horizontal snake pattern. When used in combination as a 2-step correction, the autofocus was able to successfully traverse the plate for both the vertical and horizontal snake movement patterns. The performance of the models was further quantified by performing repeated autofocus corrections at known defocus offsets. These results demonstrated that the short-range model could correct for defocus, to within the DOF within its training range. The long-range model was able to correct the focus to within the training range of the short-range model throughout its training range. When used in combination the autofocus could operate over a range of ±100 μm and correct to within the DOF of the system, to an accuracy of better than 200nm.

7. Automated easySTORM High Content Analysis

As discussed in Chapter 2, high content analysis (HCA) enables more robust image-based cell biology experiments (assays) due to increased statistical power that comes from image data acquired of 100's of fields of view (FOV) from arrays or samples prepared under the same conditions and including replicates and control samples as appropriate. Furthermore, the much higher throughput of HCA compared to manual microscopy can enable many more different samples to be studied, e.g., for cell imaging-based screens or diagnostic applications, e.g., of tissue microarrays. HCA typically entails automated microscopy of samples arrayed in multiwell plates. This involves lateral and axial motorisation and computer control of the microscope stages. Since an experiment imaging 100's of FOVs will typically take 10s to 100s of minutes, it is necessary to maintain in, or repeatedly restore the sample to, the focal plane of the objective lens. As discussed in Chapter 4, this is best realised using a hardware-based autofocus system that minimises any increase in light dose and consequent photobleaching/phototoxicity to the sample. The prospect of flexible, modular open-source HCA or slide scanning instrumentation was the motivation for the development of the optical autofocus systems discussed in Chapters 5 and 6.

In this chapter, I describe the implementation of an automated *easySTORM* microscope on both a commercial (Olympus IX81) microscope frame and on the modular open-source microscope frame (*openFrame*), with the ultimate goal of making super-resolved HCA practical and widely accessible. To date, SMLM has been predominantly limited to manual microscopy apart from pioneering reports of an automated PALM microscope (Holden et al., 2014) and an automated dSTORM/DNA PAINT microscope (Beghin et al., 2017), both implemented on commercial microscope frames. Here I report an open-source approach to super-resolved HCA that is part of a wider approach to develop modular and cost-effective open-source HCA. Besides the implementation of automated SMLM based on *easySTORM*, I briefly describe exemplar super-resolved HCA initial applications to imaging focal adhesions in melanoma cells and to phagocytosis in macrophages. I also discuss my continuing work to develop a 2-channel *openFrame*-based *easySTORM* microscope intended to double the throughput of *easySTORM* HCA.

7.1 Implementation of automated multiwell plate *easySTORM* for super-resolved HCA

I developed two different, automated easySTORM systems: the first on a motorised Olympus IX81 microscope frame, to which I added the optical autofocus system described in Chapter 6 and the second on the low-cost, modular *openFrame* platform, described in Chapter 4, that I added the optical autofocus described in Chapter 5. Here I discuss the specific hardware configurations used and the software for automated easySTORM image data acquisition, which was based on a purpose-built *µManager* 2.0 plugin that communicates - via a socket connection to the local host on the local PC - with the autofocus control software that is written in python.

7.1.1 Automated easySTORM implemented on an Olympus IX81 microscope

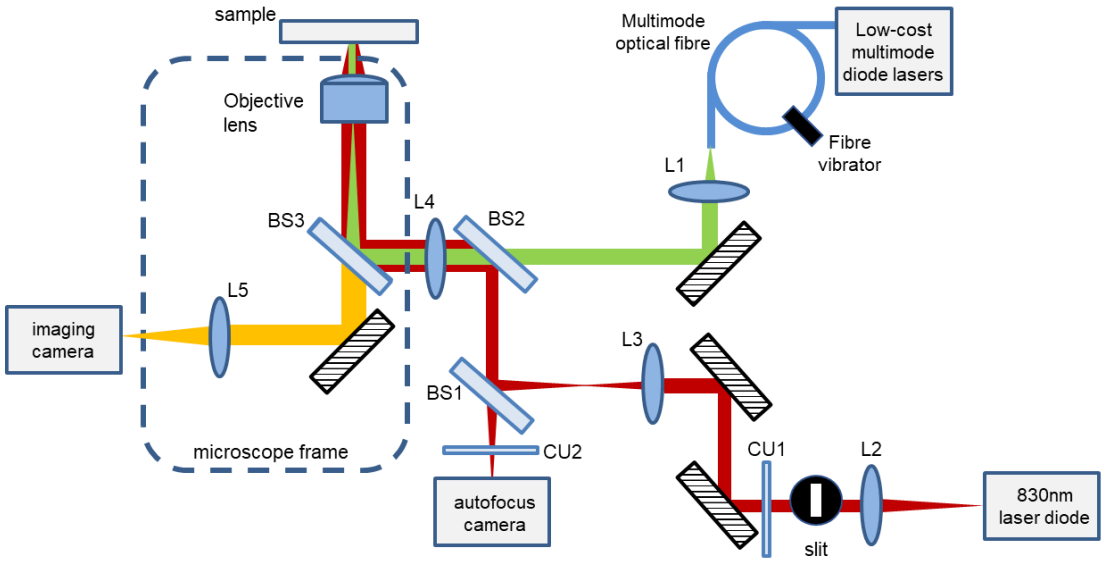

Figure 7.1. Schematic of easySTORM microscope utilizing optical autofocus. The objective lens was an oil immersion 1.3 NA 100x lens with a depth of focus of 600 nm. The focal lengths of the other lenses were L1: 50mm, L2: 18.4mm, L3: 100mm, L4: 200mm, L5: 180mm.

Figure 7.1 shows the system configuration for the implementation of automated *easySTORM* on an automated commercial (Olympus IX81) microscope frame. A motorized Marzhauser XY microscope stage (Marzhauser SCAN IM 112x74) was controlled using a Marzhauser TANGO controller to enable automated multiwell plate imaging or slide scanning. The excitation source used to provide the *easySTORM* illumination was either a homebuilt multiline laserbank (described in Chapter 4) composed of multimode diode lasers or a commercial multiline laserbank (Triline Laserbank, Cairn

Research Ltd) also based on multimode diode lasers. While both laserbanks used multimode laser diodes from Lasertack [https://www.lasertack.com/en/standard-modules], the Cairn laserbank included integrated computer-controlled laser drivers whereas the homebuilt laserbank was controlled using driver modules that I assembled around components from Lasertack and for which I used Arduinos to interface between *µManager* and the laser driver circuits. In each case, the output beams from the multimode diode lasers were combined to a collinear beam using long pass beamsplitters, and either coupled into a 0.22NA multimode optical fibre (Thorlabs FG050LGA) or a 0.1NA multimode fibre (Thorlabs FG105LVA) that was vibrated using a despeckler unit (Cairn Research Ltd, Despeckler P1350/DES/0000) to time average the speckle pattern and provide a uniform illumination for easySTORM (Kwakwa et al., 2016), as described in Chapter 3. This multimode optical fibre was connected to an *openExcite* unit like that described in Chapter 4, section 4.2, that was mounted on the rear port of the Olympus IX81 microscope frame. Here the beam was collimated by L1, a 50 mm focal length lens (Thorlabs AC254-050-A) and then steered by a mirror with tip and tilt controls to the back aperture of the objective lens – enabling switching between epifluorescence or HILO (Tokunaga, Imamoto & Sakata-Sogawa, 2008) illumination.

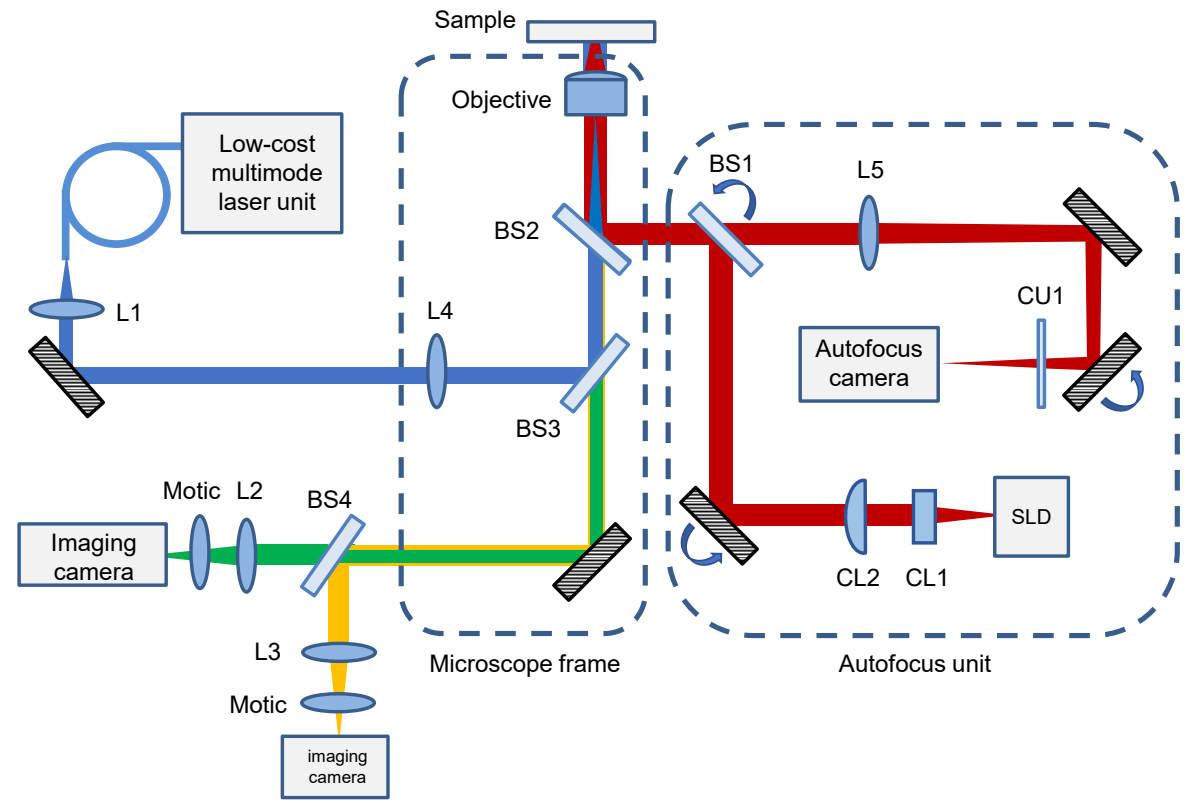

Figure 7.2. Super-resolved HCA microscope with *easySTORM* (Kwakwa et al., 2016) implemented on the *openFrame* configured with two spectrally-resolved fluorescence imaging channels.

After being reflected by the mirror, the excitation beam passes through BS2, a short-pass dichroic beamsplitter (Edmund Optics 69-220) that introduces the autofocus beam to the microscope, and then is focused onto the back focal plane of the 100x objective (Olympus, UplanFl 100x, NA 1.3, oil) by L4, a 200 mm focal length lens (Edmund Optics 49-364), being reflected by BS3, a multiline dichroic long pass dichroic beamsplitter (Chroma, ZT405/462/635/830rpc-UF2). This provides collimated widefield illumination of the sample. A 180 mm focal length tube lens L5, (Olympus Tube lens) is used to form a fluorescence image on the camera. The camera that was predominantly used on this Olympus IX81 microscope was an Andor Zyla 5.5 sCMOS, the sensor of which has a quantum efficiency (QE) of 65% and a pixel size of 6.5 µm.

7.1.2 Automated easySTORM implemented on an *openFrame* microscope

Figure 7.2 shows the system configuration for the implementation of automated *easySTORM* on an *openFrame* microscope. The configuration depicted provides simultaneous image data acquisition in two-spectral fluorescence channels, as discussed below in section 7.1.4. The motorised XY microscope stage used (Zaber ASR100B120B-E03T3A with X-MCB2 controller) has a built in (rotary quadrature) motor encoders and a travel range of 100 x 120 mm. Axial translation of the objective lens was implemented using a piezo-electric linear stage (Physik Instrumente, Q-545.140 with E-873.1AT controller), which has a 13 mm travel range and an integrated linear encoder. Excitation was provided by the homebuilt multiline laserbank described in Chapter 4 (section 4.3). The multimode diode laser beams were coupled into a 0.1 NA multimode optical fibre with a 105 µm diameter core (Thorlabs, FG105LVA) that was connected to an *openExcite* unit. The output from the optical fibre was collimated by L1, a 60 mm focal length lens (Thorlabs AC254-060-A) and this beam was then reflected off a steering mirror, which can be used to direct the beam between epifluorescence and HILO illumination. The beam was then focussed to the back aperture of the 100x objective, (Olympus UplanSApo 100x, NA 1.40, oil) by L4, a 200 mm focal length lens (Edmund Optics 49-364), passing through BS2, a short-pass dichroic beamsplitter (Edmund Optics, 69-220) that reflects light above 800 nm wavelength and is used to introduce the autofocus beam onto the optical axis of the openFrame microscope. The autofocus module used is that described in Chapter 5. The fluorescent emission from the sample is transmitted through BS2 and BS3 (Chroma, ZT405_465_625_825rpc) to form a fluorescence image at the camera. This fluorescence image can be formed either using a single tube lens of 200 mm focal length (e.g. Nikon MXA20696) or, as depicted in Figure 2, BS4, dichroic beamsplitter (Comar, 730 IK 50) can split the fluorescence

radiation into two spectrally resolved channels (e.g., AF488 and AF647), each of which includes a separate tube lens and CMOS camera with a 25 mm diameter bandpass emission filter (Semrock FF03 525/50 and the Chroma ET710/75x respectively) to minimise any spectral crosstalk from the other imaging channel. The cameras that were predominantly used were CellCam Kikkers, which have a pixel size of 4.63 microns and a quantum efficiency of 90%. These were used with either 0.5x (Motic, 1101001901791) or 0.35x (Motic, 1101001904111) demagnifiers to enable higher camera frame rates to be achieved by only reading out part of the camera sensors.

7.1.3 Development of HCA-STORM *µManager* plugin

µManager 2.0 was used to control the hardware and software to implement automated *easySTORM* on both the Olympus IX81 and *openFrame* based systems. The multi-dimension acquisition (MDA) tool inside *µManager* 2.0 was not suitable for *automated two-channel easySTORM* because it didn't have the capability to acquire all the STORM frames for one (spectral) channel before acquiring the frames for the second channel of the same FOV. Therefore, a purpose-built acquisition controlling *µManager* 2.0 plug-in called "*STORMhelper* was written in java and run inside a Conda environment.

STORMhelper controls the acquisition of widefield and STORM image frames automatically based on a table of input variables. The graphical user interface (GUI) for *STORMhelper* is shown in Figure 7.3. This enables the entry of parameters for the acquisition of multiple different channels to be added (or removed) as separate rows of the table (seen near the top of the GUI screenshot). The software will acquire image data according to the different specifications of modality and excitation wavelength in the order that the rows appear in the table. It is important to set the longer wavelength image acquisitions in a FOV before the shorter wavelength acquisitions because the higher photon energy excitation may excite and bleach the longer wavelength fluorophores.

The first column of the table describes the image data acquisition with a naming convention to include the emission wavelength of the dye and whether the acquisition mode was widefield or STORM. The second column is a drop-down list containing all the different available laser channels in the *µManager* configuration file. (The dropdown list is populated by searching within the *µManager* device property list for devices which contain "laser" in their name.) Then there are columns for activation time and activation intensity that control the excitation used to switch the fluorophore dyes into the dark state and induce fluorophore blinking. The excitation intensity is controlled by setting the modulation voltage on the Lasertack diode laser driver between 0 V and +5 V. This in turn

sets the drive current for the laser diode and hence the excitation laser power, up to the maximum output power for the specific laser.

After the activation time period has been reached, the laser intensity is changed to the excitation intensity modulation voltage value, defined in column 5 (“excitation intensity”) of the input table, that is used throughout the STORM acquisition. The typical settings used for the HCA easySTORM use a modulation voltage of 5V for activation for a period of 5-10 seconds and 2.5V during acquisition of the frames for the respective values. Column 6 (“number of frames”) sets the number of STORM frames that will be acquired. If this number of frames is set to 1, then a widefield image can be acquired. The integration time is the camera exposure in milliseconds.

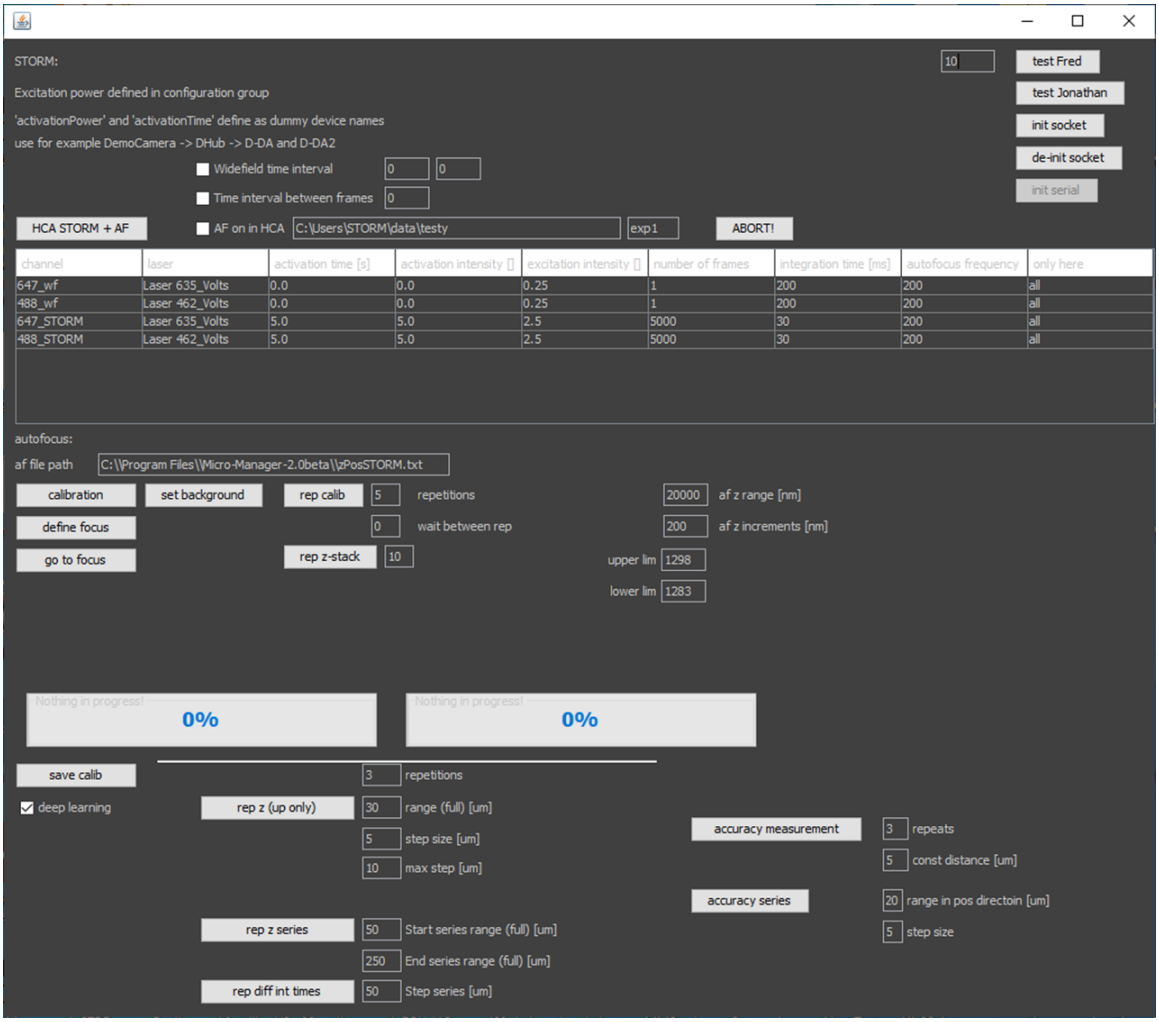

Figure 7.3. STORMhelper GUI showing the input variables in the table to control the laser and camera settings during the automated acquisition

If the autofocus module has been enabled during the acquisition, by checking the “AF on in HCA” checkbox, then the *STORMhelper* plug-in will undertake an autofocus correction every n^{th} frame during the acquisition, where n is set using the autofocus frequency column in the table. Thus, a

value of 200 in the autofocus frequency column means that the focus will be corrected every 200 frames, which interrupts the acquisition of STORM data for ~0.1 seconds. Note that, if the autofocus is in free-running self-lock mode, then the “AF on in HCA” box would not be checked.

The final column in the table (labelled “only here”) defines in which row and/or column of wells in the multiwell plate the settings should be applied. Thus, different power settings can be applied in different wells across the plate for different imaging requirements. If “all” is written into the final column, the same setting will be acquired for every FOV in the position list. The position list needs to specify the well name in the position name, i.e. “A-2” would be row A and column 2. If multiple positions have the same well name, then the plugin will create a unique folder name, such as “A2_2” instead of “A2” again. To apply the settings to only a specific row or column, the letter of the row or the number of the column for the multiwell plate must be written into the final column in the table headings. Multiple rows or columns can be input by delineating the different columns or rows with a comma. In addition, settings can be applied to specific wells by writing for example “A1” in the final column of the table.

7.1.3.1 Socket enabled communication between Python autofocus plug-in and “STORMhelper” µManager plug-in

The *STORMhelper* plug-in can connect to the autofocus software through a socket connection. A socket is an end point between a two-way communication link between two programs running separately on a computer. The socket is bound to a specific port number on the machine. The server for the socket is created in the autofocus (python) program that calculates the current defocus and the *STORMhelper* (java) plug-in is the client that sends messages to the port requesting the current defocus to be calculated. The server runs in the background whilst waiting for a connection request, which can be initiated manually inside the STORMhelper plug-in, to establish two-way communication between the two running programs. Once a connection has been accepted, the python socket waits for a message to be received requesting a defocus calculation to be performed. Once a request message is received, the python autofocus program calculates the current defocus value, which is sent back to the socket to be read by the STORMhelper Java Plugin. Then the Java script can move the stage accordingly to the correct predefined focus.

7.1.4 Simultaneously acquired two-channel *easySTORM*

An *easySTORM* image data acquisition can take ~5-30 minutes per FOV, depending on the sample, which implies 8 - 48 hours would be required for 96 FOV across a multiwell plate for each spectral imaging channel. It is clearly desirable to reduce this data acquisition time for multichannel easySTORM and to this end I have worked to implement simultaneous acquisition of *easySTORM* image data in two spectral channels using, e.g., two cooled CMOS cameras (CellCam Centro or Kikker). Figure 7.2 shows this configuration of an *openFrame*-based *easySTORM* microscope, in which the usual tube lens layer and single camera layer have been replaced by an *openFrame* layer with a dichroic beamsplitter, BS4, mounted in the *openFrame* infinity space that directs the fluorescence to two separate tube lenses and cameras. This enables the sample to be excited simultaneously at two different excitation laser wavelengths for which the outputs from two multimode diode lasers are combined in the multimode optical fibre connected to the *openExcite* module on the *openFrame* fluorescence excitation layer.

The two-channel fluorescence imaging *openFrame* layer is a standard camera layer with a 45-degree mirror positioned in the optical axis of the *openFrame* layer to which an image-splitter (home-built using standard Thorlabs components) is mounted using Thorlabs SM30 tubing connected to a filter cube that contains a short-pass dichroic beamsplitter (Comar, 730 IK 50) selected to separate the fluorescence emission from AF488 and AF647. Each spectral imaging channel is completed using a 200 mm focal length tube lens (Nikon, MXA20696), an emission filter and a camera. A Semrock FF03 525/50 emission filter was used for the AF488 channel and a Chroma ET710/75x filter was used as the emission filter for the AF647 channel. To utilise the cost-effective CellCam cooled CMOS cameras for *easySTORM*, it was decided to demagnify the size of the images so that higher frame rates (up to 30 fps) could be achieved by limiting the readout to a fraction of the camera sensor, as discussed in Chapter 4.4. This was realised using commercial 0.35x demagnifiers (Motic, 1101001904111) mounted at the focal planes of the tube lenses, to which the cameras were attached.

Figure 7.4 shows two colour *easySTORM* images, automatically acquired on this *openFrame*-based microscope, of NIH3T3 cells, in which tubulin was labelled with AF488 and mitochondria were labelled with MitoTracker™ deep red. The cells were arrayed in an 8 well chamber slide and the optical autofocus was used to provide continuous focus correction, without interruptions of the STORM acquisition, during the acquisition of the *easySTORM* image data. For these easySTORM images, 5000 frames were recorded for each FOV in each spectral channel using a CellCam Centro

camera with a 30 ms camera exposure. 3 FOVs were imaged in separate neighbouring wells of the chamber slide during a total image data acquisition time of 8 minutes. These *easySTORM* (Kwakwa et al., 2016) images were reconstructed using ThunderSTORM (Ovesný et al., 2014).

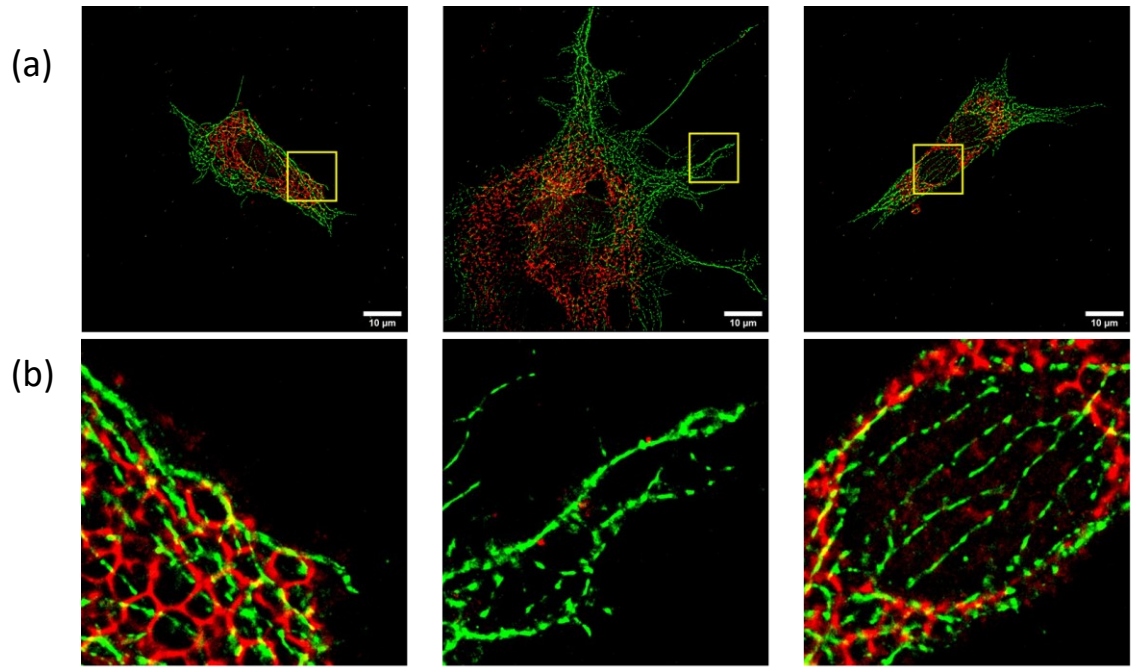

Figure 7.4. (a) *easySTORM* image of NIH3T3 cells with the tubulin labelled with AF488 and mitochondria labelled with MitoTracker™ deep red. The two channels were acquired simultaneously on the *openFrame* using a fan-cooled CMOS camera (CellCam, model Centro 200MR) with 1.4 NA objective lens. (b) shows enlarged ROIs identified by the yellow boxes in (a).

7.2 exemplar easySTORM HCA applications to cell biology

The *easySTORM* HCA system implemented on the Olympus IX81 frame, was applied to exemplar multiwell plate studies of focal adhesions in melanoma cells and of phagocytosis in THP-1 cells. On this microscope, the two-colour *easySTORM* image datasets were acquired sequentially using epi-illumination with the 2-step neural network-based autofocus described in Chapter 6. The resulting *easySTORM* data was analysed using the parallelised implementation of ThunderSTORM (Munro et al., 2019) on 4 nodes of the Imperial College London high performance computing (HPC) cluster.

7.2.1 Melanoma WM2664 multiwell plate STORM

The first exemplar application of *easySTORM* HCA was to image fixed WM2664 melanoma cells arrayed in 24 wells within a 96-well plate, which were imaged on 07/12/2020. A snake like path was used to traverse the multiwell plate and the autofocus was applied every 200 frames during the *easySTORM* acquisition. The *easySTORM* image data were acquired using an Andor Zyla 5.5 with a 30 ms exposure. An initial 5 second activation period was used, at 5V modulation, for both the AF647 and AF488 channels, before dropping the laser power modulation to 2.5V for the acquisition of the frames. 5000 frames were acquired for each FOV of 125.8 x 125.8 µm, resulting in a data volume for each FOV of ~22 Gb. Figure 7.5 shows representative widefield epifluorescence and *easySTORM* images from this experiment. An anti-Paxillin antibody conjugated to AF488 was used to label the focal adhesions structures and phalloidin-Atto 647 was used to label the F-action filaments.

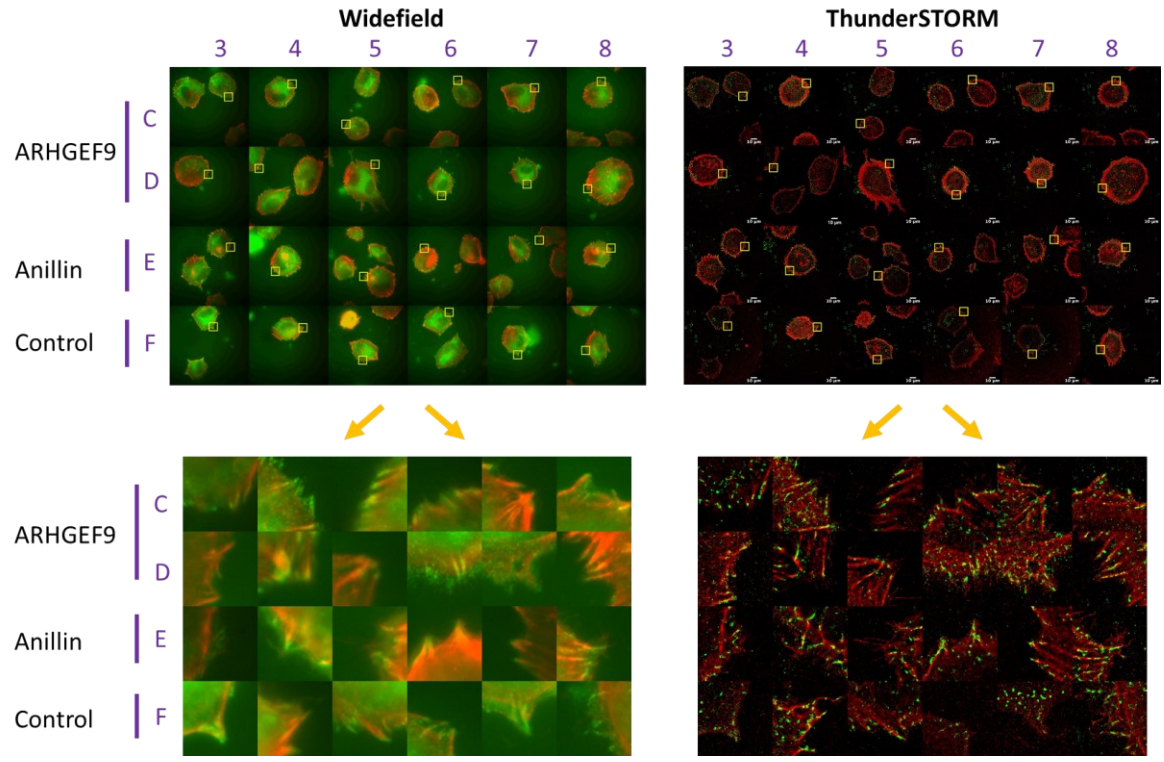

Figure 7.5. Automatically acquired widefield and easySTORM images of fixed WM266-6 Melanoma cells that were arrayed in 6x4 wells of a 96 well plate. An anti-Paxillin antibody conjugated to AF488 was used to label the focal adhesions and the F-actin was labelled using phalloidin-Atto 647. The cells were either mock treated as a control (row F), or they were incubated with siRNA to knock down the ARHGEF9 (rows C and D) and Anillin proteins (row E). The top set of images show a montage of the FOVs acquired in each well. These had a FOV of 125.8 µm x 125.8 µm. The bottom set of images show the expanded ROIs (12.8 µm x 12.8 µm) indicated by the yellow boxes in the top set of images.

The cell culture for the WM266-4 Melanoma cells is described in the Supplementary Material of our paper describing the neural network autofocus (Lightley et al., 2022). Briefly, the cells were reverse transfected with OnTArgetPlus SMARTpools targeting ARHGEF9 and ANILLIN (Dharmacon cat # L-020314-00-0005, cat # L-006838-00-0005) at a concentration of 20 μM in a 6-well plate. The transfections were carried out following the manufacturer's instructions using Lipofectamine RNAimax (Invitrogen). After 48 hours the melanoma cells were trypinised and resuspended in Dulbecco's Modified Eagle Medium (DMEM). Roughly 5000 cells in 200 μl of medium were then transferred to a 96 well glass-bottomed plate (Brooks life Science Systems, MGB096-1-2-LG-L) that had been precoated with 10 ug/ml fibronectin (Sigma-Aldrich). 10 wells for each condition were plated and the cells were allowed to spread for a period of 2.5 hours in an incubator at 37°C before any drug treatment was applied. Duplicate wells were treated with 100 μM ARP2/3 inhibitor (Hetrick et al., 2013; Yamagishi et al., 2018) (CK-666, Sigma-Aldrich), which maintains the complex in an inactive state and inhibits actin nucleation, and SMIFH2 (Rizvi et al., 2009; Kim et al., 2015) (Formin FH2 Domain Inhibitor, Abcam), which stops formin-mediated actin nucleation (50 mM). The cells that were treated with ARP2/3 inhibitor, were allowed to recover before fixation for a period of 30 minutes.

The cells were fixed by adding 200 μl of pre-warmed 4% methanol-free formaldehyde (Thermo) for 10 min at room temperature, after the medium had been removed. The cells were then washed three times with PBS, before being permeabilized using 0.1% Triton X-100 (Sigma-Aldrich) for 10 minutes at room temperature. The cells were then blocked at room temperature with 0.5% BSA in PBS for a period of 1 hour. The cells were then washed again 3 times with PBS. Then an anti-paxillin primary antibody (BD Biosciences), was added in 200 μl block solution at a concentration of 1:500. The plate was then sealed and kept at 4°C overnight. The plate was then washed again 3 times with PBS, and a secondary antibody (Alexa Fluor® 488 goat anti mouse IgG, Invitrogen) was added at a 1:1000 concentration. The plate was then incubated at room temperature for a further 2 hours, after which the plate was washed twice with PBS and phalloidin-Atto 647 (Invitrogen) dye was added at a 1:5000 concentration in PBS to stain the F-actin and incubated for 20 minutes at room temperature. The plate was then washed twice again with PBS solution. Finally, the wells were filled with 200 μl STORM buffer solution before imaging. Whilst imaging, the WM266-4 cells were maintained in DMEM, which was supplemented with 1% Penicillin-Streptomycin and 10% heat-inactivated fetal bovine serum (HI FBS; GIBCO) cultured at 37°C in 5% CO_2.

The widefield images presented in Figure 7.5 are able to show gross overall differences in the cell morphology and differences in the distribution of F-actin and focal adhesions can be seen in the expanded views. However, the easySTORM images enable a more detailed analysis of the structure

of the focal adhesions: in the control row, small, nascent focal adhesions formed at the cell periphery are indicated by the punctate Paxillin foci and in the vicinity around the focal adhesion structures, the levels of polymerased F-actin are low. This organisation of Paxillin and actin seen in the control group is characteristic of nascent focal adhesion structures which are undergoing turnover in dynamic protrusions with high actomyosin flow. This contrasts with the knock down groups in which the Paxillin is less punctate in the cells depleted with either ARHGEF9 or Anillin proteins, but rather forms elongated structures that are aligned along the F-actin. It was noted that multiple paxillin-positive structures were found aligned along single actin filaments. These preliminary results indicate that the super-resolution achievable using easySTORM can provide new information and the ability to undertake automated easySTORM HCA acquisitions can enable systematic studies of this ultrastructure, which could be further analysed using clustering analysis tools such as those described in (Pageon et al., 2016; Ricci et al., 2015; Khater, Nabi & Hamarneh, 2020).

7.2.2 THP1 cells

The second exemplar application of easySTORM HCA addressed the uptake of Streptococcus pneumoniae bacteria in human monocytic THP-1 cells, which are routinely used to model the interactions between macrophages and pathogens (Kohler et al., 2016). The presented data was imaged on 27/08/2020. The THP-1 cells were derived from an acute monocytic leukaemia patient and cultured in Roswell Park Memorial Institute-1640. For this experiment they were arrayed in a 96-well plate (Brooks life Science Systems, MGB096-1-2-LG-L) and supplemented with 10% (v/v) fetal calf serum (FCS) (Bioserum), 2 mM L-glutamine (Sigma Aldrich) and 10 mg/ml Penicillin/Streptomycin (Sigma Aldrich) and incubated at 37°C in 5% CO_2. Approximately 50,000 cells were seeded in each well and were then treated for a period of 48 hours with 10 ng/ml phorbol 12-myristate 13-acetate (PMA) (Sigma Aldrich). The cells in different rows on the multiwell plate were then incubated for between 0 to 60 minutes with Streptococcus pneumoniae immune labelled with AF488, which had been heat-killed. After the incubation, the cells were washed to remove any non-bound bacteria and then fixed with ice cold methanol for 10 minutes before being washed three times with 0.05% Triton in PBS. The cells were then blocked for 2 hours and then stained overnight with a primary monoclonal antibody for alpha-tubulin at a 1:1000 dilution in PBS at 4°C. The next day the cells were washed again 3 times in PBS, before being incubated for 20 minutes at room temperature with a 1:2000 dilution of an anti-mouse secondary antibody which was conjugated to

AF647 (ThermoFisher Scientific). The THP-1 cells were then washed again three times with PBS solution, before being imaged with fresh chemical STORM buffer.

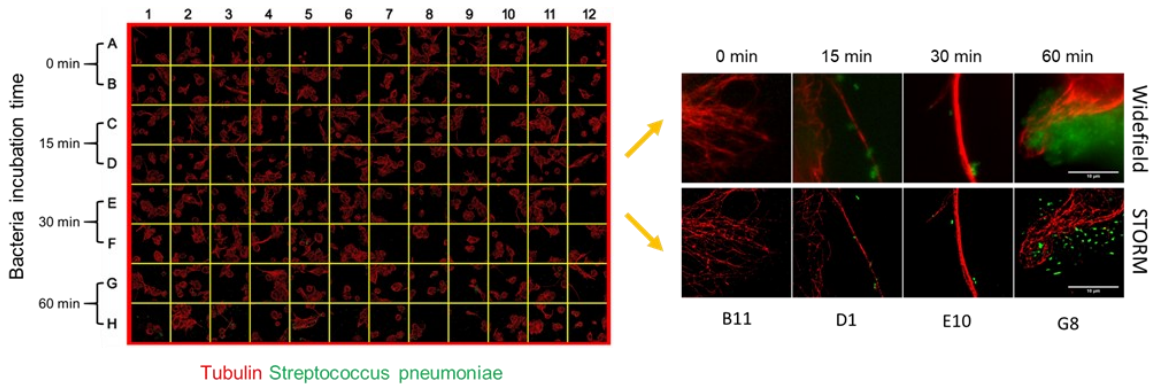

Figure 7.6. Automatically acquired easySTORM images of THP-1 cells arrayed in a 96-well plate. The THP-1 cells were incubated with Streptococcus pneumoniae bacteria and fixed for imaging. The incubation time was increased down the plate in 15-minute intervals. The alpha-tubulin was labelled with AF647 (red) and the Streptococcus pneumoniae was labelled with AF488. Exemplar expanded widefield and easySTORM images of the ROIs from some of the wells are shown in the right-hand side image. As the incubation time increased the uptake of bacteria also increased

The automated *easySTORM* image data acquisition followed a snake-pattern between wells and the 2-step neural network-based autofocus was applied every 200 frames during each *easySTORM* acquisition of 5000 frames per FOV, with a FOV being imaged in each of the 96 wells on the plate with the 2 spectrally resolved channels being acquired sequentially at each FOV. These *easySTORM* images were reconstructed using WindSTORM (Ma, Xu & Liu, 2023) implemented to run on 4 nodes of the Imperial College HPC cluster. Figure 7.6 shows the reconstructed *easySTORM* images from the 96 wells together with representative *easySTORM* and corresponding widefield epifluorescence images of expanded ROI's. It can be seen that the uptake of bacteria into the THP-1 cells increased with the incubation time and there may be an increased overlap between the bacteria and the tubulin filaments. Future work may include a systematic exploration of factors impacting the rate of internalisation of bacteria in patient-derived primary macrophages as well as models like THP-1 cells and the localisation of internalised bacteria within the cells.

7.3 Conclusion

In this chapter I have presented the application and implementation of automated HCA STORM to exemplar biological studies on both a commercial Olympus IX81 frame and an open-source microscope, the *openFrame.* There is also a discussion of the continuing work developing a 2-

channel simultaneously acquiring SMLM system on the openFrame, which improves the throughput of imaging dual channels by a factor of 2. The first implementation of this was to acquire automated simultaneous acquisitions of NIH3T3 cells, which had the mitochondria labelled with MitoTracker Deep Red and the tubulin immunolabelled with AF488. The future aims for this work is to increase the scale and throughput of imaging by automatically and simultaneously acquiring 2-channel SMLM acquisitions in a 96-well plate. In this chapter, the implementation of HCA-STORM on the Olympus IX81 to image Melanoma WM2664 cells and THP1 cells arrayed in 96-well plate formats is also presented.

8. Conclusions and Outlook

This chapter provides a summary of the conclusions and outcomes from the work described in this thesis. There is also a discussion on the outlook for future development of the reported work.

Chapter 1 provided an introduction to the work presented in all subsequent chapters in the thesis.

Chapter 2 gave a brief overview describing the historical development of microscopy. Then there was a description of the photophysical mechanisms involved in fluorescence and a definition of resolution. This chapter also gave a brief description of some commonly used microscopy illumination and imaging modalities. These included widefield epifluorescence, confocal, light-sheet microscopy, multiphoton, TIRF and OPT. There was a description for some super-resolved techniques, including SIM and STED approaches. A more detailed description of SMLM techniques, including STORM, was presented. There is still plenty of scope for future development of super-resolved techniques, which have been developed further with techniques like MinFlux, and the possibility of correlative imaging approaches where multiple imaging modalities can be used on the same FOV within a sample.

Chapter 3 described easySTORM in detail and how it can be implemented on commercial microscope frames. The openExcite module was presented and used to enable both HILO and TIRF illumination to achieve optical sectioning with easySTORM. The performance of easySTORM was verified by imaging nuclear pore complexes as a reference sample using different illumination approaches. EasySTORM was also used to acquire super-resolved immunofluorescent images of histological kidney samples in a process called “histoSTORM”. HistoSTORM was applied to both frozen and paraffin-embedded kidney samples. It was seen that the locations of the IgG deposits were consistent with those observed in EM, giving evidence that histoSTORM could be used in clinical environments. There is a hope to continue developing the idea of histoSTORM to investigate other histological samples and to determine if it could be used as an alternative of EM for clinical diagnosis in settings where there are not the facilities available or expertise required for EM.

easySTORM was initially developed and implemented on a commercial microscope frame by Kwakwa et al. I developed the *openExcite* module, which can be implemented on any microscope

frame. I verified the performance of easySTORM by imaging the nuclear pore complexes. The samples were prepared by Mi Qi Lim and Edwin Garcia. Edwin Garcia developed the staining protocols for the kidney samples and prepared all the samples used in histoSTORM and I developed the imaging protocols. The kidney histological biopsy samples were provided by Dr Candice Roufosse from the Department of Immunology and Inflammation at Imperial College London.

Chapter 4 presents the work undertaken developing a low-cost microscopy platform that can be used for several different imaging modalities. These include the development of a low-cost, modular open hardware microscope frame, called the "openFrame". This is combined with a low-cost laserbank, laser diode controllers and the openExcite module to create a low-cost microscopy system capable of achieving SMLM images. This chapter also describes the work comparing the performance of low-cost (£900 for CellCam Centro and £2000 for CellCam Kikker) cooled CMOS cameras with more expensive (~£15000-£25000) sCMOS alternatives for SMLM. The system was used to acquire easySTORM images of nuclear pore complexes using a TIRF objective on the *openFrame*, using the low-cost and cooled CellCam Kikker cameras, and home-built laserbank. In this chapter there was also a discussion of other published recent open-hardware developments and their applications for open-source microscopy. The total cost of building an openframe as an HCA capable platform for SMLM imaging is in the region of <£25,000. This is on the order of a 5-10x less than the cost of a commercial equivalent. This makes automated SMLM capability more affordable. The future aims for this work include the development of multiple *openFrame* systems for other imaging modalities including FLIM, multiphoton, phase contrast, hyperspectral etc. These systems are now being developed by PhD research students within the Biophotonics group at Imperial College. There is also further work that has already being undertaken, continuing to develop a fully automated SMLM system that is capable of simultaneously acquiring 2-channel SMLM acquisitions of a multiwell plate.

The *openFrame* concept was conceived by Professor Paul French with contributions from others within the Photonics group at Imperial College London. The initial design and development of the *openFrame* was undertaken by Simon Johnson and Martin Kehoe at the Optomechanical Instrumentation workshop within the Optics section at Imperial College London. The *openFrame* CAD design was further developed by Dr Frederik Görlitz of the Photonics Group in collaboration with Cairn Research Ltd. Further development has been undertaken in collaboration with Cairn Research Ltd, developing additional modules which are compatible with the *openFrame*. Sunil Kumar and I assembled the first *openFrame* and provided advice for iterative improvements in design. Paul

French proposed applying low-cost cooled cameras, developed for astronomy, to microscopy. Cairn Research Ltd created the CellCam. I tested and quantified the performance of the CellCam cameras for use with STORM and proposed using the Motic adapters to increase the achievable frame rates needed for SMLM. I designed and developed the laserbank and drivers and interfaced them for use with *µManager*. I implemented low cost easySTORM on the *openFrame* and demonstrated its capability by resolving nuclear pore complexes on the system. The nuclear pore complex samples were prepared by Mi Qi Lim and Edwin Garcia.

Chapter 5 describes the development of a hardware-based autofocus that does not use machine learning. It presents the iterative development of the autofocus design, starting with a knife-edge centroid metric and progressing to a rectangular slit masked beam. Finally, the design utilising a pair of orthogonal cylindrical lenses is presented. The cylindrical lens autofocus was able to operate in a single-shot functionality over a range of ±37.5 µm and as a 2-step approach over a range of ±68 µm. The autofocus was able to achieve an accuracy of <230 nm. This autofocus can be combined with the automated open-hardware platform described in chapter 4, to create an automated multiwell plate scanning system. The range of the autofocus could be extended by combining this design with machine learning, in a similar way that is described in chapter 6. This could further extend the range, as the machine learning can operate with a lower signal to noise ratio. This is the aim for future development of this autofocus. There is also an aim to allow this autofocus to be used with water or air objectives. This would require using the reflected signal from the bottom interface of the coverslip instead of the top. To do this, a lens can be introduced into the optical path which will shift the focus of the collimated autofocus beam to the front surface rather than the upper surface, when the sample is in focus of the imaging camera. This lens can be added or removed to switch between immersion media.

I developed and iterated on the design for the hardware-based autofocus. I demonstrated using offset cylindrical lenses to enable single-shot functionality. I incorporated the autofocus onto the *openFrame* to enable a low-cost HCA SMLM platform. I utilised an SLD to enable background subtraction and improve the performance of the autofocus. After I designed the autofocus and initially implemented it on the *openFrame* using Thorlabs components, Cairn Research Ltd developed a commercial version of the autofocus unit. I quantified the performance of the autofocus and wrote the "*openAF*" *µManager* autofocus plugin and python code to implement the autofocus.

Chapter 6 described the development and training of a neural network-based hardware autofocus that uses a slit to provide varying confocal parameters in its respective orthogonal axes. The two different confocal parameters gave two different metrics for the network to learn from. Namely, a slowly expanding metric for long range and a more accurate and quicker diverging metric along the other orthogonal axis. Two separate models were trained to operate as a sequential 2-step autofocus that could operate in combination over a range of ±100µm whilst having an accuracy within 200 nm and within the depth of field of the objective. The architecture of the MobileNetV2 neural network used was presented with the reasoning why it was chosen. Namely, due to its small memory footprint and its ability to not overfit to the training data. The challenges of developing a robust neural network that can operate over a period of months, under varying lab conditions, is described as well as the necessity to acquire a significantly large training dataset over a period of days. This allowed the model to be used without the need for retraining over a period of months. The autofocus was implemented on a commercial Olympus IX81 stage using an infrared laser diode source. The aim is to further develop this neural network to incorporate the cylindrical lens design. This will allow for the system to become a single shot autofocus with a well-behaved metric for the model to learn from. The currently trained model has already been used to achieve automated multiwell plate SMLM acquisitions. The aim is to continue using this automated system to acquire high-throughput automated SMLM acquisitions of chromatin and Melanoma cells.

Development of the neural network was undertaken by me in collaboration with Dr Arinbjorn Kolbeinsson and with advice from Professor Seth Flaxman. I acquired the training data, trained the model and quantified its performance. I showed the model could operate for periods of months without the need for further training after models were created from composite datasets acquired over multiple days.

Chapter 7 presented the implementation of an automated, high-content analysis system on the Olympus IX81 and the *openFrame* frames for SMLM acquisitions. This included the first implementation of a simultaneously acquired 2-channel SMLM acquisition of NIH3T3 cells, with tubulin immunolabelled with AF488 and the mitochondria labelled with MitoTracker Deep Red. This first demonstration was done automatically, imaging FOVs in 3 wells of an 8-well chamber slide. The future outlook for this work is to increase the throughput of the acquisition by automatically acquiring SMLM 2-channel acquisitions in a 96-well plate format. This would be done using the cylindrical lens based autofocus described in chapter 5, using the openframe platform. This chapter also described the implementation of HCA-easySTORM on the commercial Olympus IX81 frame using

a purpose-built *µManager* plugin, called “STORMhelper”. This system was used to automatically acquire separate SMLM multiwell acquisitions of Melanoma WM2664 cells and THP1 cells. The initial automated acquisitions of the WM2664 melanoma cells, has led to the further investigation of the focal adhesion structures using clustering analysis. This work is ongoing with the aim for further automated acquisitions using the SMLM systems.

I implemented automated HCA-capable systems on both the Olympus IX81 and *openFrame* for SMLM acquisitions. The WM2664 melanoma cells were provided by Dr Vicky Bousgouni and Professor Chris Bakal at the Institute for Cancer Research and prepared for imaging by Dr Edwin Garcia. The THP-1 cells were provided, and prepared for imaging, by Dr Riccardo Wysoczanski at the National Heart and Lung Institute. I developed and wrote the *µManager* plugin “STORMhelper” to control automated SMLM acquisitions.

8.1 Concluding remarks

This thesis has presented the work towards developing a low-cost, automated platform that can perform automated SMLM acquisitions of multiwell plates and high-content analysis. One of the major components of this work has been the development of two novel hardware-based autofocuses that can be implemented on both a standard epi-fluorescent commercial frame or on the presented modular, robust and open-hardware microscope stand, the “*openFrame*”. EasySTORM was implemented on both these systems as a cost-effective technique to image large FOVs using new low cost-cooled CMOS cameras, the CellCam Centro and CellCam Kikker. This has meant that an automated SMLM platform has been developed for approximately a fifth to a tenth of the cost of a commercial equivalent. The aim for the future development of this research would involve introducing these low-cost systems into more clinical, research and teaching environments. This will provide greater access to research-grade SMLM instrumentation. There will be further research into the application of easySTORM to histological samples as a low-cost alternative to electron microscopy. The biological work that has so far being carried out investigating the focal adhesion structure of melanoma cells, has led to further study and research. It is the aim that the platforms developed and presented in this thesis, will be used to further investigate these samples, particularly focusing on focal adhesion function, structure and clustering.

References

Abadi, M., Agarwal, A., Barham, P., Brevdo, E., Chen, Z., et al. (2016) *TensorFlow: Large-Scale Machine Learning on Heterogeneous Distributed Systems*. http://arxiv.org/abs/1603.04467.

Abbe, E. (1873) Beiträge zur Theorie des Mikroskops und der mikroskopischen Wahrnehmung. *Archiv für mikroskopische Anatomie*. 9 (1), 413–418. doi:10.1007/BF02956173.

Airy, G.B.S. (1835) On the diffraction of an object-glass with circular aperture. *SPIE milestone series*. 178, 3–11.

Almada, P., Culley, S. & Henriques, R. (2015) PALM and STORM: Into large fields and high-throughput microscopy with sCMOS detectors. *Methods*. 88, 109–121. doi:10.1016/J.YMETH.2015.06.004.

Alzubaidi, L., Zhang, J., Humaidi, A.J., Al-Dujaili, A., Duan, Y., Al-Shamma, O., Santamaría, J., Fadhel, M.A., Al-Amidie, M. & Farhan, L. (2021) Review of deep learning: concepts, CNN architectures, challenges, applications, future directions. *Journal of Big Data*. 8 (1), 53. doi:10.1186/s40537-021-00444-8.

Ambrose, B., Baxter, J.M., Cully, J., Willmott, M., Steele, E.M., Bateman, B.C., Martin-Fernandez, M.L., Cadby, A., Shewring, J., Aaldering, M. & Craggs, T.D. (2020) The smfBox is an open-source platform for single-molecule FRET. *Nature Communications*. 11 (1), 5641. doi:10.1038/s41467-020-19468-4.

Auer, A., Schlichthaerle, T., Woehrstein, J.B., Schueder, F., Strauss, M.T., Grabmayr, H. & Jungmann, R. (2018) Nanometer-scale Multiplexed Super-Resolution Imaging with an Economic 3D-DNA-PAINT Microscope. *ChemPhysChem*. 19 (22), 3024–3034. doi:https://doi.org/10.1002/cphc.201800630.

Axelrod, D., Burghardt, T.P. & Thompson, N.L. (1984) Total Internal Reflection Fluorescence. *Annual Review of Biophysics and Bioengineering*. 13 (1), 247–268. doi:10.1146/annurev.bb.13.060184.001335.

Baddeley, D., Cannell, M.B. & Soeller, C. (2010) Visualization of Localization Microscopy Data. *Microscopy and Microanalysis*. 16 (1), 64–72. doi:10.1017/S143192760999122X.

Balinovic, A., Albrecht, D. & Endesfelder, U. (2019) Spectrally red-shifted fluorescent fiducial markers for optimal drift correction in localization microscopy. *Journal of Physics D: Applied Physics*. 52 (20), 204002. doi:10.1088/1361-6463/ab0862.

Barber, P.R., Tullis, I.D.C., Pierce, G.P., Newman, R.G., Prentice, J., Rowley, M.I., Matthews, D.R., Ameer-Beg, S.M. & Vojnovic, B. (2013) The gray institute 'open' high-content, fluorescence lifetime microscopes. *Journal of Microscopy*. 251 (2), 154–167. doi:10.1111/jmi.12057.

Bates, M., Blosser, T.R. & Zhuang, X. (2005) Short-Range Spectroscopic Ruler Based on a Single-Molecule Optical Switch. *Phys. Rev. Lett.* 94 (10), 108101. doi:10.1103/PhysRevLett.94.108101.

Beghin, A., Kechkar, A., Butler, C., Levet, F., Cabillic, M., Rossier, O., Giannone, G., Galland, R., Choquet, D. & Sibarita, J.-B. (2017) Localization-based super-resolution imaging meets high-content screening. *Nature Methods*. 14 (12), 1184–1190. doi:10.1038/nmeth.4486.

Betzig, E., Patterson, G.H., Sougrat, R., Lindwasser, O.W., Olenych, S., Bonifacino, J.S., Davidson, M.W., Lippincott-Schwartz, J. & Hess, H.F. (2006) Imaging Intracellular Fluorescent Proteins at Nanometer Resolution. *Science*. 313 (5793), 1642–1645. doi:10.1126/science.1127344.

Bon, P., Bourg, N., Lécart, S., Monneret, S., Fort, E., Wenger, J. & Lévêque-Fort, S. (2015) Three-dimensional nanometre localization of nanoparticles to enhance super-resolution microscopy. *Nature Communications*. 6 (1), 7764. doi:10.1038/ncomms8764.

Bossi, M., Fölling, J., Belov, V.N., Boyarskiy, V.P., Medda, R., Egner, A., Eggeling, C., Schönle, A. & Hell, S.W. (2008) Multicolor Far-Field Fluorescence Nanoscopy through Isolated Detection of Distinct Molecular Species. *Nano Letters*. 8 (8), 2463–2468. doi:10.1021/nl801471d.

Brenner, J.F., Dew, B.S., Horton, J.B., King, T., Neurath, P.W. & Selles, W.D. (1976) An automated microscope for cytologic research a preliminary evaluation. *Journal of Histochemistry & Cytochemistry*. 24 (1), 100–111. doi:10.1177/24.1.1254907.

Bryson-Richardson, R.J., Berger, S., Schilling, T.F., Hall, T.E., Cole, N.J., Gibson, A.J., Sharpe, J. & Currie, P.D. (2007) FishNet: an online database of zebrafish anatomy. *BMC Biology*. 5 (1), 34. doi:10.1186/1741-7007-5-34.

Bugiel, I., König, K. & Wabnitz, H. (1989) Investigation of cells by fluorescence laser scanning microscopy with subnanosecond resolution. *Lasers Life Sci*. 3 (1), 47–53.

Chalfie, M., Tu, Y., Euskirchen, G., Ward, W.W. & Prasher, D.C. (1994) Green Fluorescent Protein as a Marker for Gene Expression. *Science*. 263 (5148), 802–805. doi:10.1126/science.8303295.

Chao, J., Ram, S., Ward, E.S. & Ober, R.J. (2013) Ultrahigh accuracy imaging modality for super-localization microscopy. *Nature Methods*. 10 (4), 335–338. doi:10.1038/nmeth.2396.

Coelho, S., Baek, J., Graus, M.S., Halstead, J.M., Nicovich, P.R., Feher, K., Gandhi, H., Gooding, J.J. & Gaus, K. (2023) Ultraprecise single-molecule localization microscopy enables in situ distance measurements in intact cells. *Science Advances*. 6 (16), eaay8271. doi:10.1126/sciadv.aay8271.

Collins, J.T., Knapper, J., Stirling, J., Mduda, J., Mkindi, C., Mayagaya, V., Mwakajinga, G.A., Nyakyi, P.T., Sanga, V.L., Carbery, D., White, L., Dale, S., Jieh Lim, Z., Baumberg, J.J., Cicuta, P., McDermott, S., Vodenicharski, B. & Bowman, R. (2020) Robotic microscopy for everyone: the OpenFlexure microscope. *Biomedical Optics Express*. 11 (5), 2447–2460. doi:10.1364/BOE.385729.

Coons, A.H., Creech, H.J. & Jones, R.N. (1941) Immunological Properties of an Antibody Containing a Fluorescent Group. *Proceedings of the Society for Experimental Biology and Medicine*. 47 (2), 200–202. doi:10.3181/00379727-47-13084P.

Coons, A.H., Creech, H.J., Jones, R.N. & Berliner, E. (1942) The Demonstration of Pneumococcal Antigen in Tissues by the Use of Fluorescent Antibody1. *The Journal of Immunology*. 45 (3), 159–170. doi:10.4049/jimmunol.45.3.159.

Correia, T., Lockwood, N., Kumar, S., Yin, J., Ramel, M.-C., Andrews, N., Katan, M., Bugeon, L., Dallman, M.J., McGinty, J., Frankel, P., French, P.M.W. & Arridge, S. (2015) Accelerated Optical Projection Tomography Applied to In Vivo Imaging of Zebrafish. *PLOS ONE*. 10 (8), e0136213. https://doi.org/10.1371/journal.pone.0136213.

Culley, S., Albrecht, D., Jacobs, C., Pereira, P.M., Leterrier, C., Mercer, J. & Henriques, R. (2018) Quantitative mapping and minimization of super-resolution optical imaging artifacts. *Nature Methods*. 15 (4), 263–266. doi:10.1038/nmeth.4605.

Cybulski, J.S., Clements, J. & Prakash, M. (2014) Foldscope: Origami-Based Paper Microscope. *PLOS ONE*. 9 (6), e98781. https://doi.org/10.1371/journal.pone.0098781.

Darling, C., Davis, S.P.X., Kumar, S., French, P.M.W. & McGinty, J. (2022) Single-shot optical projection tomography for high-speed volumetric imaging of dynamic biological samples. *Journal of Biophotonics*. n/a (n/a), e202200232. doi:https://doi.org/10.1002/jbio.202200232.

Davidson, M.W. & Campbell, R.E. (2009) Engineered fluorescent proteins: innovations and applications. *Nature Methods*. 6 (10), 713–717. doi:10.1038/nmeth1009-713.

Davis, S.P.X., Wisniewski, L., Kumar, S., Correia, T., Arridge, S.R., Frankel, P., McGinty, J. & French, P.M.W. (2018) Slice-illuminated optical projection tomography. *Optics Letters*. 43 (22), 5555–5558. doi:10.1364/OL.43.005555.

Delmans, M. & Haseloff, J. (2018) µCube: A Framework for 3D Printable Optomechanics. *Journal of Open Hardware*. 2 (1), 2. http://doi.org/10.5334/joh.8.

Dempsey, G.T., Bates, M., Kowtoniuk, W.E., Liu, D.R., Tsien, R.Y. & Zhuang, X. (2009) Photoswitching Mechanism of Cyanine Dyes. *Journal of the American Chemical Society*. 131 (51), 18192–18193. doi:10.1021/ja904588g.

Denk, W., Strickler, J.H. & Webb, W.W. (1990) Two-Photon Laser Scanning Fluorescence Microscopy. *Science*. 248 (4951), 73–76. doi:10.1126/science.2321027.

Deschout, H., Zanacchi, F.C., Mlodzianoski, M., Diaspro, A., Bewersdorf, J., Hess, S.T. & Braeckmans, K. (2014) Precisely and accurately localizing single emitters in fluorescence microscopy. *Nature Methods*. 11 (3), 253–266. doi:10.1038/nmeth.2843.

Diederich, B., Lachmann, R., Carlstedt, S., Marsikova, B., Wang, H., Uwurukundo, X., Mosig, A.S. & Heintzmann, R. (2020) A versatile and customizable low-cost 3D-printed open standard for microscopic imaging. *Nature Communications*. 11 (1), 5979. doi:10.1038/s41467-020-19447-9.

Diekmann, R., Kahnwald, M., Schoenit, A., Deschamps, J., Matti, U. & Ries, J. (2020) Optimizing imaging speed and excitation intensity for single-molecule localization microscopy. *Nature Methods*. 17 (9), 909–912. doi:10.1038/s41592-020-0918-5.

Ding, H., Li, F., Meng, Z., Feng, S., Ma, J., Nie, S. & Yuan, C. (2021) Auto-focusing and quantitative phase imaging using deep learning for the incoherent illumination microscopy system. *Optics Express*. 29 (17), 26385–26403. doi:10.1364/OE.434014.

Dunsby, C. (2008) Optically sectioned imaging by oblique plane microscopy. *Optics Express*. 16 (25), 20306–20316. doi:10.1364/OE.16.020306.

Endesfelder, U. & Heilemann, M. (2015) *Direct Stochastic Optical Reconstruction Microscopy (dSTORM) BT - Advanced Fluorescence Microscopy: Methods and Protocols*. In: P.J. Verveer (ed.). New York, NY, Springer New York. pp. 263–276. doi:10.1007/978-1-4939-2080-8_14.

Engelhardt, J., Keller, J., Hoyer, P., Reuss, M., Staudt, T. & Hell, S.W. (2011) Molecular Orientation Affects Localization Accuracy in Superresolution Far-Field Fluorescence Microscopy. *Nano Letters*. 11 (1), 209–213. doi:10.1021/nl103472b.

Fölling, J., Bossi, M., Bock, H., Medda, R., Wurm, C.A., Hein, B., Jakobs, S., Eggeling, C. & Hell, S.W. (2008) Fluorescence nanoscopy by ground-state depletion and single-molecule return. *Nature Methods*. 5, 943. https://doi.org/10.1038/nmeth.1257.

Fujimaki, Y. & Taniguchi, H. (2014) Reduction of speckle contrast in multimode fibers using piezoelectric vibrator. In: *Proc.SPIE*. 4 March 2014 p. 89601S. doi:10.1117/12.2037431.

Funatsu, T., Harada, Y., Tokunaga, M., Saito, K. & Yanagida, T. (1995) Imaging of single fluorescent molecules and individual ATP turnovers by single myosin molecules in aqueous solution. *Nature*. 374 (6522), 555–559. doi:10.1038/374555a0.

Garcia, E., Lightley, J., Kumar, S., Kalita, R., Gőrlitz, F., Alexandrov, Y., Cook, T., Dunsby, C., Neil, M.A., Roufosse, C.A. & French, P.M. (2021) Application of direct stochastic optical reconstruction microscopy (dSTORM) to the histological analysis of human glomerular disease. *The journal of pathology. Clinical research*. 7 (5), 438–445. doi:10.1002/cjp2.217.

Goodman, J.W. (2007) *Speckle Phenomena in Optics: Theory and Applications*. Roberts & Company. doi:9781936221141.

Göppert-Mayer, M. (1931) Über Elementarakte mit zwei Quantensprüngen. *Annalen der Physik*. 401 (3), 273–294. doi:https://doi.org/10.1002/andp.19314010303.

Görlitz, F., Kelly, D.J., Warren, S.C., Alibhai, D., West, L., et al. (2017) Open Source High Content Analysis Utilizing Automated Fluorescence Lifetime Imaging Microscopy. *JoVE*. (119), e55119. doi:doi:10.3791/55119.

Grimm, J.B., English, B.P., Choi, H., Muthusamy, A.K., Mehl, B.P., Dong, P., Brown, T.A., Lippincott-Schwartz, J., Liu, Z., Lionnet, T. & Lavis, L.D. (2016) Bright photoactivatable fluorophores for single-molecule imaging. *Nature methods*. 13 (12), 985–988. doi:10.1038/nmeth.4034.

Guo, W., Kumar, S., Görlitz, F., Garcia, E., Alexandrov, Y., Munro, I., Kelly, D.J., Warren, S., Thorpe, P., Dunsby, C. & French, P. (2019) Automated Fluorescence Lifetime Imaging High-Content Analysis of Förster Resonance Energy Transfer between Endogenously Labeled Kinetochore Proteins in Live Budding Yeast Cells. *SLAS TECHNOLOGY: Translating Life Sciences Innovation*. 24 (3), 308–320. doi:10.1177/2472630318819240.

Gustafsson, M.G.L. (2000) Surpassing the lateral resolution limit by a factor of two using structured illumination microscopy. *Journal of Microscopy*. 198 (2), 82–87. doi:https://doi.org/10.1046/j.1365-2818.2000.00710.x.

Gwosch, K.C., Pape, J.K., Balzarotti, F., Hoess, P., Ellenberg, J., Ries, J. & Hell, S.W. (2020) MINFLUX nanoscopy delivers 3D multicolor nanometer resolution in cells. *Nature Methods*. 17 (2), 217–224. doi:10.1038/s41592-019-0688-0.

Haas, M. (1997) A reevaluation of routine electron microscopy in the examination of native renal biopsies. *Journal of the American Society of Nephrology : JASN*. 8 (1), 70–76. doi:10.1681/ASN.V8170.

Haas, M., Seshan, S. v, Barisoni, L., Amann, K., Bajema, I.M., Becker, J.U., Joh, K., Ljubanovic, D., Roberts, I.S.D., Roelofs, J.J., Sethi, S., Zeng, C. & Jennette, J.C. (2020) Consensus definitions for glomerular lesions by light and electron microscopy: recommendations from a working group of the Renal Pathology Society. *Kidney international*. 98 (5), 1120–1134. doi:10.1016/j.kint.2020.08.006.

Heilemann, M., van de Linde, S., Schüttpelz, M., Kasper, R., Seefeldt, B., Mukherjee, A., Tinnefeld, P. & Sauer, M. (2008) Subdiffraction-Resolution Fluorescence Imaging with Conventional Fluorescent Probes. *Angewandte Chemie International Edition*. 47 (33), 6172–6176. doi:10.1002/anie.200802376.

Heilemann, M., Margeat, E., Kasper, R., Sauer, M. & Tinnefeld, P. (2005) Carbocyanine Dyes as Efficient Reversible Single-Molecule Optical Switch. *Journal of the American Chemical Society*. 127 (11), 3801–3806. doi:10.1021/ja044686x.

Heilemann, M., van de Linde, S., Mukherjee, A. & Sauer, M. (2009) Super-Resolution Imaging with Small Organic Fluorophores. *Angewandte Chemie International Edition*. 48 (37), 6903–6908. doi:https://doi.org/10.1002/anie.200902073.

Hell, S.W. & Wichmann, J. (1994) Breaking the diffraction resolution limit by stimulated emission: stimulated-emission-depletion fluorescence microscopy. *Opt. Lett.* 19 (11), 780–782. doi:10.1364/OL.19.000780.

Hess, S.T., Girirajan, T.P.K. & Mason, M.D. (2006) Ultra-high resolution imaging by fluorescence photoactivation localization microscopy. *Biophysical journal*. 91 (11), 4258–4272. doi:10.1529/biophysj.106.091116.

Hetrick, B., Han, M.S., Helgeson, L.A. & Nolen, B.J. (2013) Small Molecules CK-666 and CK-869 Inhibit Actin-Related Protein 2/3 Complex by Blocking an Activating Conformational Change. *Chemistry & Biology*. 20 (5), 701–712. doi:https://doi.org/10.1016/j.chembiol.2013.03.019.

Hink, M.A., Griep, R.A., Borst, J.W., van Hoek, A., Eppink, M.H.M., Schots, A. & Visser, A.J.W.G. (2000) Structural Dynamics of Green Fluorescent Protein Alone and Fused with a Single Chain Fv Protein*. *Journal of Biological Chemistry*. 275 (23), 17556–17560. doi:https://doi.org/10.1074/jbc.M001348200.

Hohlbein, J., Diederich, B., Marsikova, B., Reynaud, E.G., Holden, S., Jahr, W., Haase, R. & Prakash, K. (2022) Open microscopy in the life sciences: quo vadis? *Nature Methods*. 19 (9), 1020–1025. doi:10.1038/s41592-022-01602-3.

Holden, S.J., Pengo, T., Meibom, K.L., Fernandez, C.F., Collier, J. & Manley, S. (2014) High throughput 3D super-resolution microscopy reveals Caulobacter crescentus in vivo Z-ring organization. *Proceedings of the National Academy of Sciences of the United States of America*. 111 (12), 4566–4571. http://www.jstor.org/stable/23771107.

Holm, T., Klein, T., Löschberger, A., Klamp, T., Wiebusch, G., van de Linde, S. & Sauer, M. (2014) A blueprint for cost-efficient localization microscopy. *Chemphyschem : a European journal of chemical physics and physical chemistry*. 15 (4), 651–654. doi:10.1002/cphc.201300739.

Hooke, R. (1665) *Micrographia: or some physiological descriptions of minute bodies made by magnifying glasses, with observations and inquiries thereupon*. Courier Corporation.

Howard, A., Sandler, M., Chu, G., Chen, L.-C., Chen, B., Tan, M., Wang, W., Zhu, Y., Pang, R., Vasudevan, V., Le, Q. V. & Adam, H. (2019) *Searching for MobileNetV3*. https://arxiv.org/abs/1905.02244.

Howard, A.G., Zhu, M., Chen, B., Kalenichenko, D., Wang, W., Weyand, T., Andreetto, M. & Adam, H. (2017) *MobileNets: Efficient Convolutional Neural Networks for Mobile Vision Applications*. http://arxiv.org/abs/1704.04861.

Huang, B., Wang, W., Bates, M. & Zhuang, X. (2008) Three-Dimensional Super-Resolution Imaging by Stochastic Optical Reconstruction Microscopy. *Science*. 319 (5864), 810–813. doi:10.1126/science.1153529.

Huang, F., Hartwich, T.M.P., Rivera-Molina, F.E., Lin, Y., Duim, W.C., Long, J.J., Uchil, P.D., Myers, J.R., Baird, M.A., Mothes, W., Davidson, M.W., Toomre, D. & Bewersdorf, J. (2013) Video-rate nanoscopy using sCMOS camera–specific single-molecule localization algorithms. *Nature Methods*. 10 (7), 653–658. doi:10.1038/nmeth.2488.

Huisken, J., Swoger, J., Del Bene, F., Wittbrodt, J. & Stelzer, E.H.K. (2004) Optical Sectioning Deep Inside Live Embryos by Selective Plane Illumination Microscopy. *Science*. 305 (5686), 1007–1009. doi:10.1126/science.1100035.

Jiang, S., Bian, Z., Huang, X., Song, P., Zhang, H., Zhang, Y. & Zheng, G. (2019) Rapid and robust whole slide imaging based on LED-array illumination and color-multiplexed single-shot autofocusing. *Quantitative Imaging in Medicine and Surgery; Vol 9, No 5 (May 31, 2019): Quantitative Imaging in Medicine and Surgery (Advanced Optical Imaging in Biomedicine Special Issue)*. https://qims.amegroups.com/article/view/25836.

Jungmann, R., Steinhauer, C., Scheible, M., Kuzyk, A., Tinnefeld, P. & Simmel, F.C. (2010) Single-Molecule Kinetics and Super-Resolution Microscopy by Fluorescence Imaging of Transient Binding on DNA Origami. *Nano Letters*. 10 (11), 4756–4761. doi:10.1021/nl103427w.

Juskaitis, R. (2006) *Handbook Of Bio-logical Confocal Microscopy Cgapter 11*. Third.

Kalita, R., Flanagan, W., Lightley, J., Kumar, S., Alexandrov, Y., Garcia, E., Hintze, M., Barkoulas, M., Dunsby, C. & French, P.M.W. (2021) Single-shot phase contrast microscopy using polarisation-resolved differential phase contrast. *Journal of Biophotonics*. 14 (12), e202100144. doi:https://doi.org/10.1002/jbio.202100144.

Kasha, M. (1950) Characterization of electronic transitions in complex molecules. *Discuss. Faraday Soc.* 9 (0), 14–19. doi:10.1039/DF9500900014.

Kay, S. (1993) *Fundamentals of Statistical Signal Processing Vol. 1: Estimation Theory*. Prentice Hall PTR.

Keppler, A., Gendreizig, S., Gronemeyer, T., Pick, H., Vogel, H. & Johnsson, K. (2003) A general method for the covalent labeling of fusion proteins with small molecules in vivo. *Nature biotechnology*.21 (1). doi:10.1038/nbt765.

Keppler, A., Pick, H., Arrivoli, C., Vogel, H. & Johnsson, K. (2004) Labeling of fusion proteins with synthetic fluorophores in live cells. *Proceedings of the National Academy of Sciences of the United States of America*. 101 (27), 9955–9959. doi:10.1073/pnas.0401923101.

Khater, I.M., Nabi, I.R. & Hamarneh, G. (2020) A Review of Super-Resolution Single-Molecule Localization Microscopy Cluster Analysis and Quantification Methods. *Patterns (New York, N.Y.)*. 1 (3), 100038. doi:10.1016/j.patter.2020.100038.

Kim, H.-C., Jo, Y.-J., Kim, N.-H. & Namgoong, S. (2015) Small Molecule Inhibitor of Formin Homology 2 Domains (SMIFH2) Reveals the Roles of the Formin Family of Proteins in Spindle Assembly and Asymmetric Division in Mouse Oocytes. *PLOS ONE*. 10 (4), e0123438. https://doi.org/10.1371/journal.pone.0123438.

Kingma, D.P. & Ba, J. (2014) *Adam: A Method for Stochastic Optimization*. http://arxiv.org/abs/1412.6980.

Klar, T.A., Jakobs, S., Dyba, M., Egner, A. & Hell, S.W. (2000) Fluorescence microscopy with diffraction resolution barrier broken by stimulated emission. *Proceedings of the National Academy of Sciences*. 97 (15), 8206–8210. doi:10.1073/pnas.97.15.8206.

Kner, P., Chhun, B.B., Griffis, E.R., Winoto, L. & Gustafsson, M.G.L. (2009) Super-resolution video microscopy of live cells by structured illumination. *Nature Methods*. 6 (5), 339–342. doi:10.1038/nmeth.1324.

Köhler, A. (1893) Ein neues Beleuchtungsverfahren für mikrophotographische Zwecke. *Zeitschrift für wissenschaftliche Mikroskopie und für Mikroskopische Technik*. 10 (4), 433–440.

Köhler, A. (1894) New Method of Illumination for Photomicrographical Purposes. *Journal of the Royal Microscopical Society*. 14, 261–262.

Köhler, H. (1981) On Abbe's Theory of Image Formation in the Microscope. *Optica Acta: International Journal of Optics*. 28 (12), 1691–1701. doi:10.1080/713820514.

Kohler, T.P., Scholz, A., Kiachludis, D. & Hammerschmidt, S. (2016) Induction of Central Host Signaling Kinases during Pneumococcal Infection of Human THP-1 Cells . *Frontiers in Cellular and Infection Microbiology* .6. https://www.frontiersin.org/articles/10.3389/fcimb.2016.00048.

Kottke, T., van de Linde, S., Sauer, M., Kakorin, S. & Heilemann, M. (2010) Identification of the Product of Photoswitching of an Oxazine Fluorophore Using Fourier Transform Infrared Difference Spectroscopy. *The Journal of Physical Chemistry Letters*. 1 (21), 3156–3159. doi:10.1021/jz101300t.

Kremers, G.-J., Gilbert, S.G., Cranfill, P.J., Davidson, M.W. & Piston, D.W. (2011) Fluorescent proteins at a glance. *Journal of Cell Science*. 124 (2), 157–160. doi:10.1242/jcs.072744.

Křížek, P., Raška, I. & Hagen, G.M. (2011) Minimizing detection errors in single molecule localization microscopy. *Optics Express*. 19 (4), 3226–3235. doi:10.1364/OE.19.003226.

Kumar, S., Dunsby, C., Beule, P.A.A. De, Owen, D.M., Anand, U., Lanigan, P.M.P., Benninger, R.K.P., Davis, D.M., Neil, M.A.A., Anand, P., Benham, C., Naylor, A. & French, P.M.W. (2007) Multifocal multiphoton excitation and time correlated single photon counting detection for 3-D fluorescence lifetime imaging. *Optics Express*. 15 (20), 12548–12561. doi:10.1364/OE.15.012548.

Kumar, S., Lockwood, N., Ramel, M.-C., Correia, T., Ellis, M., Alexandrov, Y., Andrews, N., Patel, R., Bugeon, L., Dallman, M.J., Brandner, S., Arridge, S., Katan, M., McGinty, J., Frankel, P. & French, P.M.W. (2016) Quantitative in vivo optical tomography of cancer progression & vasculature development in adult zebrafish. *Oncotarget; Vol 7, No 28*. https://www.oncotarget.com/article/9756/text/.

Kurien, A.A., Larsen, C., Rajapurkar, M., Bonsib, S.M. & Walker, P. (2016) Lack of electron microscopy hinders correct renal biopsy diagnosis: A study from India. *Ultrastructural pathology*. 40 (1), 14–17. doi:10.3109/01913123.2015.1120837.

Kwakwa, K., Savell, A., Davies, T., Munro, I., Parrinello, S., Purbhoo, M.A., Dunsby, C., Neil, M.A.A. & French, P.M.W. (2016) easySTORM: a robust, lower-cost approach to localisation and TIRF microscopy. *Journal of Biophotonics*. 9 (9), 948–957.

Lai, W.L., Yeh, T.H., Chen, P.M., Chan, C.K., Chiang, W.C., Chen, Y.M., Wu, K.D. & Tsai, T.J. (2015) Membranous nephropathy: a review on the pathogenesis, diagnosis, and treatment. *Journal of the Formosan Medical Association = Taiwan yi zhi*. 114 (2), 102–111. doi:10.1016/j.jfma.2014.11.002.

Laine, R.F., Tosheva, K.L., Gustafsson, N., Gray, R.D.M., Almada, P., Albrecht, D., Risa, G.T., Hurtig, F., Lindås, A.-C., Baum, B., Mercer, J., Leterrier, C., Pereira, P.M., Culley, S. & Henriques, R. (2019) NanoJ: a high-performance open-source super-resolution microscopy toolbox. *Journal of physics D: Applied physics*. 52 (16), 163001. doi:10.1088/1361-6463/ab0261.

Lakowicz, J.R. (2011) *Principles of Fluorescence Spectroscopy*. New York, NY, UNITED STATES, Springer. http://ebookcentral.proquest.com/lib/imperial/detail.action?docID=6310585.

LeCun, Y., Bengio, Y. & Hinton, G. (2015) Deep learning. *Nature*. 521 (7553), 436–444. doi:10.1038/nature14539.

Leduc, C., Salles, A., Shorte, S.L. & Etienne-Manneville, S. (2018) Imaging Intermediate Filaments and Microtubules with 2-dimensional Direct Stochastic Optical Reconstruction Microscopy. *Journal of visualized experiments : JoVE*. (133). doi:10.3791/57087.

Legant, W.R., Shao, L., Grimm, J.B., Brown, T.A., Milkie, D.E., Avants, B.B., Lavis, L.D. & Betzig, E. (2016) High-density three-dimensional localization microscopy across large volumes. *Nature Methods*. 13 (4), 359–365. doi:10.1038/nmeth.3797.

Lelek, M., Gyparaki, M.T., Beliu, G., Schueder, F., Griffié, J., Manley, S., Jungmann, R., Sauer, M., Lakadamyali, M. & Zimmer, C. (2021) Single-molecule localization microscopy. *Nature Reviews Methods Primers*. 1 (1), 39. doi:10.1038/s43586-021-00038-x.

Li, C., Moatti, A., Zhang, X., Troy Ghashghaei, H. & Greenbaum, A. (2021) Deep learning-based autofocus method enhances image quality in light-sheet fluorescence microscopy. *Biomedical Optics Express*. 12 (8), 5214–5226. doi:10.1364/BOE.427099.

Li, H., Krishnamurthy, D., Li, E., Vyas, P., Akireddy, N., Chai, C. & Prakash, M. (2020) Squid: Simplifying Quantitative Imaging Platform Development and Deployment. *bioRxiv*. 2020.12.28.424613. doi:10.1101/2020.12.28.424613.

Li, H., Soto-Montoya, H., Voisin, M., Valenzuela, L.F. & Prakash, M. (2019) Octopi: Open configurable high-throughput imaging platform for infectious disease diagnosis in the field. *bioRxiv*. 684423. doi:10.1101/684423.

Liao, J., Bian, L., Bian, Z., Zhang, Z., Patel, C., Hoshino, K., Eldar, Y.C. & Zheng, G. (2016) Single-frame rapid autofocusing for brightfield and fluorescence whole slide imaging. *Biomedical Optics Express*. 7 (11), 4763–4768. doi:10.1364/BOE.7.004763.

Lightley, J., Görlitz, F., Kumar, S., Kalita, R., Kolbeinsson, A., Garcia, E., Alexandrov, Y., Bousgouni, V., Wysoczanski, R., Barnes, P., Donnelly, L., Bakal, C., Dunsby, C., Neil, M.A.A., Flaxman, S. & French, P.M.W. (2022) Robust deep learning optical autofocus system applied to automated multiwell plate single molecule localization microscopy. *Journal of Microscopy*. 288 (2), 130–141. doi:https://doi.org/10.1111/jmi.13020.

Lightley, J., Kumar, S., Lim, M.Q., Garcia, E., Görlitz, F., Alexandrov, Y., Parrado, T., Hollick, C., Steele, E., Roßmann, K., Graham, J., Broichhagen, J., McNeish, I.A., Roufosse, C.A., Neil, M.A.A., Dunsby, C. & French, P.M.W. (2023) openFrame: A modular, sustainable, open microscopy platform with single-shot, dual-axis optical autofocus module providing high precision and long range of operation. *Journal of Microscopy*. 292 (2), 64–77. doi:https://doi.org/10.1111/jmi.13219.

Lin, Y., Long, J.J., Huang, F., Duim, W.C., Kirschbaum, S., Zhang, Y., Schroeder, L.K., Rebane, A.A., Velasco, M.G.M., Virrueta, A., Moonan, D.W., Jiao, J., Hernandez, S.Y., Zhang, Y. & Bewersdorf, J.

(2015) Quantifying and Optimizing Single-Molecule Switching Nanoscopy at High Speeds. *PLOS ONE*. 10 (5), e0128135. https://doi.org/10.1371/journal.pone.0128135.

van de Linde, S., Krstić, I., Prisner, T., Doose, S., Heilemann, M. & Sauer, M. (2011) Photoinduced formation of reversible dye radicals and their impact on super-resolution imaging. *Photochemical & Photobiological Sciences*. 10 (4), 499–506. doi:10.1039/C0PP00317D.

LIRON, Y., PARAN, Y., ZATORSKY, N.G., GEIGER, B. & KAM, Z. (2006) Laser autofocusing system for high-resolution cell biological imaging. *Journal of Microscopy*. 221 (2), 145–151. doi:https://doi.org/10.1111/j.1365-2818.2006.01550.x.

Liu, C.-S., Hu, P.-H., Wang, Y.-H., Ke, S.-S., Lin, Y.-C., Chang, Y.-H. & Hornj, J.-B. (2010) Novel fast laser-based auto-focusing microscope. In: *2010 IEEE Sensors*. 2010 IEEE. pp. 481–485.

Liu, X., Jiang, Y., Cui, Y., Yuan, J. & Fang, X. (2022) Deep learning in single-molecule imaging and analysis: recent advances and prospects. *Chemical Science*. 13 (41), 11964–11980. doi:10.1039/D2SC02443H.

Los, G. V, Encell, L.P., McDougall, M.G., Hartzell, D.D., Karassina, N., et al. (2008) HaloTag: A Novel Protein Labeling Technology for Cell Imaging and Protein Analysis. *ACS Chemical Biology*. 3 (6), 373–382. doi:10.1021/cb800025k.

Lukyanov, K.A., Chudakov, D.M., Lukyanov, S. & Verkhusha, V. V (2005) Photoactivatable fluorescent proteins. *Nature Reviews Molecular Cell Biology*. 6 (11), 885–890. doi:10.1038/nrm1741.

Luo, Y., Huang, L., Rivenson, Y. & Ozcan, A. (2021) Single-Shot Autofocusing of Microscopy Images Using Deep Learning. *ACS Photonics*. 8 (2), 625–638. doi:10.1021/acsphotonics.0c01774.

Ma, H., Xu, J. & Liu, Y. (2022) WindSTORM: Robust online image processing for high-throughput nanoscopy. *Science Advances*. 5 (4), eaaw0683. doi:10.1126/sciadv.aaw0683.

Ma, H., Xu, J. & Liu, Y. (2023) WindSTORM: Robust online image processing for high-throughput nanoscopy. *Science Advances*. 5 (4), eaaw0683. doi:10.1126/sciadv.aaw0683.

Maia Chagas, A., Prieto-Godino, L.L., Arrenberg, A.B. & Baden, T. (2017) The €100 lab: A 3D-printable open-source platform for fluorescence microscopy, optogenetics, and accurate temperature control during behaviour of zebrafish, Drosophila, and Caenorhabditis elegans. *PLOS Biology*. 15 (7), e2002702. https://doi.org/10.1371/journal.pbio.2002702.

Martens, K.J.A., van Beljouw, S.P.B., van der Els, S., Vink, J.N.A., Baas, S., Vogelaar, G.A., Brouns, S.J.J., van Baarlen, P., Kleerebezem, M. & Hohlbein, J. (2019) Visualisation of dCas9 target search in vivo using an open-microscopy framework. *Nature communications*. 10 (1), 3552. doi:10.1038/s41467-019-11514-0.

McGinty, J., Tahir, K.B., Laine, R., Talbot, C.B., Dunsby, C., Neil, M.A.A., Quintana, L., Swoger, J., Sharpe, J. & French, P.M.W. (2008) Fluorescence lifetime optical projection tomography. *Journal of Biophotonics*. 1 (5), 390–394. doi:https://doi.org/10.1002/jbio.200810044.

McGinty, J., Taylor, H.B., Chen, L., Bugeon, L., Lamb, J.R., Dallman, M.J. & French, P.M.W. (2011) In vivo fluorescence lifetime optical projection tomography. *Biomedical Optics Express*. 2 (5), 1340–1350. doi:10.1364/BOE.2.001340.

Mehta, S.B. & Sheppard, C.J.R. (2009) Quantitative phase-gradient imaging at high resolution with asymmetric illumination-based differential phase contrast. *Optics Letters*. 34 (13), 1924–1926. doi:10.1364/OL.34.001924.

Mie, G. (1908) Beiträge zur Optik trüber Medien, speziell kolloidaler Metallösungen. *Annalen der Physik*. 330 (3), 377–445. doi:https://doi.org/10.1002/andp.19083300302.

Minsky, M. (1957) *Microscopy apparatus*.

Mlodzianoski, M.J., Schreiner, J.M., Callahan, S.P., Smolková, K., Dlasková, A., Šantorová, J., Ježek, P. & Bewersdorf, J. (2011) Sample drift correction in 3D fluorescence photoactivation localization microscopy. *Optics Express*. 19 (16), 15009–15019. doi:10.1364/OE.19.015009.

Moerner, W.E. & Kador, L. (1989) Optical detection and spectroscopy of single molecules in a solid. *Physical Review Letters*. 62 (21), 2535–2538. doi:10.1103/PhysRevLett.62.2535.

Mortensen, K.I., Churchman, L.S., Spudich, J.A. & Flyvbjerg, H. (2010) Optimized localization analysis for single-molecule tracking and super-resolution microscopy. *Nature Methods*. 7 (5), 377–381. doi:10.1038/nmeth.1447.

Munro, I., Garcia, E., Yan, M., Guldbrand, S., Kumar, S., Kwakwa, K., Dunsby, C., Neil, M.A.A. & French, P.M.W. (2019) Accelerating single molecule localization microscopy through parallel processing on a high-performance computing cluster. *Journal of Microscopy*. 273 (2), 148–160. doi:https://doi.org/10.1111/jmi.12772.

Murphy, D.B. & Davidson, M.W. (2012) *Fundamentals of Light Microscopy and Electronic Imaging*. Somerset, UNITED STATES, John Wiley & Sons, Incorporated. http://ebookcentral.proquest.com/lib/imperial/detail.action?docID=918267.

Nieuwenhuizen, R.P.J., Lidke, K.A., Bates, M., Puig, D.L., Grünwald, D., Stallinga, S. & Rieger, B. (2013) Measuring image resolution in optical nanoscopy. *Nature Methods*. 10 (6), 557–562. doi:10.1038/nmeth.2448.

Ntziachristos, V. (2010) Going deeper than microscopy: the optical imaging frontier in biology. *Nature Methods*. 7 (8), 603–614. doi:10.1038/nmeth.1483.

Nyquist, H. (1928) Certain Topics in Telegraph Transmission Theory. *Transactions of the American Institute of Electrical Engineers*. 47 (2), 617–644. doi:10.1109/T-AIEE.1928.5055024.

Oheim, M. (2011) Advances and challenges in high-throughput microscopy for live-cell subcellular imaging. *Expert Opinion on Drug Discovery*. 6 (12), 1299–1315. doi:10.1517/17460441.2011.637105.

Olivier, N., Keller, D., Rajan, V.S., Gönczy, P. & Manley, S. (2013) Simple buffers for 3D STORM microscopy. *Biomedical Optics Express*. 4 (6), 885–899. doi:10.1364/BOE.4.000885.

Osad'ko, I.S. (2005) Sub-poissonian statistics of fluorescence from a single atom driven by a continuous wave laser field. *Journal of Experimental and Theoretical Physics*. 101 (1), 64–72. doi:10.1134/1.2010662.

Ovesný, M., Křížek, P., Borkovec, J., Švindrych, Z. & Hagen, G.M. (2014) ThunderSTORM: a comprehensive ImageJ plug-in for PALM and STORM data analysis and super-resolution imaging. *Bioinformatics*. 30 (16), 2389–2390.

Paës, G. (2014) Fluorescent Probes for Exploring Plant Cell Wall Deconstruction: A Review. *Molecules*.19 (7) pp.9380–9402. doi:10.3390/molecules19079380.

Pageon, S. V, Nicovich, P.R., Mollazade, M., Tabarin, T. & Gaus, K. (2016) Clus-DoC: a combined cluster detection and colocalization analysis for single-molecule localization microscopy data. *Molecular Biology of the Cell*. 27 (22), 3627–3636. doi:10.1091/mbc.E16-07-0478.

Park, Y., Depeursinge, C. & Popescu, G. (2018) Quantitative phase imaging in biomedicine. *Nature Photonics*. 12 (10), 578–589. doi:10.1038/s41566-018-0253-x.

Pauli, W. (1925) Über den Zusammenhang des Abschlusses der Elektronengruppen im Atom mit der Komplexstruktur der Spektren. *Zeitschrift für Physik*. 31 (1), 765–783. doi:10.1007/BF02980631.

Pavani, S.R.P., Thompson, M.A., Biteen, J.S., Lord, S.J., Liu, N., Twieg, R.J., Piestun, R. & Moerner, W.E. (2009) Three-dimensional, single-molecule fluorescence imaging beyond the diffraction limit by using a double-helix point spread function. *Proceedings of the National Academy of Sciences*. 106 (9), 2995–2999. doi:10.1073/pnas.0900245106.

Pawley, J.B. (2006) *Points, Pixels, and Gray Levels: Digitizing Image Data BT - Handbook Of Biological Confocal Microscopy*. In: J.B. Pawley (ed.). Boston, MA, Springer US. pp. 59–79. doi:10.1007/978-0-387-45524-2_4.

Petráň, M., Hadravský, M., Egger, M.D. & Galambos, R. (1968) Tandem-Scanning Reflected-Light Microscope*. *Journal of the Optical Society of America*. 58 (5), 661–664. doi:10.1364/JOSA.58.000661.

Pinkard, H., Phillips, Z., Babakhani, A., Fletcher, D.A. & Waller, L. (2019) Deep learning for single-shot autofocus microscopy. *Optica*. 6 (6), 794–797. doi:10.1364/OPTICA.6.000794.

Pitrone, P.G., Schindelin, J., Stuyvenberg, L., Preibisch, S., Weber, M., Eliceiri, K.W., Huisken, J. & Tomancak, P. (2013) OpenSPIM: an open-access light-sheet microscopy platform. *Nature Methods*. 10 (7), 598–599. doi:10.1038/nmeth.2507.

Ploem, J.S. (1967) The use of a vertical illuminator with interchangeable dichroic mirrors for fluorescence microscopy with incidental light. *Zeitschrift fur wissenschaftliche Mikroskopie und mikroskopische Technik*. 68 (3), 129–142.

Prakash, K. (2021) Laser-free super-resolution microscopy. *Philosophical Transactions of the Royal Society A: Mathematical, Physical and Engineering Sciences*. 379 (2199), 20200144. doi:10.1098/rsta.2020.0144.

Prasher, D.C., Eckenrode, V.K., Ward, W.W., Prendergast, F.G. & Cormier, M.J. (1992) Primary structure of the Aequorea victoria green-fluorescent protein. *Gene*. 111 (2), 229–233. doi:https://doi.org/10.1016/0378-1119(92)90691-H.

Rai Dastidar, T. & Ethirajan, R. (2020) Whole slide imaging system using deep learning-based automated focusing. *Biomedical Optics Express*. 11 (1), 480–491. doi:10.1364/BOE.379780.

Rankin, B.R., Moneron, G., Wurm, C.A., Nelson, J.C., Walter, A., Schwarzer, D., Schroeder, J., Colón-Ramos, D.A. & Hell, S.W. (2011) Nanoscopy in a living multicellular organism expressing GFP. *Biophysical journal*. 100 (12), L63-5. doi:10.1016/j.bpj.2011.05.020.

Rayleigh (1879) XXXI. Investigations in optics, with special reference to the spectroscope. *The London, Edinburgh, and Dublin Philosophical Magazine and Journal of Science*. 8 (49), 261–274. doi:10.1080/14786447908639684.

Ricci, M.A., Manzo, C., García-Parajo, M.F., Lakadamyali, M. & Cosma, M.P. (2015) Chromatin fibers are formed by heterogeneous groups of nucleosomes in vivo. *Cell*. 160 (6), 1145–1158. doi:10.1016/j.cell.2015.01.054.

Richards, B., Wolf, E. & Gabor, D. (1959) Electromagnetic diffraction in optical systems, II. Structure of the image field in an aplanatic system. *Proceedings of the Royal Society of London. Series A. Mathematical and Physical Sciences*. 253 (1274), 358–379. doi:10.1098/rspa.1959.0200.

Rizvi, S.A., Neidt, E.M., Cui, J., Feiger, Z., Skau, C.T., Gardel, M.L., Kozmin, S.A. & Kovar, D.R. (2009) Identification and Characterization of a Small Molecule Inhibitor of Formin-Mediated Actin Assembly. *Chemistry & Biology*. 16 (11), 1158–1168. doi:https://doi.org/10.1016/j.chembiol.2009.10.006.

Rothemund, P.W.K. (2006) Folding DNA to create nanoscale shapes and patterns. *Nature*. 440 (7082), 297–302. doi:10.1038/nature04586.

Rust, M.J., Bates, M. & Zhuang, X. (2006) Sub-diffraction-limit imaging by stochastic optical reconstruction microscopy (STORM). *Nature Methods*. 3 (10).

Sage, D., Kirshner, H., Pengo, T., Stuurman, N., Min, J., Manley, S. & Unser, M. (2015) Quantitative evaluation of software packages for single-molecule localization microscopy. *Nature Methods*. 12, 717. https://doi.org/10.1038/nmeth.3442.

Sage, D., Pham, T.-A., Babcock, H., Lukes, T., Pengo, T., et al. (2019) Super-resolution fight club: assessment of 2D and 3D single-molecule localization microscopy software. *Nature Methods*. 16 (5), 387–395. doi:10.1038/s41592-019-0364-4.

Samanta, S., Gong, W., Li, W., Sharma, A., Shim, I., Zhang, W., Das, P., Pan, W., Liu, L., Yang, Z., Qu, J. & Kim, J.S. (2019) Organic fluorescent probes for stochastic optical reconstruction microscopy (STORM): Recent highlights and future possibilities. *Coordination Chemistry Reviews*. 380, 17–34. doi:https://doi.org/10.1016/j.ccr.2018.08.006.

Sandler, M., Howard, A., Zhu, M., Zhmoginov, A. & Chen, L.-C. (2018) *MobileNetV2: Inverted Residuals and Linear Bottlenecks*. http://arxiv.org/abs/1801.04381.

Sandmeyer, A., Lachetta, M., Sandmeyer, H., Hübner, W., Huser, T. & Müller, M. (2021) Cost-Effective Live Cell Structured Illumination Microscopy with Video-Rate Imaging. *ACS Photonics*. 8 (6), 1639–1648. doi:10.1021/acsphotonics.0c01937.

Sauer, M. (2013) Localization microscopy coming of age: from concepts to biological impact. *Journal of Cell Science*. 126 (16), 3505–3513. doi:10.1242/jcs.123612.

Schnitzbauer, J., Strauss, M.T., Schlichthaerle, T., Schueder, F. & Jungmann, R. (2017) Super-resolution microscopy with DNA-PAINT. *Nature Protocols*. 12 (6), 1198–1228. doi:10.1038/nprot.2017.024.

Scott, D.W. (1985) Averaged Shifted Histograms: Effective Nonparametric Density Estimators in Several Dimensions. *The Annals of Statistics*. 13 (3), 1024–1040. http://www.jstor.org/stable/2241123.

Sharonov, A. & Hochstrasser, R.M. (2006) Wide-field subdiffraction imaging by accumulated binding of diffusing probes. *Proceedings of the National Academy of Sciences*. 103 (50), 18911–18916. doi:10.1073/pnas.0609643104.

Sharpe, J. (2003) Optical projection tomography as a new tool for studying embryo anatomy. *Journal of Anatomy*. 202 (2), 175–181. doi:https://doi.org/10.1046/j.1469-7580.2003.00155.x.

Sharpe, J., Ahlgren, U., Perry, P., Hill, B., Ross, A., Hecksher-Sørensen, J., Baldock, R. & Davidson, D. (2002) Optical Projection Tomography as a Tool for 3D Microscopy and Gene Expression Studies. *Science*. 296 (5567), 541–545. doi:10.1126/science.1068206.

Shen, F., Hodgson, L. & Hahn, K. (2006) [32] - Digital Autofocus Methods for Automated Microscopy. In: J.B.T.-M. in E. Inglese (ed.). *Measuring Biological Responses with Automated Microscopy*. Academic Press. pp. 620–632. doi:https://doi.org/10.1016/S0076-6879(06)14032-X.

Shimomura, O., Johnson, F.H. & Saiga, Y. (1962) Extraction, Purification and Properties of Aequorin, a Bioluminescent Protein from the Luminous Hydromedusan, Aequorea. *Journal of Cellular and Comparative Physiology*. 59 (3), 223–239. doi:https://doi.org/10.1002/jcp.1030590302.

Shore, I. & Moss, J. (2002) Electron microscopy in diagnostic renal pathology. *Current Diagnostic Pathology*. 8 (4), 207–215. doi:https://doi.org/10.1054/cdip.2002.0123.

Siedentopf, H. & Zsigmondy, R. (1903) Uber Sichtbarmachung und Größenbestimmung ultramikoskopischer Teilchen, mit besonderer Anwendung auf Goldrubingläser. *Annalen der Physik*. 315, 1–39.

Silvestri, L., Müllenbroich, M.C., Costantini, I., di Giovanna, A.P., Mazzamuto, G., Franceschini, A., Kutra, D., Kreshuk, A., Checcucci, C., Toresano, L.O., Frasconi, P., Sacconi, L. & Pavone, F.S. (2021) Universal autofocus for quantitative volumetric microscopy of whole mouse brains. *Nature Methods*. 18 (8), 953–958. doi:10.1038/s41592-021-01208-1.

Singer, C. (1914) Notes on the Early History of Microscopy. *Proceedings of the Royal Society of Medicine*. 7 (Sect Hist Med), 247–279.

Small, A. & Stahlheber, S. (2014) Fluorophore localization algorithms for super-resolution microscopy. *Nature Methods*. 11 (3), 267–279. doi:10.1038/nmeth.2844.

Sparks, H., Dent, L., Bakal, C., Behrens, A., Salbreux, G. & Dunsby, C. (2020) Dual-view oblique plane microscopy (dOPM). *Biomedical Optics Express*. 11 (12), 7204–7220. doi:10.1364/BOE.409781.

Stokes, G.G. (1852) XXX. On the change of refrangibility of light. *Philosophical Transactions of the Royal Society of London*. 142, 463–562. doi:10.1098/rstl.1852.0022.

Sun, Y., Duthaler, S. & Nelson, B.J. (2004) Autofocusing in computer microscopy: Selecting the optimal focus algorithm. *Microscopy Research and Technique*. 65 (3), 139–149.

Talbot, C.B., McGinty, J., Grant, D.M., McGhee, E.J., Owen, D.M., Zhang, W., Bunney, T.D., Munro, I., Isherwood, B., Eagle, R., Hargreaves, A., Dunsby, C., Neil, M.A.A. & French, P.M.W. (2008) High speed unsupervised fluorescence lifetime imaging confocal multiwell plate reader for high content analysis. *Journal of Biophotonics*. 1 (6), 514–521. doi:10.1002/jbio.200810054.

Theer, P., Mongis, C. & Knop, M. (2014) PSFj: know your fluorescence microscope. *Nature Methods*. 11 (10), 981–982. doi:10.1038/nmeth.3102.

Thevathasan, J.V., Kahnwald, M., Cieśliński, K., Hoess, P., Peneti, S.K., et al. (2019) Nuclear pores as versatile reference standards for quantitative superresolution microscopy. *Nature Methods*. 16 (10), 1045–1053. doi:10.1038/s41592-019-0574-9.

Tian, L. & Waller, L. (2015) Quantitative differential phase contrast imaging in an LED array microscope. *Optics Express*. 23 (9), 11394–11403. doi:10.1364/OE.23.011394.

Tokunaga, M., Imamoto, N. & Sakata-Sogawa, K. (2008) Highly inclined thin illumination enables clear single-molecule imaging in cells. *Nature Methods*. 5 (2), 159. doi:10.1038/nmeth1171.

Tokunaga, M., Kitamura, K., Saito, K., Iwane, A.H. & Yanagida, T. (1997) Single molecule imaging of fluorophores and enzymatic reactions achieved by objective-type total internal reflection fluorescence microscopy. *Biochemical and biophysical research communications*. 235 (1), 47–53. doi:10.1006/bbrc.1997.6732.

Vesely, P. (2007) Handbook of Biological Confocal Microscopy, 3rd ed. By James B. Pawley, Editor. Springer Science + Business Media, LLC, New York (2006). ISBN 10: 0-387-25921-X; ISBN 13: 987-0387-25921-5; hardback; 28 + 985 pages. *Scanning*. 29 (3), 91. doi:https://doi.org/10.1002/sca.20059.

Vinegoni, C., Pitsouli, C., Razansky, D., Perrimon, N. & Ntziachristos, V. (2008) In vivo imaging of Drosophila melanogaster pupae with mesoscopic fluorescence tomography. *Nature Methods*. 5 (1), 45–47. doi:10.1038/nmeth1149.

WANG, E., BABBEY, C.M. & DUNN, K.W. (2005) Performance comparison between the high-speed Yokogawa spinning disc confocal system and single-point scanning confocal systems. *Journal of Microscopy*. 218 (2), 148–159. doi:https://doi.org/10.1111/j.1365-2818.2005.01473.x.

Weening, J.J., D'Agati, V.D., Schwartz, M.M., Seshan, S. v, Alpers, C.E., et al. (2004) The classification of glomerulonephritis in systemic lupus erythematosus revisited. *Journal of the American Society of Nephrology : JASN*. 15 (2), 241–250. doi:10.1097/01.asn.0000108969.21691.5d.

White, J.G. & Amos, W.B. (1987) Confocal microscopy comes of age. *Nature*. 328 (6126), 183–184. doi:10.1038/328183a0.

Wilson, T. (2011a) Optical sectioning in fluorescence microscopy. *Journal of Microscopy*. 242 (2), 111–116. doi:https://doi.org/10.1111/j.1365-2818.2010.03457.x.

Wilson, T. (2011b) Resolution and optical sectioning in the confocal microscope. *Journal of Microscopy*. 244 (2), 113–121. doi:https://doi.org/10.1111/j.1365-2818.2011.03549.x.

Wollman, A.J.M., Nudd, R., Hedlund, E.G. & Leake, M.C. (2022) From Animaculum to single molecules: 300 years of the light microscope. *Open Biology*. 5 (4), 150019. doi:10.1098/rsob.150019.

Xin, K., Jiang, S., Chen, X., He, Y., Zhang, J., Wang, H., Liu, H., Peng, Q., Zhang, Y. & Ji, X. (2021) Low-cost whole slide imaging system with single-shot autofocusing based on color-multiplexed illumination and deep learning. *Biomedical Optics Express*. 12 (9), 5644–5657. doi:10.1364/BOE.428655.

Yamagishi, Y., Oya, K., Matsuura, A. & Abe, H. (2018) Use of CK-548 and CK-869 as Arp2/3 complex inhibitors directly suppresses microtubule assembly both in vitro and in vivo. *Biochemical and Biophysical Research Communications*. 496 (3), 834–839. doi:https://doi.org/10.1016/j.bbrc.2018.01.143.

Yazdanfar, S., Kenny, K.B., Tasimi, K., Corwin, A.D., Dixon, E.L. & Filkins, R.J. (2008) Simple and robust image-based autofocusing for digital microscopy. *Optics Express*. 16 (12), 8670–8677.

Zanella, F., Lorens, J.B. & Link, W. (2010) High content screening: seeing is believing. *Trends in Biotechnology*. 28 (5), 237–245. doi:https://doi.org/10.1016/j.tibtech.2010.02.005.

Zernike, F. (1942a) Phase contrast, a new method for the microscopic observation of transparent objects. *Physica*. 9 (7), 686–698. doi:https://doi.org/10.1016/S0031-8914(42)80035-X.

Zernike, F. (1942b) Phase contrast, a new method for the microscopic observation of transparent objects part II. *Physica*. 9 (10), 974–986. doi:https://doi.org/10.1016/S0031-8914(42)80079-8.

Zipfel, W.R., Williams, R.M. & Webb, W.W. (2003) Nonlinear magic: multiphoton microscopy in the biosciences. *Nature Biotechnology*. 21 (11).

Appendix

A1. Permission to reproduce third party work

JOHN WILEY AND SONS LICENSE
TERMS AND CONDITIONS
Mar 26, 2023

This Agreement between Mr. Jonathan Lightley ("You") and John Wiley and Sons ("John Wiley and Sons") consists of your license details and the terms and conditions provided by John Wiley and Sons and Copyright Clearance Center.

License Number	5516441230858
License date	Mar 26, 2023
Licensed Content Publisher	John Wiley and Sons
Licensed Content Publication	Journal of Microscopy
Licensed Content Title	Surpassing the lateral resolution limit by a factor of two using structured illumination microscopy
Licensed Content Author	M. G. L. Gustafsson
Licensed Content Date	Dec 24, 2001
Licensed Content Volume	198
Licensed Content Issue	2
Licensed Content Pages	6
Type of use	Dissertation/Thesis
Requestor type	University/Academic
Format	Electronic
Portion	Figure/table
Number of figures/tables	1
Will you be translating?	No
Title	Development of open source microscopy including optical autofocus for automated imaging and single molecule localisation microscopy
Institution name	Imperial College London

Expected presentation date	May 2023
Portions	Figure 1 Mr. Jonathan Lightley
Requestor Location	United Kingdom Attn: Mr. Jonathan Lightley
Publisher Tax ID	EU826007151
Total	0.00 GBP
Terms and Conditions	

TERMS AND CONDITIONS

This copyrighted material is owned by or exclusively licensed to John Wiley & Sons, Inc. or one of its group companies (each a"Wiley Company") or handled on behalf of a society with which a Wiley Company has exclusive publishing rights in relation to a particular work (collectively "WILEY"). By clicking "accept" in connection with completing this licensing transaction, you agree that the following terms and conditions apply to this transaction (along with the billing and payment terms and conditions established by the Copyright Clearance Center Inc., ("CCC's Billing and Payment terms and conditions"), at the time that you opened your RightsLink account (these are available at any time at http://myaccount.copyright.com).

Terms and Conditions

- The materials you have requested permission to reproduce or reuse (the "Wiley Materials") are protected by copyright.
- You are hereby granted a personal, non-exclusive, non-sub licensable (on a stand-alone basis), non-transferable, worldwide, limited license to reproduce the Wiley Materials for the purpose specified in the licensing process. This license, **and any CONTENT (PDF or image file) purchased as part of your order,** is for a one-time use only and limited to any maximum distribution number specified in the license. The first instance of republication or reuse granted by this license must be completed within two years of the date of the grant of this license (although copies prepared before the end date may be distributed thereafter). The Wiley Materials shall not be used in any other manner or for any other purpose, beyond what is granted in the license. Permission is granted subject to an appropriate acknowledgement given to the author,

title of the material/book/journal and the publisher. You shall also duplicate the copyright notice that appears in the Wiley publication in your use of the Wiley Material. Permission is also granted on the understanding that nowhere in the text is a previously published source acknowledged for all or part of this Wiley Material. Any third party content is expressly excluded from this permission.

- With respect to the Wiley Materials, all rights are reserved. Except as expressly granted by the terms of the license, no part of the Wiley Materials may be copied, modified, adapted (except for minor reformatting required by the new Publication), translated, reproduced, transferred or distributed, in any form or by any means, and no derivative works may be made based on the Wiley Materials without the prior permission of the respective copyright owner.**For STM Signatory Publishers clearing permission under the terms of the STM Permissions Guidelines only, the terms of the license are extended to include subsequent editions and for editions in other languages, provided such editions are for the work as a whole in situ and does not involve the separate exploitation of the permitted figures or extracts,** You may not alter, remove or suppress in any manner any copyright, trademark or other notices displayed by the Wiley Materials. You may not license, rent, sell, loan, lease, pledge, offer as security, transfer or assign the Wiley Materials on a stand-alone basis, or any of the rights granted to you hereunder to any other person.

- The Wiley Materials and all of the intellectual property rights therein shall at all times remain the exclusive property of John Wiley & Sons Inc, the Wiley Companies, or their respective licensors, and your interest therein is only that of having possession of and the right to reproduce the Wiley Materials pursuant to Section 2 herein during the continuance of this Agreement. You agree that you own no right, title or interest in or to the Wiley Materials or any of the intellectual property rights therein. You shall have no rights hereunder other than the license as provided for above in Section 2. No right, license or interest to any trademark, trade name, service mark or other branding ("Marks") of WILEY or its licensors is granted hereunder, and you agree that you shall not assert any such right, license or interest with respect thereto

- NEITHER WILEY NOR ITS LICENSORS MAKES ANY WARRANTY OR REPRESENTATION OF ANY KIND TO YOU OR ANY THIRD PARTY, EXPRESS, IMPLIED OR STATUTORY, WITH RESPECT TO THE MATERIALS OR THE ACCURACY OF ANY INFORMATION CONTAINED IN THE MATERIALS, INCLUDING, WITHOUT LIMITATION, ANY IMPLIED WARRANTY OF MERCHANTABILITY, ACCURACY, SATISFACTORY QUALITY,

FITNESS FOR A PARTICULAR PURPOSE, USABILITY, INTEGRATION OR NON-INFRINGEMENT AND ALL SUCH WARRANTIES ARE HEREBY EXCLUDED BY WILEY AND ITS LICENSORS AND WAIVED BY YOU.

- WILEY shall have the right to terminate this Agreement immediately upon breach of this Agreement by you.

- You shall indemnify, defend and hold harmless WILEY, its Licensors and their respective directors, officers, agents and employees, from and against any actual or threatened claims, demands, causes of action or proceedings arising from any breach of this Agreement by you.

- IN NO EVENT SHALL WILEY OR ITS LICENSORS BE LIABLE TO YOU OR ANY OTHER PARTY OR ANY OTHER PERSON OR ENTITY FOR ANY SPECIAL, CONSEQUENTIAL, INCIDENTAL, INDIRECT, EXEMPLARY OR PUNITIVE DAMAGES, HOWEVER CAUSED, ARISING OUT OF OR IN CONNECTION WITH THE DOWNLOADING, PROVISIONING, VIEWING OR USE OF THE MATERIALS REGARDLESS OF THE FORM OF ACTION, WHETHER FOR BREACH OF CONTRACT, BREACH OF WARRANTY, TORT, NEGLIGENCE, INFRINGEMENT OR OTHERWISE (INCLUDING, WITHOUT LIMITATION, DAMAGES BASED ON LOSS OF PROFITS, DATA, FILES, USE, BUSINESS OPPORTUNITY OR CLAIMS OF THIRD PARTIES), AND WHETHER OR NOT THE PARTY HAS BEEN ADVISED OF THE POSSIBILITY OF SUCH DAMAGES. THIS LIMITATION SHALL APPLY NOTWITHSTANDING ANY FAILURE OF ESSENTIAL PURPOSE OF ANY LIMITED REMEDY PROVIDED HEREIN.

- Should any provision of this Agreement be held by a court of competent jurisdiction to be illegal, invalid, or unenforceable, that provision shall be deemed amended to achieve as nearly as possible the same economic effect as the original provision, and the legality, validity and enforceability of the remaining provisions of this Agreement shall not be affected or impaired thereby.

- The failure of either party to enforce any term or condition of this Agreement shall not constitute a waiver of either party's right to enforce each and every term and condition of this Agreement. No breach under this agreement shall be deemed waived or excused by either party unless such waiver or consent is in writing signed by the party granting such waiver or consent. The waiver by or consent of a party to a breach of any provision

of this Agreement shall not operate or be construed as a waiver of or consent to any other or subsequent breach by such other party.

- This Agreement may not be assigned (including by operation of law or otherwise) by you without WILEY's prior written consent.
- Any fee required for this permission shall be non-refundable after thirty (30) days from receipt by the CCC.
- These terms and conditions together with CCC's Billing and Payment terms and conditions (which are incorporated herein) form the entire agreement between you and WILEY concerning this licensing transaction and (in the absence of fraud) supersedes all prior agreements and representations of the parties, oral or written. This Agreement may not be amended except in writing signed by both parties. This Agreement shall be binding upon and inure to the benefit of the parties' successors, legal representatives, and authorized assigns.
- In the event of any conflict between your obligations established by these terms and conditions and those established by CCC's Billing and Payment terms and conditions, these terms and conditions shall prevail.
- WILEY expressly reserves all rights not specifically granted in the combination of (i) the license details provided by you and accepted in the course of this licensing transaction, (ii) these terms and conditions and (iii) CCC's Billing and Payment terms and conditions.
- This Agreement will be void if the Type of Use, Format, Circulation, or Requestor Type was misrepresented during the licensing process.
- This Agreement shall be governed by and construed in accordance with the laws of the State of New York, USA, without regards to such state's conflict of law rules. Any legal action, suit or proceeding arising out of or relating to these Terms and Conditions or the breach thereof shall be instituted in a court of competent jurisdiction in New York County in the State of New York in the United States of America and each party hereby consents and submits to the personal jurisdiction of such court, waives any objection to venue in such court and consents to service of process by registered or certified mail, return receipt requested, at the last known address of such party.

WILEY OPEN ACCESS TERMS AND CONDITIONS

Wiley Publishes Open Access Articles in fully Open Access Journals and in Subscription journals offering Online Open. Although most of the fully Open

Access journals publish open access articles under the terms of the Creative Commons Attribution (CC BY) License only, the subscription journals and a few of the Open Access Journals offer a choice of Creative Commons Licenses. The license type is clearly identified on the article.

The Creative Commons Attribution License

The Creative Commons Attribution License (CC-BY) allows users to copy, distribute and transmit an article, adapt the article and make commercial use of the article. The CC-BY license permits commercial and non-

Creative Commons Attribution Non-Commercial License

The Creative Commons Attribution Non-Commercial (CC-BY-NC)License permits use, distribution and reproduction in any medium, provided the original work is properly cited and is not used for commercial purposes.(see below)

Creative Commons Attribution-Non-Commercial-NoDerivs License

The Creative Commons Attribution Non-Commercial-NoDerivs License (CC-BY-NC-ND) permits use, distribution and reproduction in any medium, provided the original work is properly cited, is not used for commercial purposes and no modifications or adaptations are made. (see below)

Use by commercial "for-profit" organizations

Use of Wiley Open Access articles for commercial, promotional, or marketing purposes requires further explicit permission from Wiley and will be subject to a fee.

Further details can be found on Wiley Online Library http://olabout.wiley.com/WileyCDA/Section/id-410895.html

Other Terms and Conditions:

v1.10 Last updated September 2015
Questions? customercare@copyright.com.

SPRINGER NATURE LICENSE
TERMS AND CONDITIONS
Mar 26, 2023

This Agreement between Mr. Jonathan Lightley ("You") and Springer Nature ("Springer Nature") consists of your license details and the terms and conditions provided by Springer Nature and Copyright Clearance Center.

License Number	5516440992756
License date	Mar 26, 2023
Licensed Content Publisher	Springer Nature
Licensed Content Publication	Nature Methods
Licensed Content Title	Sub-diffraction-limit imaging by stochastic optical reconstruction microscopy (STORM)
Licensed Content Author	Michael J Rust et al
Licensed Content Date	Aug 9, 2006
Type of Use	Thesis/Dissertation
Requestor type	academic/university or research institute
Format	electronic
Portion	figures/tables/illustrations
Number of figures/tables/illustrations	1
High-res required	no
Will you be translating?	no
Circulation/distribution	1 - 29
Author of this Springer Nature content	no
Title	Development of open source microscopy including optical autofocus for automated imaging and single molecule localisation microscopy
Institution name	Imperial College London
Expected presentation date	May 2023
Portions	Figure 1(a) Mr. Jonathan Lightley
Requestor Location	United Kingdom Attn: Mr. Jonathan Lightley

Total 0.00 GBP

Terms and Conditions

Springer Nature Customer Service Centre GmbH Terms and Conditions

The following terms and conditions ("Terms and Conditions") together with the terms specified in your [RightsLink] constitute the License ("License") between you as Licensee and Springer Nature Customer Service Centre GmbH as Licensor. By clicking 'accept' and completing the transaction for your use of the material ("Licensed Material"), you confirm your acceptance of and obligation to be bound by these Terms and Conditions.

1. **Grant and Scope of License**

    1. The Licensor grants you a personal, non-exclusive, non-transferable, non-sublicensable, revocable, world-wide License to reproduce, distribute, communicate to the public, make available, broadcast, electronically transmit or create derivative works using the Licensed Material for the purpose(s) specified in your RightsLink Licence Details only. Licenses are granted for the specific use requested in the order and for no other use, subject to these Terms and Conditions. You acknowledge and agree that the rights granted to you under this License do not include the right to modify, edit, translate, include in collective works, or create derivative works of the Licensed Material in whole or in part unless expressly stated in your RightsLink Licence Details. You may use the Licensed Material only as permitted under this Agreement and will not reproduce, distribute, display, perform, or otherwise use or exploit any Licensed Material in any way, in whole or in part, except as expressly permitted by this License.

    2. You may only use the Licensed Content in the manner and to the extent permitted by these Terms and Conditions, by your RightsLink Licence Details and by any applicable laws.

    3. A separate license may be required for any additional use of the Licensed Material, e.g. where a license has been purchased for print use only, separate permission must be obtained for electronic re-use. Similarly, a License is only valid in the language selected and does not apply for editions in other languages unless additional translation rights have been granted separately in the License.

    4. Any content within the Licensed Material that is owned by third parties is expressly excluded from the License.

5. Rights for additional reuses such as custom editions, computer/mobile applications, film or TV reuses and/or any other derivative rights requests require additional permission and may be subject to an additional fee. Please apply to journalpermissions@springernature.com or bookpermissions@springernature.com for these rights.

2. **Reservation of Rights**

   Licensor reserves all rights not expressly granted to you under this License. You acknowledge and agree that nothing in this License limits or restricts Licensor's rights in or use of the Licensed Material in any way. Neither this License, nor any act, omission, or statement by Licensor or you, conveys any ownership right to you in any Licensed Material, or to any element or portion thereof. As between Licensor and you, Licensor owns and retains all right, title, and interest in and to the Licensed Material subject to the license granted in Section 1.1. Your permission to use the Licensed Material is expressly conditioned on you not impairing Licensor's or the applicable copyright owner's rights in the Licensed Material in any way.

3. **Restrictions on use**

   1. Minor editing privileges are allowed for adaptations for stylistic purposes or formatting purposes provided such alterations do not alter the original meaning or intention of the Licensed Material and the new figure(s) are still accurate and representative of the Licensed Material. Any other changes including but not limited to, cropping, adapting, and/or omitting material that affect the meaning, intention or moral rights of the author(s) are strictly prohibited.

   2. You must not use any Licensed Material as part of any design or trademark.

   3. Licensed Material may be used in Open Access Publications (OAP), but any such reuse must include a clear acknowledgment of this permission visible at the same time as the figures/tables/illustration or abstract and which must indicate that the Licensed Material is not part of the governing OA license but has been reproduced with permission. This may be indicated according to any standard referencing system but must include at a minimum 'Book/Journal

title, Author, Journal Name (if applicable), Volume (if applicable), Publisher, Year, reproduced with permission from SNCSC'.

4. **STM Permission Guidelines**

1. An alternative scope of license may apply to signatories of the STM Permissions Guidelines ("STM PG") as amended from time to time and made available at https://www.stm-assoc.org/intellectual-property/permissions/permissions-guidelines/.

2. For content reuse requests that qualify for permission under the STM PG, and which may be updated from time to time, the STM PG supersede the terms and conditions contained in this License.

3. If a License has been granted under the STM PG, but the STM PG no longer apply at the time of publication, further permission must be sought from the Rightsholder.
Contact journalpermissions@springernature.com or bookpermissions@springernature.com for these rights.

5. **Duration of License**

1. Unless otherwise indicated on your License, a License is valid from the date of purchase ("License Date") until the end of the relevant period in the below table:

Reuse in a medical communications project	Reuse up to distribution or time period indicated in License
Reuse in a dissertation/thesis	Lifetime of thesis
Reuse in a journal/magazine	Lifetime of journal/magazine
Reuse in a book/textbook	Lifetime of edition
Reuse on a website	1 year unless otherwise specified in the License
Reuse in a presentation/slide kit/poster	Lifetime of presentation/slide kit/poster. Note: publication whether electronic or in print of presentation/slide kit/poster may require further permission.
Reuse in conference proceedings	Lifetime of conference proceedings
Reuse in an annual report	Lifetime of annual report
Reuse in training/CME materials	Reuse up to distribution or time period indicated in License

Reuse in newsmedia	Lifetime of newsmedia
Reuse in coursepack/classroom materials	Reuse up to distribution and/or time period indicated in license

6.
7. **Acknowledgement**

    1. The Licensor's permission must be acknowledged next to the Licensed Material in print. In electronic form, this acknowledgement must be visible at the same time as the figures/tables/illustrations or abstract and must be hyperlinked to the journal/book's homepage.

    2. Acknowledgement may be provided according to any standard referencing system and at a minimum should include "Author, Article/Book Title, Journal name/Book imprint, volume, page number, year, Springer Nature".

8. **Reuse in a dissertation or thesis**

    1. Where 'reuse in a dissertation/thesis' has been selected, the following terms apply: Print rights of the Version of Record are provided for; electronic rights for use only on institutional repository as defined by the Sherpa guideline (www.sherpa.ac.uk/romeo/) and only up to what is required by the awarding institution.

    2. For theses published under an ISBN or ISSN, separate permission is required. Please contact journalpermissions@springernature.com or bookpermissions@springernature.com for these rights.

    3. Authors must properly cite the published manuscript in their thesis according to current citation standards and include the following acknowledgement: '*Reproduced with permission from Springer Nature*'.

9. **License Fee**

   You must pay the fee set forth in the License Agreement (the "License Fees"). All amounts payable by you under this License are exclusive of any sales, use, withholding, value added or similar taxes, government fees or levies or other assessments. Collection and/or remittance of such taxes to the relevant tax authority shall be the responsibility of the party who has the legal obligation to do so.

10. **Warranty**

    1. The Licensor warrants that it has, to the best of its knowledge, the rights to license reuse of the Licensed Material. **You are solely responsible for ensuring that the material you wish to license is original to the Licensor and does not carry the copyright of another entity or third party (as credited in the published version).** If the credit line on any part of the Licensed Material indicates that it was reprinted or adapted with permission from another source, then you should seek additional permission from that source to reuse the material.

    2. EXCEPT FOR THE EXPRESS WARRANTY STATED HEREIN AND TO THE EXTENT PERMITTED BY APPLICABLE LAW, LICENSOR PROVIDES THE LICENSED MATERIAL "AS IS" AND MAKES NO OTHER REPRESENTATION OR WARRANTY. LICENSOR EXPRESSLY DISCLAIMS ANY LIABILITY FOR ANY CLAIM ARISING FROM OR OUT OF THE CONTENT, INCLUDING BUT NOT LIMITED TO ANY ERRORS, INACCURACIES, OMISSIONS, OR DEFECTS CONTAINED THEREIN, AND ANY IMPLIED OR EXPRESS WARRANTY AS TO MERCHANTABILITY OR FITNESS FOR A PARTICULAR PURPOSE. IN NO EVENT SHALL LICENSOR BE LIABLE TO YOU OR ANY OTHER PARTY OR ANY OTHER PERSON OR FOR ANY SPECIAL, CONSEQUENTIAL, INCIDENTAL, INDIRECT, PUNITIVE, OR EXEMPLARY DAMAGES, HOWEVER CAUSED, ARISING OUT OF OR IN CONNECTION WITH THE DOWNLOADING, VIEWING OR USE OF THE LICENSED MATERIAL REGARDLESS OF THE

FORM OF ACTION, WHETHER FOR BREACH OF CONTRACT, BREACH OF WARRANTY, TORT, NEGLIGENCE, INFRINGEMENT OR OTHERWISE (INCLUDING, WITHOUT LIMITATION, DAMAGES BASED ON LOSS OF PROFITS, DATA, FILES, USE, BUSINESS OPPORTUNITY OR CLAIMS OF THIRD PARTIES), AND WHETHER OR NOT THE PARTY HAS BEEN ADVISED OF THE POSSIBILITY OF SUCH DAMAGES. THIS LIMITATION APPLIES NOTWITHSTANDING ANY FAILURE OF ESSENTIAL PURPOSE OF ANY LIMITED REMEDY PROVIDED HEREIN.

11. Termination and Cancellation

1. The License and all rights granted hereunder will continue until the end of the applicable period shown in Clause 5.1 above. Thereafter, this license will be terminated and all rights granted hereunder will cease.

2. Licensor reserves the right to terminate the License in the event that payment is not received in full or if you breach the terms of this License.

12. General

1. The License and the rights and obligations of the parties hereto shall be construed, interpreted and determined in accordance with the laws of the Federal Republic of Germany without reference to the stipulations of the CISG (United Nations Convention on Contracts for the International Sale of Goods) or to Germany´s choice-of-law principle.

2. The parties acknowledge and agree that any controversies and disputes arising out of this License shall be decided exclusively by

the courts of or having jurisdiction for Heidelberg, Germany, as far as legally permissible.

3. This License is solely for Licensor's and Licensee's benefit. It is not for the benefit of any other person or entity.

Questions? For questions on Copyright Clearance Center accounts or website issues please contact springernaturesupport@copyright.com or +1-855-239-3415 (toll free in the US) or +1-978-646-2777. For questions on Springer Nature licensing please visit https://www.springernature.com/gp/partners/rights-permissions-third-party-distribution

Other Conditions:

Version 1.4 - Dec 2022

Questions? customercare@copyright.com.

SPRINGER NATURE LICENSE
TERMS AND CONDITIONS
Mar 26, 2023

This Agreement between Mr. Jonathan Lightley ("You") and Springer Nature ("Springer Nature") consists of your license details and the terms and conditions provided by Springer Nature and Copyright Clearance Center.

License Number	5516431282870
License date	Mar 26, 2023
Licensed Content Publisher	Springer Nature
Licensed Content Publication	Nature Methods
Licensed Content Title	Fluorophore localization algorithms for super-resolution microscopy
Licensed Content Author	Alex Small et al
Licensed Content Date	Feb 27, 2014
Type of Use	Thesis/Dissertation
Requestor type	academic/university or research institute
Format	electronic
Portion	figures/tables/illustrations
Number of figures/tables/illustrations	1
High-res required	no
Will you be translating?	no
Circulation/distribution	1 - 29
Author of this Springer Nature content	no
Title	Development of open source microscopy including optical autofocus for automated imaging and single molecule localisation microscopy
Institution name	Imperial College London
Expected presentation date	May 2023
Portions	Figure 1 Mr. Jonathan Lightley
Requestor Location	United Kingdom Attn: Mr. Jonathan Lightley
Total	0.00 GBP

Terms and Conditions

Springer Nature Customer Service Centre GmbH Terms and Conditions

The following terms and conditions ("Terms and Conditions") together with the terms specified in your [RightsLink] constitute the License ("License") between you as Licensee and Springer Nature Customer Service Centre GmbH as Licensor. By clicking 'accept' and completing the transaction for your use of the material ("Licensed Material"), you confirm your acceptance of and obligation to be bound by these Terms and Conditions.

1. **Grant and Scope of License**

    1. The Licensor grants you a personal, non-exclusive, non-transferable, non-sublicensable, revocable, world-wide License to reproduce, distribute, communicate to the public, make available, broadcast, electronically transmit or create derivative works using the Licensed Material for the purpose(s) specified in your RightsLink Licence Details only. Licenses are granted for the specific use requested in the order and for no other use, subject to these Terms and Conditions. You acknowledge and agree that the rights granted to you under this License do not include the right to modify, edit, translate, include in collective works, or create derivative works of the Licensed Material in whole or in part unless expressly stated in your RightsLink Licence Details. You may use the Licensed Material only as permitted under this Agreement and will not reproduce, distribute, display, perform, or otherwise use or exploit any Licensed Material in any way, in whole or in part, except as expressly permitted by this License.

    2. You may only use the Licensed Content in the manner and to the extent permitted by these Terms and Conditions, by your RightsLink Licence Details and by any applicable laws.

    3. A separate license may be required for any additional use of the Licensed Material, e.g. where a license has been purchased for print use only, separate permission must be obtained for electronic re-use. Similarly, a License is only valid in the language selected and does not apply for editions in other languages unless additional translation rights have been granted separately in the License.

    4. Any content within the Licensed Material that is owned by third parties is expressly excluded from the License.

5. Rights for additional reuses such as custom editions, computer/mobile applications, film or TV reuses and/or any other derivative rights requests require additional permission and may be subject to an additional fee. Please apply to journalpermissions@springernature.com or bookpermissions@springernature.com for these rights.

2. **Reservation of Rights**

   Licensor reserves all rights not expressly granted to you under this License. You acknowledge and agree that nothing in this License limits or restricts Licensor's rights in or use of the Licensed Material in any way. Neither this License, nor any act, omission, or statement by Licensor or you, conveys any ownership right to you in any Licensed Material, or to any element or portion thereof. As between Licensor and you, Licensor owns and retains all right, title, and interest in and to the Licensed Material subject to the license granted in Section 1.1. Your permission to use the Licensed Material is expressly conditioned on you not impairing Licensor's or the applicable copyright owner's rights in the Licensed Material in any way.

3. **Restrictions on use**

   1. Minor editing privileges are allowed for adaptations for stylistic purposes or formatting purposes provided such alterations do not alter the original meaning or intention of the Licensed Material and the new figure(s) are still accurate and representative of the Licensed Material. Any other changes including but not limited to, cropping, adapting, and/or omitting material that affect the meaning, intention or moral rights of the author(s) are strictly prohibited.

   2. You must not use any Licensed Material as part of any design or trademark.

   3. Licensed Material may be used in Open Access Publications (OAP), but any such reuse must include a clear acknowledgment of this permission visible at the same time as the figures/tables/illustration or abstract and which must indicate that the Licensed Material is not part of the governing OA license but has been reproduced with permission. This may be indicated according to any standard referencing system but must include at a minimum 'Book/Journal

title, Author, Journal Name (if applicable), Volume (if applicable), Publisher, Year, reproduced with permission from SNCSC'.

4. **STM Permission Guidelines**

1. An alternative scope of license may apply to signatories of the STM Permissions Guidelines ("STM PG") as amended from time to time and made available at https://www.stm-assoc.org/intellectual-property/permissions/permissions-guidelines/.

2. For content reuse requests that qualify for permission under the STM PG, and which may be updated from time to time, the STM PG supersede the terms and conditions contained in this License.

3. If a License has been granted under the STM PG, but the STM PG no longer apply at the time of publication, further permission must be sought from the Rightsholder.
Contact journalpermissions@springernature.com or bookpermissions@springernature.com for these rights.

5. **Duration of License**

1. Unless otherwise indicated on your License, a License is valid from the date of purchase ("License Date") until the end of the relevant period in the below table:

Reuse in a medical communications project	Reuse up to distribution or time period indicated in License
Reuse in a dissertation/thesis	Lifetime of thesis
Reuse in a journal/magazine	Lifetime of journal/magazine
Reuse in a book/textbook	Lifetime of edition
Reuse on a website	1 year unless otherwise specified in the License
Reuse in a presentation/slide kit/poster	Lifetime of presentation/slide kit/poster. Note: publication whether electronic or in print of presentation/slide kit/poster may require further permission.
Reuse in conference proceedings	Lifetime of conference proceedings
Reuse in an annual report	Lifetime of annual report
Reuse in training/CME materials	Reuse up to distribution or time period indicated in License

Reuse in newsmedia	Lifetime of newsmedia
Reuse in coursepack/classroom materials	Reuse up to distribution and/or time period indicated in license

6.
7. **Acknowledgement**

    1. The Licensor's permission must be acknowledged next to the Licensed Material in print. In electronic form, this acknowledgement must be visible at the same time as the figures/tables/illustrations or abstract and must be hyperlinked to the journal/book's homepage.

    2. Acknowledgement may be provided according to any standard referencing system and at a minimum should include "Author, Article/Book Title, Journal name/Book imprint, volume, page number, year, Springer Nature".

8. **Reuse in a dissertation or thesis**

    1. Where 'reuse in a dissertation/thesis' has been selected, the following terms apply: Print rights of the Version of Record are provided for; electronic rights for use only on institutional repository as defined by the Sherpa guideline (www.sherpa.ac.uk/romeo/) and only up to what is required by the awarding institution.

    2. For theses published under an ISBN or ISSN, separate permission is required. Please contact journalpermissions@springernature.com or bookpermissions@springernature.com for these rights.

    3. Authors must properly cite the published manuscript in their thesis according to current citation standards and include the following acknowledgement: '*Reproduced with permission from Springer Nature*'.

9. **License Fee**

   You must pay the fee set forth in the License Agreement (the "License Fees"). All amounts payable by you under this License are exclusive of any sales, use, withholding, value added or similar taxes, government fees or levies or other assessments. Collection and/or remittance of such taxes to the relevant tax authority shall be the responsibility of the party who has the legal obligation to do so.

10. **Warranty**

    1. The Licensor warrants that it has, to the best of its knowledge, the rights to license reuse of the Licensed Material. **You are solely responsible for ensuring that the material you wish to license is original to the Licensor and does not carry the copyright of another entity or third party (as credited in the published version).** If the credit line on any part of the Licensed Material indicates that it was reprinted or adapted with permission from another source, then you should seek additional permission from that source to reuse the material.

    2. EXCEPT FOR THE EXPRESS WARRANTY STATED HEREIN AND TO THE EXTENT PERMITTED BY APPLICABLE LAW, LICENSOR PROVIDES THE LICENSED MATERIAL "AS IS" AND MAKES NO OTHER REPRESENTATION OR WARRANTY. LICENSOR EXPRESSLY DISCLAIMS ANY LIABILITY FOR ANY CLAIM ARISING FROM OR OUT OF THE CONTENT, INCLUDING BUT NOT LIMITED TO ANY ERRORS, INACCURACIES, OMISSIONS, OR DEFECTS CONTAINED THEREIN, AND ANY IMPLIED OR EXPRESS WARRANTY AS TO MERCHANTABILITY OR FITNESS FOR A PARTICULAR PURPOSE. IN NO EVENT SHALL LICENSOR BE LIABLE TO YOU OR ANY OTHER PARTY OR ANY OTHER PERSON OR FOR ANY SPECIAL, CONSEQUENTIAL, INCIDENTAL, INDIRECT, PUNITIVE, OR EXEMPLARY DAMAGES, HOWEVER CAUSED, ARISING OUT OF OR IN CONNECTION WITH THE DOWNLOADING, VIEWING OR USE OF THE LICENSED MATERIAL REGARDLESS OF THE

FORM OF ACTION, WHETHER FOR BREACH OF CONTRACT, BREACH OF WARRANTY, TORT, NEGLIGENCE, INFRINGEMENT OR OTHERWISE (INCLUDING, WITHOUT LIMITATION, DAMAGES BASED ON LOSS OF PROFITS, DATA, FILES, USE, BUSINESS OPPORTUNITY OR CLAIMS OF THIRD PARTIES), AND WHETHER OR NOT THE PARTY HAS BEEN ADVISED OF THE POSSIBILITY OF SUCH DAMAGES. THIS LIMITATION APPLIES NOTWITHSTANDING ANY FAILURE OF ESSENTIAL PURPOSE OF ANY LIMITED REMEDY PROVIDED HEREIN.

11. Termination and Cancellation

1. The License and all rights granted hereunder will continue until the end of the applicable period shown in Clause 5.1 above. Thereafter, this license will be terminated and all rights granted hereunder will cease.

2. Licensor reserves the right to terminate the License in the event that payment is not received in full or if you breach the terms of this License.

12. General

1. The License and the rights and obligations of the parties hereto shall be construed, interpreted and determined in accordance with the laws of the Federal Republic of Germany without reference to the stipulations of the CISG (United Nations Convention on Contracts for the International Sale of Goods) or to Germany´s choice-of-law principle.

2. The parties acknowledge and agree that any controversies and disputes arising out of this License shall be decided exclusively by

the courts of or having jurisdiction for Heidelberg, Germany, as far as legally permissible.

3. This License is solely for Licensor's and Licensee's benefit. It is not for the benefit of any other person or entity.

Questions? For questions on Copyright Clearance Center accounts or website issues please contact springernaturesupport@copyright.com or +1-855-239-3415 (toll free in the US) or +1-978-646-2777. For questions on Springer Nature licensing please visit https://www.springernature.com/gp/partners/rights-permissions-third-party-distribution

Other Conditions:

Version 1.4 - Dec 2022

Questions? customercare@copyright.com.

A2. Open source EasySTORM component parts lists

The parts list for the open source components to enable EasySTORM on an Openframe as downloaded on 19/11/2023 from https://www.imperial.ac.uk/photonics/research/biophotonics/instruments--software/super-resolved-microscopy/easystorm/

OpenFrame components

You can fabricate these components using the openFrame CAD files or they can be purchased from from Cairn Research Ltd

Item	Quantity
Stage adapter layer	1
Focusing layer	1
65mm standard layer	2
Base layer	1
Piezo stage mount (precise alignment)	
Cube insert (32mm Cairn)	3
Cube adapter (25mm Cairn / Thorlabs)	2
C Mount port	1
Sideport mirror mount	1
35mm silver coated right angled mirror (Edmund Optics)	
Blanking plate	3
Mounting feet for botton port	
Set of tools, screws etc	1
Total cost ~£3200	

Excitation Sources

Lasertack diode lasers mounted in metal boxes:

Item	Quantity	Supplier	Part number
405 nm, 350mW, (with laserdriver)	1	Lasertack	LDM-405-350-C
462 nm, 1400mW, (with laserdriver)	1	Lasertack	LDM-462-1400-C
520 nm, 1000mW, (with laserdriver)	1	Lasertack	LDM-520-1000-C
635 nm, 700mW, (with laserdriver)	1	Lasertack	LDM-638-700-C
Metal box	4	RS	508-7377
Post for laserbox	4	DIY	

Controller for Lasertack diode lasers:

Item	Quantity	Supplier	Part number
MB-5 box	4	RS	401-9610

Arduino uno	4	RS	769-7409
jumper wires	4	RS	791-6454
jumper wires female/female	4	RS	791-6450
res 29.4kO	1	RS	683-3421
res 20kO	1	RS	125-1166
cap 100nF	1	RS	711-1396
headers 1	1	RS	681-2988
headers 2	1	RS	681-2963
board	4	RS	897-1635
ps 12V	4	RS	880-8372
serial male	1	RS	472-758
serial female	1	RS	472-764
serial cable	8	RS	182-8783
DAC TLV5618	4	Mouser	595-TLV5618AIP
kettle lead	4	RS	426-389
power socket	4	RS	487-832
USB cable	4	RS	182-8833
Total cost ~£410			

Components for beam combiner and fibre launch:

Item	**Quantity**	**Supplier**	**Part number**
mirror mount with mirror	8	Thorlabs	KM100-E02
beam combiner mount	3	Thorlabs	FMP1/M
exitation filter mount	4	Thorlabs	CP32/M
posts	13	Thorlabs	TR75/M
post holders	13	Thorlabs	UPH75/M
lens mount	2	Thorlabs	CP33/M
lens	1	Thorlabs	AC254-030-A-ML
rods	1	Thorlabs	ER3-P4
xy mount	1	Thorlabs	CXY1
fiber plate FPC	1	Thorlabs	SM1FC
fiber plate APC	1	Thorlabs	SM1FCA
fiber 50 µm core APC	1	Thorlabs	FG050UGA-CUSTOM
fiber 100 µm core APC	1	Thorlabs	FG100UGA-CUSTOM
Total cost ~£1600			

Filters:

Item	**Quantity**	**Supplier**	**Part number**
405/10nm OD4 12.5mm	1	Edmund	65072
467/10nm OD4 12.5mm	1	Edmund	39308
636/10nm OD4 12.5mm	1	Edmund	65106
520/10nm OD4 12.5mm	1	Edmund	65093
427LP dichroic 25mm	1	Edmund	86389

482LP dichroic 25mm	1	Edmund	86324
613LP dichroic 25mm	1	Edmund	86394
Total cost ~£1000			
Total for 4-line exciation source	**~4560**		

Focusing Layer

Item	Supplier	Part #	Quantity
100x 1.3NA 0.17/INF Plan Fluor objective lens	Amscope	PF100X-INF	1
13mm travel piezo stage	PI	Q-545.140	1
Piezo servo controller, 1-axis	PI	E-873	1
Total cost ~£3,600			

Sample Stage

Item	Supplier	Part #	Quantity	Cost
Zaber motorised stage with adapter plate, mutwell plate insert, 2-axis stepper motor controller and joystick	Laser 2000	ASR100B120B-T3-K0047, AP131, AM109, X-MCB2-KX14BG and X-JOY3-PTB2	1	£7,355.00
or				
Manual microscope stage (Olympus)	Thorlabs	CS S2001	1	£705.00

OpenExcite

Item	Supplier	Part #	Quantity
Fibre connector [FC-APC]	Thorlabs	SM1FCA	1
Lens tube	Thorlabs	SM1L15	1
Slotted lens tube for fibre connector	Thorlabs	SM1L20C	1
Fibre collimating lens [45mm]	Thorlabs	AC254-045-A	1
SM1 to SM2 adapter	Thorlabs	SM2A6	1
25mm clear aperture iris	Thorlabs	SM2D25D	1
SM2 to SM1 adapter	Thorlabs	SM1A2	1
90 degree kinematic mount (elliptical hole)	Thorlabs	KCB1E/M	1
1" elliptical mirror (EO2 coating)	Thorlabs	BBE1-E02	1
100mm post holder	Thorlabs	UPH100/M	1
100mm post	Thorlabs	TR100/M	1
SM1 to SM30 adapter	Thorlabs	SM1A16	1

Tube lens tube	Thorlabs	SM30L30	2
Tube lens tube	Thorlabs	SM30L10	1
30mm diameter lens [150mm] from Edmund	Edmund Optics	#32-502	1
Total cost ~£665			

Dichroic layer

Filter sets for 405nm, 462nm, 635nm, 830nm cube:

Item	Supplier	Part #	Cost
Excitation filter	Chroma	DC/ZET405/465/625/825x	£470.00
Dichroic	Chroma	DC/ZT405/465/625/825rpc-UF2	£550.00
Emission filter	Chroma	DC/ZET405/465/625/825m	£810.00
		Filter set total	£1,830.00

Filter sets for 405nm, 528nm, 635nm, 830nm cube:

Item	Supplier	Part #	Cost
Excitation filter	not yet available		
Dichroic	Chroma	DC/ZT405/528/640/830rpc-UF2	£470.00
Emission filter	Chroma	DC/ZET405/528/640/830m	£550.00
			£810.00

Camera Port

SM30 Camera Port:

Item	Supplier	Part #	Quantity
SM1 to c-mount adapter	Thorlabs	SM1A10	1
Non-rotating translating SM1 mount	Thorlabs	SM1ZM	1
SM30 to SM1 adapter	Thorlabs	SM1A15	1
SM30 threaded tube 3"	Thorlabs	SM30L30	2
SM30 tube clamp	Thorlabs	SM30TC	1
Post assembly, 30mm	Thorlabs	UPH30/M	1
Post, 20mm	Thorlabs	TR20/M	1
SM1 Tube, 10mm	thorlabs	SM1L03	1
Total cost ~£300			

Cameras:

Item	Supplier	Part #	Quantity	Cost

Fan cooled Camera	Cairn Research Ltd	Cellcam Centro	1	<£1000
TE cooled Camera	Cairn Research Ltd	Cellcam Kikker	1	<£1000

Total System Cost

Subsystem	**Cost**
openFrame	£3,200.00
Excitation sources	£4,560.00
Focusing layer	£3,600.00
openExcite	£665.00
Dichroic layer	£1,830.00
camera port	£1,300.00
TOTAL	**£15,155.00**
Plus	
manual micrscope stage	<£1000
or	
Motorised micrscope stage	>~£6000

A3. Components list for an easySTORM microscope implemented on an openFrame

The parts list to implement easySTORm on an openFrame using components available from Cairn Research as downloaded on 19/11/2023 from:

https://www.imperial.ac.uk/photonics/research/biophotonics/instruments--software/fluorescence-microscopy/openframe/

openFrame components:

Hardware components for motorised *openFrame* fluorescence microscope (for latest version see https://www.imperial.ac.uk/photonics/research/biophotonics/instruments--softwa

Item	Multiple openFrame components?	Cairn part #	Cairn part qty	Equivalent openFrame part #	Indicative price (£)	Quantity	CAD available (permissive licence)	Purpose/notes	Additional parts needed for functional layer
openFrame base plate	No	P1500/BAS/000	1	OF-LL-BP	389	1	Y	Allows for attachment of microscope frame to optical bench	4x M4x12 countersunk screws for 2x OF-CL-LC (e.g. Accu, SPK-M4-12-A2) 2x springs for 2x OF-CL-LC (e.g. (Lee Spring, LCM035A 08 S) 2x 4mm x 6mm dowel pins (e.g. Accu, HDP-4-6-A1)
openFrame 80mm layer base (configured for 2-position slider)	Yes	P1500/080/000	1	OF-LL-80		1	Y	Allows for coupling out of fluorescence light. Cairn version comes with 2x 4mm x 6mm dowel pins (Accu, HDP-4-6-A1) Each OF-CL-LC comes with 1x spring (Lee Spring, LCM035A 08 S and 2x M4x12 screws (Accu, SPK-M4-12-A2) in the Cairn part	4x M4x12 countersunk screws for 2x OF-CL-LC (e.g. Accu, SPK-M4-12-A2) 2x springs for 2x OF-CL-LC (e.g. (Lee Spring, LCM035A 08 S) 2x 4mm x 6mm dowel pins (e.g. Accu, HDP-4-6-A1) 2x 4mm x 6mm dowel pins (e.g. Accu, HDP-4-6-A1)
		P1500/CMT/080	2	OF-CL-LC		2	Y		
		P1500/DCS/000	1	OF-CL-SM2		2	Y		
				OF-AD-SBSM2-CM	2687	2	Y		
				OF-AC-2P-OD		2	Y		
				OF-IN-2P-OD		1	Y		
				OF-AD-HA-IN-2P-OD		4	Y		
				OF-HA-2P-OD		2	Y		
		P1500/MIR/000	2			2	N	(This is a mirror)	
openFrame 80mm layer base (configured for single position mirror)	Yes	P1500/080/000	1	OF-LL-80		1	Y	Allows for coupling out of fluorescence light. Cairn version comes with 2x 4mm x 6mm dowel pins (Accu, HDP-4-6-A1) Each OF-CL-LC comes with 1x spring (Lee Spring, LCM035A 08 S and 2x M4x12 screws (Accu, SPK-M4-12-A2) in the Cairn part	Mirror prism (e.g. Edmund 89-632) 4x M4x12 countersunk screws for 2x OF-CL-LC (e.g. Accu, SPK-M4-12-A2) 2x springs for 2x OF-CL-LC (e.g. (Lee Spring, LCM035A 08 S) 2x 4mm x 6mm dowel pins (e.g. Accu, HDP-4-6-A1)
		P1500/CMT/080	1	OF-CL-LC		2	Y		
		P1500/BLK/SM2	1	OF-PP-SM2	1119	1	Y		
		P1500/INS/000	1	OF-CL-SM2		1	Y		
		P1500/SPT/000	1	OF-AD-SBSM2-CM		1	Y		
				OF-IN-65-MCH		1	Y		
				OF-AD-MCH-M4S		1	Y		
				OF-AC-00		1	Y		
openFrame tube lens layer	No	P1500/030/000	1					Allows tube lens to be attached to layer above whilst not protruding too much into the layer below. Cairn version comes with 2x 4mm x 6mm dowel pins (Accu, HDP-4-6-A1)	Tube lens
				OF-LL-TL	263	1	Y		
				OF-AD-SM2-TL-NIKON	195	0/1	Y	Allows fitting of Nikon tube lens	4x M4x12 countersunk screws for 2x OF-CL-LC (e.g. Accu, SPK-M4-12-A2)
				OF-AD-SM2-TL-OLYMPUS	475	0/1	Y	Allows fitting of Olympus tube lens	2x springs for 2x OF-CL-LC (e.g. (Lee Spring, LCM035A 08 S)
				OF-CL-LC		2	Y	Each OF-CL-LC comes with 1x spring (Lee Spring, LCM035A 08 S and 2x M4x12 screws (Accu, SPK-M4-12-A2) in the Cairn part	2x 4mm x 6mm dowel pins (e.g. Accu, HDP-4-6-A1)
openFrame 65mm layer with 2 ports (configured for use as excitation layer)	Yes	P1500/065/000	1	OF-LL-65		1	Y	Allows coupling in of illumination light. Cairn version comes with 2x 4mm x 6mm dowel pi	Cube, dichroic, filters
								Each OF-CL-LC comes with 1x spring (Lee Spring, LCM035A 08 S and 2x M4x12 screws	
		Part of P1500/065/000	N/A	OF-CL-LC		2	Y	(Accu, SPK-M4-12-A2) in the Cairn part	4x M4x12 countersunk screws for 2x OF-CL-LC (e.g. Accu, SPK-M4-12-A2)
		P1500/INS/000	1	OF-IN-65-MCH	727	1	Y		2x springs for 2x OF-CL-LC (e.g. (Lee Spring, LCM035A 08 S)
		P1500/BLK/035	1	OF-PP-SM30		1	Y		2x 4mm x 6mm dowel pins (e.g. Accu, HDP-4-6-A1)
		P1500/EPI/030	1	OF-CL-SM30		1	Y		
		P1500/BLK/035	1	OF-AC-00		1	Y		
openFrame focus layer	Yes	P1500/002/000	1	OF-LL-FL-MOT		1	Y	Allows focussing via objective translation and coupling in of autofocus light	PI Q.545 and driver
		P1500/BLK/035	1	OF-PP-SM30		1	Y	Port plug	Objective
		P1500/PZO/MNT	1	OF-AD-FL-PZ-PI-Q545	1011	1	Y	openFrame, Adapter, From Focussing layer To Piezo Z-stage for PI Q545	4x M4x12 countersunk screws for 2x OF-CL-LC (e.g. Accu, SPK-M4-12-A2)
		Part of P1500/002/000	N/A	OF-AD-PZ-PI-Q545-OBH		1	Y		2x springs for 2x OF-CL-LC (e.g. (Lee Spring, LCM035A 08 S)
		Part of P1500/002/000	N/A	OF-AD-OBH-M25-60		1	Y		2x 4mm x 6mm dowel pins (e.g. Accu, HDP-4-6-A1)
		Part of P1500/002/000	N/A	OF-AD-M25-RMS-4S		0/1	Y	only needed for RMS objectives	
openFrame stage plate adpater layer	No	P1500/STG/000	1	OF-LL-SP	325	1	Y	Allows easy attachment of microscope stage to *openFrame*	2x 4mm x 6mm dowel pins (e.g. Accu, HDP-4-6-A1)
		Part of P1500/STG/000	N/A	e.g. OF-AD-SP-ZAB-PZ-PI-Q545					Adapter to stage
openFrame transilluminator	Yes	P1136/001/000	1	OF-AD-SP-TI-PILLAR		1	Y	Allows for attachment of transilluminator	LED
		Part of P1136/001/000	N/A	OF-TI-PILLAR		1	Y	Transillumination pillar	
		Part of P1136/001/000	N/A	OF-AD-TI-PILLAR-TI-ARM	473	1	Y		
		Part of P1136/001/000	N/A	OF-TI-ARM		1	Y		
		Part of P1136/001/000	N/A	OF-AD-TI-ARM-SM2		1	Y		
Interlocked safety cover for slide holder	No	Standard printed		S1500/ISL/001	309.25	0/1	N	Reccommended for safety reasons	
		High quality printed		S1500/ISL/002	428	0/1	N		
		CNC machined		S1500/ISL/003	739.6	0/1	N		
Interlocked safety cover for multiwell plates	No	Standard printed		S1500/IMW/001	309.25	0/1	N	Reccommended for safety reasons	
		High quality printed		S1500/IMW/002	428	0/1	N		
		CNC machined		S1500/IMW/003	739.6	0/1	N		
Dichroic cube	No	N/A		Can use CM1-DCH/M	141.5	1	N	Alternative cubes can also be used	Filters and dichroic
Cairn Prices updated 25/07/2023									

openFrame nomenclature:

Nomenclature		Component type								Code	Item	Notes
OpenFrame		**Layer**	-	**Size/function**	-		-		-			
OF	-	LL	-	65	-		-		-	OF-LL-65	openFrame, Layer, 65mm	
OF	-	LL	-	80	-		-		-	OF-LL-80	openFrame, Layer, 80mm	
OF	-	LL	-	TL	-		-		-	OF-LL-TL	openFrame, Layer, tube lens spacer	
OF	-	LL	-	BP	-		-		-	OF-LL-BP	openFrame, Layer, base plate	
OF	-	LL	-	SP	-		-		-	OF-LL-SP	openFrame, Layer, stage plate	Separate pieces needed to adapt to each stage (see adapters)
OF	-	LL	-	FL	-	MOT	-		-	OF-LL-FL-MOT	openFrame, Layer, Focusing Layer, motorised z options	
		Layer Insert	-	**Size/function**	-	**Insert**	-	**Type**	-			
OF	-	IN	-	MCH	-		-		-	OF-IN-MCH	openFrame, Layer insert, For holding mirror/cube via adapter	Mirror/cube holder insert
OF	-	IN	-	2P	-	OD	-		-	OF-IN-2P-OD	openFrame, Layer insert, For 2-position slider, Positions go Opposite Direction ports	Port switching insert
		Port Plug	-	**Size/function**	-		-		-			
OF	-	PP	-	SM30	-		-		-	OF-PP-SM30	openFrame, Port plug, For SM30 tube OD	SM30 has 35mm OD
OF	-	PP	-	SM2	-		-		-	OF-PP-SM2	openFrame, Port plug, For SM2 tube OD	SM2 has 55.9mm OD
		Aperture Cover plate	-	**Size/function**	-		-		-			
OF	-	AC	-	00	-		-		-	OF-AC-00	openFrame, Aperture cover plate, Type 00	Works for OF-LL-65, OF-LL-FL-XXXX
OF	-	AC	-	2P-OD	-		-		-	OF-AC-2P-OD	openFrame, Aperture cover plate, For OF-IN-2P-OD	
		Clamp	-	**Size/function**	-		-		-			
OF	-	CL	-	LC	-		-		-	OF-CL-LC	openFrame, clamp, For attaching layers	2 clamps per layer
OF	-	CL	-	SM30	-		-		-	OF-CL-SM30	openFrame, C-clamp, For SM30 OD	SM30 has 35mm OD
OF	-	CL	-	SM2	-		-		-	OF-CL-SM2	openFrame, C-clamp, For SM2 OD	SM30 has 35mm OD
		Handle	-	For	-		-		-			
OF	-	HA	-	2P-OD	-		-		-	OF-HA-2P-OD	openFrame, Handle, For OF-IN-2P-OD	
OF	-	HA	-	AC-00	-		-		-	OF-HA-AC-00	openFrame, Handle, For OF-AC-00	
		Transilluminator	-	**Size/function**	-		-		-			
OF	-	TI	-	PILLAR	-		-		-	OF-TI-PILLAR	openFrame, Transilluminator, Basic pillar with stage mounting attachment	
OF	-	TI	-	ARM	-		-		-	OF-TI-ARM	openFrame, Transilluminator, Basic arm	
		Adapter	-	**From**	-	**To**	-	**Type**	-	**Subvariant**		
OF	-	AD	-	SBSM30	-	CM	-		-	OF-AD-SBSM30-CM	openFrame, Adapter, From SM30 smoothbore, To C-mount	Uses SM30 tube OD
OF	-	AD	-	SBSM2	-	CM	-		-	OF-AD-SBSM2-CM	openFrame, Adapter, From SM2 smoothbore, To C-mount	Uses SM2 tube OD
OF	-	AD	-	SP	-	TI-PILLAR	-		-	OF-AD-SP-TI-PILLAR	openFrame, Adapter, From stage plate, To transillumination pillar	
OF	-	AD	-	TI-PILLAR	-	TI-ARM	-		-	OF-AD-TI-PILLAR-TI-ARM	openFrame, Adapter, From transillumination pillar, To transillumination arm	
OF	-	AD	-	TI-ARM	-	LED	-	CAIRN	-	OF-AD-TI-ARM-LED-CAIRN	openFrame, Adapter, From transillumination arm, To LED holder for Cairn LEDs	
OF	-	AD	-	MCH	-	M4S	-		-	OF-AD-MCH-M4S	openFrame, Adapter, From OF-IN-65-MCH, To hold a 4S degree mirror (e.g. Edmund 89-632)	
OF	-	AD	-	FL	-	PZ-PI	-	Q545	-	OF-AD-FL-PZ-PI-Q545	openFrame, Adapter, From Focussing layer To Piezo Z-stage for PI Q545	
OF	-	AD	-	SP	-	ZAB	-	PZ-PI	-	OF-AD-SP-ZAB-PZ-PI-Q545	openFrame, Adapter, From stage plate, To Zaber stage, Assuming motorised PI piezoelectric Z-stage, with PI Q.545 stage	
OF	-	AD	-	PZ-PI	-	Q545	-	OBH	-	OF-AD-PZ-PI-Q545-OBH	openFrame, Adapter, From PI Q.545 piezo, To objective holder	
OF	-	AD	-	OBH	-	M25	-	60	-	OF-AD-OBH-M25-60	openFrame, Adapter, From Objective holder, To M25x0.75 thread, For 60mm parfocal distance objectives	
OF	-	AD	-	M25	-	RMS	-	4S	-	OF-AD-M25-RMS-4S	openFrame, Adapter, From M25x0.75 thread for 60mm parfocal distance objectives, To RMS thread, For 45mm parfocal distance objectives	
OF	-	AD	-	SM2	-	TL	-	NIKON	-	OF-AD-SM2-TL-NIKON	openFrame, Adapter, From SM2, To Nikon Tube lens thread	
OF	-	AD	-	SM2	-	TL	-	OLYMPUS	-	OF-AD-SM2-TL-OLYMPUS	openFrame, Adapter, From SM2, To Olympus Tube lens thread	
OF	-	AD	-	LL	-	SM1	-		-	OF-AD-LL-SM1	openFrame, Adapter, From Layer, To SM1	
OF	-	AD	-	HA	-	IN-2P-OD	-		-	OF-AD-HA-IN-2P-OD	openFrame, Adapter, From handle, To OF-IN-2P-OD	

OF-LL-65 *openExcite:*

openExcite , including manual control of excitation beam (e.g. for HILO, TIRF)

Baseline components

Common components for options (A) and (B)					
Item	**Part #**	**Manufacturer**	**Quantity**	**Price (£)**	**Purpose/notes**
30mm diameter Tube lens [150mm] from Edmund	#32-502	Thorlabs	1	104.55	Focuses illumination light down to objective back aperture (Focal length may need to be extended if there is more than ~100mm of optical path from this lens to the objective flange)
Fibre collimating lens [45mm]	AC254-045-A	Thorlabs	1	65.51	Collimates illumination light
Laser delivery (multimode, 105 um diameter core, 0.1 NA) optical fibre	FG105LVA custom patch cord	Thorlabs	1	CUSTOM	FC-APC termination at the illuminator end is recommended to reduce power being back-coupled into source laser(s). NA and MMF diameter can be changed to adjust, e.g., excitation field of illumination, opportunity for TIRF. An armoured fibre is preferred for safety reasons
Fibre connector [FC-APC]	SM1FCA	Thorlabs	1	26.87	For attching fibre to *openExcite* module
90 degree kinematic mount (elliptical hole)	KCB1E/M	Thorlabs	1	163.85	Allows mounting/control of steering mirror
1" elliptical mirror (EO2 coating)	BBE1-E02	Thorlabs	1	95.88	Steering mirror
SM1 to SM30 adapter	SM1A16	Thorlabs	1	18.32	Couples steering mirror holder to SM30 tube
Tube lens tube (30mm ID, 3" long)	SM30L30	Thorlabs	2	33.2	Extends tube system
Tube lens tube (30mm ID, 2" long)	SM30L20	Thorlabs	1	28.91	Holds lens for focusing beam onto objective back aperture and allows coupling to microscope frame via SM30 clamp
Slotted lens tube for collimating lens	SM1L30C	Thorlabs	1	58.09	Allows adjustment of collimating lens
					Need to choose (A) or (B):
A) Simplest *openExcite* module					
Lens tube (1.5")	SM1L15	Thorlabs	1	12.74	Extends tube system
B) *openExcite* with power attenuation					
Filter slider	CFS1/M	Thorlabs	1	133.64	Allows for sliding of filters into/out of the beam path
1" diameter ND filter	CHOOSE AS APPROPRIATE		1	CUSTOM	Attenuates excitation beam
Lens tube (0.5")	SM1L05	Thorlabs	1	10.22	Extends tube system
SM1 tube coupler	SM1T2	Thorlabs	1	17.39	Allows connection of tube ends of same gender
Optional support for *openExcite* module					
Lens tube clamp	SM1TC	Thorlabs	1	36.9	
75mm post holder [CHECK LENGTH]	UPH75/M	Thorlabs	1	27.31	To support *openExcite* module in case of accidental knocks, etc.
Post swivel base	UPH/A	Thorlabs	1	17.74	
75mm post [CHECK LENGTH]	TR75/M	Thorlabs	1	4.61	
Note: it is esential that the laser beam path is fully enclosed to ensure laser safety					
Thorlabs and Edmund prices updated on 19/05/2023					

OF-LL-80 Camera Port:

Basic *openFrame* camera layer - single port

Item	Part #	Manufacturer	Quantity	Price (£)	Purpose/notes
You will need a camera - some options are listed here					
CellCam Kikker 100MT camera for fluorescence imaging	DCC/KIK/003	Cairn	0/1	3325	monochrome TE-cooled CMOS with with back-illuminated SONY IMX492 CMOS sensor
Trigger box for CellCam Kikker	P555/MM/KIK	Cairn	0/1	650	trigger box for CellCam Kikker
CellCam Centro 200MR CMOS for lower-cost fluorescence	DCC/CEN/000	Cairn	0/1	1238	monochrome fan-cooled CMOS with SONY IMX183 sensor
CellCam Rana 200CR colour CMOS	DCC/RAN/000	Cairn	0/1	971.66	colour fan-cooled CMOS with SONY IMX183 sensor
Need to choose between (A), (B) or (C)					
(A) Simplest implementation using tube lens layer inside *openFrame* stack					
openFrame, Adapter, From SM2 smoothbore, To C-mount	OF-AD-SBSM2-CM	Cairn	0/1	100	Allows coupling of camera to SM2 layer via clamp - included in OF-LL-80 if purchaed from Cairn
(B) Implementation using tube lens layer inside *openFrame* stack and Thorlabs parts as opposed to OF-AD-SBSM2-CM					
SM2 threaded tube 3"	SM2L30	Thorlabs	1	29.99	Allows coupling to 80mm SM2 layer via clamp
SM2 to SM1 adapter	SM1A2	Thorlabs	1	20.88	Allows coupling of SM2 layer to c-mount adapter
SM1 to c-mount adapter	SM1A10	Thorlabs	1	16.37	Allows coupling of camera to tube system
(C) Implementation using external tube lens *instead of* using tube lens layer inside openFrame stack, e.g. to add image splitter, etc.					
Tube lens (to be mounted in SM2 tube)	e.g., Nikon #58-520	Edmund Optics	1	305.15	Focuses light onto image plane
SM2 threaded tube 6"	SM2E60	Thorlabs	1	53.51	Allows coupling to 80mm SM2 layer via clamp
SM2 threaded tube 3"	SM2L30	Thorlabs	1	29.99	Extends tube system
SM2 to SM1 adapter	SM1A2	Thorlabs	1	20.88	Allows coupling of SM2 layer to c-mount adapter
SM1 to c-mount adapter	SM1A10	Thorlabs	1	16.37	Allows coupling of camera to tube system
Optional upgrade:					
Non-rotating translating SM1 mount	SM1ZM	Thorlabs	1	142.38	Allows fine adjustment of focus of camera image
Thorlabs and Edmund prices updated on 19/05/2023					
Cairn Prices updated 25/07/2023					

openAF (cage System):

openAF - optical autofocus components for use with oil-immersion objective lenses

Item	Part #	Manufacturer	Quantity	Price	Total	Notes
Choose between common components with (A) self-built cage-based assembly, (B) prefabricated mechanical assembly, or (C) Premade system						
Common optomechanics/light source/detection components for options (A) and (B). Not needed for option (C)						
Autofocus short-pass dichroic (e.g.) Edmund Optics	69-220	Edmund Optics	1	140.25	140.25	
50:50 beamsplitter	47-026	Edmund Optics	1	130.05	130.05	
Cylindrical lens CL1	LJ1227L1-B	Thorlabs	1	77.75	77.75	
Cylindrical lens CL2	LJ1960L1-B	Thorlabs	1	54.82	54.82	
Camera tube lens L5	AC254-200-B	Thorlabs	1	76.22	76.22	
Superluminescent diode (wavelength to match autofocus dichroic), fibre-coupled	SLD-840F50P05S-TOSA9	Superlum Diodes Ltd	1	420	420	
SLD mount with TEC	LDM9T/M	Thorlabs	1	689.06	689.06	
Superluminescent diode driver	LDC205C	Thorlabs	1	889.94	889.94	It may be possible to use a cheaper diode power supply
Ø25 mm AR-Coated Absorptive Neutral Density Filter, 650-1050 nm	NE10A-B	Thorlabs	1	66.15	66.15	
CMOS camera	CM3-U3-31S4M	FLIR	1	578	578	
					3122.24	
(A) Self-assembly openFocus optomechanics						
Cage rods 1.5" x4	ER1.5-P4	Thorlabs	1	18.02	18.02	
Cage rods 2" x4	ER2-P4	Thorlabs	2	18.8	37.6	
Cage rods 4" x4	ER4-P4	Thorlabs	3	21.89	65.67	
Cage rod holder x4	ERSCB-P4	Thorlabs	2	47.25	94.5	
Dichroic holding cube	CM1-DCH/M	Thorlabs	1	141.5	141.5	
SM1 cage plate (SM1 threaded)	CP33/M	Thorlabs	4	14.32	57.28	
SM1 cage plate (SM05 threaded)	CP32/M	Thorlabs	1	15.19	15.19	
Right angle kinematic mount	KCB1E/M	Thorlabs	2	163.85	327.7	
Elliptical 1" mirrors	BBE1-E02	Thorlabs	2	95.88	191.76	
Fibre connector [FC-APC] [CHOOSE FIBRE TYPE AS APPROPRIATE]	SM1FCA	Thorlabs	1	26.87	26.87	For attching fibre to AF
30mm cage translator for 1" optics	CXY1A	Thorlabs	2	151.1	302.2	One could be replaced with a kinematic mirror and some cage rods for the camera
SM1 to c-mount adapter	SM1A10	Thorlabs	1	16.37	16.37	
75mm post holder [CHECK LENGTH NEEDED FOR YOUR SYSTEM]	UPH75/M	Thorlabs	3	27.31	81.93	
Post swivel base	UPHA	Thorlabs	3	17.74	53.22	
75mm post [CHECK LENGTH NEEDED FOR YOUR SYSTEM]	TR75/M	Thorlabs	3	4.61	13.83	
CUSTOM CL PAIR HOLDER/SPACER	CUSTOM	CUSTOM	1		0	
CUSTOM SHIELDING	CUSTOM	CUSTOM	1		0	
					1443.64	
(B) Prefabricated openFocus optomechanical assembly						
Cairn openFocus module skeleton (optical/mechanical components not included) - this will require additional parts and assembly/alignment work	TBD	Cairn	1	1200	**1200**	
(C) Complete openFocus - all components included						
Cairn openFocus module - premade	TBD	Cairn	1	10000	**10000**	
The openAF system can be adapted for use with air or water immersion objective lenses (working on reflection from lower surface of coverslip)						
Thorlabs and Edmund prices updated on 19/05/2023						
Cairn Prices updated 25/07/2023						

Excitation Sources:

Multimode diode laser excitation sources
(no shielding parts included)

Item	Part #	Manufacturer	Quantity needed	Qty per unit	Price per unit (£, RS prices do not include VAT)	Price per unit (GBP)	Total (GBP)	Notes
Need to choose between (A) Self-assembly 4 line multimode diode laserbank, (B) 6 line proprietary multimode diode laserbank, (C) 7 line proprietary multimode diode laserbank, (D) Self-assembly single line laserbank, (E) other laser sources								
(A) Self-assembly 4 line multimode diode laserbank (405/462/520/635 nm - other lasers and dicrhoics can be substituted to change wavelengths available)								
405 nm, 350mW, (with laser driver)	LDM-405-350-C	Lasertack	1	1	EUR 328.30	285.621	£285.62	
462 nm, 1400mW, (with laser driver)	LDM-462-1400-C	Lasertack	1	1	EUR 406.66	353.7942	£353.79	
520 nm, 1000mW, (with laser driver)	LDM-520-1000-C	Lasertack	1	1	EUR 554.99	482.8413	£482.84	
635 nm, 700mW, (with laser driver)	LDM-638-700-C	Lasertack	1	1	EUR 345.83	300.8721	£300.87	
Laser driver with TEC controller and Peltier cooler	PD-01359	Laser tack	4	1	EUR 135	117.45	£469.80	
Metal box	146-5333	RS	4	1	14.94	11.41	£45.64	
Copper post for laserbox	CUSTOM	CUSTOM	4	N/A		CUSTOM	CUSTOM	
MB-5 box	401-9610	RS	4	1	10.22	10.22	£40.88	
Arduino Uno	769-7409	RS	4	1	20.55	20.55	£82.20	
Jumper wires	791-6454	RS	4	1	3.12	3.12	£12.48	
Jumper wires female/female	791-6450	RS	4	1	3.12	3.12	£12.48	
Resistor 29.4kO	683-3421	RS	4	25	0.525	0.525	£0.08	
Resistor 20kO	125-1166	RS	4	20	2.36	2.36	£0.47	
Capacitor 100nF	711-1396	RS	4	100	5.8	5.8	£0.23	
Headers	681-2988	RS	4	10	1.2	1.2	£0.48	
Solderable breadboard	897-1635	RS	4	1	1.57	1.57	£6.28	
DAC TLV5618	595-TLV5618AIP	Mouser	4	1	12.49	12.49	£49.96	
Kettle lead (IEC plug)	426-389	RS	4	1	9.2	9.2	£36.80	
Power socket	487-832	RS	4	1	6.22	6.22	£24.88	
USB cable	182-8833	RS	4	1	3.82	3.82	£15.28	
Power supply	880-8408	RS	4	1	20.89	20.89	£83.56	
Mirror mount 1/2"	KM05/M	Thorlabs	8	1	31.64	31.64	£253.12	
Mirror mount 1"	KM100	Thorlabs	1	1	31.39	31.39	£31.39	
Hex-key thumb screw	HKTS-5/64	Thorlabs	1	1	20.9	20.90	£20.90	
1/2" Mirror	BB05-E02	Thorlabs	8	1	41.78	41.78	£334.24	
1" Mirror	BB1-E02	Thorlabs	1	1	60.92	60.92	£60.92	
Pedestal post	PH20E/M	Thorlabs	13	1	20.09	20.09	£261.17	Look for packs of 5
Posts	TR30/M	Thorlabs	13	1	4.04	4.04	£52.52	Look for packs of 5
Clamping fork	CF125C/M	Thorlabs	13	1	9.44	9.44	£122.72	Look for packs of 5
Beam combiner mount	FMP1/M	Thorlabs	3	1	13.81	13.81	£41.43	
SM1 cage plate	CP33/M	Thorlabs	3	1	14.32	14.32	£42.96	
Adjustable iris	SM1D12D	Thorlabs	1	1	57.44	57.44	£57.44	
Extension Rods	ER3-P4	Thorlabs	1	1	20.34	20.34	£20.34	
Extension Rods	ER05-P4	Thorlabs	2	1	15.57	15.57	£31.14	
XY mount	CXY1A	Thorlabs	1	1	151.1	151.10	£151.10	
Fibre plate FC/PC	SM1FC	Thorlabs	1	1	25.33	25.33	£25.33	
Fibre plate APC	SM1FCA	Thorlabs	1	1	26.87	26.87	£26.87	
Coupling lens	A260TM-A	Thorlabs	1	1	72.72	72.72	£72.72	
SM1 to M9 x 0.5 Lens Cell Adapter	S1TM09	Thorlabs	1	1	19.66	19.66	£19.66	
405/10nm OD4 12.5mm	65-072	Edmund Optics	1	1	136	136.00	£136.00	
467/10nm OD4 12.5mm	39-308	Edmund Optics	1	1	136	136.00	£136.00	
636/10nm OD4 12.5mm	65-106	Edmund Optics	1	1	136	136.00	£136.00	
427LP dichroic 25mm	86-389	Edmund Optics	1	1	225.25	225.25	£225.25	
480LP dichroic 25mm	86-391	Edmund Optics	1	1	191.25	191.25	£191.25	482 no longer in stock (86-324)
613LP dichroic 25mm	86-394	Edmund Optics	1	1	225.25	225.25	£225.25	
						TOTAL	**£4,980.36**	
(B) 6 line proprietary multimode diode laserbank (405/445/470/520/530/640 nm)								
LDI-6 - 6 line laser diode illuminator (lines should match filter cube)	D89/15000-06	Cairn	1	1		14957.02	£14,957.02	
Fibre patch cord for multiline illuminator	M93L02	Thorlabs	1	1		178.73	£178.73	
						TOTAL	**£15,135.75**	
(C) 7 line proprietary multimode diode laserbank (405/445/470/520/530/555/640 nm)								
LDI-7 - 7 line laser diode illuminator (lines should match filter cube)	D89/15000-07	Cairn	1	1		22255.76	£22,255.76	
Fibre patch cord for multiline illuminator	BFY400LS02	Thorlabs	1	1		301.26	£301.26	
	ADASMA	Thorlabs	1	1		13.97	£13.97	
	M93L02	Thorlabs	1	1		178.73	£178.73	
						TOTAL	**£22,749.72**	
Multimode diode lasers deliverd by multimode optical fibres (with vibrator) are a cost-effective means to provide the high exctation intensities for SMLM (easySTORM) In principle, any laser engine can be used for excitation and should ideally be delivered via an optical fibre with a FC-APC connector. Single mode lasers may provide superior performance for TIRF but some despeckling may be required (e.g., by vibrating the multimode optical fibre) and the illumination may not be as uniform as that obtained with multimode diode lasers								
(D) Self-assembly single line laserbank (choose which laser to use)								
CHOOSE A LASER - example used here is: 635 nm, 700mW, (with laser driver)	LDM-638-700-C	Lasertack	1	1	EUR 345.83	300.8721	£300.87	
Laser driver with TEC controller and Peltier cooler	PD-01359	Laser tack	1	1	EUR 135	117.45	£117.45	
Metal box	146-5333	RS	1	1	14.94	11.41	£11.41	
Copper post for laserbox	CUSTOM	CUSTOM	1	N/A	CUSTOM	CUSTOM	CUSTOM	
MB-5 box	401-9610	RS	1	1	10.22	10.22	£10.22	
Arduino Uno	769-7409	RS	1	1	20.55	20.55	£20.55	
Jumper wires	791-6454	RS	1	1	3.12	3.12	£3.12	
Jumper wires female/female	791-6450	RS	1	1	3.12	3.12	£3.12	
Resistor 29.4kO	683-3421	RS	1	25	0.525	0.525	£0.02	
Resistor 20kO	125-1166	RS	1	20	2.36	2.36	£0.12	
Capacitor 100nF	711-1396	RS	1	100	5.8	5.8	£0.06	
Headers	681-2988	RS	1	10	1.2	1.2	£0.12	
Solderable breadboard	897-1635	RS	1	1	1.57	1.57	£1.57	
DAC TLV5618	595-TLV5618AIP	Mouser	1	1	12.49	12.49	£12.49	
Kettle lead (IEC plug)	426-389	RS	1	1	9.2	9.2	£9.20	
Power socket	487-832	RS	1	1	6.22	6.22	£6.22	
USB cable	182-8833	RS	1	1	3.82	3.82	£3.82	
Power supply	880-8408	RS	1	1	20.89	20.89	£20.89	
Hex-key thumb screw	HKTS-5/64	Thorlabs	1	1	20.9	20.90	£20.90	
Mirror mount 1/2"	KM05/M	Thorlabs	2	1	31.64	31.64	£63.28	
1/2" Mirror	BB05-E02	Thorlabs	2	1	41.78	41.78	£83.56	
Pedestal post	PH20E/M	Thorlabs	4	1	20.09	20.09	£80.36	
Posts	TR30/M	Thorlabs	4	1	4.04	4.04	£16.16	
Clamping fork	CF125C/M	Thorlabs	4	1	9.44	9.44	£37.76	
SM1 cage plate	CP33/M	Thorlabs	1	1	14.32	14.32	£14.32	
Extension Rods	ER3-P4	Thorlabs	1	1	20.34	20.34	£20.34	
Extension Rods	ER05-P4	Thorlabs	1	1	15.57	15.57	£15.57	
xy mount	CXY1A	Thorlabs	1	1	151.1	151.10	£151.10	
fiber plate FC/PC	SM1FC	Thorlabs	1	1	25.33	25.33	£25.33	
fiber plate APC	SM1FCA	Thorlabs	1	1	26.87	26.87	£26.87	
Coupling lens	A260TM-A	Thorlabs	1	1	72.72	72.72	£72.72	
SM1 to M9 x 0.5 Lens Cell Adapter	S1TM09	Thorlabs	1	1	19.66	19.66	£19.66	
CHOOSE A FILTER FOR SUPERLUMINESCENCE SUPPRESSION: e.g. 636/10nm OD4 12.5mm	65-106	Edmund Optics	1	1	136	136.00	£136.00	
						TOTAL	**£783.93**	
(E) Other laser sources								
You will need to ensure adequate filling of the modes of the fibre to achieve uniform illumination, and use an appropriate dichroic in the microscope								
Thorlabs, RS, Mouser and Edmund prices updated on 19/05/2023								

Transillumination:

Transillumination components

Item	Part #	Manufacturer	Quantity	Price	Total	Notes
Pre-assembled transilluminator						
Rack and pinion tilt-back transmitted illumination pillar.	P1136/000/000	Cairn	1	1650	1650	
Rack and pinion non-tilting transmitted illumination pillar.	P1136/000/0NT	Cairn	1	875	875	
Simple transmitted illumination pillar with LED mount.	P1136/001/000	Cairn	1	473	473	
LED adapter plate for rack and pinion pillar.	P1136/LED/000	Cairn	1	250	250	
Aura Lite head and controller	P1135/000/002	Cairn	1	1500	1500	
Aura Pro head and controller	P1135/000/003	Cairn	1	1975	1975	
Single channel white MonoLED illuminator.	P1125/000/WHT	Cairn	1	1040	1040	
Cairn Prices updated 25/07/2023						

A4. Github links

openFrame CAD files available at:

https://github.com/ImperialCollegeLondon/openFrame

openAF plugin available at:

https://github.com/ImperialCollegeLondon/openAF

ClusDoC available at:

https://github.com/yalexand/Imperial-ClusDoC